CORA Cork Open Research Archive
Cartlann Taighde Oscailte Chorcaí

Title	Multi–scale simulation of hybrid inorganic–organic films
Authors	Muriqi, Arbresha
Publication date	2023
Original Citation	Muriqi, A. 2023. Multi–scale simulation of hybrid inorganic–organic films. PhD Thesis, University College Cork.
Type of publication	Doctoral thesis
Rights	© 2023, Arbresha Muriqi. - https://creativecommons.org/licenses/by-nc-nd/4.0/
Download date	2026-11-15 00:56:47
Item downloaded from	https://hdl.handle.net/10468/15385



UCC
University College Cork, Ireland
Coláiste na hOllscoile Corcaigh

Multi–Scale Simulation of Hybrid Inorganic–Organic Films

Arbresha Muriqi

Thesis submitted for the degree of

Doctor of Philosophy



National University of Ireland, Cork

Tyndall National Institute

Supervisor: Dr. Michael Nolan

March 2023

Table of content

Declaration 1

Author contributions 1

Acknowledgements 3

List of publications 4

Abstract 6

Chapter 1: Background, motivation and goals

1.1 Introduction on hybrid inorganic-organic films 8

1.2 Overview of thin film deposition techniques 9

1.3 Theoretical modelling of new MLD processes 15

1.4 Goals of my PhD thesis 15

1.5 References 18

Chapter 2: Literature review

2.1 Fundamentals of MLD 19

2.2 Inorganic precursors employed in MLD for hybrid films 23

2.3 Organic precursors employed in MLD for hybrid films 24

2.4 MLD processes for hybrid inorganic-organic films 26

2.5 Crystalline MLD hybrid films 49

2.6 MLD processes for organic polymers 51

2.7 VPI processes for hybrid inorganic-organic polymer films 55

2.8 DFT studies on MLD processes 57

2.9 Summary 58

2.10 References 61

Chapter 3: Theoretical background and methods

3.1 The many-body problem 70

3.2 Computational methodology 82

3.3 References 88

Chapter 4: Modelling of Al-based hybrid films

4.1 Introduction 90

4.2 Modelling of Alucone films 91

4.3 Modelling of hybrid Al_2O_3 films using aromatic precursors 104
4.4 Modelling of Alucone films grown with DMAI 116
4.5 Conclusion 121
4.6 References 123

Chapter 5: Modelling of Ti-based hybrid films

5.1 Introduction 124
5.2 Conclusion 144
5.3 References 145

Chapter 6: Modelling of Mg, Ce and chitin-based hybrid films

6.1 Introduction 146
6.2 Modelling of Magnesicone films 147
6.3 Modelling of Ceria hybrid films 157
6.4 Modelling of Alumochitin and Titanochitin hybrid films 166
6.5 Conclusion 181
6.6 Reference 184

Chapter 7: Modelling of VPI processes

7.1 Introduction 186
7.2 Modelling of Ru VPI films 187
7.3 Modelling of In_2O_3 and ZnO VPI films 194
7.4 Conclusion 205
7.5 References 207

Chapter 8: Precursor chemistry

8.1 Introduction 208
8.2 Copper and Silver precursors 210
8.3 Copper precursors 216
8.4 Cerium and Ytterbium precursors 221
8.5 Yttrium precursors 231
8.6 Europium precursors 239
8.7 Manganese precursors 248
8.8 Conclusion 256

8.9 References 259

Chapter 9: Conclusion

9.1 Summary 261

9.2 Future work 263

9.3 References 265

Declaration

I, Arbresha Muriqi, certify that this thesis is my own work and has not been submitted for another degree at University College Cork or elsewhere.

Author contributions

My contribution to the work described in this thesis was to perform density functional theory (DFT) calculations, analyse and present results, prepare manuscripts and respond to reviewers. For chapters with experimental work, all materials preparation and characterisation were performed by our experimental collaborators.

Për mamin dhe babin

Acknowledgements

Pursuing this PhD has been an incredible experience and I am immensely grateful to all the individuals who have played a part in this journey.

First, I would like to express my deepest gratitude to my supervisor Dr. Michael Nolan. I am deeply thankful for your support, encouragement and assistance throughout every step of my PhD. Beyond the role as a supervisor, you have been a true role model, and I consider myself fortunate to have had the opportunity to work under your guidance.

I would like to thank my thesis committee, Prof. Ralf Tonner-Zech and Dr. Ian Povey for their feedback and valuable discussions. I thank the whole HYCOAT team, especially Jolien Dendooven and Christophe Detavernier for their guidance throughout this project. I would also like to express gratitude to all my collaborators for the significant contribution on different parts of my thesis.

I acknowledge funding through European Union's Horizon 2020 research and innovation program under the Marie Sklodowska-Curie (grant agreement No. 765378). I also acknowledge Tyndall National Institute for providing access to High-Performance Computing resources and also Irish Centre for High-End Computing (ICHEC).

I am very grateful to all the members of the MMD group for the invaluable assistance and the numerous opportunities I've had to learn from each of them. Special thanks goes to Cara and Rita for all the empathic conversations and the wonderful friendship we've cultivated during these years.

A heartfelt thank you to Dona, Bule, Diellza, Gjylije and Leonora for being amazing friends all these years and for being the ones I can always rely on. The warm laughter, uplifting moments and the countless joyful memories hold a significance beyond words for me.

To my beloved grandparents, your love, wisdom, and belief in me have been a cornerstone of my life. Thank you from the depths of my heart for being my source of inspiration and strength. All my gratitude and appreciation to my dad Idriz, my mom Fatime, my brothers Arbër and Ardit and my beloved Serafina. Thank you for your unconditional love. Every day I am motivated by you to become a better person, and I earnestly hope to make you proud. Lots of love to my niece Anika and nephew Kaan, whose tiny moments of joy serve me as daily reminders of life's simple pleasures and wonders.

List of publications

1. **Arbresha Muriqi** and Michael Nolan "First principles study of reactions in alucone growth: the role of the organic precursor", *Dalton Transactions*, 2020, 49, 8710–8721. doi.10.1039/d0dt01376e.

2. **Arbresha Muriqi,** Maarit Karppinen and Michael Nolan "Role of terminal groups in aromatic molecules on the growth of Al_2O_3-based hybrid materials", *Dalton Transactions*, 2021, 50, 17583–17593. doi.10.1039/D1DT03195C.

3. **Arbresha Muriqi** and Michael Nolan, "Role of Titanium and Organic Precursors in Molecular Layer Deposition of 'Titanicone' Hybrid Materials", *Beilstein Journal of Nanotechnology*, 2022, 1240–1255. doi.10.3762/bjnano.13.103.

4. Jeroen Kint, Felix Mattelaer, Sofie S. T. Vandenbroucke, **Arbresha Muriqi**, Matthias M. Minjauw, Mikko Nisula, Philippe M. Vereecken, Michael Nolan, Jolien Dendooven and Christophe Detavernier "Molecular Layer Deposition of "Magnesicone", a Magnesium-based Hybrid Material", *Chemistry of Materials*, 2020, 32, 11, 4451–4466. doi.10.1021/acs.chemmater.9b05116. **Experimental work was carried out at Ghent University Ghent, Belgium.**

5. Nils Boysen, Bujamin Misimi, **Arbresha Muriqi**, Jan-Lucas Wree, Tim Hasselmann, Detlef Rogalla, Tobias Haeger, Detlef Theirich, Michael Nolan, Thomas Riedl and Anjana Devi "A carbene stabilized precursor for the spatial atomic layer deposition of copper thin films", *Chemical Communication*, 2020, 56**,** 13752–13755. doi.10.1039/d0cc05781a. **Experimental work was carried out at Ruhr University Bochum, Bochum, Germany.**

6. Parmish Kaur, **Arbresha Muriqi**, Jan-Lucas Wree, Ramin Ghiyasi, Muhammad Safdar, Michael Nolan, Maarit Karppinen and Anjana Devi "Atomic/Molecular Layer Deposition of Cerium (III) Hybrid Thin Films using Rigid Organic Precursors", *Dalton Transactions*, 2022, 51**,** 5603–5611. doi.10.1039/D2DT00353H. **Experimental work was carried out at Ruhr University Bochum, Bochum, Germany and Aalto University, Espoo, Finland.**

7. Parmish Kaur, Lukas Mai, **Arbresha Muriqi**, David Zanders, Ramin Ghiyasi, Muhammad Safdar, Nils Boysen, Manuela Winter, Michael Nolan, Maarit Karppinen and Anjana Devi "Rational Development of Guanidinate and Amidinate based Cerium and Ytterbium Complexes as Atomic Layer Deposition Precursors: Synthesis, Modelling, and Application", *Chemistry–A European Journal*, 2021, 27, 4913–4926. doi.10.1002/chem.202003907. **Experimental work was carried out at Ruhr University Bochum, Bochum, Germany and Aalto University, Espoo, Finland.**

8. Sebastian M. J. Beer, Nils Boysen, **Arbresha Muriqi**, David Zanders, Thomas Berning, Detlef Rogalla, Claudia Bock, Michael Nolan and Anjana Devi "A study on the influence of ligand variation on formamidinate complexes of yttrium: New precursors for atomic layer deposition of yttrium oxide", *Dalton Transactions*, 2021, 50, 12944–12956. doi.10.1039/D1DT01634B. **Experimental work was carried out at Ruhr University Bochum, Bochum, Germany.**

9. Sebastian M. J. Beer, **Arbresha Muriqi**, Patrick Lindner, Manuela Winter, Detlef Rogalla, Michael Nolan, Andreas Ney, Jörg Debus and Anjana Devi "Ferromagnetic Europium Sulfide Thin Films: Influence of Precursors on Magneto-Optical Properties", *Chemistry of Materials*, 2022, 34, 1, 152–164. doi.10.1021/acs.chemmater.1c02958. **Experimental work was carried out at Ruhr University Bochum, Bochum, Germany.**

10. Nithin Poonkottil, Eduardo Solano, **Arbresha Muriqi**, Matthias M. Minjauw, Matthias Filez, Michael Nolan, Christophe Detavernier and Jolien Dendooven, "Spatially Templated Nanolines of Ru and RuO_2 by Sequential Infiltration Synthesis", *Chemistry of Materials*, 2022, 34, 24, 10347–10360. doi.10.1021/acs.chemmater.2c01866. **Experimental work was carried out at Ghent University, Ghent, Belgium.**

Abstract

The discovery of novel materials and associated process chemistries is crucial for the realization of higher performance electronic devices and the progress of nanotechnology in general. Hybrid materials are a special class of materials with unusual features which are attracting great interest for a wide range of applications. The unique properties of hybrid materials arise from the combination of advantages of both building blocks, i.e., inorganic and organic, which allow material functionalities that are not present in the individual components to be engineered. The properties of these materials can be also tuned depending on the requirements of the application by the choice of the components. Hybrid films are fabricated using molecular layer deposition (MLD) technique, a variant of the widely used atomic layer deposition (ALD) technique, which enables precision and control at the atomistic scale. In recent years, many MLD processes for hybrid films have been developed. However, much less is known about the growth mechanism of hybrid MLD films.

In my thesis I used first principles density functional theory (DFT) simulations to investigate the key steps in the mechanism of hybrid film deposition through MLD, to address open questions around earlier MLD experiments and to predict the most suitable precursors for deposition processes. We build up an atomistic level understanding of the growth chemistry of different types of hybrid films by modelling the relevant MLD deposition processes. In particular, deep investigations on how precursor atomic structure determines film growth, stability and flexibility is carried out. We focus on the key MLD process chemistries, namely alucone and titanicone films, both of high interest for passivation layers in batteries. We assist the interpretation of experimental findings by showing for the first time why the ethylene glycol precursor performs poorly in making stable alucone films and why glycerol is better. For titaiocone films we highlight the role of the substrate and the titanium containing precursors on the initial MLD steps and in film production. We have also predicted that aromatic molecules are a good choice for stable hybrid films and their chemistry can be manipulated without impacting on the stability and this has been borne out by experimental work. Furthermore, we predict suitable MLD chemistries for production of hybrid antibacterial materials. We also study the diffusion phenomena of MLD precursors into polymeric substrates with the vapour phase infiltration (VPI) technique to understand the chemical interactions and corroborate the experimental data on Ru nanostructures and self-healing materials. Finally, we

provide atomic level understanding around novel organometallic precursors and predict their applicability for deposition of oxide and hybrid thin films. The work in my thesis illustrates the key role of atomistic simulations in materials and process development.

Chapter 1

Background, motivation and goals

1.1 Introduction on hybrid inorganic-organic films

The demands on materials for the miniaturization of electronic devices, the discovery of new materials for different layers in nanoelectronic devices, integration of ICT into healthcare and on-device power storage have dramatically increased. Electronic devices are often composed of nanoscale materials. These can be multi-layer stacks of thin films of different materials or extremely complex three-dimensional nanostructures with features as small as a few nanometres. At such small scale the properties of the materials surface and interface have significant effects on device performance. Therefore, it is important that the methods we use to fabricate these devices have nanoscale precision.

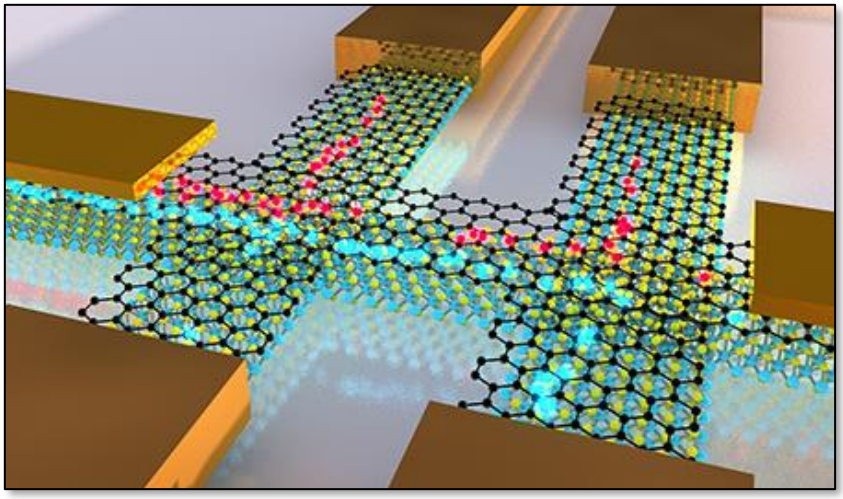


Figure 1 Nanostructure sheets at atomic scale. [1]

Hybrid inorganic-organic materials are a special class of materials that are attracting great interest in many economically and socially relevant technological applications due to their diphasic and tunable inorganic-organic structure. Hybrid materials combine the advantages of solids and polymer/organics to produce novel materials with properties not possible in the individual materials or to provide a key intermediate structure in the production of porous

materials. In recent years molecular layer deposition (MLD) has been developed as an exciting approach that enables the fabrication of ultrathin and conformal hybrid films using sequential, self-limiting reactions. MLD is a variant of the well-known atomic layer deposition (ALD) technique, [2, 3] which is already extensively used in semiconductor industry. MLD enables precision control of the properties of a hybrid material, allowing it to be tuned to the desired application.

As an example, MLD hybrid films are very promising for Li-ion batteries as they are expected to extend their lifetime by solving the serious issue of degradation over time. This is possible by coating the anode with a hybrid material, where as a result of their flexibility the hybrid films can stretch and contract as lithium ions migrate around the battery and this significantly reduces the amount of stress on the anode thus reducing degradation. Additionally, these materials hold a great promise in packaging, encapsulation, solar cells and biomedical applications. [4, 5]

Although a number of MLD processes for hybrid films have been developed, as technology continues to advance, the requirements for these films, their performance and their thickness are becoming more and more strict, and it is becoming increasingly difficult to keep up to these commercial standards. However, the performance of these films can be improved with better mechanistic understanding of the MLD deposition process, which informs a rational approach to the design of new deposition processes. With this in mind, the aim of my PhD thesis is to build up an atomistic level understanding of the MLD chemistry of the deposition of a range of hybrid inorganic-organic materials.

1.2 Overview of thin film deposition techniques

The development of thin films with well-controlled properties is vital for the future of nanotechnology in many applications. Thin films are mostly fabricated via a deposition process, either physical or chemical, which can also impact the properties of the deposited film. For the purpose of my work, in this chapter we focus more on atomic layer deposition (ALD), molecular layer deposition (MLD) and vapor phase infiltration (VPI), and describe briefly physical vapour deposition (PVD) and chemical vapor deposition (CVD) for completeness. A detailed elucidation of all deposition techniques can be found in the Handbook of Thin Film Process Technology. [6]

1.2.1 Physical vapor deposition (PVD)

The physical vapor deposition (PVD) method is widely used for the deposition of metals, alloys, and organic materials. In PVD the material transitions from a condensed phase to a vapor phase and then back to a thin film on a substrate in the presence of a vacuum. The average thickness of various PVD coatings is 2-5 microns. This deposition technique encompasses *sputtering*, *evaporation*, and *ion plating*. PVD deposited films exhibit excellent mechanical properties like hardness and wear resistance and are mostly employed in optical, optoelectronic, microelectronic, and magnetic devices. [7]

1.2.2 Chemical vapor deposition (CVD)

Chemical vapor deposition (CVD) is defined as a vacuum deposition technique that uses chemical reactions of gaseous precursors at a heated surface to produce high quality and high-performance solid materials. CVD is a relatively low-cost deposition technique. The process is mostly used in the semiconductor industry for the fabrication of thin films with a typical thickness 5-10 microns. Variants of CVD include: atmospheric pressure CVD (APCVD), low-pressure CVD (LPCVD), ultrahigh vacuum CVD (UHVCVD), sub-atmospheric CVD (SACVD). These techniques differ mainly by the operating conditions, but they all have the same fundamental chemistry. [8]

1.2.3 Atomic layer deposition (ALD)

Atomic layer deposition (ALD) is a thin film deposition technique that enables the deposition of a variety of thin film materials from the vapor phase. ALD is a modification of the CVD technique. In contrast to CVD, in ALD, gaseous precursors are separately pulsed into the reactor and chemisorb individually onto the substrate, rather than reacting in the gas-phase, which is the origin of the self-limiting nature of ALD, allowing fine control over film deposition and high uniformity and conformality. **Fig. 2** schematically shows an ALD process. One growth cycle of an ALD process consists of the following steps:

1. exposure to a pulse of the inorganic precursor,
2. purge of the reaction chamber,
3. exposure to a pulse of the co-reactant,
4. purge of the reaction chamber.

The individual gas-surface reactions are called “half-reactions”. During each half-reaction, the precursor is pulsed into a chamber under vacuum for a certain amount of time to allow the precursor to fully react with the substrate surface through a self-limiting reactions. Chemisorption ends when all reactive sites are consumed, thus leaving no more than one monolayer at the surface. This self-limiting growth in the ALD process indicates that the amount of material deposited in each reaction cycle is constant. After each precursor pulse the chamber is purged with an inert carrier gas (typically N_2 or Ar) to remove any unreacted precursor or reaction byproducts. The repetition of the ALD cycles will build up a solid inorganic film of high conformity and uniformity and precise thickness control at Ångstrom level. The thickness range of ALD films is usually 1-500 nm. ALD is widely used in microelectronics, energy storage systems, catalysis, and medical areas. [2, 3]

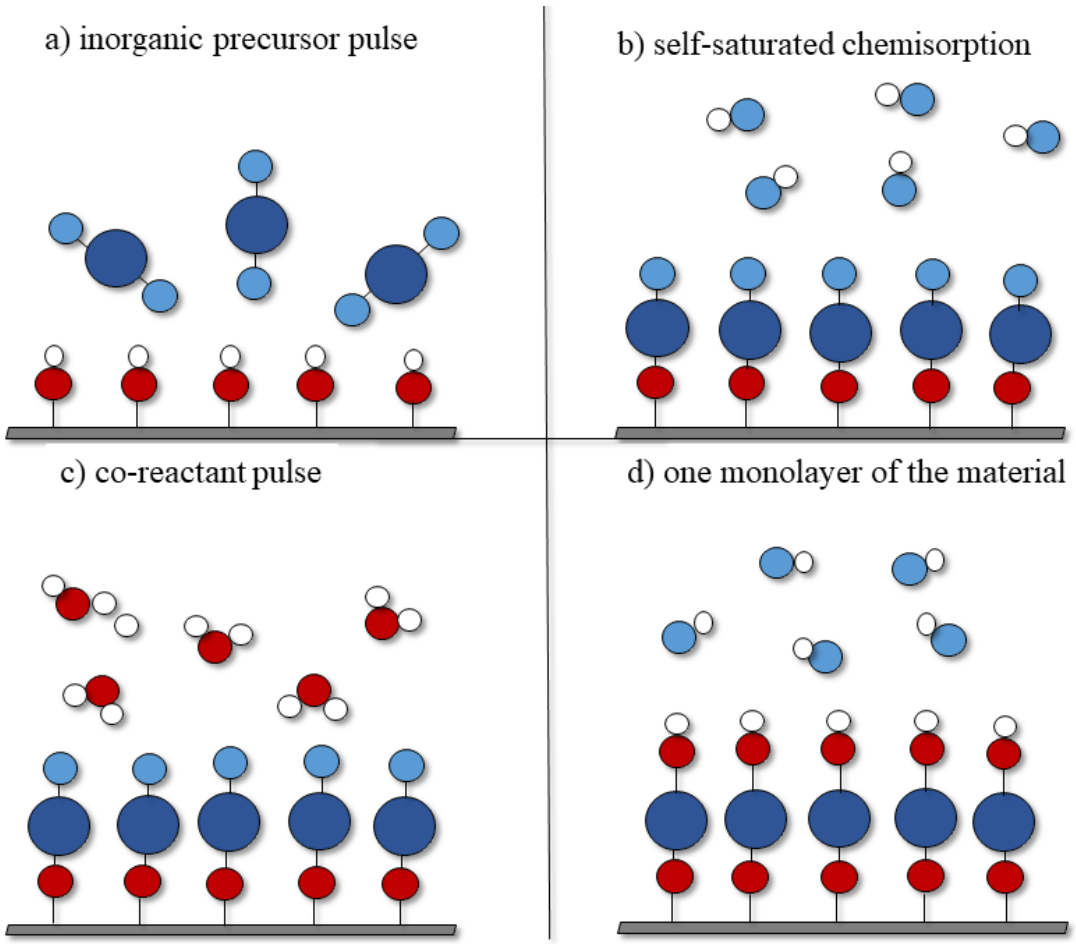


Figure 2 A schematic representation of the initial ALD deposition cycle.

1.2.4 Molecular layer deposition (MLD)

Molecular layer deposition (MLD) is a thin film deposition technique used for the fabrication of hybrid inorganic-organic and pure organic thin films. Similar to ALD, MLD is based on sequential and self-limiting surface reactions. The difference between ALD and MLD is that while ALD uses inorganic precursors and oxygen, sulfur or nitrogen containing molecules to grow oxides, sulphides or nitrides, MLD uses inorganic precursors coupled with bifunctional organic molecules to prepare hybrid inorganic-organic films or only bifunctional organic molecules to prepare pure organic films. Hence, ALD features preciseness in arranging atoms for inorganic materials in a layer-by-layer mode and MLD assembles molecular fragments accurately for hybrid inorganic-organic and pure organic materials. One growth cycle of an MLD process for hybrid inorganic-organic films consists of four steps:

1. exposure to a pulse of the inorganic precursor,
2. purge of the reaction chamber,
3. exposure to a pulse of the organic precursor,
4. purge of the reaction chamber.

Fig. 3 schematically shows an MLD process. In the first step the inorganic precursor is pulsed into the reactor, where it chemisorbs on the surface and reacts rapidly with the surface active groups. Once all surface groups are consumed and the surface saturation is reached, the excess precursor molecules and the released byproductes are removed by purging with an inert gas (typically N_2 or Ar). This first half-reaction is the same as in ALD of inorganic materials.
In the second step, an organic precursor which must have sufficient vapor pressure, stability at the reaction temperature and is reactive towards the inorganic precursor is pulsed into the reactor where it reacts at the inorganic precursor molecules bound at the surface. Again, after the saturation is reached, the excess precursor molecules and the released byproductes are removed by purging with an inert gas. This second half-reaction leaves the surface covered with a molecular layer terminated with active groups of the organic precursor ready to interact with inorganic precursor molecules in the next cycle. The repetition of the MLD cycles will lead to high-quality thin films with excellent precision for the film thickness and composition. [4, 5, 9, 10] Additionally, in MLD the functional groups or the structure of the organic precursors can be tailored to achieve a desired film property or film thickness. This advantage

makes MLD films useful for example in battery electrode coatings [11] or as photoresists in lithographic applications. [12]

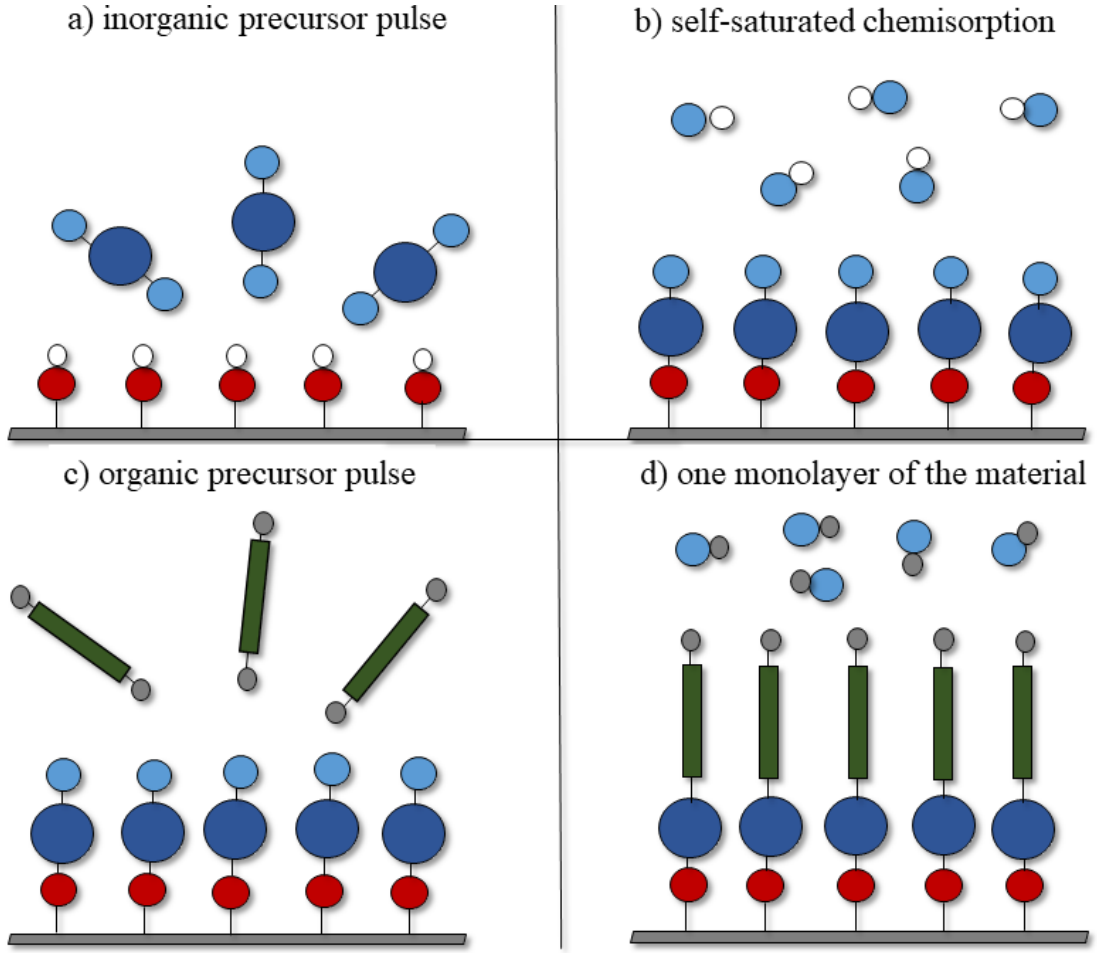


Figure 3 A schematic representation of the initial MLD deposition cycle.

1.2.5 Vapor phase infiltration (VPI)

Vapor-phase infiltration (VPI) is a modification of the ALD technique that enables the hybridization of polymers by incorporating inorganic precursors uniformly into the polymer matrix. The key difference between ALD and VPI lies on the substrate-precursor interactions. While in ALD precursor molecules are adsorbed on the substrate surface, in the VPI process precursor molecules are diffused into the substrate or polymer matrix, **Fig. 4**.

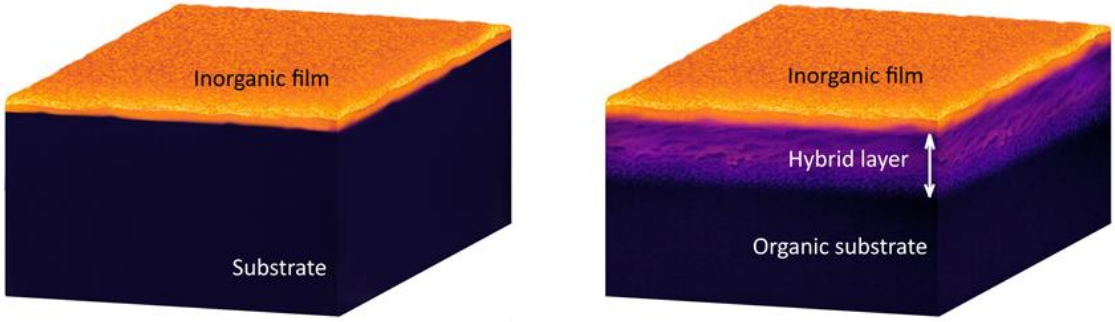


Figure 4 A schematic representation of the difference between ALD resulting thin-film deposition (left) and the VPI resulting hybrid polymer (right).

One growth cycle of a VPI process for hybrid inorganic-organic polymers consists of four steps:

1. exposure to a pulse of the inorganic precursor,
2. purge of the reaction chamber,
3. exposure to a pulse of the oxidation/reducing agent,
4. purge of the reaction chamber.

In the first step, the inorganic precursor is pulsed into the reactor. During this step the inorganic molecules bind with the surface functionalities on the surface and in the bulk. After purging, the oxidation or reducing agent is pulsed into the reactor where it reacts with the first precursor present in the bulk. The resulting polymer-inorganic hybrid films can display very good electrical, optical, and mechanical properties useful for various technological applications. [13-15]

Since the potential of this technique to create hybrid materials was discovered, several variations with different process parameters and names are developed, including: sequential infiltration synthesis (SIS), sequential vapor infiltration (SVI) and multi-pulse infiltration (MPI). However, the atomic-scale mechanisms are identical in all the variations, so they can all be grouped under the more general term which we will use throughout my thesis, namely VPI. [13]

1.3 Theoretical modelling of new MLD processes

Knowledge around precursor chemistries and reaction mechanisms is crucial for the development of new MLD processes for hybrid inorganic-organic films. Computational modelling is a powerful tool that allows us to investigate and understand the atomic level details of the precursor chemistry and the MLD thin film deposition process. Using computational modelling we can predict how the organic precursor atomic structure determines film growth, stability and flexibility and which inorganic precursors are the most convenient for the deposition process. Using theoretical results to inform experiments also makes the whole development process more sustainable. It simplifies the investigation of new thin film deposition chemistries, while less resources and time are also wasted on trial and error.

1.4 Goals of my PhD thesis

Despite the growing interest in these hybrid materials, the lack of theoretical research on hybrid MLD films means that in contrast to ALD of solids, there remains little detailed understanding of the reaction mechanisms and suitable chemistries for hybrid film growth while the atomistic origin of many empirical experimental results are still unknown.

Given this significant challenge, the goal of my research is to use first principles simulations to determine and predict potential MLD chemistries in hybrid film growth, expand our understanding of the growth mechanism of hybrid MLD films and investigate the routes towards novel MLD processes and deposition chemistries for hybrid materials. We also use first principles simulations to study the diffusion phenomena of different precursors into polymeric substrates with the VPI technique and to understand the chemical interactions of the precursors with the polymers.

Moreover, as precursor chemistry plays a key role on the structure, composition, properties and stability of thin films, we also explore atomistic level details of new precursors for different deposition processes. We theoretically predict which precursors will be best for deposition processes, by evaluating (i) precursor stability using simple thermodynamics for precursor decomposition and (ii) precursor reactivity by simulating the chemical reactions with possible co-reactants.

The thesis opens with a literature review on the existing MLD processes for hybrid inorganic-organic and pure organic films and VPI processes for hybrid polymers in **Chapter 2**. A detailed description of the computational methodology is described in the **Chapter 3**. In **Chapters 4** to **8**, the results of ten scientific publications are presented.

In **Chapter 4** we present a detailed comparison between alucones grown with ethylene glycol (EG) and glycerol (GL) precursors to assist the interpretation of experimental findings regarding the differences in the alucone films grown with EG and GL. We found that EG and GL can lie flat and create so-called "double reactions" through the reaction of the two terminal hydroxyl groups with the surface fragments. While this phenomenon removes all active hydroxyl sites for EG and leaves the surface with no active groups to react with the inorganic precursor in the next cycle, GL has an extra hydroxyl group that will be available to react with the inorganic precursor in the next cycle and this will allow the growth to proceed. This study shows for the first time why the EG precursor performs poorly in making stable alucone films and why GL is better. We also present new aromatic organic precursors as alternative, which in contrast to aliphatic organic precursors like EG and GL avoid the unwanted double reactions and enable the ideal layer-by-layer MLD film growth. We show that aromatic molecules have an additional superiority over aliphatic molecules as we can functionalise the core of aromatics to target particular properties while promoting the deposition of thicker and thereby more flexible hybrid films. This work has been highly beneficial for the experimentalists and it allows them to make better choices of organic precursors in the future.

Chapter 5 highlights the role of the phase of titanium dioxide (TiO_2) surface and titanium tetrachloride ($TiCl_4$) and tetrakis(dimethylamido)titanium ($Ti(DMA)_4$) precursors in production of titanicone films. In this study we show that the right surface/Ti-precursor combination can determine the orientation of EG and GL molecules. Moreover, we provide motivation for the experimentalists to develop a new rutile TiO_2-$TiCl_4$-EG/GL based hybrid film suggesting that the desired film growth, flexibility and stability can be achieved.

Chapter 6, **7** and **8** describe the results of combined experimental and computational studies. In **Chapter 6** we support experimental data by predicting suitable MLD chemistries for production of new hybrid materials which are magnesicone, hybrid ceria-organics and metallochitin hybrid films. In **Chapter 7** we presented the first atomistic level studies of infiltration of precursors into polymer films which have enabled production of nm-scale Ru lines for interconnects and self-healing polymer materials. Finally, in **Chapter 8** we provided atomic level details on new cerium (Ce), ytterbium (Yb), copper (Cu), yttrium (Y), europium

(Eu) and manganese (Mn) precursors. The stability and reactivity we evaluated for these precursors allowed us to suggest to experimentalists which precursors would be more convenient for the deposition processes. The precursors we predicted were successfully employed for the deposition of metal oxides and hybrid materials.

This thesis is finalized with a conclusion and outlook over the field of MLD hybrid films and VPI hybrid polymers in **Chapter 9**.

1.5 References

1. https://icn2.cat/en/news/4656-numerical-methods-for-quantum-transport-simulation-in-condensed-matter-a-review. 18 February 2021.
2. M. Leskelä, M. Ritala, *Thin Solid Films*, **2002**, 409, 138–146.
3. R. W. Johnson, A. Hultqvist, S. F. Bent, *Materials Today*, **2014**, 17, 236–246.
4. S. M. George, *Chemical Reviews*, **2012**, 110, 111–131.
5. P. Sundberg, M. Karppinen, *Beilstein Journal of Nanotechnology*, **2014**, 5, 1104–1136.
6. K. Seshan, Handbook of Thin Film Deposition Processes and Techniques, *Noyes Publications*, **2002**, Santa Clara, California.
7. J. E. Mahan, Physical Vapor Deposition of Thin Films, *Wiley-Interscience*, **2000**, Colorado, United States.
8. M. Hitchman, K. Jensen, Chemical vapor deposition: Principles and applications, *Academic Press*, **1993**, London, United Kingdom.
9. X. Meng, *Journal of Materials Chemistry A*, **2017**, 5, 18326–18378.
10. J. Multia, M. Karppinen, *Advanced Materials Interfaces*, **2022**, 9, 2200210.
11. Y. He, D. M. Piper, M. Gu, J. J. Travis, S. M. George, S-H. Lee, A. Genc, L. Pullan, J. Liu, S. X. Mao, J-G. Zhang, Ch. Ban, Ch. Wang, *ACS Nano*, **2014**, 8, 11816–11823.
12. D. H. Kim, S. E. Atanasov, P. Lemaire, K. Lee, G. N. Parsons, *ACS Applied Materials and Interfaces*, **2015**, 7, 3866–3870.
13. C. Z. Leng, M. D. Losego, *Materials Horizons*, **2017**, 4, 747–771.
14. I. Azpitarte, M. Knez, *MRS Communications*, **2018**, 8, 727–741.
15. A. Subramanian, N. Tiwale, Ch-Y. Nam, *JOM-Journal of the Minerals, Metals & Materials Society*, **2019**, 71, 185–196.

Chapter 2

Literature review

2.1 Fundamentals of MLD

2.1.1 Surface chemistry in MLD

The understanding of the reaction mechanisms of current molecular layer deposition (MLD) processes is essential for future innovation for depositing hybrid inorganic-organic thin films by MLD. To understand the growth mechanism of MLD films, the nature of the MLD growth steps must be understood. **Fig. 1** presents a schematic of the growth steps in both MLD half cycles.

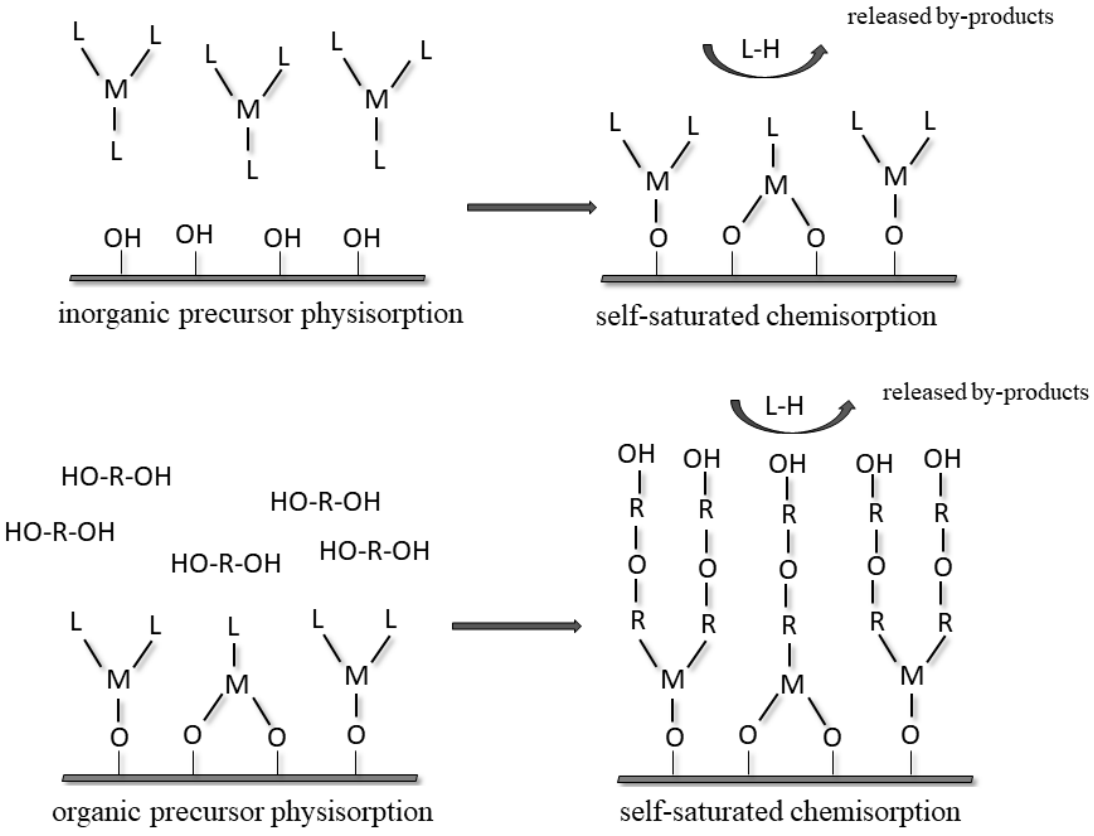


Figure 1 A schematic representation of MLD growth steps. M-metal, L-metal ligands, R-organic backbone and OH-active groups of organic molecules.

The first step in each MLD half-cycle is the molecular physisorption of a precursor onto a surface. The role of surface reactive sites is crucial as reaction intermediates. The surface is usually covered with hydroxyl groups which serve as reactive linkers for condensation

reactions with metals. The second step is chemisorption, where the inorganic precursor reacts with surface reactive sites via the corresponding linking chemistry which leads to the formation of new O-metal bonds. The metal precursor step changes the surface termination, leaving the surface with new reactive sites that enable the chemisorption of the organic precursor. The organic precursor reacts at the resulting surface by bonding covalently with the metal sites, releasing metal ligands and again changes the surface termination leaving it with another reactive molecular layer ready for the next pulse. By-products are released after each precursor pulse as a result of the ligand exchange reactions. [1-4]

Surface reactions for the hybrid films grown with trimethylaluminium (TMA) and ethylene glycol (EG) are interpreted as follow:

$$|\text{–OH} + \text{Al(CH}_3\text{)}_3\,(g) \rightarrow |\text{–O–Al(CH}_3\text{)}_2 + \text{CH}_4\,(g) \quad (1)$$

$$|\text{–O–Al(CH}_3\text{)}_2 + 2\text{HOCH}_2\text{CH}_2\text{OH}\,(g) \rightarrow |\text{–O–Al(OCH}_2\text{CH}_2\text{OH)}_2 + 2\text{CH}_4\,(g) \quad (2)$$

2.1.2 MLD process features

The MLD deposition process is generally evaluated by monitoring the film growth rate as a function of deposition parameters such as precursor pulse length, purge length, deposition temperature etc. The growth rate is expressed as the growth per cycle (GPC) value and is calculated from the total film thickness divided by the number of precursor cycles applied.

In MLD, the precursor-surface reactions occur in a self-limiting, surface-saturated manner. In order to ensure the self-limiting growth, sufficiently long precursor pulsing times have to be allowed in each step. This allows surface saturation and its full coverage with precursor molecules after each precursor pulsing step.

In addition, the purging times must be sufficiently long so that all unreacted precursor molecules and released by-product molecules can be removed in order to avoid the chemical reactions of molecules at gas phase and the undesired CVD film growth. However, very long purge times can also limit the deposition rate of the process. [5]

In the ideal MLD film growth, the GPC value is expected to increase and saturate with increasing the pulse length of either precursor and the film thickness shows a linear dependence on the number of deposition cycles, **Fig 2**. [2]

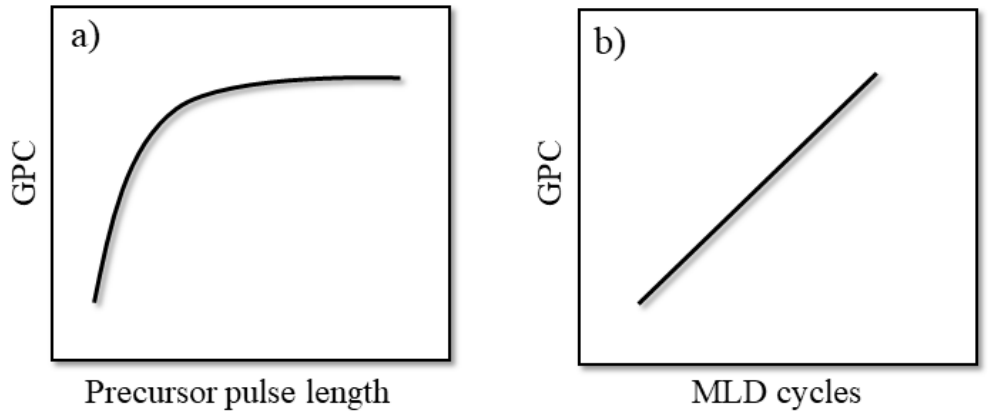


Figure 2 Ideal MLD process shows a) saturation of the GPC value with increasing precursor pulse lengths and b) linear dependence of the GPC on the number of MLD cycles.

Temperature is also a very important factor for the successful deposition of MLD films. The range of temperature in which the film growth remains constant and the self-limiting stage after each precursor pulse is reached is known as "MLD window". Temperatures above this range lead to precursor decomposition or precursor desorption while temperatures below this range lead to insufficient precursor reactivity or precursor condensation. All these phenomena can promote a non-ideal film growth, as indicated in **Fig. 3 (a)**.

In addition, for most of the MLD films, it was observed that even within the MLD window, the GPC decreases with increasing the temperature, **Fig. 3 (b)**. This can be related to (i) the tendency of the metal precursor to remain in excess in the porous organic layer more readily at low temperatures, and/o (ii) the tendency of the sticky low vapour pressure organic molecule to get incorporated as a kind of reservoir within the growing film at low temperatures. In both cases the excess precursors would act as extra reaction sites for the film growth. The decomposition of the MLD film at high temperatures might also be a reason for the decrease of GPC.

Another very important factor that can enhance or inhibit the film growth, especially in the initial steps, is the deposition surface. To enhance film growth, a compatibility of chemistries between the deposition surface and the growing film must exist. [2, 4]

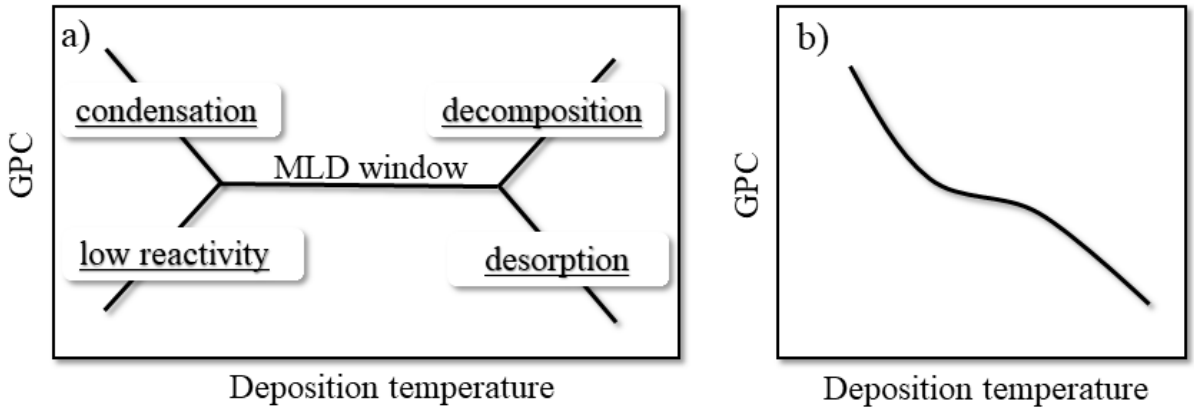


Figure 3 Dependence of the film growth on the deposition temperature: a) within the MLD window the GPC remains constant with increasing temperature and b) the GPC value often decreases with increasing deposition temperature.

2.1.3 MLD precursor requirements

Precursor chemistry plays a key role in MLD. The chemical properties of the selected precursor molecules define the structure, composition and stability of the deposited material. Therefore, MLD precursors must fulfil a list of requirements. First, precursors should be commercially available or easy to synthesise and handle. Second, as for the ALD process, the precursors in the MLD process must be chemically stable in the deposition temperature range so that they do not undergo thermal decomposition and must have sufficient vapor pressure to achieve sufficient precursor dosing. [6] MLD precursors should not decompose until they have reached the surface and nor should the by-products released after the precursors have reacted with the surface. This is essential for self-limiting growth. Generally, gaseous and liquid precursors are more preferred as they have enough vapour pressure at room temperature and require limited to no heating.

MLD precursors should also be sufficiently reactive towards the surface and towards each other. For this, the inorganic precursors should consist of reactive ligands attached to the metal atom and the organic precursors should consist of reactive functional groups attached to the organic backbone. This enables surface saturation in a short time and ensures a reasonable deposition rate. The MLD surface-precursor and precursor-precursor reactions should have large negative ΔG values which shows that the free energy of the final product is lower than the free energy of the reactants. The negative ΔG values signify the exothermic (favourable) surface-precursor and precursor-precursor reactions. [2, 7-10]

2.1.4 MLD film characterisation

The deposited MLD thin films are generally characterized by multiple techniques. For the chemical properties of MLD films which include elemental composition, bonding features, chemical state and local symmetry, techniques such as X-ray photoelectron spectroscopy (XPS), [11] Fourier transform infrared spectroscopy (FTIR), [12] Raman spectroscopy, [13] angle resolved XPS, [14] and resonant inelastic X-ray scattering (RIXS) are applied. [15] For their physical properties, such as the magnetic and optical properties and ionic conductance, alternating current impedance (AC impedance), [16] ultraviolet-visible spectroscopy (UV-VIS) [17] and vibrating sample magnetometer (VSM) [18] are employed.

Mechanical properties such as elastic modulus, hardness and fragmentation are measured through nanoindentation and optical microspectroscopy. [19] For the film structure, roughness and morphology, techniques as transmission electron microscopy (TEM), [20] atomic force microscopy (AFM), [21] scanning electron microscopy (SEM), [22] and energy dispersive X-ray spectroscopy (EDX) [23] are used. Crystal structure and orientation is evaluated through optical microscopy, [13] grazing incidence X-ray diffraction (GIXRD) [14] and grazing incidence wide-angle X-ray scattering (GIWAXS). [24] Finally, the film thickness is evaluated via X-ray reflectivity (XRR) and spectroscopic ellipsometry (SE). [11]

2.2 Inorganic precursors employed in MLD for hybrid films

The inorganic precursors employed in MLD for hybrid inorganic-organic films are generally very similar to those used in ALD processes for inorganic films. At first most of the MLD inorganic precursors were based on the metals Al, Ti and Zn. Inorganic precursors based in these metals tend to also be the most common precursors in ALD. [2-4, 7-9] Later on, the library of metallic precursors expanded to include many other metal components from s-block, d-block, p-block and f-block of the periodic table. The choice of the metallic precursor depends on the desired functionalities of the deposited film, e.g., s-block metal → battery, [25] d-block metal → magnetism [26] or catalysis, f-block metal→ luminescence. [27]

MLD requires metallic precursors with reactive ligands (halide ions or organic ligands) attached to the metal atom so that they can successfully chemisorb on the surface and react with the available organic molecules. The variety of ligands employed in MLD is the same as in ALD and is relatively large including different halides, alkyls, alkoxides, alkyl amides,

cyclopentadienyls and metallocenes, while homoleptic and heteroleptic precursors have been utilized. The choice of the ligands attached to the metal atom is highly motivated by the stability and the sublimation temperature of the metallic precursor, which must match well with stability and the sublimation temperature of the employed organic precursor.

The choice of the ligand size is very tricky in MLD. Bulky ligands usually cause steric hindrance and can block the active sites in the surface, leading to films with low GPCs. On the other hand, it was noticed that metallic precursors with small ligands tend to infiltrate into the porous MLD film during the deposition process and cause so the "reservoir" effect, which complicates the growth and leads to low GPCs. [28] These deviations from the ideal behaviour can be improved by optimizing the process parameters. [9]

2.2.1 Reservoir effect

While in the ideal MLD the precursor molecules chemisorb on the substrate surface where the film growth happens, it was found that in reality this is not always the case. Very often precursor molecules infiltrate into the growing film and undergo the reservoir-like effect as reported also for ALD. [29, 30] In reference [11] the growth of alucone films is demonstrated using the sequential exposures of trimethylaluminum (TMA) and ethylene glycol (EG). Films were deposited in a wide range of temperatures from 85°C to 175°C. It was found that the GPC of the film decreased from 4.0 Å/cycle at 85°C to 0.4 Å/cycle at 175°C and it was believed that this decrease of GPC with temperature was due to the infiltration of TMA molecules into the growing film. TMA infiltration was observed also for alucone films grown in a three-step ABC reaction sequence using ethanolamine (EA) and maleic anhydride (MA) as organic reactants where the film growth rapidly decreased from 24 Å/cycle at 90°C to 4 Å/cycle at 170°C. [20] The infiltration phenomenon can be avoided with long purge times, however, the very long purge times significantly decrease the GPC. [5] It was found that except of TMA, other metallic precursor molecules such as diethylzinc (DEZ) [31] and also organic molecules as EG [32] also undergo the reservoir-like effect.

2.3 Organic precursors employed in MLD for hybrid films

The proper design of organic precursors is very important in MLD of hybrid films. The organic precursor consists of a backbone that can be aliphatic or aromatic which remains in the hybrid

film and the functional groups which are mostly responsible for the reactivity towards the inorganic precursor.

Organic precursors with hydroxyl (OH), [33] thiol (SH), [34] amino (NH_2), [35] carboxylic acid (COOH) [36] and sulfonic acid (SO_3H) [15] terminal groups have successfully been employed in MLD for the deposition of hybrid films. The choice of the terminal group naturally defines which atom of the organic precursor (O, N or S) is bonded to the metal atom of the inorganic precursor in the resultant hybrid film and this is important for the film properties.

As mentioned above, MLD precursor must meet some requirements, such as have sufficient vapor pressure, be stable at the reaction temperature and be reactive towards the inorganic precursor. However, finding organic precursors that meet these requirements is not that simple. For example, many organic precursors reveal low vapour pressure at room temperature and heating is needed to reach the sufficient precursor supply. Additionally, organic precursors that exhibit a balance between the thermal stability and reactivity are rare. Organic precursors used in MLD must have sufficient thermal stability to be transported into the reactor in the gas phase without decomposing and at the same time be reactive towards the inorganic precursor to get involved in the MLD reactions. [6]

Thermogravimetric analysis (TGA) and differential scanning calorimetry (DSC) have been utilized as convenient techniques to study the volatility and thermal stability of precursors and select the best candidates for a successful MLD film deposition. [37]
In the ideal case, the GPC of one MLD cycle would correspond to the length of the metal-organic unit length. However, in practice much smaller GPC values are observed. This because many organic precursors are flexible molecules that may lie flat and react twice with the surface through the terminal groups. Ideally, the organic precursor molecule should react with one surface site only and remain upright. The phenomenon of the organic precursor molecules lying flat and reacting with the surface with both active groups is known as the “double reaction” phenomenon. **Fig. 4** shows both orientations cases possible for organic molecules. These double reactions will reduce the number of active groups in the surface, depress the film GPC and give less flexible films. [38-40]

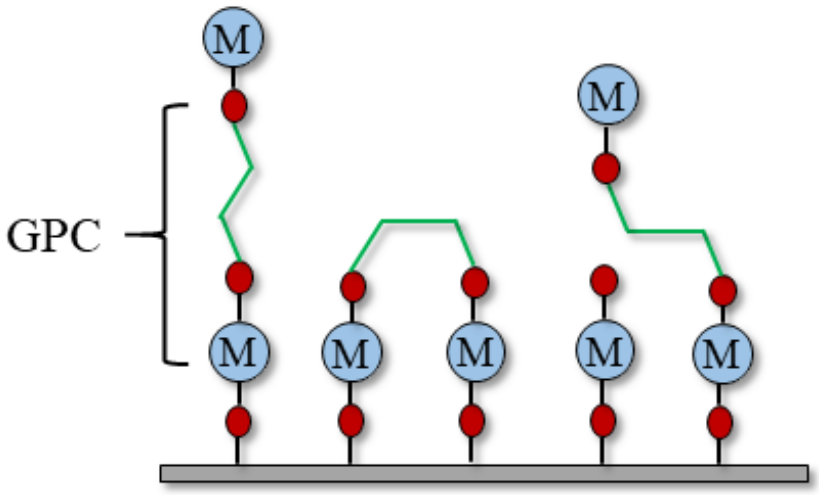


Figure 4 Ideally, the organic precursor molecule reacts with one surface site only and remains in the upright configuration (left). The organic precursors can also tilt (right) or lie flat and react twice with the surface (middle).

One way to avoid this phenomenon is by using aromatic based organic precursors instead of alkyl based organic precursors. Because of their stiff backbone, such molecules have been considered as a possible solution to reduce the number of double reactions that hinder the film growth. In addition, aromatic molecules are of high interest as they are easy to work with, stable in air, volatile when heated and thermally stable. [41] Other possible solutions for the reduction of double reactions are considered and these include: using heterobifunctional precursor molecules, [42] using precursors in which ring-opening reactions occur [43] and by using a three step or four step reaction sequence. [20] Similar to metallic precursors, organic precursor molecules can also undergo the "reservoir" effect, which causes derivations from the ideal growth and leads to low film GPCs. [32]

2.4 MLD processes for hybrid inorganic-organic films

Hybrid inorganic-organic MLD films are ultrathin films with high flexibility, tunable properties and excellent mechanical and electronic properties resulting from the combination of the individual properties of the organic and inorganic components that are incorporated into the film. [2, 3, 44-46] A special class of hybrid inorganic-organic films are metal alkoxides known as metalcones. Metalcones are fabricated with MLD using halide or organometallic precursors and organic alcohols. These films are described as O-M-O-$(CH_x)_y$-O-M-O.

Metalcones are known to be flexible in nature due to the flexible organic backbones present in their architectures and with excellent mechanical properties at the atomic and molecular level arising from the metallic precursors. [38, 39, 47]

The first metalcone films were aluminium based and were known as "alucones. [11] Soon after, other metalcone groups were developed, such as the titanium, zinc, hafnium, magnesium and vanadium based metalcones known as "titanicones", [48] "zincones", [40] "hafnicones, [49] "magnesicones" [32] and "vanadicones", [23] respectively. While the variety of functional groups of organic molecules has increased and other organic backbones, e.g. aromatic rings, have been used, the field tends to use the term "metalcone" as a general description for these hybrid materials.

2.4.1 Aluminium based processes

Alucone films were the first metal based MLD processes reported. The predominant aluminium precursor employed in alucone film growth is trimethylaluminium (TMA, $Al(CH_3)_3$) combined with variety of organic molecules including ethylene glycol (EG), [11, 33, 50-53] glycerol (GL), [25, 33, 52] 1,4 butanediol (BDO), 1,6 hexanediol (HDO), [19] 1,10-decanediol (DDO), [54] 1,4-butynediol (BDy), [55] triethanolamine (TEA), [56] hydroquinone (HQ), [50, 51, 57-59] quinizarin (H_2Qz), [60] 8-hydroxyquinoline (8-HQ), [61] 4-aminophenole (AP), [59] p-penilendiamine (PD), [59, 62] 7-octenytrichlorosilane (7-OTS), [63, 64] trimethyl-trivinylcyclotrisilazane (V_3N_3), [65] 2,4,6,8-tetramethyl-2,4,6,8-tetravinylcyclotetrasiloxane (V_4D_4), [66] ethanolamine (EA), [20, 67] terephthaloyl chloride (TC), [68] maleic anhydride (MA), [20] methyl-methacrylate (MMA), [67] phenol, 3-(trifluoromethyl) phenol, 2-fluoro-4-(trifluoromethyl)benzaldehyde, [43] ε-caprolactone (LAC), [69] glycdiol, [70-72] oxalic acid (OX), malonic acid, succinic acid, glutaric acid, pimelic acid, suberic acid, sebacic acid, [36] tricarballylic acid, *trans*-aconitic acid, L-glutamic acid, [73] benzene dicarboxylic acid and 1,2,4,5-benzene tetracarboxylic acid. [74] Dimethyl aluminum isopropoxide (DMAI, $(CH_3)_2Al(OC(CH_3)_2)$) has also successfully been employed in combination with EG for alucone films. [5]

The first reported alucones were grown using TMA and ethylene glycol (EG, $HO(CH_2)_2OH$) as MLD precursors, [11] which to date remain the most common precursors used to deposit these films. The deposition was done on Al_2O_3 surfaces in a temperature range of 85°C to 175°C. In situ QCM and ex situ XRR experiments showed that surface reactions were

saturating and self-limiting and the film growth was linear with the number of TMA-EG cycles. The GPC of the resulting films was temperature dependent and it decreased from 4.0 Å/cycle at 85°C to 0.4 Å/cycle at 175°C.

Given the decrease of the GPC with increasing temperature, alternative mechanisms, which lead to small GPCs, were proposed. During the film growth, TMA molecules may diffuse into the MLD film in addition to reacting with -OH species, causing the "reservoir" effect. Moreover, as FTIR and QCM measurements showed no noticeable O-H stretching vibrations, it was assumed that the two terminal groups of the EG molecules might have reacted with surface -$AlCH_3$ species by Lewis acid/base interactions resulting in the double reactions. **Fig. 5** shows schematically the MLD reaction products between TMA and EG in the upright and flat configuration. The resulting alucone films were not stable in air and their composition changed due to either dehydration or dehydrogenation. [11]

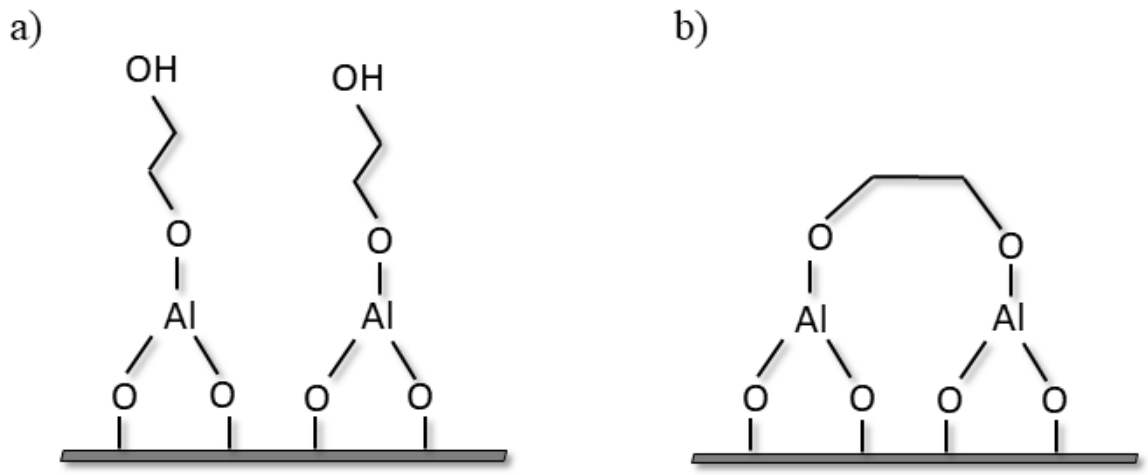


Figure 5 Schematic illustration of reactions between TMA and a) EG molecule in the upright configuration and b) EG in the lying flat configuration.

Alucone films have been tested as materials in gas-barrier and Li-ion battery applications. However, films with organics with a short carbon chain length are relatively brittle. Therefore, later on, similar molecules to EG, 1,4 butanediol (BDO, $HO(CH_2)_4OH$) and 1,6 hexanediol (HDO, $HO(CH_2)_6OH$) were combined with TMA. Films were deposited on a Si surface in a temperature that ranges from 100°C to 160°C. BDO and HDO have a longer carbon chain compared to EG and therefore the resulting films displayed greater flexibility and higher GPCs. However, the GPC of the resulting films also decreased with increasing the temperature, most

probably due to the double reactions which for BDO and HDO are more favourable than for EG owing to the longer carbon chain length. [19]

In another study, TMA was combined with HDO and 1, 10-decanediol (DDO, $HO(CH_2)_{10}OH$) to demonstrate an effective approach to tune mechanic properties of the films. Films were deposited on a Si surface at130°C. The obtained GPC values are 3.2 Å/cycle for the TMA-HDO process and 3.7 Å/cycle for the TMA-DDO process. As DFT calculations indicated a height of 8.4 Å for the upright configuration of HDO in the TMA-HDO process, [19] the obtained GPCs for the TMA-HDO and TMA-DDO suggest that organic molecules are either tilted or lie in a flat configuration and form the double reactions. However, it was noticed that the stretchability increases with increasing chain length, showing that the flexibility of the films can be increased through the control over the organic precursor chain length. [54]

As the investigated organic molecules for alucone films resulted in double reactions, which lead to unstable films with low GPCs and poor quality, the possibility to avoid the unwanted double reactions was explored by combining with TMA with a *sp*-hybridized precursor, 1,4-butynediol (BDy, $HOCH_2C{\equiv}CCH_2OH$). The process was developed at 80°C on KBr pellets. To evaluate film properties, TMA-BDy films were compared to TMA-BDO films. Unfortunately, the properties of TMA-BDy films were similar to those of TMA-BDO films, with a obtained GPC value of 0.8-0.9 Å/cycle, suggesting the occurrence of double reactions regardless of the presence of carbon-carbon triple bonds. [55] **Fig. 6** shows schematically the MLD reaction product of TMA and BDy.

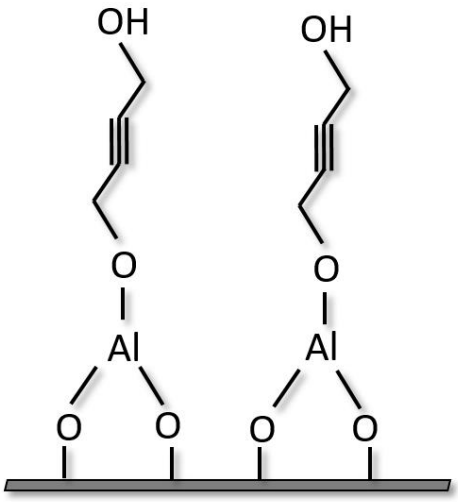


Figure 6 Schematic illustration of reactions between TMA and BDy.

Another common organic molecule now used widely in alucone film growth is glycerol (GL, $HOCH(CH_2OH)_2$). [25, 33, 52] In contrast to EG, BDO and HDO, and BDy, which are diol molecules, GL is a triol and has an extra OH group. In a recent study, [33] a direct comparison between alucone films grown using EG and GL molecules was done. Both films were deposited in a range of temperature 100°C to 145°C on a Si surface. While linear and saturated growth was obtained in this temperature range, a decrease in GPC with increasing temperature was observed for both processes. However, the decrease was less pronounced for the GL based process. For the EG based process, the GPC decreased from 2.2 Å/cycle at 100°C to 1.1 Å/cycle at 145°C; for the GL based process, the GPC decreased from 3.0 Å at 100°C to 2.5 Å at 145°C. **Fig. 7 (c)** shows the growth profile observed for both films. The decrease in GPC was attributed to the double reactions of the EG and GL at the surface which are more likely to appear at high temperatures. For EG, double reactions leave the surface with no OH sites as shown in **Fig. 7 (a)** so the growth is less favourable, while for GL, the third OH group is available and promotes film growth, as shown in **Fig. 7 (b)**. The third OH group of GL leads to increased bridging in the structure and therefore to better mechanical properties of the film. [33] TMA-GL films were also successfully employed to modify nano-Si electrodes and significantly improved the mechanical properties and electrochemical performances of the Si anode. [25]

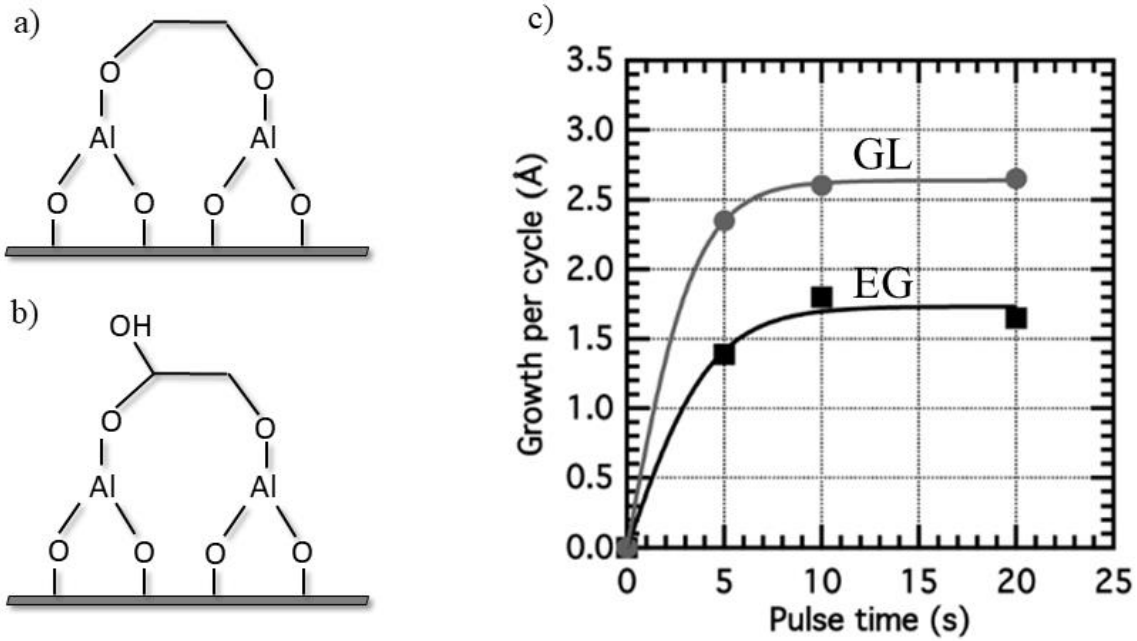


Figure 7 Schematic illustration of reactions between TMA and a) EG molecule in the flat configuration b) GL molecule in the lying flat configuration and c) growth profile of EG and GL based alucones. [33]

In addition to aluminium alkoxides, amine containing alucone films were also fabricated by employing tertiary amine groups into the organic linkage. [56, 75] Triethanolamine (TEA, $N(CH_2CH_2OH)_3$) was coupled with TMA for amine containing films in a temperature range 150°C -195°C on a SiO_2 surface. **Fig. 8** shows the possible MLD product from TMA and TEA. The TMA-TEA process resulted in temperature depended where the growth decreased from 6.7 Å/cycle at 150°C to 0.8 Å/cycle at 195°C. It was believed that the decrease of the GPC of TMA-TEA at higher deposition temperatures is due to TMA diffusion out of the film. Films were considered relatively stable because any film degradation occurred primarily during the deposition process. Films indicated absorptive and colour-changing properties which make these films attractive for sensor and filtration applications. [56]

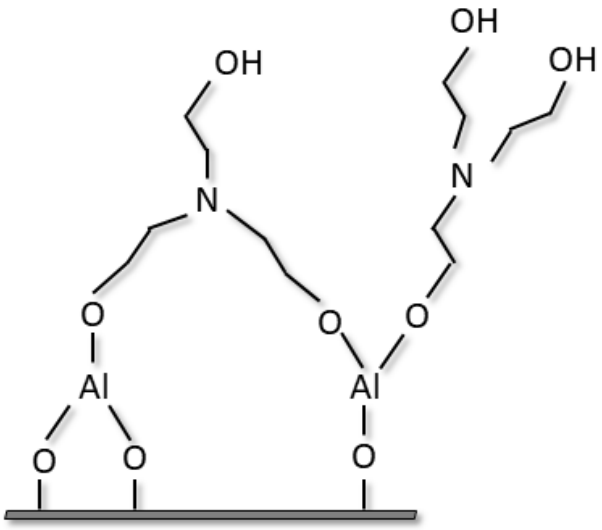


Figure 8 Schematic illustration of reactions between TMA and TEA.

To avoid the unwanted double reactions of the homobifunctional organic molecules discussed above, heterobifunctional organic molecules were also suggested as a possible solution. This because heterobifunctional organic molecules might react with the surface preferentially with only one terminal active group. Glycidol (GLY, $C_3H_6O_2$) is a heterobifunctional organic molecule that was combined with TMA in a two-step reaction to deposit solid alucone films. [70-72] In reference [70] films were deposited in a temperature range of 90°C to 150°C on a Si surface. It was assumed that, GLY undergoes a ring-opening reaction that yields to Al-O-CH_2-$CH(CH_3)$-CH_2-OH or Al-O-CH_2-$CH(CH_2$-$CH_3)$-OH species. The remaining OH groups then react with TMA during the next step. It was found that the GPC of TMA-GLY films

decreases from 2.4 Å/cycle at 90°C to 0.6 Å/cycle at 150°C. The obtained GPC value showed that although GLY is a heterobifunctional organic molecule, it was not successful in preventing the double reactions. However, the resulting films were highly conformal and more stable in air compared to TMA-EG films. [70]

Cyclic ε-caprolactone (LAC, $C_6H_{10}O_2$) also undergoes ring opening reactions when combined with TMA. TMA- ε-caprolactone films were deposited in a temperature range of 60°C to 120°C on Si substrate. This process resulted in temperature depended with GPCs decreasing from 0.75 Å/cycle at 60°C to 0.08 Å/cycle at 120°C. However, deposited films showed good stability over 30 days in ambient. [69]

Alucone films were also fabricated by combining TMA with seven different carboxylic acids including: oxalic acid (HO_2CCO_2H), malonic acid ($HO_2CCH_2CO_2H$), succinic acid ($HO_2C(CH_2)_2CO_2H$), glutaric acid ($HO_2C(CH_2)_3CO_2H$), pimelic acid ($HO_2C(CH_2)_5CO_2H$), suberic acid ($HO_2C(CH_2)_6CO_2H$) and sebacic acid ($HO_2C(CH_2)_8CO_2H$). The selected organic molecules range from 2 to 10 carbon atoms in the molecular structure. Films were deposited on Si surfaces and the MLD processes were performed at a deposition temperature ranging between 114°C and 332°C. Exceptionally high GPCs were achieved for all processes, where the highest GPC was 43 Å/cycle for the TMA-pimelic acid process. This GPC is much higher than expected, as the length of the carbonic chain of the pimelic acid molecule is much smaller (≈ 16 Å). This high GPC might be a result of a condensation reaction of pimalic acid. However, this is difficult to assess from experimental work. Temperature dependent growth was observed for all systems but no details on how much the growth decreases were given. All processes yielded smooth, transparent and with a high refractive index. Moreover, all films were stable in contact with water, except TMA-oxalic acid films and TMA-malonic acid films. [36]

Later on, glutaric acid, tricarballylic acid ($HO_2CCH(CH_2CO_2H)_2$, *trans*-aconitic acid (HO_2C-CH_2-CO_2HC=CH-CO_2H) and the L-glutamic acid (HO_2C-$(CH_2)_2CHNH_2CO_2H$) were combined with TMA. Films were deposited on Si surfaces in a wide temperature range, from 150°C to 350°C. Apart from the TMA-tricarballylic acid films, for which an ideal growth was found, the other processes were temperature dependent and the GPCs decreased with increasing the deposition temperatures. It was proposed that the decrease in GPC when increasing temperature may be from the formation of volatile complexes that etch the surface, or alternatively, the increased steric hindrance of the active sites as a result of increased thermal motion of the precursor molecules at higher temperatures. It seemed like the presence of double

bonds pushed more towards bridge-complexing mode and introduced more stiffness in the film, which then affected the structural properties of the film. Also, the combination of NH_2 and COOH, seemed to induce a higher structural order in the material. [73]

In search of molecules that avoid double reactions, aromatic molecules such as hydroquinone (HQ, $C_6H_6O_2$)), [50, 51, 57-59, 76] quinizarin (H_2Qz, $C_{14}H_8O_4$), [60] and p-phenylenediamine (PD, $C_6H_8N_2$), [59, 62] were also combined with TMA. Due to their stiff backbone, aromatic molecules are expected to be less flexible and reduce the possibility of double reactions on the surface, yielding higher GPCs and more stable hybrid films. In reference [58] HQ was combined with TMA to fabricate alucone coatings for Si electrodes. TMA-HQ films were deposited directly on the nano-Si composite electrodes in a temperature of 150°C. The electrodes were coated with five cycles of TMA-HQ films where each cycle gave a GPC of 7.5 Å/cycle. A Si anode that is reversible and capable of high performance and high rate was demonstrated by applying these robust and conductive TMA-HQ coatings. [58]

In another study TMA-HQ films deposited in a temperature range 150°C to 225°C on a Si surface gave a GPC of 4.1 Å/cycle at 150°C that decreases to 3.5 Å/cycle when the temperature is increased to 225°C. The GPC of the films revealed that the possibility of the occurrence of any "double reactions" is dismissed even with some tilting of the organic. Films were not fully air stable, however, degradation in ambient conditions occurred slowly enough that it was possible to characterize the films. [77] To enhance stability and make characterization more reliable, protection of the films was done by an additional capping with an Al_2O_3 layer. [77]
PD has also been reported to react with TMA for the growth of alucone films. In contrast to HQ, PD contains two NH_2 active groups instead of OH groups and therefore during the MLD process Al-N bonds are formed instead of Al-O bonds. The deposition of TMA-PD films was done on a Si surface in a temperature range of 200°C to 400°C. The deposited films showed poor stability in air, similar to TMA-HQ films, [77] which was however dramatically improved by alloying with Al_2O_3 layers. Moreover, the 1:4 alloy (TMA-PD/Al_2O_3) displayed tunable electrical properties. [62] **Fig. 9** shows the MLD reaction products of TMA with (**a**) HQ and (**b**) PD.

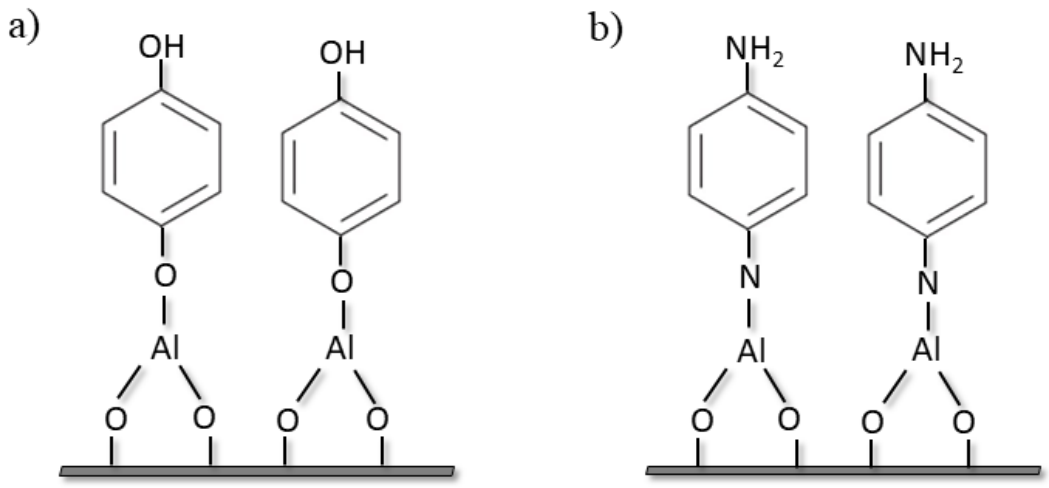


Figure 9 Schematic illustration of reactions between TMA and a) HQ and b) PD.

In a recent study TMA-H_2Qz films were deposited at 175°C on a Si surface gave a GPC of 28 Å/cycle. Films were quite stable in air. The large conjugated system of H_2Qz together with its low sublimation temperature (130°C) and the good reactivity made this molecule very attractive for the development of other MLD films based on H_2Qz along many different technological pathways. [60]

In another study TMA was combined with 1,2, 1,3, and 1,4 benzene dicarboxylic acid ($C_6H_4(CO_2H)_2$) molecules, 1,3,5-benzene tricarboxylic acid ($C_6H_3(CO_2H)_3$) and 1,2,4,5-benzene tetracarboxylic acid ($C_6H_2(CO_2H)_4$). The temperature range for all processes was 186°C to 332°C. The deposition was done on Si surfaces. Obtained GPCs of all processes were in the range of 2.5 - 13.4 Å/cycle and these decrease as the temperature increases. The decrease of the GPC with increasing the temperature was partly attributed to the infiltration of TMA molecules into the film and partly to the high thermal motion which prevents the adsorbed organic molecules to arrange in the ideal configuration in the substrate. However, the origin for the lower GPC at higher temperatures is very difficult to assess without closer investigations. FTIR measurements proved the hybrid nature of the films while XRD revealed their amorphous character. [74]

A three-step reaction sequence that includes heterobifunctional and ring-opening organic precursors was also suggested to avoid double reactions of organic molecules. The purpose of the ring opening reactant in the process is to generate a new functional groups that does not react with the initial surface species.

The first reported ABC process employed TMA as metal source, ethanolamine (EA, $HO(CH_2)_2NH_2$) as a heterobifunctional organic molecule and maleic anhydride (MA, $C_4H_2O_3$) as a contributant in the ring opening reaction. **Fig. 10** shows schematically the possible reaction between the three molecules in a MLD reaction. The growth of this film was done in a temperature range of 90°C to 170°C on a ZrO_2 surface. While the ABC surface reactions displayed self-limiting growth, GPCs were temperature dependent and varied from 24 Å /cycle at 90°C to 4.0 Å /cycle at 170°C. The high GPCs make the TMA-EA-MA films very attractive for applications that require flexible or sacrificial films. The decrease of the GPC with temperature is attributed to the infiltration of TMA molecules into the film and the CVD reactions with EA molecules during the EA precursor pulse. To avoid infiltration and CVD reactions, very long TMA purge times are required, and this significantly decreases the deposition rates. It was found that after aging in the air, the thickness of the TMA-EA-MA film decreased by 5.8%, compared to a decrease of 20% for the TMA-EG film. [20]

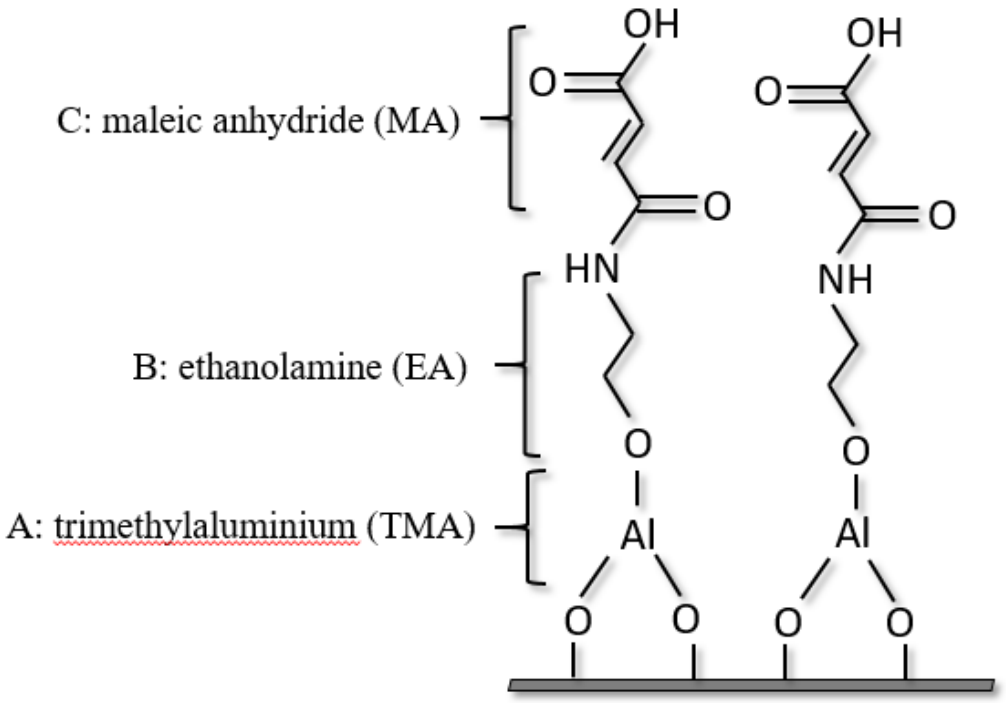


Figure 10 Schematic illustration of an MLD process based on an ABC reaction sequence, where A-TMA, B-EA and C-MA.

Later on, other ring opening processes that include three precursors were developed including the TMA with EG and terephthaloyl chloride (TC, $C_6H_4(CO_2Cl)_2$), [68] TMA with EA and methyl-methacrylate (MMA, CH_2=$CCOOCH_3$), [67] TMA with 3-(trifluoromethyl)phenol

($F_3CC_6H_4OH$) and O_3, and TMA with 2-fluoro-4-(trifluoromethyl)benzaldehyde ($F_3CFC_6H_3COH$) and O_3, [43] processes.

To avoid the "reservoir" effect of TMA, DMAI was considered as an alternative MLD precursor for alucones. [5] Compared to TMA, DMAI is a bulkier molecule. Moreover, DMAI is known to tend toward the dimeric state through bridge bond formation by the alkoxy groups, as evidenced by MS analysis and studies of other alkylaluminum alkoxides. [78-80] DFT studies also show that the dominant form of DMAI in area selective ALD (AS-ALD) reactions is dimeric. [81] Hence, DMAI is expected to minimize the amount of precursor infiltration. In the first reported films deposited with DMAI as metal source, EG was used as organic precursor. It was observed that the DMAI-EG process is temperature dependent and the GPC decreases with increasing the temperature (no information on how much was given).

A lower GPC was achieved for the DMAI-EG film compared to the TMA-EG film. However, the deposition rate (nm/s) of DMAI-EG process was found to be higher in comparison to the TMA-EG process. In terms of stability (architecture and thickness), the degradation behavior of the DMA-EG films upon ambient exposure was similar to TMA-EG films. [5]

2.4.2 Titanium based processes

For titanicone films the most common inorganic precursor is titanium tetrachloride ($TiCl_4$) which was employed extensively with EG, [48, 53, 82-91] and GL. [48, 52, 91-93] Other organic molecules like 2,4-hexadiyne-1,6-diol (HDy), [94] triethanolamine (TEA), [56] fumaric acid (FC), [95] 4,4′-oxydianiline (ODA), [35, 41, 96] HQ, [41, 97-100] 4-aminophenol (AP), [41, 42] p-phenylenediamine (PD), [41] 2,6-naphthalenedicarboxylic acid (2,6-NDC), [16] maleic acid (MA), [101, 102] ethylene diamine (ED), [103] malonyl chloride (MC), [103] and 4-aminobenzoic acid [76] have also been coupled with $TiCl_4$ for titanicone films. Titanium isopropoxide (TTIP) was also used in combination with HQ, [104] curcumin (Cur), [104, 105] octenyltrichlorosilane (7-OTS), [106] thymine, uracil or adenine, [65] glycine and L-aspartic acid, [107] L-lysine, glycine, L-aspartic acid, L-arginine, thymine, uracil [108] for the deposition of titanicone films. A titanicone MLD process using tetrakis(dimethylamido)titanium ($Ti(DMA)_4$) with EG has also been reported. [91]

In reference [48] a direct comparison between titanicone films grown with titanium tetrachloride ($TiCl_4$) and ethylene glycol (EG) and titanicone films grown with $TiCl_4$ and

glycerol (GL) was done. Both films were deposited on Si surfaces. The obtained GPC value for the $TiCl_4$-EG films was ~4.5 Å/cycle from 90°C to 115°C and dropped significantly to 1.5 Å/ cycle at 135°C. It was assumed that this drop could be related to desorption of unreacted $TiCl_4$ species at 135°C. In addition, it was proposed that this reduction could also be caused by the desorption of $Ti(-O(CH_2)_2O-)_2$ species or double reactions of the organic precursor in which the molecule lies flat binding to Ti sites with both terminal groups. However, these are all difficult to confirm from the experiments. The thickness and thickness reduction with temperature increment observed for $TiCl_4$-EG films was similar to the thickness and thickness reduction observed for alucone films grown using TMA and EG (4.0 Å/cycle at 85°C to 0.4 Å/cycle at 175°C) [11] and zincone films grown using diethyl zinc (DEZ) and EG (4.0 Å/ cycle at 90°C to 0.25 Å /cycle at 170°C). [109] For $TiCl_4$-GL films the GPC was 2.8 Å/cycle at 130°C and it decreased to 2.1 Å/cycle at 210°C. The thickness of $TiCl_4$-GL films was similar to the thickness of alucone films grown using TMA and GL (2.5 Å/cycle). [110] Similar, GPCs of $TiCl_4$-EG and $TiCl_4$-GL films were achieved also in reference [92] ($TiCl_4$-EG: 4.5 Å/cycle at 115°C; $TiCl_4$-GL: 2.2 Å/cycle at 150°C). Nanoindentation analyses revealed that $TiCl_4$-GL films had a higher elastic modulus and hardness than $TiCl_4$-EG. Further annealing experiments also showed that $TiCl_4$-GL films had a higher thermal stability compared to $TiCl_4$-EG. This most probably because of the extra OH group in GL that leads to higher network connectivity. [48]

Titanicone films were also grown by combining $TiCl_4$ with 2,4-hexadiyne-1,6-diol (HDy, $HOCH_2C{\equiv}C\text{-}C{\equiv}CCH_2OH$) under ultraviolet (UV) polymerization in a substrate temperature of 100°C. These films were coupled with TiO_2 ALD inorganic films which were deposited at the same temperatures. The GPC of the $TiCl_4$-HDy film was ~6 Å/cycle. The resulting $TiCl_4$-HDy/TiO_2 thin films revealed good mechanical and thermal stability and a large-scale uniformity. [94]

$TiCl_4$ was combined with triethanolamine (TEA) and compared to TMA-TEA films. While TMA-TEA films showed a decrease in GPC from 6.7 Å/cycle at 150°C to 0.8 Å/cycle at 195°C, for $TiCl_4$-TMA films the GPC decreased from 5.2 Å/cycle at 150°C to 2 Å/cycle at 195°C. Although $TiCl_4$-TMA films resulted in less temperature dependent, these films were less air-stable compared to TMA-TEA films. Both films revealed responsive properties which makes these films very attractive for sensor and filtration applications. [56] Apart from TEA, $TiCl_4$ was also combined with other NH_2 containing molecules such as ethylenediamiamine (ED, $C_2H_4(NH_2)_2$) and 4-aminobenzoic acid ($NH_2C_6H_4CO_2O$). [76]

Fumaric acide (FC, $HO_2CHCHCO_2H$) was used to deposit titanicones together with $TiCl_4$ on a Si surface in a temperature range of 180°C to 350°C. A temperature dependent growth characteristic was again observed with the GPC decreasing from 1.10 Å/cycle at 180°C to 0.49 Å/cycle at 300°C. This reduction was attributed to the increased thermal motion and desorption of molecules on the growth surface. FTIR spectra indicated that the hybrid film shows a stable bridging bonding mode between Ti and the acid group at temperatures under 200°C and a high bridging/bidentate mixed bonding mode at temperatures over 250°C and 300°C. [95] **Fig. 11** shows all possible binding modes for FC with $TiCl_4$.

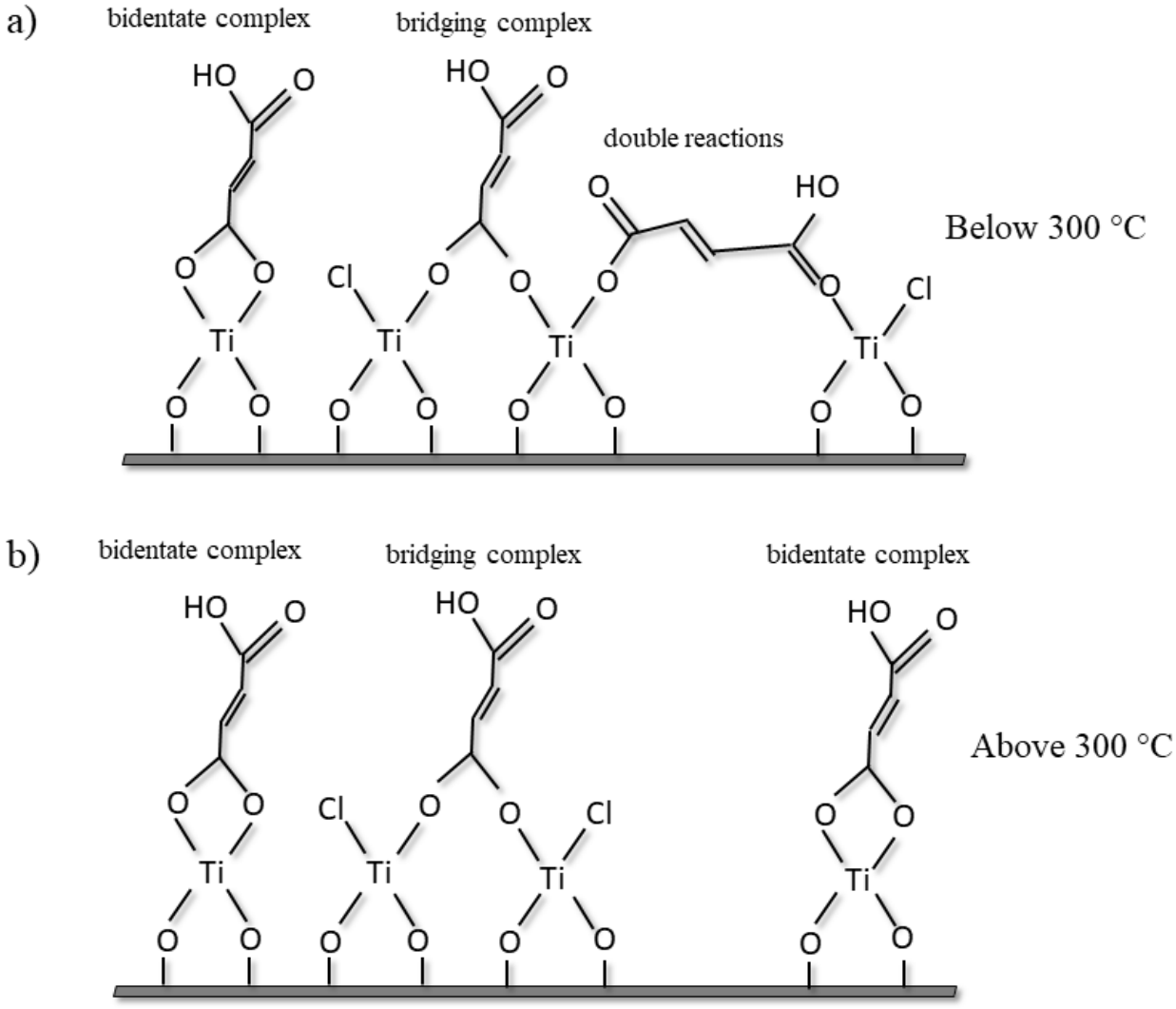


Figure 11 Schematic illustration of reactions between $TiCl_4$ and FC. The possible bonding situations: a) below 300°C is bidentate, bridging and double reaction and b) above 300 °C is bidentate and bridging.

Other acid molecules such as maleic acid (MA, $HO_2(CH)_2CO_2H$) [101, 102] and 2,6 naphthalene dicarboxylic acid (2,6-NDC, $C_{10}H_6(CO_2H)_2$) [16] were also successful when coupled with $TiCl_4$ for the deposition of $TiCl_4$-MA films and $TiCl_4$-MA/TiO_2 alloys.

$TiCl_4$ was also coupled with different aromatic molecules including hydroquinone (HQ), [41, 97-100] p-phenylenediamine (PD), [41] 1,4 aminophenol (AP, HOC_6H_4OH) [41, 42] and 4,4′-oxydianiline (ODA, $O(C_6H_4\text{-}NH_2)_2$). [35, 41, 96] In a recent study a comparison between titanicones grown different aromatic molecules was done by developing four MLD processes based on $TiCl_4$ and HQ, PD, AP and ODA. All processes yielded amorphous thin films. The highest achieved GPC, 10 Å/cycle, was for the $TiCl_4$-AP process. For the $TiCl_4$-HQ process a hybrid film with an intermediate GPC 4.3 Å/cycle was achieved while for the ODA- and PDA based processes the GPCs were considerably lower, 1.4 Å/cycle and 1.2 Å/cycle, respectively (**Fig. 13**). The observations were attributed to (i) the higher reactivity of the OH groups in comparison to the NH_2 groups towards $TiCl_4$, (ii) the higher tendency of a heterobifunctional molecules to remain in an upright configuration and avoid unwanted double reactions and reach the ideal MLD film growth. [41] MLD reaction products are shown in **Fig. 12**.

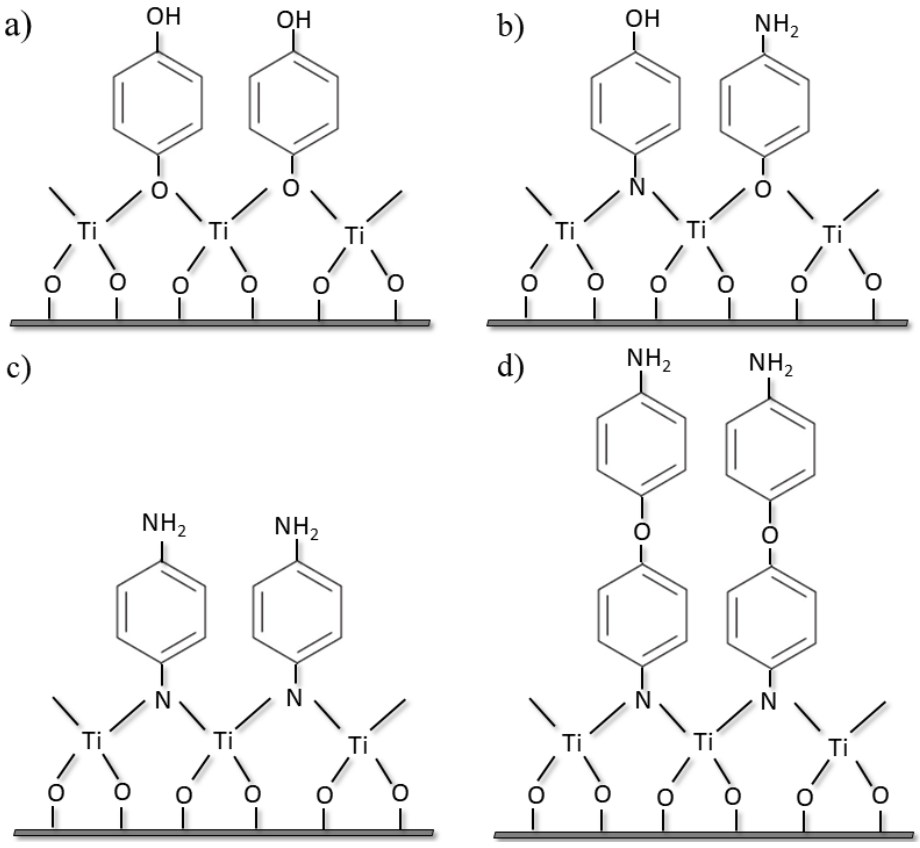


Figure 12 Schematic illustration of reactions between $TiCl_4$ and a) HQ, b) AP, c) PD and d) ODA.

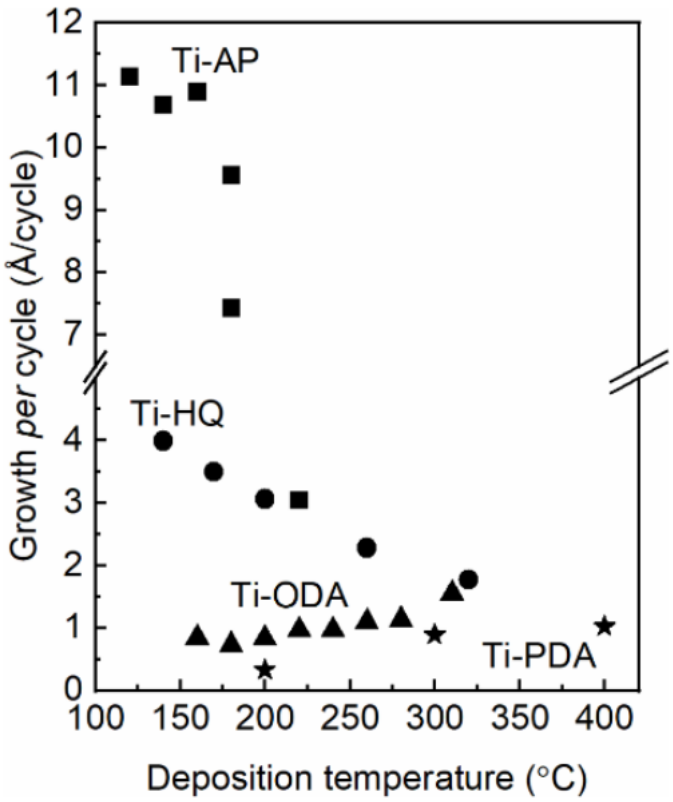


Figure 13 Deposition temperature profiles for the four Ti-organic ALD/MLD processes investigated. [41]

A four step ABCB reaction process was developed using $TiCl_4$ (A), ethanolamine (EA) (B) as a heterobifunctional molecule and malonyl chloride (MC, $CH_2(COCl)_2$**)** (C) as a homobifunctional molecule. The combination of a hetero and homo bifunctional organic molecules promotes selectivity of coupling reactions in each step of the process. The deposition of films was done on CuO nanowires. The resulting films were then annealed in H_2/Ar atmosphere at 600°C for 2h, to produce nanoporous N-doped TiO_2 nanotubes. [103]Possible reaction mechanism is shown in **Fig. 14**.

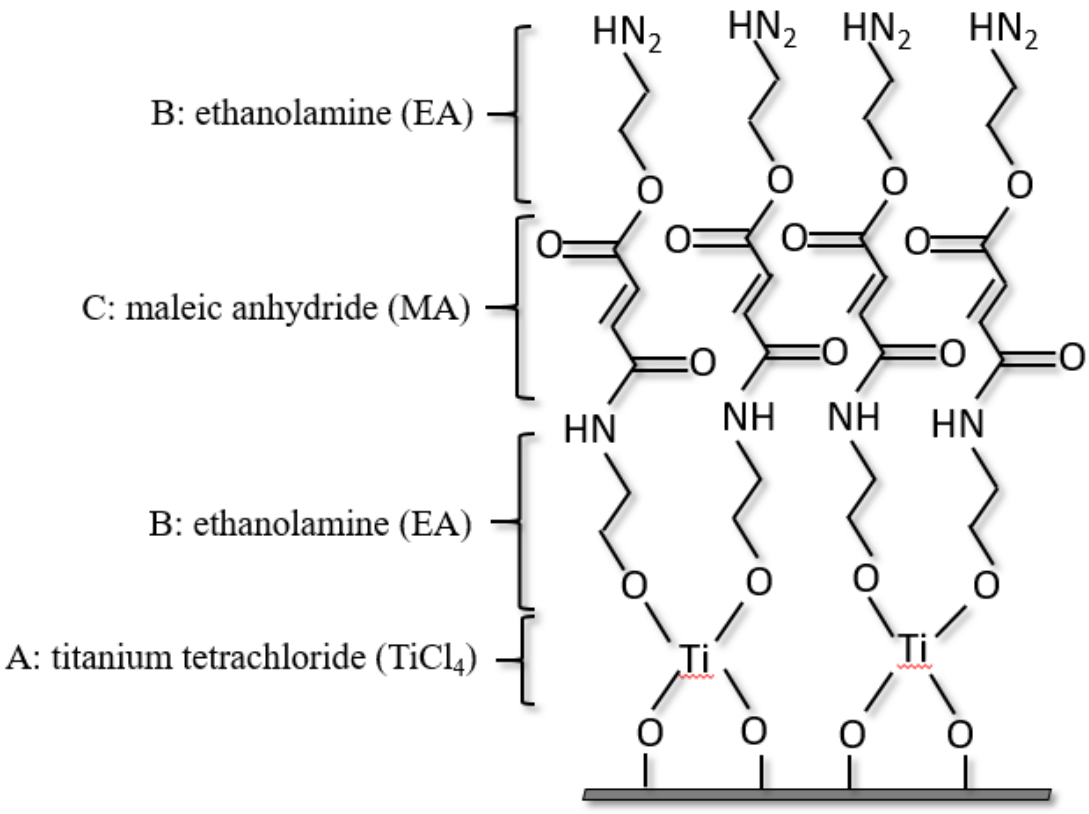


Figure 14 Schematic illustration of a MLD process based on ABCB reaction sequence, where A-$TiCl_4$, B-EA and C-MA.

Another titanium inorganic precursor employed in MLD is titanium isopropoxide (TTIP, $Ti(OCH(CH_3)_2)_4$). TTIP was successful for the fabrication of TiO_2-curcumin (Cur, $C_{21}H_{20}O_6$)/HQ superlattices showing visible-light absorption. [104]

TTIP was also coupled with different amino acids to produce highly bioactive materials. In reference [107] TTIP-glycine ($H_2NCH_2CO_2H$), TTIP-L-aspartic acid ($HO_2CCH_2CHNH_2CO_2H$), TTIP-succinic acid and TTIP-L-arginine ($CN(CH_2)_3CHCO_2H$) processes were developed. The growth was done on Si surfaces and in a temperature range from 160°C to 375°C for all processes. All processes showed self-limiting growth with a decrease in the GPC at high temperatures (the exact GPCs are not given). All films were amorphous and hydrophilic, with a notable bioactivity and are promising for the future design of scaffold for tissue engineering.

TTIP was also coupled with nucleobases thymine ($C_5H_6N_2O_2$), uracil ($C_4H_4N_2O_2$) and adenine ($C_5H_5N_5$) to fabricate bioactive films. Films were deposited on Si surfaces at a deposition temperature of 225°C to 350°C. The TTIP-thymine and TTIP-uracil processes were

temperature depended while the TTIP-adenine process was relatively constant between 250°C to 300°C (the exact GPC are not given). TTIP-adenine films also showed a higher stability upon exposure to air. [65]

Apart from $TiCl_4$ and TTIP, another titanium precursors recently used in MLD is tetrakis(dimethylamido)titanium ($Ti(DMA)_4$, TDMAT, $Ti(N(CH_3)_2)_4$). $Ti(DMA)_4$ was coupled with the most common organic molecules in MLD, EG and GL. For $Ti(DMA)_4$-EG films the growth initiates, but terminates after only 5 to 10 cycles, which may be attributed to the double reactions phenomenon where both terminal OH groups of EG react with the surface. In contrast to EG based films, steady growth was achieved for $Ti(DMA)_4$-GL films because of the third OH group of the GL molecule. However, the influence of temperature was noticed also for the GL based films. The GPC decreased from 0.9 Å/cycle at 80°C to 0.2 Å/cycle at 160°C, **Fig. 15**. [91]

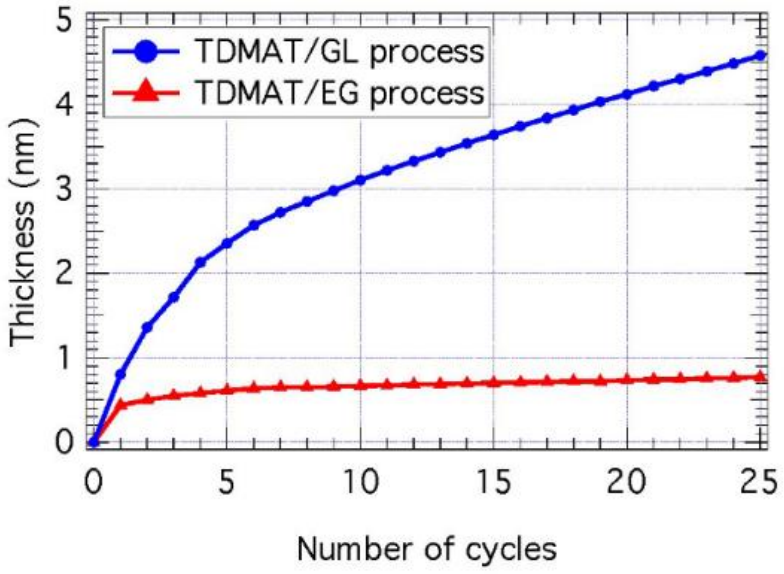


Figure 15 Growth profile of $Ti(DMA)_4$-EG films and $Ti(DMA)_4$-GL based titanicones. [91]

2.4.3 Zinc based processes

Diethylzinc (DEZ) was coupled with a wide range of organic precursors such as: ethylene glycol (EG), [53, 109, 111-115] glycerol (GL), [31, 52, 111] 2,4-hexadiyne-1,6-diol (HDy), [114] 1,5-pentanedithiol (PDT), [116] ethanolamine (EA), maleic anhydride (MA), [117] glycdiol, [72] HQ, [57, 92, 118-136] 4-aminophenol (AP), [136-138] 4,4′-oxydianiline (ODA),

[136] curcumin (Cur), [105] 8-hydroxyquinoline (8-HQ), [61, 76, 139] trihydroxybenzene (THB), [140] 1,4-phenylene diisocyanate (PDIC), ethylenediamine (ED), [141] and azobenzen [142] for the deposition of zincone MLD films.

The first reported zincone films were deposited using diethylzinc (DEZ, $Zn(CH_3CH_2)_2$) and ethylene glycol (EG). Films were deposited on a Si surface. It was found that the film growth was temperature dependent and decreased from 4.0 Å/cycle at 90°C to 0.25 Å/cycle at 170°C. The reduction of the GPC with increasing the temperature was attributed to the infiltration of DEZ molecules into the film, similar to TMA. [11] FTIR spectra also revealed that at higher temperatures no OH groups were observed after the EG pulse, suggesting that double reactions occur for EG. DEZ-GL films were also deposited on carbon nanotubes at a temperature 150°C where a GPC of 1.3 Å/cycle was achieved. [52]

A DEZ-2,4-hexadiyne-1,6-diol (HDy) process was also reported. Films were deposited on a Si surface in a temperature range of 100°C to 150°C. This process yielded films with a GPC of 5.2 Å/cycle with an excellent stability in air up to 400°C. [114] The MLD reaction product of DEZ and HDy is shown in **Fig. 16**.

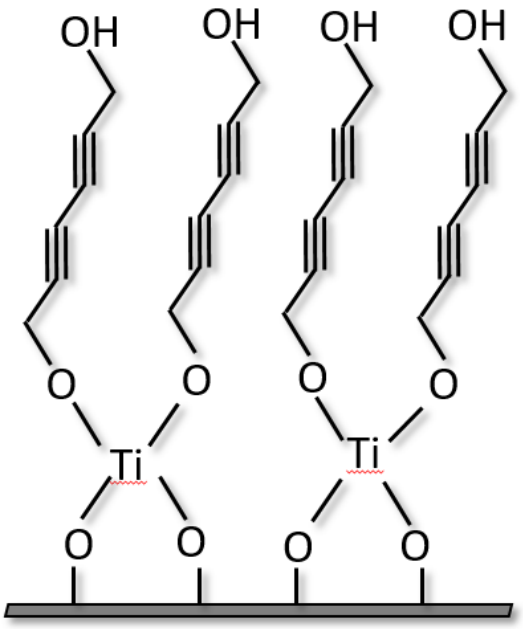


Figure 16 Schematic illustration of reactions between DEZ and HDy.

Highly conductive films were fabricated by employing DEZ and HQ as MLD precursors. The high conductivity was driven from the π-orbitals in conjugated chains of (-O-phenyl-O-Zn-)n. A GPC of 1.6 Å/cycle was achieved at 150°C for these films. [132]

ZnO-organic superlattice films were also fabricated by using HQ and terephthalic acid (TPA, $C_6H_4(CO_2H)_2$) as organic linkers. It was found that the two organic molecules affect differently the electrical transport properties of the resulting films. TPA layers act as electrical barriers by depressing the electrical conductivity even in low concentrations. On the other hand HQ layers increase the electrical conductivity, which is supposed to arise from the presence of the delocalised electrons. [120]

DEZ- trihydroxybenzene (THB, $C_6H_3(OH)_3$) films were also fabricated in a temperature range of 100°C to 160°C on a Si surface. A GPC of 2.6 Å/cycle was obtained for these films at 100°C. DEZ-THB films were combined with ZnO layers where the resulting ZnO/DEZ-THB films exhibited good stability and field effect mobility. [140] **Fig 17** shows the MLD reaction product of DEZ and THB.

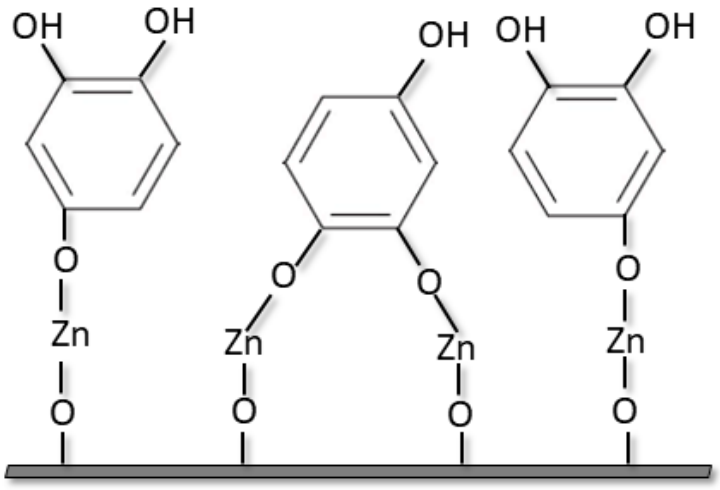


Figure 17 Schematic illustration of reactions between DEZ and THB.

4-Aminophenol (AP) was also combined with DEZ where a relatively low GPC of 1.1 Å/cycle was achieved and remained constant in the deposition temperature range of 140°C to 200°C. However, this process yielded to air stable, smooth and uniform Zn-hybrid films. [138]

Azobenzene dicarboxylic acid (AZO, $N_2(C_6H_4CO_2H)_2$) was also combined with DEZ for the successful fabricate ZnO/DEZ-azobenzene superlattice. The possible MLD reaction product is

shown in **Fig. 18**. The resulting superlattice provided a remarkable suitable environment for the efficient (and reversible) photoisomerization of the azobenzene moieties upon light illumination. [142]

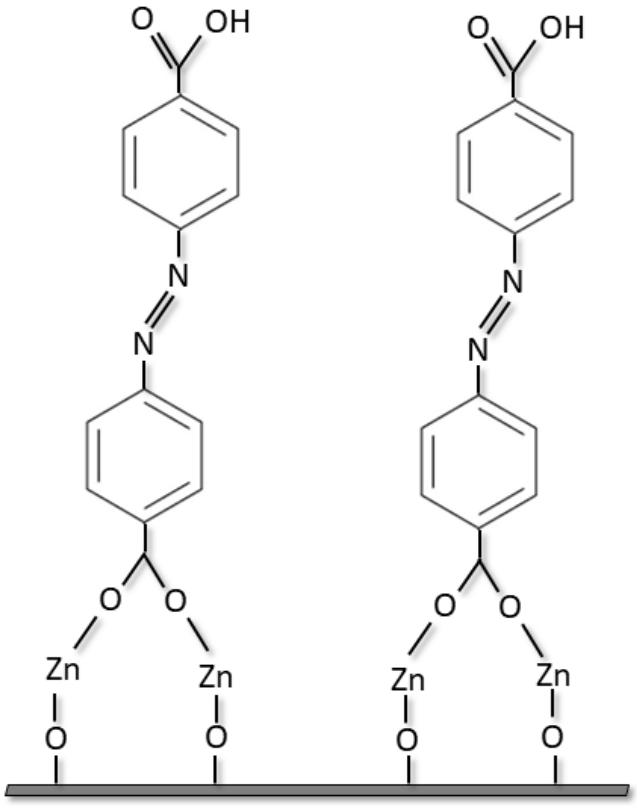


Figure 18 Schematic illustration of reactions between DEZ and AZO.

ABC processes have also been reported for Zn-hybrid films. In a recent study, Zn-hybrid films were grown using DEZ, ethanolamine (EA) and maleic acid (MA) as MLD precursors. The GPC is 4.4 ± 0.2 Å/cycle and films were stable in ambient air. DEZ-EA-MA films were then calcinated with the purpose to remove the organic part and enhance the film porosity. [117]

A four-step ABCB MLD sequence using precursors DEZ (A), ethylenediamine (ED) (B) and **1**,4-phenylene diisocyanate (PDIC, $C_6H_4(NCO)_2$) (C) was also reported and is shown schematically in **Fig. 19**. The resulting films were successful for the stabilization of the Li metal anode. [141]

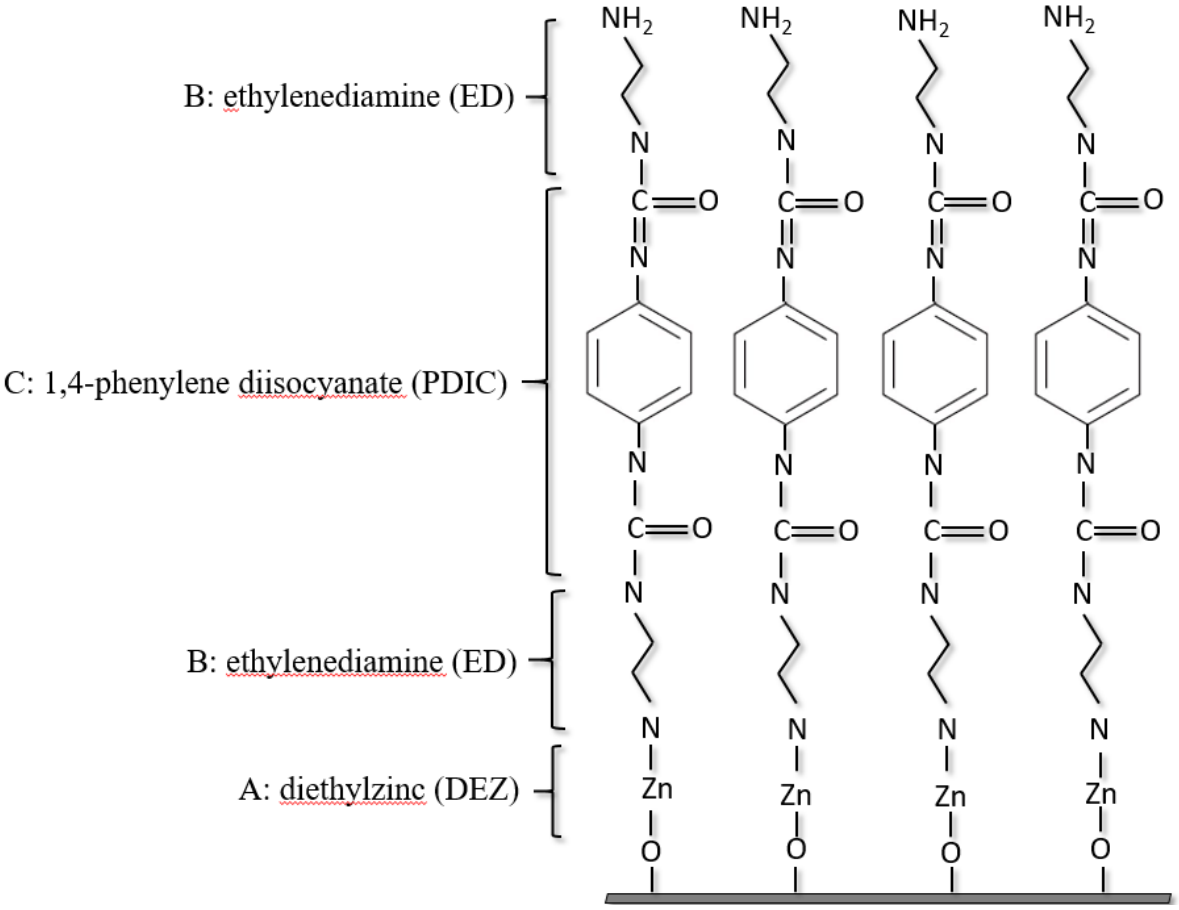


Figure 19 Schematic illustration of a Zn-based MLD process based on an ABCB reaction sequence, where A-DEZ, B-ED and C- PDIC.

2.4.4 Other metal-based processes

Apart from aluminium, titanium and zinc based processes, many other MLD processes based on other metals are developed. These processes have mostly used EG and GL as organic molecules.

One group of metalcones is "tincone". Tincones were grown using tetrakisdimethylaminotin ($Sn(DMA)_4$, $Sn((N(CH_3)_2)_4)$ as inorganic precursor and glycerol (GL) or ethylene glycol (EG). [143] $Sn(DMA)_4$-EG and $Sn(DMA)_4$-GL films were grown in a temperature range of 75°C-200°C on a Si surface. For the EG based process the growth started but rapidly decreased over the first 50 cycles. At the temperature of 100°C, the GPC for the $Sn(DMA)_4$-EG films was 0.1 Å/cycle. For the $Sn(DMA)_4$-GL films the GPC was stable for up to 200 cycles. However, the GPC decreases with increasing temperature from 1.3 Å/cycle at 75°C to less than 0.1 Å/cycle at 200°C. The GPC of 0.1 Å/cycle is very small even in case of double reactions. It seems more

like some desorption or decomposition has taken place. However, the morphology of the films was found to be smooth with a low surface roughness. [143]

For vanadicone films, tetrakisethylmethylaminovanadium ($V(EMA)_4$, $V(N(CH_3CH_2)(CH_3))_4$), which was already successfully implemented in ALD for V_2O_5, was coupled with EG and GL. [23] Films were deposited in a temperature range from 80°C to 180°C. SE measurements showed that the growth started for both processes, however, for EG based vanadicones the film growth slowed down during the first 10 cycles and finally at cycle 100, the GPC dropped below 0.1 Å/cycle. After 300 cycles the film thickness remained unmeasurable with XRR, as the thickness was less than a few nanometers. The $V(EMA)_4$-GL process, on the other hand, resulted in linear growth. After the first 10 cycles, the GPC stabilized to 0.7 Å/cycle and this GPC remained stable for up to at least 500 cycles. FTIR and XPS techniques also revealed the hybrid nature of the $V(EMA)_4$-GL films. The difference between EG and GL based vanadicones film growth was again attributed to the extra OH group of GL compared to EG, which allows film growth to continue even with the double reactions. The resulting hybrid $V(EMA)_4$-GL films were annealed in inert atmosphere (He) and compared to ALD V_2O_5, where He annealed vanadicone films exhibited improved capacity and performance over the V_2O_5 films. [23]

For zirconium films a zirconium tert-butoxide (ZTB, $Zr(OC(CH_3)_3]_4$)-EG process was developed and it yielded to films with a GPC of 1.6 Å/cycle at 105°C to 0.3 Å/cycle at 195°C. The decrease of the GPC with temperature was partly attributed to enhanced diffusion of ZTB into the film at lower temperatures and more double reaction of EG at higher temperatures. It was confirmed that the combination of ALD ZrO_2 films and MLD ZBT-EG films leads to materials with tunable optical properties and very promising electrical properties. [144]

Hafnicone films were fabricated in a temperature range of 105°C to 205°C using tetrakisdimethylamidohafnium ($Hf(DMA)_4$, $Hf((N(CH_3)_2)_4$) as Hf source and EG as co-reactant. Hafnicone film growth was temperature depended and decreased from 1.2 Å/cycle at 105°C to 0.4 A/cycle at 205°C. XRR studies showed that the deposited films were very stable with time while nanoindentation measurements determined an elastic modulus of 47 ± 2 and hardness 2.6 ± 0.2 GPa. [49]

A mangancone MLD process was developed using bis(ethylcyclopentadienyl)manganese ($Mn(CpEt)_2$) and EG as precursors but there have been no more details reported. [92] Other MLD process developed so far are presented in the **Table 1.**

Table 1 MLD processes developed for hybrid inorganic-organic films.

Li(thd) 2,5-dihydroxyterephthalic acid [145] terephthalic acid (TPA) [146-148] (1,4-benzenedisulfonate (BDS) [15] 4,4′-azobenzenedicarboxylic acid (AZO) [148, 149] pyridinedicarboxylate (3,5-PDC) [12, 148] dilithium 2-aminoterephthalate ($TPANH_2$) [150] 2,6-naphthalenedicarboxylic acid (NDC) [148] 4,4′-biphenyldicarboxylic acid (BPDC) [148]	**$Cu(dmap)_2$** hydroquinone (HQ) [151] terephthalic acid (TPA) [151] 4,4′-oxydianiline (ODA) [151] p-phenylenediamine (PPDA) [151] 1,4-benzenedithiol (BDT) [151]
LiHMDS hydroquinone (HQ) [152] ethylene glycol (EG) [153]	**$Cu(thd)_2$** terephthalic acid (TPA) [154]
LiO^tBu propanediol (PD) [155] ethylene glycol (EG) [156]	**$Ta(OEt)_2$** pyromellitic dianhydride (PMDA) [157] diaminohexane (DAH) [157]
Na(thd) pyridinedicarboxylate (3,5-PDC) [12] uracil [158] adenine [158]	**$Mo(CO)_6$** ethanethiolate [159] butanethiolate [159] benzenethiolate [159]
K(thd) pyridinedicarboxylate (3,5-PDC) [12] terephthalic acid (TPA) [147]	**$Mn(CpEt)_2$** ethylene glycol (EG) [160]
$Mg(thd)_2$ pyridinedicarboxylate (3,5-PDC) [12] terephthalic acid (TPA) [147]	**$Mn(thd)_3$** terephthalic acid (TPA) [161]
$Mg(CpMe)_2$ ethylene glycol (EG) [32] glycerol (GL) [32]	**$FeCl_3$** terephthalic acid (TPA) [17, 18, 162] 4,4′-azobenzenedicarboxylic acid (AZO) [149, 163, 164]
$Nb(OEt)_2$ hydroquinone (HQ) [165]	**$Fe(acac)_3$** terephthalic acid (TPA) [162]
$Sr(thd)_2$ pyridinedicarboxylate (3,5-PDC) [12] terephthalic acid (TPA) [147]	**$Cp_2Fe_2(CO)_4$** hydroquinone (HQ) [166]
$Ba(thd)_2$ pyridinedicarboxylate (3,5-PDC) [12] terephthalic acid (TPA) [147] uracil [158] adenine [158]	**$Fe_2(O^tBu)_6$** ethanolamine (EA) [167] malonyl chloride (MC) [156] ethylene glycol (EG) [168]
$La(thd)_3$ terephthalic acid (TPA) [147, 169] uracil, adenine [158]	**$Fe(hfa)_2TMEDA$** oxalic acid (OX) [170]
$ZrCl_4$ 2,6-naphthalenedicarboxylate (2,6-NDC) [16, 171] biphenyl-4,4′-dicarboxylate (BP-4,4′-DC) [171]	**$Co(thd)_2$** terephthalic acid (TPA) [161]

2-amino-terephthalic acid (TPA-NH_2) [172, 173]	
$Zr(DMA)_4$ ethylene glycol (EG) [174]	**$Co(acac)_3$** terephthalic acid (TPA) [161]
$HfCl_4$ 2,6-naphthalenedicarboxylic acid (2,6-NDC) [16]	**$Ni(thd)_2$** terephthalic acid (TPA) [14]
$Hf(EMA)_4$ hydroquinone (HQ) [175]	**$Ni(mamb)_2$** 4-mercaptophenol (4MP) [176]
$Hf(DMA)_4$ ethylene glycol (EG) [49, 53, 92] glycerol (GL) [92] hydroquinone (HQ) [92] malonyl chloride (MC) [177] ethylene diamine (ED) [177]	**$Ca(thd)_2$** pyridinedicarboxylate (3,5-PDC) [12] terephthalic acid (TPA) [147, 169] 4,4′-azobenzenedicarboxylic acid (AZO) [149]
$V(EMA)_4$ ethylene glycol (EG) [23] glycerol (GL) [23]	**$VO(Cl)_3$** ethylene glycol (EG) [178]
$V(CO)_6$ tetracyanoethylene (TCNE) [179]	**INCA** hydroquinone (HQ) [180, 181]
$Yb(thd)_3$ pyrazinedicarboxylic acid [182]	**$Er(thd)_3$** pyrazinedicarboxylic acid [182]
$Yb(dpdmg)_3$ IR-806 [183]	**$Er(dpdmg)_3$** IR-806 [183]
$Y(thd)_3$ pyrazinedicarboxylic acid [182]	**$Ce(dpdmg)_3$** hydroquinone (HQ) [27] terephthalic acid (TPA) [27]

2.5 Crystalline MLD hybrid films

Currently, of a very high interest are the hybrid materials in which the organic ligands act as bridges between the metal centres to form infinite 1D, 2D, or 3D structures. [184, 185] These materials are often referred to as metal-organic framework (MOF) materials and are characterized by their crystalline structure and high porosity. [186] The type of the linker molecule and the introduction of new molecules into the pores notably refine mechanical and chemical properties of the material. Due to their especial properties, MOFs are very promising materials in many application areas such as luminescence, energy conversion and storage, gas storage and separation, catalysis, optics and electronics. [187-190]

The first reported crystalline films deposited via MLD were Cu-terephthalate thin films of a MOF-like structure. These crystalline films were deposited using copper 2,2,6,6-tetramethyl-3,5-heptanedione as metal source and terephthalic acid (TPA) as organic component in a

temperature range of 180°C -190°C. At a higher temperature an amorphous film is delivered and the GPC decreased from 3 Å/cycle at 180°C to 0.2 Å/cycle at 260°C. [154]

Crystalline 1D dimethyl dithiooxamidato-copper (Cu-DMD) films were also recently reported where the attractive property of these films was the semiconductor-to-metal transition achieved with a post deposition reductive annealing. [13]

Lithium β-diketonate Li(thd) or calcium β-diketonate $Ca(thd)_2$ (th:2,2,6,6-tetramethyl-3,5-heptanedionate) were also employed as the metal precursor in combination with TPA as the organic linker to fabricate highly crystalline Li-TPA and Ca-TPA films in a wide deposition temperature range where both films revealed promising mechanical properties. [146, 169]

Later on, TPA-based crystalline films were also reported for many other metals (Na, K, Ca, Sr, Ba, Fe, La, Eu, Mg). [147, 191]

Aromatic diols have also been reported to yield crystalline metal-organic films. Crystalline Li–organic thin films were deposited with lithium bis(trimethylsilyl)amide (LiHMDS) and hydroquinone (HQ) as precursors. It was found that the deposited films undergo a reversible structural transformation upon exposure to ambient humid air. DFT calculations suggest that this may be related to an unsaturated Li site in the crystal structure. [152] The photo switchable azobenzene dicarboxylic acid precursor also yielded crystalline metal-organic films when combined with Li, Ca [149] and Fe. [163]

Adenine and uracil are two other organic molecules that were successfully employed for crystal films when combined with sodium [158] and positive signs of crystallinity have been observed also for (Y,Yb,Er)-pyrazine, [182] Cu-PPDA, [151] Zn-glutarate [192] and Ti-thymine [108] processes.

More recent studies focus on Li-organic crystalline films formed using Li precursors and different organic linkers: Li-1,3-propanediol (PD), [155] Li-dihydroxyterephthalic acid (DHTP), [145] Li-3,5-pyridinedicarboxylic acid (PDC), Li-2,6-naphthalenedicarboxylic acid (NDC), Li-4,4′-biphenyldicarboxylic acid (BPDC), and Li-4,4′-azobenzenedicarboxylic acid (AZO). [148]

In general, most of metals that lead to crystalline MLD films belong in the -s group of periodic table. This most probably due to the nonoriented ionic bonds formed between the metal cations and organic linkers which possess more spatial freedom to adjust to the coordination requirements of the specific crystal structure. Covalent bonds in contrast are more strictly

oriented and predetermined to a certain spatial coordination symmetry. It also seems like for higher valent (transition) metals, small ligands are more preferred. For example, the Na(thd)-nucleobase with one ligand led to highly crystal films, $Ba(thd)_2$-nucleobase with two ligands led to partly crystalline films and $La(thd)_3$-nucleobase with three ligands led to completely amorphous films. [158] Ligand steric effects may also be important. The $FeCl_3$-TPA process leads to crystalline films while $Fe(acac)_3$, an iron precursor with bulkier ligands yielded amorphous films. [162] Steric hindrance caused by the bulky ligands apparently complicates the building-up of the new coordination bonds and thereby the coordination network structure.

Precursor pulse duration might also have an effect on the crystallinity of the films. For example, the Li(thd) precursor in combination with DHTP led to crystalline films with short Li(thd) precursor pulse and to amorphous films with long Li(thd) pulses. [145] It was also found that multidentate organic linkers promote the crystallinity of the film due to the higher degree of freedom for possible coordination modes provided by the involvement of the different binding sites of the molecule. [12]

Crystallinity of the MLD hybrid films is often reflected in the measured density values. For crystalline films the density is usually lower compared to the related amorphous films. This because crystal structures have a high level of porosity, while the varied bond lengths/angles in amorphous films often lead to denser packing.

2.6 MLD processes for organic polymers

MLD is also employed for the deposition of pure organic polymer films. The first reported organic films deposited via MLD were polyimides. Later on, many other organic polymer groups such as polyamide, polyurea, polyurethane, polythiurea, polyester and polyimine thin films were deposited using MLD.

Polyimides. Depending on the backbone of the organic precursors, polyimides can be classified to be aliphatic, semi-aromatic or aromatic. Up to date, all MLD polyimide processes reported to date use pyromellitic dianhydride (PMDA) as raw material.

For semi-aliphatic polyimides PMDA was combined with ethane-1,2-diamine (ED) and hexane -1,6-diamine (HD), where GPCs of 3.9 Å/cycle and 5.8 Å/cycle were achieved at 160°C. The achieved GPCs indicate that the growth is far from ideal as the chain lengths of ED and HD

containing polyimide units are 9.8 Å and 14.5 Å, respectively. [193] In a later study, polyimides were again deposited using PMDA and HD where a GPC of 5.6 Å/cycle was achieved at the temperature of 170°C. [157] **Fig. 20** shows the orientation of organic molecules in **(a)** ideal organic film growth and **(b)** nonideal organic film growth.

PMDA was also combined with a wide range of aromatic precursors for aromatic polyimides. 4,4'-Oxydianiline (ODA) has been used as a second precursors in several studies. The highest achieved GPC for PMDA-ODA polymer films was 6.7 Å/cycle on an unnamed substrate while the GPC of 4.9 Å/cycle was obtained on Si (100). [194] PMDA-ODA films were also grown on Au-coated Si substrate modified with AP to gain a surface terminated with NH_2 groups where a GPC of 2.0 Å/cycle was achieved at 170°C. [195, 196] The obtained GPC values of all processes with ODA were far from the ideal PMDA-ODA monolayer (14.9 Å).

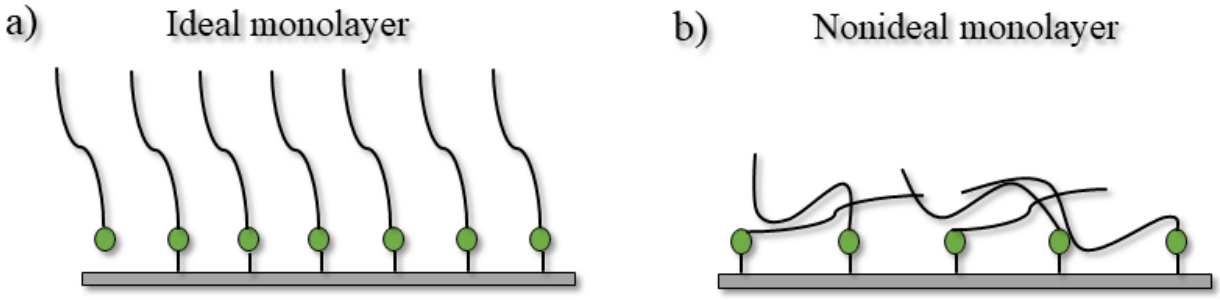


Figure 20 Schematic illustration of a) ideal growth of a MLD monolayer with all the polymer chains standing up to form a monolayer and b) nonideal growth of the MLD monolayer with polymer chains lying flat.

Aromatic polyimides were also fabricated using 1,4-diaminobenzene (PPDA) as a precursor together with PMDA. [193, 197] For PMDA-PPDA polymer films deposited on Si(100) substrate at the deposition temperature of 160°C a GPC of 1.4 Å/cycle was achieved, which is far from that expected for a calculated PMDA-PPDA monolayer (14 Å). [193] PMDA-PPDA polyimides were also deposited on a modified Si(100) surface with MA at room temperature but no details for the film thickness were given. [197] PMDA was combined with 4-nitrobenzene-1, 3-diamine (DNB) as well but the successful film growth was not achieved due to the weak bonds between the two precursors. [198]

Polyamides. Polyamides are also classified in aliphatic, semi-aromatic and aromatic. Diamines and acyl dichlorides have been used as precursors to fabricate MLD polyamides.

The typical example of aliphatic polyamides is nylon, which in MLD has been deposited from precursors with different chain lengths. Hexanedioyl dichloride and hexane-1,6-diamine are the shortest monomers used to make nylon 66. [199, 200] The highest GPCs that were achieved for nylon 66 are 13.1 Å/cycle at 60°C on Si(100) substrate [199] and 19 Å/cycle at 80°C on KBr substrate. [200] The GPCs are higher than the calculated unit-chain length of the repeating unit 17.4 Å, and this is attributed to the CVD type growth.

Heptane-1,7-diamine and nonanedioyl dichloride were used to deposit nylon 79 at room temperature. The achieved GPC value 18 Å/cycle was quiet close to the calculated unit-chain length of the repeating unit 22 Å. [201] In another study, systems where four precursors were used to deposit polyamines were developed but the achieved GPCs were not discussed. [202]

The first reported semi-aromatic polyamides were deposited using butane-1,4-diamine and terephthaloyl dichloride on Si (100) substrates. [203] Achieved GPC value was only 2 Å/cycle at 85°C. This was attributed to the flat orientation of the oligomer units, suggesting that double reactions occur during the film growth.

So far, only one aromatic polyamide polymer was fabricated with MLD using terephthaloyl dichloride and 1,4-diaminobenzene as precursors. The achieved GPC varied between 0.5 and 3.3 Å/cycle at 145 °C. This is way shorter when compared to the calculated unit-chain length of the repeating unit, which is 12.9 Å. The low GPC is again attributed to the flat orientation of the polymer chains. [204]

Polyureas. Polyureas are synthesized from the reaction between an isocyanate and an amine precursor. Depending on the diisocyanate used to fabricate the polymer, polyureas can be classified in aliphatic polyureas and aromatic polyureas. Aliphatic polyureas have always been grown using 1, 4-diisocyanatobutane (PDIC) as first precursor. 1,4-Diisocyanatobutane was combined with ethane-1,2-diamine, N-(2-aminoethyl)ethane -1,2-diamine, N,N-bis(2-amino-ethyl)ethane-1,2-diamine and tris(2-aminoethyl)amine on Si (100) substrates at room temperature where GPCs of 6.3 Å/cycle, 6.7 Å/cycle, 3.2 Å/cycle, and 3.1 Å/cycle, respectively, were achieved. These are smaller when compared to the calculated chain lengths for the respective systems which are 13.5 Å, 17.2 Å, 20.9 Å, and 17.2 Å, suggesting that the ideal growth was not achieved. [205]

Aromatic polyureas were grown from 1,4-diisocyanatobenzene and ethane-1,2- diamine on Ge (100) at room temperature. FTIR demonstrated the formation of urea linkages, and suggested that double reactions of the ethane-1,2-diamine molecule occur. [206] Same precursors were used again in another study to deposit the polyurea films on Si (100), treated with 3-

aminopropyltriethoxysilane to obtain amino groups on the surface. [207] Deposition was done in a temperature range of 25°C to 100°C. The film growth was temperature depended changing from 4.1 Å/cycle at 25°C to 0.4 Å/cycle at 100 °C. The low GPCs suggest that a full monolayer coverage was not achieved as the highest GPC value was well below the PDIC+ED molecule length of (12.6 Å). However, films were stable in ambient air and when annealed at least up to 250°C.

In another study, a GPC of 5.3 Å/cycle was achieved for 1,4-diisocyanatobenzene-ethane-1,2-diamine film at room temperature. [208] 2,2'-(propane-2,2-diylbis (oxy))-diethanamine was also combined with 1,4-diisocyanatobenzene for polyurea films. Films were deposited on Si (100) at room temperature. The GPC of the deposited film was 6.5 Å/cycle, which is considerably low when compared to the unit-chain length (18 Å). [209]

Other polymers. Beside the polymers discussed above, there are also several studies on other interesting polymers such as polyurethanes, polythiourea, polyesters and polyimines deposited with MLD.

Polyutheranes are fabricated with MLD by combining isocyanates with different alcohols. 1,4-Diisocyanatobenzene was employed as isocyanate and it was combined with but-2-yne-1,4-diol and terephthalic acid (bis(2-hydroxyethyl) for polyutheranes where GPCs of 9.5 Å/cycle and 6.1 Å/cycle were achieved, showing that the growth was not linear. [210]

For polythiourea MLD films, 1,4-diisothiocyanatobenzene precursor was combined with ethane-1,2-diamine at a deposition temperature of 50°C on Si and SiO_2 nanoparticles. The obtained GPCs were 1.9 Å/cycle and 2.8 Å/cycle, respectively and these are much smaller when compared to the calculated chain length for one unit of 13.8 Å. [211]

Another group of organic polymers are polyesters which in MLD are deposited using the reactions between various acids and alcohols. Terephthaloyl dichloride and ethylene glycol were used as MLD precursors for the deposition of polyesters. The deposition was done on Si(100) substrates in a temperature range of 145°C to 175°C. The highest GPC 3.3 Å/cycle at 145°C was much smaller than the length of one polymer unit which is 11 Å. [212]

For polyimines, terephthalaldehyde and 1,4-diaminobenzene were used as MLD precursors. [213-115] In reference [214] films were grown in room temperature on Au-coated glass substrates with a self-assembled monolayer of 11-amino-1-undecanethiol. A GPC of 10 Å/cycle was achieved in the first six cycles, after which the GPC started to fall. [214] Polyimide films showed promising features for sensitization in photovoltaic devices. [216, 217]

2.7 VPI processes for hybrid inorganic-organic polymer films

Vapor phase infiltration (VPI) technique is a variation of ALD where instead of solid inorganic substrates, a soft material such as a polymer is used, enabling so the fabrication of polymer-based hybrid materials. The first studies on VPI focused on the impact of the hybridization on the mechanical properties of the polymers, whereas more recent studies show that chemical and physical properties of polymers are modified as well, allowing a much wider range of potential applications for the polymer based hybrid materials. [218] A simplified or idealized schematic of VPI process is shown in **Fig. 21**.

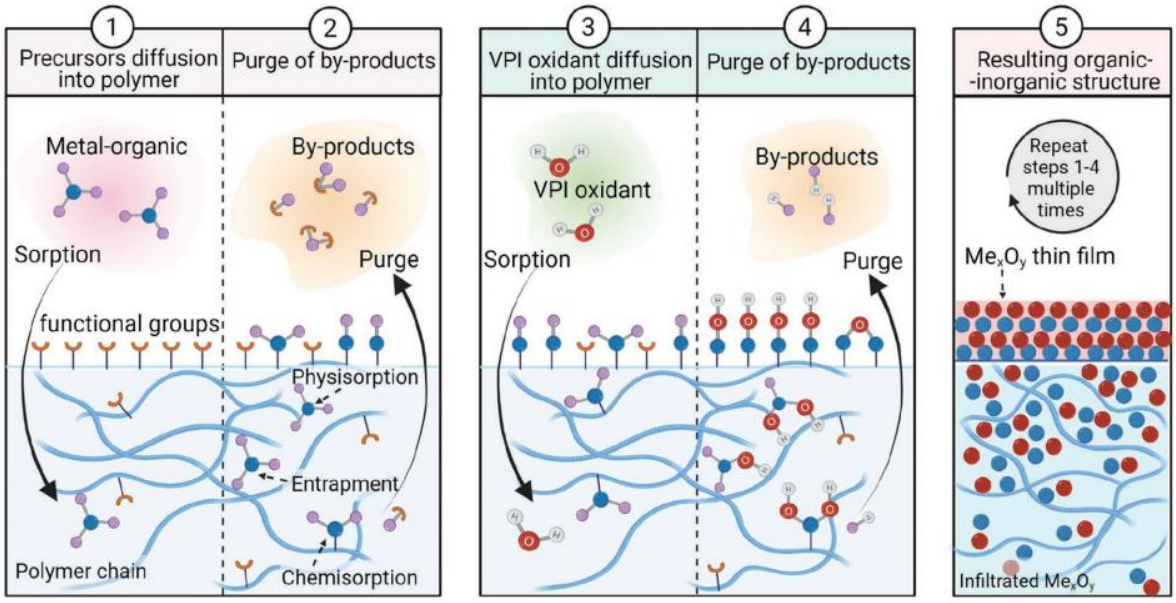


Figure 21 Schematic of the inorganic-organic hybrid material fabrication by VPI. Steps 1 to 2 and 3 to 4 indicate the individual exposure and purge steps of the two precursors in one VPI cycle and the sorption, binding, and reaction events during those steps. Step 5 is a schematic of the resulting polymeric hybrid material with a thin film coating and a blended inorganic subsurface. [219]

It was demonstrated that even polytetrafl uoroethylene (PTFE) polymer, which is well known for its great chemical and thermal stability, can be transformed into a PTFE-metal hybrid material with significantly improved mechanical properties only by applying metal-oxide (ZnO, ZrO_2 and Al_2O_3) precursors to PTFE. [220]

In another study the growth of ALD Al_2O_3 in polyamide was done and the influence of temperature on surface mineralization was analysed. It was found that a hybrid layer between Al_2O_3 and the polymer is formed to depths of 120 nm at 60°C, while no mineralization occurred at 120°C. The hybrid Al_2O_3-polymer layer formed at low temperatures improved the

mechanical performance of the thin films and opened new horizons for application as encapsulation barrier layers. [221]

Except from the temperature, the mineralization can be influenced also from the crystallinity of the substrate. It was found that the infiltration of trimethylaluminium (TMA) in semicrystalline polyethylene terephthalate (PET) decreases for high crystallinity levels of the polymer. The low infiltration in the crystalline areas is attributed to the reduction of the diffusion coefficient and accessible active groups in these areas. [222]

To investigate how infiltration effects the mechanical properties of different polymers Al_2O_3 was infiltrated in nylon 6, polypropylene (PP), and Pellethane. The Young's modulus were found to increase the most for pellethane. It was assumed that the formation of new intra-chain bonds is responsible for the stiffening of the elastomer. For nylon 6 the modules also increased and they seemed to be depended on the number of infiltration cycles. On the other hand for PP the chemical stability prevented significant change of the mechanical properties. [223]

The VPI mineralization has also demonstrated to improve the stability of polymers. Kevlar fibres were infiltrated with ZnO and tested for their stability upon UV light. Due to the formation of the hybrid material 90% of its modulus of toughness is preserved even after 24 hours of UV irradiation and also the decomposition temperature of Kevlar increased by 10°C. [224]

In another study, the synthesis of polymer based hybrid films of ZnO nanostructures grown directly on a modified polyetherimide (ULTEM) surface by photo-oxidation was discussed. This study showed that the growth type that takes place is highly depended on the surface modification mode, as depending on the time of the photo-oxidative process applied on the polymer, two different types of growth can occur. When short time pre-oxidative treatments are performed, ALD like reactions occurre and the growth of ZnO films takes place above the polymer surface. In contrary, when long time pre-oxidative treatments are performed, due to the decrease of molar masses of the polymer, VPI like reactions occur where the metal precursors infiltrate into the polymer. [225]

The VPI process is also an excellent technique for the fabrication of highly conductive hybrid materials. Polyaniline (PANI)-ZnO hybrids with conductivities as high as 18.42 S/cm were fabricated through infiltration of ZnO into the PANI polymer. [226]

A conversation of nonconductive PMMA-InOxHy VIP films into a porous and conductive In_2O_3 upon annealing with O_2 was also demonstrated in a recent study, opening so a new horizons for templating precise conductive architectures, with application to water remediation, sensors, electrodes etc. [227]

The infiltration of In_2O_3 and Ga_2O_3 into poly(methyl methacrylate) (PMMA) thin films was reported using TMIn and TMGa, respectively, with water. It was found that both metallic precursors react reversibly with carbonyl groups of PMMA, with significantly lower affinity when compared to TMA. DFT calculations also revealed that the association energy is three times greater for TMA than for either TMIn or TMGa, indicating that the kinetics of activated diffusion within the film are far more rapid for TMIn and TMGa than for TMA. For In_2O_3 VPI enables the deposition of films with tens of nanometres, under conditions that would give no film growth in flat inorganic substrates in a ALD process. [228]

In a recent study a Al_2O_3-poly(butylene succinate) (PBS) VPI process was developed and investigated for the first time. A detailed characterisation of the film revealed chemical and physical modification of the polymer in terms of reduced thermal stability and increased UV shielding. [229]

2.8 DFT studies on MLD processes

The first density functional theory (DFT) studies on hybrid materials focused on the structure and properties of these films. [127, 152] As an example, DFT was employed to derive bonding structures for different ZnO: hydroquinone (HQ) superlattice (SL) films. [127] In this study DFT was a useful guidelines for the band structure engineering through small and experimentally possible modifications of the organic component. The thermal conductivity and thermoelectric properties of the Zn:HQ SL were also predicted with DFT where the comparisons with the bulk ZnO indicated reduced thermal conductivities for the ZnO:HQ SL systems, consistent with the experimental data. [127]

In another example, the crystal structure of MLD films grown with lithium bis(trimethylsilyl)amide (LiHMDS) and HQ as precursors was predicted with DFT. [152] The predicted structure with DFT was confirmed by comparing with XRD patterns and FTIR spectra. The deposited films undergo a reversible structural transformation upon exposure to ambient humid air. DFT calculations suggest that this may be related to an unsaturated Li site in the crystal structure (3-coordinated). [152]

In a recent study the molecular mechanism of alucone films grown with trimethylaluminium (TMA) and ethylene glycol (EG), ethylenediamine (ED) and oxalic acid (OX) organic molecules on a SiO_2 surface was explored with DFT calculations. This work shows that TMA

can be easily adsorbed and dissociated on the hydroxylated SiO_2 surface. It was also found that all organic molecules react with the methyl terminated surface through four-membered ring (4MR) and six-membered ring (6MR) pathways and their reactivity follows the trend EG > OX > ED. This study provides theoretical guidance for the growth of alucones and also for other MLD grown metalcones [230]

DFT calculations were also successfully employed to investigate and understand the infiltration of ZnO into the Kevlar polymer with VPI deposition technique. [224] DFT predicted that the final structure of VPI is likely to consist of a hybrid material composed of nanoclusters of ceramic ZnO and covalently cross-linked Kevlar chains. These findings were also supported from the XRD patterns of the samples experimentally.

2.9 Summary

Despite the increasing interest in and importance of hybrid inorganic-organic films in multiple technologies, and the increasing number of MLD processes developed for a broad range of materials to date, in contrast to ALD of solids, there is very little microscopic understanding of the reaction mechanisms and suitable chemistries for hybrid film growth. In addition, the origin of some key findings from experimental studies is also missing. In this regard, several questions that remain still open in the field can be addressed using density functional theory (DFT) studies:

1. **How do metal precursors determine film growth, stability and flexibility?**

One of the target properties needed in a hybrid film is to promote the deposition of a stable and flexible hybrid film with a growth per cycle (GPC) that corresponds to the inorganic-organic unit length. In practice, however, these properties are achieved depending on the precursors employed to deposit the relevant films. How do precursors affect these properties? This question can be addressed with modelling of MLD process and the calculation of surface-precursor and precursor-precursor reaction energies with DFT.

2. **Why does glycerol (GL) yield thicker films compared to ethylene glycol (EG) in hybrid film growth?**

Ethylene glycol (EG) and glycerol (GL) are two organic molecules with a very similar chemical structure. However, many studies, as described in this chapter, e.g. **Fig. 15**, have shown that GL is a more suitable precursor for the deposition of hybrid films, giving thicker films and higher GPCs. Why? In my work this question is addressed by modelling the MLD process for alucone films, which are the prototype example of hybrid films, and by studying the interactions between timethylaluminium (TMA) with EG and GL.

3. Is it possible to get the desired film growth with aliphatic organic precursors?

Aliphatic organic precursors in general have been found to give hybrid films with small GPC (especially at high temperatures). But, is it possible that the right surface/inorganic precursor combination can enable the ideal configuration of these aliphatic organic molecules? In my work we determined this by modelling the MLD process for titanicone films using three different surface models which are anatase TiO_2, rutile TiO_2 and Al_2O_3 and two different inorganic precursors, titanium tetrachloride ($TiCl_4$) and tetrakis(dimethylamido)titanium ($Ti(DMA)_4$).

4. What are the advantages of aromatic MLD precursors over aliphatic MLD precursors?

Studies have shown that the desired film growth of hybrid films can be achieved by using aromatic organics instead of aliphatic organics. Why this and what is the superiority of aromatic organics over aliphatic organics? We address this question by exploring the chemistry of aromatic organics in hybrid film growth. The role of the ring functionalisation is also investigated.

5. How can we make better precursor choices for a deposition process?

Precursor chemistry is key for the successful deposition of thin films. To make sure that the right precursors are being chosen, a combination of theoretical and experimental data is needed. DFT allows us to perform a rapid screening to understand in detail the geometry and reactivity of precursors and predict which precursors would be best for deposition processes. In this way less resources and time are wasted on experiments.

6. How does the temperature impact the chemistry in hybrid film growth?

For most of the reported MLD processes for hybrid films the GPC decreases significantly with increasing the temperature. What happens at high temperatures? Can desorption or decomposition reactions occur? Do the organic molecules replace the pre-adsorbed molecules during the second half-cycle of MLD process? These question can be addressed in the future by modelling these reactions and performing molecular dynamic (MD) calculations to investigate the chemistry of MLD films in presence of temperature.

2.10 References

1. S. D. Elliott, *Semiconductor Science and Technology*, **2012**, 27, 074008.
2. P. Sundberg, M. Karppinen, *Beilstein Journal of Nanotechnology*, **2014**, 5, 1104–1136.
3. X. Meng, *Journal of Materials Chemistry A*, **2017**, 5, 18326–18378.
4. J. Multia, M. Karppinen, *Advanced Materials Interfaces*, **2022**, 9, 2200210.
5. H. Jain, M. Creatore, P. Poodt, *Dalton Transactions*, **2022**, 51**,** 7918–7927.
6. R. K. Kanjolia, J. Anthis, R. Odedra, P. Williams, P. N. Heys, *ECS Transactions*, **2008**, 16, 79–86.
7. R. W. Johnson, A. Hultqvist, S. F. Bent, *Materials Today*, **2014**, 17, 236–246.
8. M. Leskelä, M. Ritala, *Thin Solid Films*, **2002**, 409, 138–146.
9. A. Devi, *Coordination Chemistry Reviews*, **2013**, 257, 3332–3384.
10. J. Multia, A. Khayyami, J. Heiska, M. Karppinen, *Journal of Vacuum Science & Technology A*, **2020**, 38, 052406.
11. N. M. Adamczyk, A. A. Dameron, S. M. George, *Chemistry of Materials*, **2008**, 20, 3315–3326.
12. J. Penttinen, M. Nisula, M. Karppinen, *Chemistry—A European Journal*, **2019**, 25, 11466–11473.
13. M. Nisula, A. J. Karttunen, E. Solano, G. C. Tewari, M. Karppinen, M. Minjauw, H. S. Jena, P. V. D. Voort, D. Poelman, Ch. Detavernier, *ACS Applied Materials & Interfaces*, **2021**, 13, 10249–10256.
14. A. Philip, S. Vasala, P. Glatzel, M. Karppinen, *Dalton Transactions*, **2021**, 50, 16133–16138.
15. J. Heiska, O. Sorsa, T. Kallio, M. Karppinen, *Chemistry—A European Journal*, **2021**, 27, 8799–8803.
16. M. Rogowska, P. A. Hansen, H. H. Sønsteby, J. Dziadkowiec, H. Valen, O. Nilsen, *Dalton Transactions*, **2021**, 50, 12896–12905.
17. A. Philip, J. P. Niemelä, G. C Tewari, B. Putz, Th. E. J. Edwards, M. Itoh, I. Utke, M. Karppinen, *ACS Applied Materials & Interfaces*, **2020**, 12, 21912–21921.
18. J. P. Niemelä, A. Philip, N. Rohbeck, M. Karppinen, J. Michler, I. Utke, *ACS Applied Nano Materials*, **2021**, 4, 1692–1701.
19. Y. S. Park, H. Kim, B. Cho, Ch. Lee, S. E. Choi, M. M. Sung, J. S. Lee, *ACS Applied Materials & Interfaces*, **2016**, 8, 17489–17498.
20. B. Yoon, D. Seghete, A. S. Cavanagh, S. M. George, *Chemistry of Materials*, **2009**, 21, 5365–5374.
21. R. A. Hall, S. M. George, Y. Kim, W. Hwang, M. E. Samberg, N. A. M. Riviere, R. J. Narayan, *Jom*, **2014**, 66, 649–653.
22. O. Nilsen, V. Miikkulainen, K. B. Gandrud, E. Østreng, A. Ruud, *Physica Status Solidi (A) Applications and Materials Science*, **2014**, 211, 357–367.
23. K. Kerckhove, F. Mattelaer, J. Dendooven, Ch. Detavernier, *Dalton Transactions*, **2017**, 46, 4542–4553.
24. S. Lee, M. Kim, G. Baek, H. Kim, T. Thi N. Van, D. Gwak, K. Heo, B. Shong, J. S. Park, *ACS Applied Materials & Interfaces*, **2020**, 12, 43212–43221.

25. D. M. Piper, J. J. Travis, M. Young, S. B Son, S. Ch. Kim, K. H. Oh, S. M. George, Ch. Ban, S. H. Lee, *Advanced Materials*, **2014**, 26, 1596–1601.
26. C. Y. Kao, B. Li, Y. Lu, J. W. Yoo, A. J. Epstein, *Journal of Materials Chemistry C*, **2014**, 2, 6171–6176.
27. P. Kaur, A. Muriqi, J. L. Wree, R. Ghiyasi, M. Safdar, M. Nolan, M. Karppinen, A. Devi, *Dalton Transactions*, **2022**, 51, 5603–5611.
28. H. Jain, P. Poodt, *Dalton Transactions*, **2021**, 50, 5807–5818.
29. E. Østreng, H. H. Sønsteby, T. Sajavaara, O. Nilsen, H. Fjellvåg, *Journal of Materials Chemistry C*, **2013**, 1, 4283–4290.
30. D. J. Comstock, J. W. Elam, *The Journal of Physical Chemistry C*, **2013**, 117, 1677–1683.
31. Q. Peng, B. Gong, R. M. VanGundy, G. N. Parsons, *Chemistry of Materials*, **2009**, 21, 820–830.
32. J. Kint, F. Mattelaer, S. S. T. Vandenbroucke, A. Muriqi, M. M. Minjauw, M. Nisula, Ph. M. Vereecken, M. Nolan, J. Dendooven, Ch. Detavernier, *Chemistry of Materials*, **2020**, 32, 4451–4466.
33. K. Kerckhove, M. K. S. Barr, L. Santinacci, P. M. Vereecken, J. Dendooven, Ch. Detavernier, *Dalton Transactions*, **2018**, 47, 5860–5870.
34. D. J. Hagen, A. Devi, *Dalton Transactions*, **2018**, 47, 15791–15800.
35. A. Sood, P. Sundberg, J. Malm, M. Karppinen, *Applied Surface Science*, **2011**, 257, 6435–6439.
36. K. B. Klepper, O. Nilsen, P. A. Hansen, H. Fjellvåg, *Dalton Transactions*, **2011**, 40, 4636–4646.
37. P. Kaur, L. Mai, A. Muriqi, D. Zanders, R. Ghiyasi, M. Safdar, N. Boysen, M. Winter, M. Nolan, M. Karppinen A. Devi, *Chemistry–A European Journal*, **2021**, 27, 4913–4926.
38. S. M. George, B. H. Lee, B. Yoon, A. I. Abdulagatov, R. A. Hall, *Journal of Nanoscience and Nanotechnology*, **2011**, 11, 7948–7955.
39. B. H. Lee, B. Yoon, A. I. Abdulagatov, R. A. Hall, S. M. George, *Advanced Functional Materials*, **2013**, 23, 532–546.
40. B. Yoon, J. L. O'Patchen, D. Seghete, A. S. Cavanagh, S. M. George, *Chemical Vapor Deposition*, **2009**, 15, 112–121.
41. A. Tanskanen, P. Sundberg, M. Nolan, M. Karppinen, *Thin Solid Films*, **2021**, 736, 138896.
42. P. Sundberg, M. Karppinen, *European Journal of Inorganic Chemistry*, **2014**, 6, 968–974.
43. L. Keskiväli, M. Putkonen, E. Puhakka, E. Kenttä, J. Kint, R. K. Ramachandran, Ch. Detavernier, P. Simell, *ACS Omega*, **2018**, 3, 7141–7149.
44. W. Al Zoubi, M. P. Kamil, S. Fatimah, N. Nisa, Y. G. Ko, *Progress in Materials Science*, **2020**, 112, 100663.
45. P. G. Romero, *Advanced Materials*, **2001**, 13, 163–174.
46. P. Judeinstein, C. Sanchez, *Journal of Materials Chemistry*, **1996**, **6**, 511–525.
47. B. H. Lee, V. R. Anderson, S. M. George, *ECS Transactions*, **2011**, 41, 131.
48. A. I. Abdulagatov, R. A. Hall, J. L. Sutherland, B. H. Lee, A. S. Cavanagh, S. M. George, *Chemistry of Materials*, **2012**, 24, 2854–2863.
49. B. H. Lee, V. R. Anderson, S. M. George, *ACS Applied Materials & Interfaces*, **2014**, 6, 16880–16887.
50. J. W. Dumont, S. M. George, *Journal of Physical Chemistry C*, **2015**, 119, 14603–14612.

51. O. L. Shalev, N. Leifer, M. Ejgenberg, H. Aviv, Il. Perelshtein, *Batteries & Supercaps*, **2021**, 4, 1739–1748.
52. J. J. Brown, R. A. Hall, P. E. Kladitis, S. M. George, V. M. Bright, *ACS Nano*, **2013**, 7, 7812–7823.
53. N. E. Richey, S. Borhan, S. F. Bent, *Dalton Transaction*, **2021**, 50, 4577–4582.
54. J. P. Niemelä, N. Rohbeck, J. Michler, I. Utke, *Dalton Transactions*, **2020**, 49, 10832–10838.
55. D. Choudhury, G. Rajaraman, S. K. Sarkar, **2018**, 108, 01A108.
56. P. C. Lemaire, C. J. Oldham, G. N. Parsons, *Journal of Vacuum Science & Technology A Vacuum Surfaces and Films*, **2016**, 34, 01A134.
57. T. Tynell, I. Terasaki, H. Yamauchi, M. Karppinen, *Journal of Materials Chemistry A*, **2013**, 1, 13619–13624.
58. D. M. Pipera, Y. Lee, S. B. Son, T. Evans, F. Lin, D. Nordlund, X. Xiao, S. M. Georg, S. H. Lee, Ch. Ban, *Nano Energy*, **2016**, 22, 202–210.
59. F. Yang, J. Brede, H. Ablat, M. Abadia, L. Zhang, C. Rogero, S. D. Elliott, M. Knez, *Advanced Materials & Interfaces*, **2017**, 4, 1700237.
60. P. A. Hansen, O. Nilsen, *Dalton Transactions*, **2021**, 50, 8307–8313.
61. O. Nilsen, K. R. Haug, T. Finstad, *Chemical Vapor Deposition*, **2013**, 19, 174–179.
62. W. Zhou, J. Leem, I. Park, Y. Li, Z. Jin, Y. S. Min, *Journal of Materials Chemistry*, **2012**, 22, 23935–23943.
63. K. S. Han, Y. Park, G. Han, B. H. Lee, K. H. Lee, D. H Son, S. Im, M. M. Sung, *Journal of Materials Chemistry*, **2012**, 22, 19007–19013.
64. J. Huang, M. Lee, A. T. Lucero, L. Cheng, M. W. Ha, J. Kim, *Japanese Journal of Applied Physics*, **2016**, 55, 4–8.
65. K. Ashurbekova, K. Ashurbekova, B. A. Lerma, I. Šarić, L. Barandiaran, E. Modin, M. Petravić, R. P. Jimenez, M. Knez, *ACS Applied Nano Materials*, **2022**, 5, 2762–2768.
66. K. Ashurbekova, K. Ashurbekova, I. Saric, E. Modin, M. Petravic, I. Abdulagatov, A. Abdulagatova, M. Knez, *Chemical Communication*, **2021**, 57, 2160–2163.
67. S. T. Oyakhire, H. Ablat, N. E. Richey, S. F. Bent, *Journal of Vacuum Science & Technology A*, **2022**, 40, 023405.
68. A. Lushington, J. Liu, M. N. Bannis, B. Xiao, S. Lawes, R. Li, X. Sun, *Applied Surface Science*, **2015**, 357, 1319–1324.
69. B. Gong, G. N. Parsons, *ECS Journal of Solid State Science and Technology*, **2012**, 1, 210–215.
70. B. Gong, Q. Peng, G. N. Parsons, *The Journal of Physical Chemistry B*, **2011**, 115, 5930–5938.
71. Y. Lee, B. Yoon, A. S. Cavanagh, S. M. George, *Langmuir*, **2011**, 27, 15155–15164.
72. B. Gong, J. C. Spagnola, G. N. Parsons, *Journal of Vacuum Science & Technology A Vacuum Surfaces and Films*, **2012**, 30, 01A156.
73. K. B. Klepper, O. Nilsen, S. Francis, H. Fjellvåg, *Dalton Transactions*, **2014**, 43, 3492–3500.
74. K. B. Klepper, O. Nilsen, H. Fjellvåg, *Dalton Transaction*, **2010**, 39, 11628–11635.
75. N. Bahlawane, D. Arl, J. S. Thomann, N. Adjeroud, K. Menguelti, D. Lenoble, *Surface and Coatings Technology*, **2013**, 230, 101–105, 2013.

76. O. Nilsen, K. Klepper, H. Nielsen, H. Fjellvaåg, *ECS Transactions*, **2008**, 16, 3–14.
77. S. Lee, G. H. Baek, J. H. Lee, D. W. Choi, B. Shong, J. S. Park, *Applied Surface Science*, **2018**, 458, 864–871.
78. C. Ehm, G. Antinucci, P. H. M. Budzelaar, V. Busico, *Journal of Organometallic Chemistry*, **2014**, 772, 161–171.
79. S. E. Potts, G. Dingemans, C. Lachaud, W. M. M. Kessels, *Journal of Vacuum Science & Technology A Vacuum Surfaces and Films*, **2012**, 30, 021505.
80. S. Y. Lee, B. Luo, Y. Sun, J. M. White, Y. Kim, *Applied Surface Science*, **2004**, 222, 234–242.
81. H. G. Kim, M. Kim, B. Gu, M. R. Khan, B. G. Ko, S. Yasmeen, Ch. S. Kim, S. H. Kwon, J. Kim, J. Kwon, K. Jin, B. Cho, J. S. Chun, B. Shong, H. B. R. Lee, *Chemistry of Materials*, **2020**, 32, 8921–8929.
82. S. Wu, Z. Wang, S. Xiong, Y. Wang, *Journal of Membrane Science*, **2019**, 578, 149–155.
83. R. R. Amashaev, N. M. R. Alikhanov, A. M. Ismailov, I. M. Abdulagatov, *Journal of Vacuum Science & Technology A*, **2022**, 40, 052401.
84. S. Ishchuk, D. H. Taffa, O. Hazut, N. Kaynan, R. Yerushalmi, *ACS Nano*, **2012**, 6, 7263–7269.
85. Q. Dong, J. Jiang, S. Li, M. Yu, *Journal of Membrane Science*, **2021**, 622, 119040.
86. Q. Dong, Z. Song, F. Zhou, H. Li, M. Yu, *Microporous Mesoporous Materials*, **2019**, 281, 9–14.
87. Z. Song, M. Fathizadeh, Y. Huang, K. H. Chu, Y. Yoon, L. Wang, W. L. Xu, M. Yu, *Journal of Membrane Science*, **2016**, 510, 72–78.
88. D. Sarkar, S. Ishchuk, D. H. Taffa, N. Kaynan, B. A. Berke, T. Bendikov, R. Yerushalmi, *The Journal of Physical Chemistry C*, **2016,** 120, 3853–3862.
89. R. L. Patel, Y. B. Jiang, X. Liang, *Ceramics International*, **2015**, 41, 2240–2246.
90. D. Sarkar, D. H. Taffa, S. Ishchuk, O. Hazut, H. Cohen, G. Toker, M. Asschera, R. Yerushalmi, *Chemical Communication*, **2014**, 50, 9176–9178.
91. K. Kerckhove, F. Mattelaer, D. Deduytsche, P. M. Vereecken, J. Dendooven, Ch. Detavernier, *Dalton Transactions*, **2016**, 45, 1176–1184.
92. A. I. Abdulagatov, K. E. Terauds, J. J. Travis, A. S. Cavanagh, R. Raj, S. M. George, *Journal of Physical Chemistry C*, **2013**, 117, 17442–17450.
93. Z. C. Huertas, D. Settipani, C. Flox, J. R. Morante, T. Kallio, J. J. Biendicho, *Scientific Reports*, **2022**, 12, 137.
94. K. H. Yoon, K. S. Han, M. M. Sung, *Nanoscale Research Letters*, **2012**, 7, 2–7.
95. Y. Q. Cao, L. Zhu, X. Li, Z. Y. Cao, D. Wu, A. D. Li, *Dalton Transactions*, **2015**, 44, 14782–14792.
96. P. Sundberg, A. Sood, X. Liu, L. S. Johansson, M. Karppinen, *Dalton Transactions*, **2012**, 41, 10731–10739.
97. J. P. Niemelä, M. Karppinen, *Dalton Transactions*, **2015**, 44, 591–597.
98. J. W. Jung, K. S. Han, K. H. Yoon, L. Lee, Y. E. K. Lee, Ch. H. Lee, S. U. Lee, M. M. Sung, *Organic Electronics*, **2018**, 52, 237–242.
99. J. B. Fang, S. Z. Chang, Q. Ren, T. Q. Zi, D. Wu, A. D. Li, *ACS Applied Materials & Interfaces*, **2021**, 13, 32520–32530.

100. J. P. Niemelä, A. Giri, P. E. Hopkins, M. Karppinen, *Journal of Materials Chemistry A*, **2015**, 11527–11532.
101. Y. Q. Cao, W. Zhang, L. Xu, Ch. Liu, L. Zhu, L. G. Wang, D. Wu, A. D. Li, G. Fang, *Langmuir*, **2019**, 35, 3020–3030.
102. C. Liu, Y. Q. Cao, D. Wu, A. D. Li, *IEEE Electron Device Letters*, **2020**, 41, 155–158.
103. Ch. Chen, P. Li, G. Wang, Y. Yu, F. Duan, C. Chen, W. Song, Y. Qin, M. Knez, *Angewandte Chemie*, **2013**, 52, 9196–9200.
104. A. Philip, R. Ghiyasi, M. Karppinen, *ChemNanoMat*, **2021**, 7, 253–256.
105. A. Philip, R. Ghiyasi, M. Karppinen, *Molecules*, **2021**, 27, 3214.
106. B. H. Lee, K. H. Lee, S. Im, M. M. Sung, *Organic Electronic*, **2008**, 9, 1146–1153.
107. L. Momtazi, D. A. Dartt, O. Nilsen, J. R. Eidet, *Journal of Biomedical Materials Research*, **2018**, 106, 3090–3098.
108. L. Momtazi, H. H. Sønsteby, D. A. Dartt, J. R. Eidet, O. Nilsen, *RSC Advances*, **2017**, 7, 20900–20907.
109. B. Yoon, J. L. O'Patchen, D. Seghete, A. S. Cavanagh, S. M. George, *Chemcal Vapor Deposition*, **2009**, 15, 112–121.
110. S. B. Son, Y. Wang, J. Xu, X. Li, M. Groner, A. Stokes, Y. Yang, Y. T. Cheng, Ch. Ban, *ACS Applied Materials & Interfaces*, **2017**, 9, 40143–40150.
111. X. Xu, H. Wang, J. Wang, M. Muhammad, Z. Wang, P. Chen, W. Zhao, B. Kang, J. Zhang, Ch. Li, Y. Duan, *ACS Applied Energy Materials*, **2020**, 3, 4208–4216.
112. A. Perrotta, R. Berger, F. Muralter, A. M. Coclite, *Dalton Transactions*, **2019**, 48, 14178–14188.
113. X. Liang, Y. B. Jiang, A. W. Weimer, *Journal of Vacuum Science & Technology A Vacuum Surfaces and Films*, **2012**, 30, 01A108.
114. S. Cho, G. Han, K. Kim, M. M. Sung, *Angewandte Chemie*, **2011**, 23, 2794–2798.
115. T. Mu, Y. Zhao, C. Zhao, N. G. Holmes, Sh. Lou, J. Li, W. Li, M. He, Y. Sun, C. Du, R. Li, J. Wang, G. Yin, X. Sun, *Advanced Functional Materials*, **2021**, 31, 1–9.
116. M. Włodarski, M. Putkonen, M. Norek, *Coatings*, **2020**, 10, 459.
117. R. Berger, M. Seiler, A. Perrotta, A. M. Coclite, *Materials*, **2021**, 14, 1418.
118. G. Marin, R. Funahashi, M. Karppinen, *Advanced Engineering Materials*, **2020**, 22, 2000535.
119. J. Huang, A. T. Lucero, L. Cheng, H. J. Hwang, M. W. Ha, J. Kim, *Applied Physics Letters*, **2015**, 106, 123101.
120. R. Ghiyasi, G. C. Tewari, M. Karppinen, *Journal of Physical Chemistry C*, **2020**, 124, 13765–13770.
121. G. Luka, L. Wachnicki, B. S. Witkowski, R. Jakiela, I. S. Virt, *Materials & Design*, **2017**, 119, 297–302.
122. T. Tynell, A. Giri, J. Gaskins, P. E. Hopkins, P. Mele, K. Miyazakid, M. Karppinen, *Journal of Materials Chemistry A*, **2014**, 2, 12150–12152.
123. J. Liu, B. Yoon, E. Kuhlmann, M. Tian, J. Zhu, S. M. George, Y. C. Lee, R. Yang, *Nano Letters*, **2013**, 13, 5594–5599.
124. A. J. Karttunen, L. Sarnes, R. Townsend, J. Mikkonen, M. Karppinen, *Advanced Electronic Materials*, **2017**, 3, 1600459.
125. B. Yoon, B. H. Lee, S. M. George, *ECS Transactions*, **2011**, 41, 271.

126. H. Song, S. T. Hwang, B. H. Choi, *Thin Solid Films*, **2020**, 706, 138082.
127. A. J. Karttunen, T. Tynell, M. Karppinen, *Nano Energy*, **2016**, 22, 338–348.
128. F. Krahl, Y. Ge, M. Karppinen, *Semiconductor Science and Technology*, **2020**, 36, 025012.
129. C. Liu, J. Bin Fang, Y. Q. Cao, D. Wu, A. D. Li, *Applied Physics Letters*, **2020**, 117, 031601.
130. J. Huang, H. Zhang, A. Lucero, L. Cheng, S. KC, J. Wang, J. Hsu, K. Cho, J. Kim, *Journal of Materials Chemistry C*, **2016**, 4, 2382–2389.
131. T. Tynell, M. Karppinen, *Thin Solid Films*, **2014**, 551, 23–26.
132. B. Yoon, B. H. Lee, S. M. George, *Journal of Physical Chemistry C*, **2012**, 16, 24784–24791.
133. F. Krahl, A. Giri, M. S. Bin Hoque, L. Sederholm, P. E. Hopkins, M. Karppinen, *Journal of Physical Chemistry C*, **2020**, 124, 24731–24739.
134. G. Marin, T. Tynell, M. Karppinen, *Journal of Vacuum Science & Technology A*, **2019**, 37, 020906.
135. A. J. Karttunen, T. Tynell, M. Karppinen, *Journal of Physical Chemistry C*, **2015**, 119, 13105–13114.
136. T. Tynell, H. Yamauchi, M. Karppinen, *Journal of Vacuum Science & Technology A Vacuum Surfaces and Films*, **2014**, 32, 01A105.
137. P. Sundberg, A. Sood, X. Liu, M. Karppinen, *Dalton Transactions*, **2013**, 42, 15043–15052.
138. A. Sood, P. Sundberg, M. Karppinen, *Dalton Transactions*, **2013**, 42, 3869–3875.
139. A. Räupke, F. Albrecht, J. Maibach, A. Behrendt, A. Polywka, R. Heiderhoff, J. Helzel, T. Rabe, H. H. Johannes, W. Kowalsky, E. Mankel, T. Mayer, P. Görrn, T. Riedl, *ESC Transactions*, **2014**, 64, 1607–1607.
140. K. S. Han, M. M. Sung, *Journal of Nanoscience and Nanotechnology*, **2014**, 14, 6137–6142.
141. Y. Sun, C. Zhao, K. R. Adair, Y. Zhao, L. V. Goncharova, J. Liang, C. Wang, J. Li, R. Li, M. Cai, T. K. Sham X. Sun, *Energy & Environmental Science*, **2021**, 14, 4085–4094.
142. A. Khayyami, M. Karppinen, *Chemistry of Materials*, **2018**, 30, 5904–5911.
143. K. Kerckhove, J. Dendooven, Ch. Detavernier, *Journal of Vacuum Science and Technology*, **2018**, 36, 051506.
144. B. H. Lee, V. R. Anderson, S. M. George, *Chemical Vapor Deposition*, **2013**, 19, 204–212.
145. J. Heiska, M. Karppinen, *Dalton Transactions*, **2022**, 51, 4246–4251.
146. M. Nisula, M. Karppinen, *Nano Letters*, **2016**, 16, 1276–1281.
147. J. Penttinen, M. Nisula, M. Karppinen, *Chemistry—A European Journal*, **2017**, 23, 18225–18231.
148. J. Multia, J. Heiska, A. Khayyami, M. Karppinen, *ACS Applied Materials & Interfaces*, **2020**, 12, 41557–41566.
149. A. Khayyami, A. Philip, J. Multia, M. Karppinen, *Dalton Transactions*, **2020**, 49, 11310–11316.
150. J. Heiska, M. Nisula, E. Rautama, A. J. Karttunen, M. Karppinen, *Dalton Transactions*, **2020**, 49, 1591–1599.
151. D. J. Hagen, L. Mai, A. Devi, J. Sainio, M. Karppinen, *Dalton Transactions*, **2018**, 47, 15791–15800.

152. M. Nisula, J. Linnera, A. J. Karttunen, M. Karppinen, *Chemistry—A European Journal*, **2017**, 23, 2988–2992.
153. J. Heiska, M. Madadi, M. Karppinen, *Nanoscale Advances*, **2020**, 2, 2441–2447.
154. E. Ahvenniemi, M. Karppinen, *Chemical Communnications*, **2016**, 52, 1139–1142.
155. H. Wang, K. E. Gregorczyk, S. B. Lee, G. W. Rubloff, C. F. Lin, *Journal of Physical Chememistry C*, **2020**, 124, 6830–6837.
156. E. Kazyak, M. Shin, W. S. Lepage, T. H. Cho, N. P. Dasgupta, *Chemical Communications*, **2020**, 56, 15537–15540.
157. L. D. Salmi, E. Puukilainen, M. Vehkamäki, M. Heikkilä, M. Ritala, *Chemical Vapor Deposition*, **2009**, 15, 221–226.
158. Z. Giedraityte, J. Sainio, D. Hagen, M. Karppinen, *Journal of Physical Chemistry C*, **2017**, 121, 17538–17545.
159. J. Shi, L. Zeng, Sh. Nikzad, D. M. Koshy, A. S. Asundi, C. MacIsaac, S. F. Bent, *Journal of Vacuum Science & Technology A*, **2022**, 40, 012402.
160. D. S. Bergsman, J. G. Baker, R. G. Closser, C. MacIsaac, M. Lillethorup, A. L. Strickler, L. Azarnouche, L. Godet, S. F. Bent, *Advanced Functional Materials*, **2019**, 29, 1–11.
161. E. Ahvenniemi, M. Karppinen, *Dalton Transactions*, **2016**, 45, 10730–10735.
162. A. Tanskanen, M. Karppinen, *Scientific Reports*, **2018**, 8, 1–8, 2018.
163. A. Khayyami, A. Philip, M. Karppinen, *Angewandte Chemie*, **2019**, 131, 13534–13538.
164. A. Philip, Y. Zhou, G. C. Tewari, S. Dijken, M. Karppinen, *Journal of Materials Chemistry C*, **2022**, 10, 294–300.
165. S. Zhu, Y. Yang, J. Liu, J. Sun, *Journal of Materials Chemistry A*, **2020**, 8, 25371–25381.
166. A. Tanskanen, M. Karppinen, *Dalton Transactions*, **2015**, 44, 19194–19199.
167. S. Zhao, J. Yang, F. Duan, B. Zhang, Y. Liu, B. Zhang, Ch. Chen, Y. Qin, *Journal of Colloid and Interface Science*, **2021**, 598, 45–55.
168. C. Chen, F. Duan, Sh. Zhao, W. Wang, F. Yang, W. Nuansing, B. Zhang, Y. Qin, M. Knez, *Applied Catalysis B: Environmental*, **2019**, 248, 218–225.
169. E. Ahvenniemi, M. Karppinen, *Chemistry of Materials*, **2016**, 28, 6260–6265.
170. J. E. Bratvold, G. Carraro, D. Barreca, O. Nilsen, *Applied Surface Science*, **2015**, 347, 861–867.
171. K. B. Lausund, M. S. Olsen, P. A. Hansen, H. Valen, O. Nilsen, *Journal of Materials Chemistry A*, **2020**, 8, 2539–2548.
172. K. B. Lausund, V. Petrovic, O. Nilsen, *Dalton Transactions*, **2017**, 46, 16983–16992.
173. A. G. Sobas, K. B. Lausund, M. C. D Koning, V. Petrovic, S. M. Chavan, M. W. Smith, O. Nilsen, *Global Challenges*, **2021**, 5, 2100001.
174. Z. Chen, H. Wang, X. Wang, P. Chen, Y. Liu, H. Zhao, Y. Zhao, Y. Duan, *Scientific Reports*, **2017**, 7, 1–9.
175. J. Lei, W. J. Ding, C. Liu, D. Wu, W. M. Li, A. D. Li, *APL Materials*, **2021**, 9, 121110.
176. L. Lee, J. Park, K. Seok Han, R. Saravana Kumar, M. Mo Sung, *Applied Surface Science*, **2019**, 476, 897–904.
177. M. H. Tseng, D. Y. Su, G. L. Chen, F. Y. Tsai, *ACS Applied Materials & Interfaces*, **2021**, 13, 27392–27399.
178. A. I. Abdulagatov, K. N. Ashurbekova, K. N. Ashurbekova, R. R. Amashaev, M. K. Rabadanov, I. M. Abdulagatov, *Russian Journal of Applied Chemistry*, **2018**, 91, 347–359.

179. C. Y. Kao, J. W. Yoo, Y. Min, A. J. Epstein, *ACS Applied Materials & Interfaces*, **2012**, 4, 137–141.
180. S. Lee, G. Baek, J. H. Lee, T. T. N. Van, A. A. Saad, B. Shong, J. S. Park, *Applied Surface Science*, **2020**, 525, 146383.
181. S. H. Lee, H. J. Jeong, K. L. Han, G. Baek, J. S. Park, *Journal of Materials Chemistry C*, **2021**, 9, 4322–4329.
182. Z. Giedraityte, M. Tuomisto, M. Lastusaari, M. Karppinen, *ACS Applied Materials & Interfaces*, **2018**, 10, 8845–8852.
183. M. Tuomisto, Z. Giedraityte, L. Mai, A. Devi, V. Boiko, K. Grzeszkiewicz, D. Hreniak, M. Karppinen, M. Lastusaari, *Journal of Luminescence*, **2019**, 213, 310–315.
184. S. Kitagawa, M. Kondo, *Bulletin of the Chemical Society of Japan*, **1998**, 71, 1739–1753.
185. F. Containing, L. Rectangular, *Journal of the American Chemical Society*, **1995**, 117, 10401–10402.
186. S. R. Batten, N. R. Champness, X. M. Chen, J. G. Martinez, S. Kitagawa, L. Öhrström, M. O'Keeffe, M. P. Suh, J. Reedijk, *Pure and Applied Chemistry*, **2013**, 85, 1715.
187. J. L. C. Rowsell, O. M. Yaghi, *Microporous Mesoporous Materials*, **2004**, 73, 3–14.
188. M. D. Allendorf, A. Schwartzberg, V. Stavila, A. A. Talin, *Chemistry—A European Journal*, **2011**, 17, 11372–11388.
189. L. E. Kreno, K. Leong, O. K. Farha, M. Allendorf, R. P. Duyne, J. T. Hupp, *Chemical Reviews*, **2012**, 112, 1105–1125.
190. Y. Chen, S. Ma, *Reviews in Inorganic Chemistry*, **2012**, 32, 81–100.
191. Z. Giedraityte, L. S. Johansson, M. Karppinen, *RSC Advances*, **2016**, 6, 103412–103417.
192. L. D. Salmi, M. Mattinen,T. Niemi, M. J. Heikkilä, K. Mizohata, S. Korhonen, S. P. Hirvonen, J. Räisänen, M. Ritala, *Advanced Materials & Interfaces*, **2017**, 4, 4–9.
193. M. Putkonen, J. Harjuoja, T. Sajavaara, L. Niinistö, *Journal of Materials Chemistry*, **2007**, 17, 664–669.
194. T. Yoshimura, S. Tatsuura, W. Sotoyama, *Applied Physics Letters*, **1991**, 59, 482–484.
195. S. Yoshida, T. Ono, M. Esashi, *Micro Nano Letters*, **2010**, 5, 321–323.
196. S. Haq, N. V. Richardson, *Journal of Physical Chemistry B*, **1999**, 103, 5256–5265.
197. T. Bitzer, N. V. Richardson, *Applied Physical Letters*, **1997**, 71, 1890–1892.
198. T. Bitzer, N. V. Richardson, *Applied Surface Science*, **1999**, 144, 339–343.
199. H. L. Shao, S. Umemoto, T. Kikutani, N. Okui, *Polymer*, **1997**, 38, 459–462.
200. Y. Du, S. M. George, *Journal of Physical Chemistry C*, **2007**, 111, 8509–8517.
201. A. Kubono, N. Yuasa, H. L. Shao, S. Umemoto, N. Okui, *Thin Solid Films*, **1996**, 289, 107–111.
202. A. Nagai, H. Shao, S. Umemoto, T. Kikutani, N. Okui, *High Performance Polymers*, **2001**, 13, 169–179.
203. Q. Peng, K. Efimenko, J. Genzer, G. N. Parsons, *Langmuir*, **2012**, 28, 10464–10470.
204. N. M. Adamczyk, A. A. Dameron, S. M. George, *Langmuir*, **2008**, 24, 2081–2089.
205. H. Zhou, M. F. Toney, S. F. Bent, *Macromolecules*, **2013**, 46, 5638–5643.
206. A. Kim, M. A. Filler, S. Kim, S. F. Bent, *Journal of the American Chemical Society*, **2005**, 127, 6123–6132.
207. P. W. Loscutoff, H. Zhou, S. B. Clendenning, S. F. Bent, *ACS Nano*, **2010**, 4, 331–341.
208. C. Prasittichai, H. Zhou, S. F. Bent, *ACS Applied Materials Interfaces*, **2013**, 5, 13391.

209. H. Zhou, S. F. Bent, *ACS Applied Materials & Interfaces*, **2011**, 3, 505–511.
210. J. S. Lee, Y. J. Lee, E. L. Tae, Y. S. Park, K. B. Yoon, *Materials Research Society Symposium Proceedings*, **2004**, 821, 129–140.
211. P. W. Loscutoff, H. B. R. Lee, S. F. Bent, *Chemistry of Materials*, **2010**, 22, 5563–5569.
212. T. V. Ivanova, P. S. Maydannik, D. C. Cameron, *Journal of Vacuum Science & Technology A Vacuum Surfaces*, **2012**, 30, 01A121.
213. T. Yoshimura, S. Tatsuura, W. Sotoyama, A. Matsuura, T. Hayano, *Applied Physical Letters*, **1992**, 60, 268–270.
214. T. Yoshimura, Y. Kudo, *Applied Physics Express*, **2009**, 2, 0155021–0155023.
215. T. Yoshimura, S. Ito, T. Nakayama, K. Matsumoto, *Applied Physical Letters*, **2007**, 91, 1–4.
216. T. Yoshimura, R. Ebihara, A. Oshima, *Journal of Vacuum Science & Technology A Vacuum Surfaces*, **2011**, 29, 051510.
217. T. Yoshimura, S. Ishii, *Journal of Vacuum Science & Technology A Vacuum Surfaces*, **2013**, 31, 031501.
218. M. D. Losego, Q. Peng, *Surface Modification Polymers: Methods and Applications*, **2019**, 135–159.
219. O. Yurkevich, E. Modin, I. Šarić, M. Petravić, M. Knez, *Advanced Materials*, **2022**, 34, 1–9.
220. S. M. Lee, V. Ischenko, E. Pippel, A. Masic, O. Moutanabbir, P. Fratzl, M. Knez, *Advanced Functional Materials*, **2011**, 21, 3047–3055.
221. Y. Sun, R. P. Padbury, H. I. Akyildiz, M. P. Goertz, J. A. Palmer, J. S. Jur, *Chemical Vapor Deposition*, **2013**, 19, 134–141.
222. R. P. Padbury, J. S. Jur, *Journal of Vacuum Science & Technology A Vacuum Surfaces*, **2015**, 33, 01A112.
223. C. D. McClure, C. J. Oldham, G. N. Parsons, *Surface and Coatings Technology*, **2015**, 261, 411–417.
224. I. Azpitarte, A. Zuzuarregui, H. Ablat, L. R. Rubio, A. L. Ortega, S. D. Elliott, M. Knez, *Chemistry of Materials*, **2017**, 29, 10068–10074.
225. G. Pellegrino, S. C. Carroccio, F. Ruffino, G. G. Condorelli, G. Nicotra, V. Privitera, G. Impellizzeria, *RSC Advances*, **2018**, 8, 521–530.
226. W. Wang, Ch. Chen, Ch. Tollan, F. Yang, M. Beltrán, Y. Qin, M. Knez, *ACS Applied Materials & Interfaces*, **2017**, 9, 27964–27971.
227. A. D. Taggart, N. Jeon, V. Rozyyev, E. Karapetrova, N. J. Zaluzec, R. Z. Waldman, S. B. Darling, J. W. Elam, A. B. F. Martinson, *Journal of Physical Chemistry C*, **2021**, 125, 21191–21198.
228. R. Z. Waldman, N. Jeon, D. J. Mandia, O. Heinonen, S. B. Darling, A. B. F. Martinson, *Chemistry Materials*, **2019**, 31, 5274–5285.
229. A. Motta, G. Seguini, M. Perego, R. Consonni, A. C. Boccia, G. Ambrosio, C. Baratto, P. Cerruti, M. Lavorgna, S. Tagliabue, C. Wiemer, *ACS Applied Polymer Materials*, **2022**, 4, 7191–7203.
230. Zh. Zhou, X. Zhang, R. Xu, L. Xu, Y. Ding, H. Xiao, X. Li, A. Li, G. Fang, *Materials Today Communications*, **2022**, 105061.

Chapter 3

Theoretical background and methods

3.1 The many-body problem

The objective of quantum chemistry is the solution of the time-independent many-body Schrödinger equation. For a system with N electrons, with coordinates $\{\boldsymbol{r}_1 \ldots \boldsymbol{r}_N\}$, and M nuclei, with coordinates $\{\boldsymbol{R}_1 \ldots \boldsymbol{R}_M\}$ the time-independent Schrödinger equation is: [1]

$$\mathcal{H}\,\Psi(\mathbf{r};\mathbf{R}) \;=\; \mathrm{E}\,\Psi(\mathbf{r};\mathbf{R}) \tag{1}$$

In equation (1), $\mathcal{H}$ is the Hamiltonian operator, E is the total energy of the system and Ψ is the many-body wavefunction describing the N electrons and all nuclei. While the Hamiltonian operator comprises functions for all the kinetic and potential energies of the system, the wavefunction comprises the characteristics of all particles in the system. The Hamiltonian in the absence of electric or magnetic fields can be written as: [2]

$$\mathcal{H} \;=\; \kappa_{\mathrm{n}} + \;\kappa_{\mathrm{e}} \;+\; \mathcal{V}_{\mathrm{nn}} \;+\; \mathcal{V}_{\mathrm{ne}} + \;\mathcal{V}_{\mathrm{ee}} \tag{2}$$

In equation (2), κ_{e} is the kinetic energy of the electrons, κ_{n} is the kinetic energy of nuclei, $\mathcal{V}_{\mathrm{en}}$ is the potential energy of electron-nucleus Coulomb interactions, $\mathcal{V}_{\mathrm{ee}}$ is the potential energy of electron-electron Coulomb interactions and $\mathcal{V}_{\mathrm{nn}}$ is the potential energy of nucleus-nucleus Coulomb interactions. Utilizing atomic units, where the electron mass and charge, m_e and e, the reduced Planck's constant, $\hbar$, and $4\pi\epsilon_0$ (ϵ_0 - vacuum permittivity) are all set to 1, the Hamiltonian takes the simplified form: [2]

$$\mathcal{H} = -\sum_{\mathrm{A}} \frac{1}{2\mathrm{m_A}} \nabla_{\mathrm{A}}^2 - \sum_{\mathrm{i}} \frac{1}{2} \nabla_{\mathrm{i}}^2 + \sum_{\mathrm{A>B, A\neq B}} \frac{\mathrm{Z_A Z_B}}{\mathrm{R_{AB}}} - \sum_{A} \sum_{\mathrm{i}} \frac{Z_A}{\mathrm{rA_i}} + \sum_{\mathrm{i>j}} \frac{1}{\mathrm{r_{ij}}} \tag{3}$$

In equation (3), $\mathrm{m_A}$ is the mass of nucleus A, $\mathrm{Z_A}$ is the atomic number of nucleus A and ∇^2 is the Laplacian operator. In Cartesian coordinates ($\boldsymbol{r} = (x, y, z)$) the Laplacian operator is:

$$\nabla^2 = \frac{\partial^2}{\partial \mathrm{x}^2} - \frac{\partial^2}{\partial \mathrm{y}^2} - \frac{\partial^2}{\partial \mathrm{z}^2} \tag{4}$$

As the Schrödinger equation considers the Coulomb interaction between all electrons in a system, the exact solution of this equation for systems that have more than one electron is not possible. This is known as the "many-body problem". In order to find a solutions to the

Schrödinger equation for systems that have more than one electron, approximations must be applied.

One trivial way to solve this problem is to consider ions as having only one electron. This takes away $\mathcal{V}_{ee}$ and allows us to compute the atomic orbitals. Another widely used approach to solve the many-body problem is by applying the Born-Oppenheimer approximation. [3] Born-Oppenheimer approximation states that electrons and nuclei move on different time frames as a result of their different masses; the electrons are considered dynamic as they move much faster compared to nuclei which are assumed to remain static. Based on this, nuclei are considered to have no kinetic energy ($\kappa_n = 0$) while the nuclei – nuclei interaction is constant, $\mathcal{V}_{nn}$= constant. The Hamiltonian describing only the electrons is denoted as $\mathcal{H}_e$ and has the form:

$$\mathcal{H}_e = -\sum_i \frac{1}{2}\nabla_i^2 - \sum_A \sum_i \frac{Z_A}{rA_i} + \sum_{i>j} \frac{1}{r_{ij}} \tag{5}$$

This approximation solves the Schrödinger equation by considering the nuclei positions in a system fixed, enabling us so to find the lowest energy geometry of the system:

$$\mathcal{H}_e \psi_e = E_e \psi_e \tag{6}$$

Nevertheless, the Born-Oppenheimer approximation still considers the potential energy of electron-electron Coulomb interactions, $\mathcal{V}_{ee}$.

The Linear Combination of Atomic Orbitals (LCAO) is another approximation that can be used to solve the many-body problem. LCAO describes the unknown molecular orbital as a linear, infinite expansion of a set of known functions, χ_i, each of which has a weight of c_i in the expansion. Molecular orbitals are computed from combining the known atomic orbitals. LCAO is described with the equation:

$$\Xi = \sum_i^{\infty} c_i \chi_i \tag{7}$$

The Variational Principle approximation is also used. It states that the best value for any variable parameter in an approximate wavefunction is the value that gives the lowest energy for the ground state.

3.1.1 Hartree and Hartree-Fock approximations

The Hartree method is a way to simplify the wavefunction and the calculation of the energy of a multi-electron system by presupposing that the electrons move independently and do not interact with each-other, and their motion is uncorrelated. [4, 5] On that account, for single electrons an effective Hamiltonian h(i) can be written leading to:

$$\mathcal{H} = \sum_{i} h(i) \tag{8}$$

Based on this, the interactions are described as one electron interacting with an average potential of the remaining (N-1) atoms. The modified Schrödinger equation to describe the $_i$th electron is:

$$\hbar_i \psi_i(r_i) = \varepsilon_i \psi_i(r_i) \tag{9}$$

For a system with N electrons, the wavefunction is a product of one electron wavefunctions:

$$\psi_H(r_n) = \prod_{n} \psi_n(r_n) \tag{10}$$

The total energy is the sum of the one-electron energies, i.e:

$$E_H = \varepsilon_1 + \varepsilon_2 \ldots + \varepsilon_n \tag{11}$$

Nevertheless, the Hartree approximation has some severe issues. First of all, the wavefunction determined with equation (10) does not account for the correlated motion of electrons and is therefore an independent particle wavefunction. Second, this approximation labels uniquely each electron, which is inconsistent with the behaviour of the electrons under exchange of 2 electrons. In brief, the wavefunction has to be anti-symmetric when particles are exchanged as the wavefunction and the properties of electrons cannot change depending on the electron labels. This is illustrated by employing a permutation operator P_{kl} as follows:

$$P_{kl}\psi(1,2 \ldots \mathbf{k}, \mathbf{l} \ldots n) = \lambda\psi(1,2 \ldots \mathbf{l}, \mathbf{k} \ldots n) \tag{12}$$

In equation (12), electrons k and l are exchanged and λ is a number. Physical properties of the system are not affected by the operation P_{kl}. When P_{kl} is employed for the second time, the equation is:

$$P_{kl}\psi(1,2 \ldots k, l \ldots n) = \lambda^2\psi(1,2 \ldots l, k \ldots n) \tag{13}$$

As the second permutation returns the original function, $\lambda = \pm 1$. The correct form of electrons is described with the anti-symmetric function, $\lambda = -1$. $\lambda = +1$ describes bosons such as photons. At any time, only two electrons can be exchanged. This fact makes every other permutation to be considered as anti-symmetric while still describing the same system. This way of approximating the wavefunction is known as the Slater Determinant or the Hartree-Fock wavefunction. The Hartree-Fock wave function is a determinant form:

$$\Psi_{\mathrm{HF}} = \frac{1}{\sqrt{n!}} \begin{bmatrix} \psi_1(1) & \psi_1(2) & \psi_1(3) & & \psi_1(n) \\ \psi_2(1) & \psi_2(2) & \psi_2(3) & \cdots & \psi_2(n) \\ \psi_3(1) & \psi_3(2) & \psi_3(3) & & \psi_3(n) \\ & \vdots & & \ddots & \vdots \\ \psi_n(1) & \psi_n(2) & \psi_n(3) & \cdots & \psi_n(n) \end{bmatrix} \tag{14}$$

The Hartree wavefunction is the diagonal of this function and the determinant accounts for all 2-electron permutations. The convenience of this approximation is that it considers the antisymmetry under electron exchange and some correlation, meaning that the motion of electrons with the same spin is correlated and as a consequence the wavefunction stays constant under exchange of electrons. The energy of the system utilizing the Hartree-Fock wavefunction is:

$$\begin{aligned} \mathrm{E_{HF}} = & \sum_{\mathrm{k}} \langle \psi_{\mathrm{k}}(\mathrm{i}) | \mathrm{h}(\mathrm{i}) | \psi_{\mathrm{k}}(\mathrm{i}) \rangle \\ & + \sum_{\mathrm{k}} \sum_{\mathrm{k} \neq \mathrm{l}} \left[\langle \psi_{\mathrm{k}}(\mathrm{i}) \psi_{\mathrm{l}}(\mathrm{j}) | \mathrm{h_{ij}} | \psi_{\mathrm{k}}(\mathrm{i}) \psi_{\mathrm{l}}(\mathrm{j}) \rangle \right] - \left[\langle \psi_{\mathrm{k}}(\mathrm{i}) \psi_{l}(\mathrm{j}) | \mathrm{h_{ij}} | \psi_{\mathrm{l}}(\mathrm{i}) \psi_{\mathrm{k}}(\mathrm{j}) \rangle \right] \\ & = \mathrm{h_k} + \sum_{\mathrm{k}} 2\mathrm{J_{kl}} - \mathrm{K_{kl}} \end{aligned} \tag{15}$$

In equation (15), $\mathrm{h_k}$ is the single electron kinetic energy operator, $\mathrm{J_{kl}}$ is the the Coulomb interaction, as in the Hartree Approximation and $\mathrm{K_{kl}}$ is the Fock exchange interaction. The Fock exchange interaction, $\mathrm{K_{kl}}$ is a result of the anti-symmetry under electron exchange. The anti-symmetry in electron exchange means that electrons cannot have the same quantum numbers, and this is the Pauli exclusion principle. Nonetheless, the Hartree-Fock is a static system so correlation is not fully considered. The energy associated with electron correlation is:

$$\mathrm{E_{correlation}} = \mathrm{E_{exact}} - \mathrm{E_{HF}} \tag{16}$$

In equation (16), $\mathrm{E_{exact}}$ is the exact energy of the system and $\mathrm{E_{HF}}$ is the energy computed using the Hartree-Fock approximation. The so called post-HF method, Configuration Interaction

(CI), allows for an estimation of the correlation energy. This method demonstrates the exact wavefunction as a linear combination of N-electron single particle functions.

This leads to the complete Cl-matrix which incorporates the ground state and all possible "excited states" of the given system formed by promoting electrons from occupied electrons to empty orbitals. As a result, the exact wavefunction, Ψ is:

$$\langle\psi\rangle = c_0|\psi_{HF}\rangle + c_s|S\rangle + c_D|D\rangle + \ldots + c_n|n\rangle \quad (17)$$

In equation (17), Ψ_{HF} - HF wavefunction, c - weight, $|S\rangle$ - the terms for single excitations, $|D\rangle$ - the terms for double excitation. The ground state and excited state energies can be estimated from the eigenvalues of the CI matrix, where the higher eigenvalues are upper limits for the various excited states and the lowest eigenvalue is an upper limit to the ground state energy. This is known as full-CI and has the form:

$$E_{Cl} = E_{HF} + E'_{correlation} \quad (18)$$

In equation (18), E_{HF} is the energy computed using the Hartree-Fock approximation and $E'_{correlation}$ is the correlation energy. Although the full-Cl method, for a given one electron basis set, is the most precise method to get the energy of the system, still it is not computationally tractable for systems that contain more than 10 to 15 electron. This is because this method requires solving for an large set of N-electron functions. [6]

3.1.2 Density functional theory (DFT)

Another solution to the many-body problem is taking into consideration the electron density instead of the wave function, which immediately reduces the dimensionality of the problem from 3N (N-number of electrons) to 3. The equation for the electron density n(r) is: [7, 8]

$$n(\mathbf{r}) = N \int d\mathbf{r}_2 \ldots \int dr_N \, \psi^*(\mathbf{r}, \mathbf{r_2} \ldots \mathbf{r}_N)\psi(\mathbf{r}, \mathbf{r}_2 \ldots \mathbf{r}_N) \quad (19)$$

Electron density is the measure of the relative amount of charge in a volume d**r**, given $N - 1$ electrons at arbitrary positions defined by the wave function Ψ. Thomas and Fermi, in 1926 and 1927, for the first time suggested the use of the electron density instead of the wavefunction to describe all the information of the electronic system. However, the approximation they used for the kinetic energy was unable to sustain a bound state. In 1964, Hohenberg and Kohn proved two theorems that are the basics of modern density functional theory (DFT). A functional in

DFT is like a function, but instead of taking a number as its argument, a functional maps a function to a number.

Hohenberg-Kohn theorems

Hohenberg and Kohn developed two theorems. [9] The first Hohenberg-Kohn theorem states that the external potential, $\mathcal{V}_{ext}$, is a functional of the electron density. When the electron-nucleus interaction, $\mathcal{V}_{ne}$, is relabelled as an external potential, $\mathcal{V}_{ext}$, equation (5) for the Hamiltonian takes the form:

$$\mathcal{H} = \kappa_e + \mathcal{V}_{ee} + \mathcal{V}_{ext} \tag{20}$$

Based on this theorem, the many-body ground state of the system is dependent only on the functional of the electron density, n, which is unique to the system, as κ_e and $\mathcal{V}_{ee}$ are universal and can be computed explicitly independent of the system. The second Hohenberg-Kohn theorem states that the ground state energy is the minimum of the functional $E_{HK}[n]$ which describes the total energy for any applied external potential:

$$E_{GS} = \min(E_{HK}[n]) = E_{HK}(n_o) \tag{21}$$

Therefore, the total energy can be restated and presented as a functional of the wavefunction:

$$E[\psi] = \langle\psi|\mathcal{H}|\psi\rangle = \langle\psi|\kappa_e + \mathcal{V}_{ee}|\psi\rangle + \langle\psi|\mathcal{V}_{ext}|\psi\rangle \tag{22}$$

We can also present the same equation as a functional of electron density:

$$E_{HK}[n(r)] = \kappa_e[n(r)] + \mathcal{V}_{ee}[n(r)] + \mathcal{V}_{ext}[n(r)] = F_{HK}[n(r)] + \int n(r)\mathcal{V}_{ext}(r)dr \tag{23}$$

In equation (23), $F_{HK}[n(r)]$ is universally valid but unknown functional which describes the potential and kinetic energies $\mathcal{V}_{ee}[n(r)]$ and $\kappa_e[n(r)]$. $\int n(r)\mathcal{V}_{ext}(r)dr$ describes the electron-nucleus interaction. The ground state energy and electron density of any system would be determined accurately if the term $F_{HK}[n(r)]$ would be exactly known. [10] To now there is no exact expression for $F_{HK}[n(r)]$.Therefore, in order to employ DFT, an approximation of $F_{HK}[n(r)]$ is required and this is what differs DFT from HF; DFT employs approximations to the functional to solve an exact theory, HF focuses on exact solutions to an approximate theory.

Kohn-Sham Ansatz

In order to make a practical application of the Hohenberg and Kohn theorems, without knowing the exact form of the functional $F_{HK}[n(r)]$, the Kohn-Sham Ansatz proposed a new scheme which presumes that a non-interacting system with ground-state density that is the same with that of the real interacting system exists, and is considered a reference. [11] Based on this scheme the electrons are replaced with fictitious non-interacting particles, while the density n(r) is:

$$n(r) = \sum_i |\phi_i(r)|^2 \tag{24}$$

The particles occupy the Kohn-Sham (KS) orbitals ϕi, and this allows the computation of the kinetic energy. Considering this scheme, equation (22) can be expressed as the Kohn-Sham functional:

$$E_{KS}[n(r)] = \sum_i \langle \phi \left| -\frac{1}{2}\nabla_r^2 \right| \phi \rangle + \frac{1}{2}\iint \frac{n(r)n(r')}{|r-r'|} dr dr' + E_{xc}[n(r)] + \int \mathcal{V}_{ext} r(n) r dr \tag{25}$$

The term $\sum_i \langle \phi \left| -\frac{1}{2}\nabla_r^2 \right| \phi \rangle$ allows the computation of the kinetic energy while the exchange-correlation functional $E_{xc}[n(r)]$ contains the non-classical kinetic energy difference between the interacting system (real system) and non-interacting system (reference system). Utilising the variational principle and applying it to equation (25), the Schrödinger-like Kohn-Sham equation to describe the ground state energy is:

$$E_0 = \left(-\frac{1}{2}\nabla_r^2 + \int \frac{n(r')}{|r-r'|} dr' + \frac{\partial E_{xc}[n(r)]}{\partial n(r)} + \mathcal{V}_{ext}(r) \right) \phi(r) = \varepsilon_i \phi_i(r) \tag{26}$$

In equation (26), E_{XC} describes all correlation effects and exchange effects and it contains all unknowns. The exchange correlation potential is written as:

$$\mathcal{V}_{xc} = \frac{\partial E_{xc}}{\partial n} \tag{27}$$

The exact ground state energies and ground state electron densities would be calculated with the Kohn-Sham equations if $\mathcal{V}_{xc}$ and E_{xc} would be known.

3.1.3 Implementation of DFT

Basis sets

For our calculations we used two different simulation packages: VASP [12] uses planewave basis set for periodic calculations of surface chemistry and TURBOMOLE [13] uses localised basis sets for calculations of gas phase species.

Planewave basis sets

In section 3.1.1 we discussed LCAO as an approximation to solve the Schrödinger equation. A major task is to find suitable forms of these atomic orbitals, known as basis sets. In periodic systems, that is solid and surfaces, the basis set is a set of plane waves. Basis set functions, α_j ($\boldsymbol{r}$) can be used to describe the Kohn-Sham orbitals, ϕ. [14]

$$\phi_n(r) = \sum_{j}^{\infty} c_j^n \alpha_j(r) \tag{28}$$

Based on the Bloch theorem: in a periodic model electrons move with a periodic potential, the electron wavefunctions and the effective potential will have a periodicity that is equal to the lattice parameter of the model. [15] This applies also for the non-interacting Kohn-Sham particles and therefore the Kohn-Sham orbitals can be expressed as:

$$\phi_n(r) = e^{iq\cdot r} u(r) \tag{29}$$

In equation (29), $e^{iq\cdot r}$ is the plane wave and u(r) is a function with the same periodicity as the crystal lattice. The function u(r) can also be expressed as a linear combination of plane waves with wave vectors in the reciprocal lattice denoted as K:

$$u(r) = \sum_{k\in K} c_k e^{ik\cdot r}\, u(r) \tag{30}$$

In equation (30), c_k is a set of expansion coefficients. The combination of equations (29) and (30) allows to present the single particle wave function in terms of a plane wave basis set:

$$\phi_n(r) = \sum_{k\in K} c_k^n e^{(q+k)\cdot r} \tag{31}$$

In equation (31), q is a wave vector in the first Brillouin zone of the reciprocal lattice vectors and $\boldsymbol{k} \in \boldsymbol{K}$ is an infinite set of reciprocal lattice vectors. An infinite set of vectors can not be used in practice and therefore the basis set of planewaves is fixed to $\boldsymbol{k} > \boldsymbol{k_{max}}$ and a cut-off is

chosen so that the wavefunction is described with reasonable accuracy. The magnitude of the cut-off energy determines the accuracy of the calculation. By employing a finite basis set, the solution of Kohn-Sham equation is reduced to a matrix equation, similar to Hartree-Fock, and is expressed as:

$$\mathrm{HC} = \mathrm{SCE} \tag{32}$$

In equation (32), H is the Hamiltonian matrix from the single-particle Hamiltonian operators, C is a square matrix arising from the expansion coefficients, S is the overlap matrix of basis functions and E is a diagonal matrix which contains the energy eigenvalues.

Local basis sets

This basis set is composed of atomic orbitals centered at each nucleus of the molecule and are most commonly used for molecular calculations. There are few types of atomic orbitals that can be used such as Gaussian-type orbitals GTO), Slater-type orbitals (STO), or numerical atomic orbitals (NAO). Out of the three, the GTO is the most popular as it allows an efficient implementations of Hartree–Fock methods. The Gaussian function can be written as a fixed sum over a linear combination of primitive Gaussian functions where each primitive Gaussian function is specified by a fixed orbital exponent and these are weighted by contraction coefficients. [16]

The basis set that consists of the minimum number of basis functions needed to describe the ground states of the component atoms in a molecule is known as the “minimal” basis sets. The size of a basis function on an atom cannot vary when the nature of the surrounding atoms changes, this as the contraction coefficients and orbital exponents are fixed. However, when each orbital in the minimal basis set is replaced with two basis functions that differ in size, this problem is solved. During the self-consistent-field process the coefficients for each basis function on the atom are optimized and hence the contribution of the atomic orbital to the molecular orbitals can be obtained. [17]

Basis sets which consist of multiple basis functions which correspond to each valence atomic orbital are called valence double, triple, quadruple – zeta. Since the different orbitals of the split have different spatial extents, the combination allows the electron density to adjust its spatial extent appropriate to the particular molecular environment. [18]

Pseudopotentials

In plane-wave implementations, we divide the system into nuclei, core electrons and valence electrons. In contrast to the valence electrons, the core electrons do not contribute in bond formation or in the properties of the material as they are localised and bound very strongly to their nuclei. By considering only the valence electrons, this approximation, also known as ”frozen core approximation” reduces the degrees of freedom significantly. Nevertheless, to remain orthonormality to the core wavefunctions, the valence electrons wavefunctions vary quickly or strongly oscillate in the vicinity of the ions, and in order to describe this behaviour a large number of basis set functions would be required. However, to avoid the use of a large number of basis sets, the ion potential is replaced with a pseudopotential at a ”core distance” r_c. The wave function and potential are then exactly described for $r > r_c$. Pseudopotential is used when $r < r_c$, **Fig. 1**.

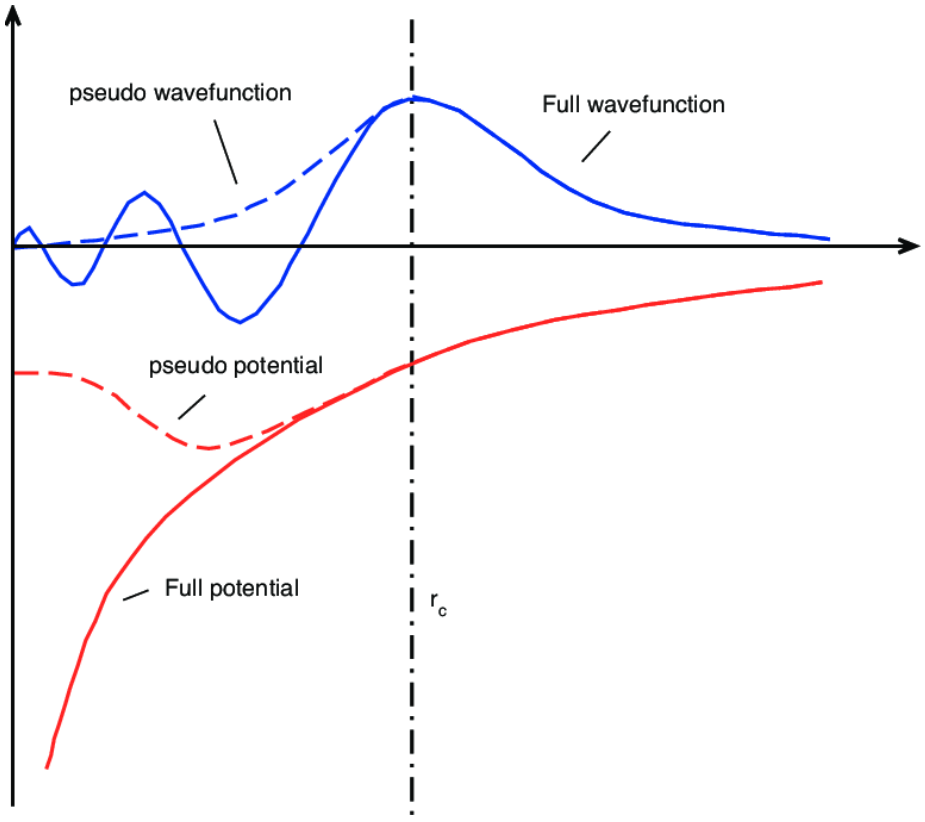


Figure 1 Comparison between the wavefunction of the pseuropotential (red) to the one in real potential (blue), $r < r_c$. [19]

Projector Augmented Waves (PAW)

The projector augmented wave method (PAW) when in combination with pseudopotentials enable the performance of density functional theory calculations with a greater computational efficiency. [20] Based on PAW, the space is divided in the core region (close to $\mathbf{r} < \mathbf{r_c}$) and interstitial region (far from the ions $\mathbf{r} > \mathbf{r_c}$). In this method, the Kohn-Sham orbital is then presented as a sum of three contributions:

$$\phi_n(r) = \tilde{\phi}_n(r) + \sum_a \phi_n^a(r) - \sum_a \tilde{\phi}_n^a(r) \tag{33}$$

In equation (33), $\tilde{\phi}_n(r)$ is the pseudo wavefunction set, $\sum_a \phi_n^a(r)$ is the summations of the all-electron ($\phi_n^a(\mathbf{r})$) for all ions in the core region of the system and $\sum_a \tilde{\phi}_n^a(r)$ is the pseudo-one-centre functions ($\tilde{\phi}_n^a(\boldsymbol{r})$) for all ions in the core region of the system. When $\phi_n^a(\boldsymbol{r})$ and $\tilde{\phi}_n^a(\boldsymbol{r})$ are expressed in terms of partial and pseudo partial wave basis sets, $\{\alpha i\}$ and $\{\tilde{\alpha} i\}$, equation (33) takes the form:

$$|\phi_n\rangle = |\tilde{\phi}_n\rangle + \sum_a \sum_i (|\alpha_i^a I\rangle - |\tilde{\alpha}_i^a I\rangle)\langle p_i^a|\tilde{\phi}_n\rangle \tag{34}$$

In equation (34), P_i^a describes the species-specific projector functions.

Approximations to the exchange-correlation functional

Local density approximation (LDA) uses the electron density at r to define the approximate exchange correlation functional. The general form of LDA is: [4]

$$E_{xc}^{LDA}[n(r)] = \int n(r)\, \epsilon_{XC}\big(n(r)\big) dr \tag{35}$$

In equation (35), $\epsilon_{XC}\big(n(r)\big)$ is the exchange-correlation energy per particle of a uniform homogenous electron gas of density ($\boldsymbol{r}$) and it is expressed as the sum of correlation and exchange contributions.

$$\epsilon_{XC} = \epsilon_C - \epsilon_X \tag{36}$$

While ϵ_X is known analytically, the term ϵ_C is known known analytically only for high and very low densities. The LDA method is relatively accurate for extended systems with a medium

variation in the electron density and therefore it is best employed for solid-state physics, but can not be used for molecules.

Generalised gradient approximation (GGA) which uses the information about the local electron density and the local gradient in the electron density. [21] GGA is expressed as a functional of density, n, and its gradient, ∇n with the equation:

$$\mathrm{E}_{\mathrm{XC}}^{\mathrm{GGA}} = \int \mathrm{f}(\mathrm{n}, \nabla \mathrm{n})\mathrm{dr} \tag{37}$$

Due to the many ways in which the information from the electron density gradient can be included into GGA, there are a large number of distinct GGA functionals. The most widely used are Perdew-Wang functional (PW91), [22] the Perdew – Burke – Ernzerhof (PBE) [23] both for exchange correlation and the Lee-Yang-Parr functional (LYP) [24] for correlation. GGA functionals have their limitations the same as all approximations. These include the underestimation of band gaps [25-27] and favouring of delocalisation of charges, where both arise from the self-interaction error. [28] Other approximations such as DFT+U and hybrid DFT are applied in order to reduce the problems with GGA. DFT+U method uses an empirical parameter U to correct the localisation of states. In hybrid DFT a functional is defined that includes contributions from both exact Hartree-Fock exchange and approximate DFT exchange. A well-defined and popular hybrid DFT method is PBE0 and it has the following composition:

$$E_{XC}^{PBE0} = \frac{1}{4}E_X^{HF} + \frac{3}{4}E_X^{PBE} + E_C^{PBE} \tag{38}$$

In equation (38), E_X^{HF} is the exchange energy, E_X^{PBE} is the PBE exchange energy and the E_C^{PBE} is the correlation energy. The parameters determine the hybrid functional, specifying how much of the exact exchange is mixed in. Hybrid DFT performs better than LDA or even GGA in predicting molecular geometries and many other properties. Another hybrid DFT method is B3LYP using the Becke 3-parameter hybrid exchange functional and the Lee-Yang-Parr correlation functional. [29]

3.1.4 DFT-D3 approach

The DFT-D3 method is a specific approach in DFT to account for van der Waals (vdW) interactions, which traditional DFT often misses. The DFT-D3 method introduces a term to the

total energy that depends on the interatomic distances and precomputed dispersion coefficients for each atom pair, effectively capturing long-range attractive forces. This improves accuracy in describing the properties without greatly increasing computational cost. [30]

3.2 Computational methodology

The computational work in this thesis is carried out using two different simulation packages: Vienna Ab initio Simulation Package (VASP) [12] and TURBOMOLE. [13]

3.2.1 Periodic calculations

We have employed VASP 5.4 [12] for the periodic plane wave basis set calculations in **Chapter 4**, **5**, **6** and **7**. The valence electron-core electron interactions are described by the projector augmented wave method (PAW). [20, 31] The valence electronic configuration for each atomic species is shown in **Table 1**. The exchange-correlation functional is approximated by the Perdew-Burke-Ernzerhof (PBE) [23] approximation for all systems. The energy convergence criteria was set to 1×10^{-4} eV and the geometry convergence criterion for the forces is 2×10^{-2} eVÅ^{-1} for all systems. Calculations are performed in vacuum conditions at zero Kelvin and zero GPa.

Table 1 Valence electron configurations for each element used in VASP calculations.

Atomic species	Valence Electron Configuration
Al	$3s^2\ 3p^1$
Ti	$3d^3\ 4s^1$
Mg	$2s^2\ 2p^6$
Zr	$5s^2\ 4d^2$
Ce	$4f^1\ 5s^2\ 5p^6\ 5d^1\ 6s^2$
In	s^2p^1
Zn	$d^{10}p^2$
Cl	s^2p^5
O	$2s^2\ 2p^4$
N	$2s^2\ 2p^3$
C	$2s^2\ 2p^2$
H	$1s^1$

Adsorption and interaction energies were calculated using the equation:

$$\mathrm{E_{ads/int}} = \sum \mathrm{E_p} - \sum \mathrm{E_r} \tag{39}$$

In equation (38), E_p-energy of products, E_r-energy of reactants. A negative $E_{ads}/_{int}$ signifies an exothermic interaction and therefore the adsorption or interaction is favourable. Within a class of similar reactions, reactions that are more exothermic have more negative energies.

For the example of titanium chloride ($TiCl_4$) adsorbing on the anatase titanium oxide (TiO_2) surface in titanicone film growth:

$$\mathrm{E_{ads}} = [\mathrm{E(TiCl_4 - HO - surface)}] - [\mathrm{E(TiCl_4)} + \mathrm{E(HO - surface)}]$$

For the example of the ethylene glycol (EG) or glycerol (GL) interacting with $TiCl_3$ terminated anatase TiO_2 surface in titanicone film growth:

$$\mathrm{E_{int}} = [\mathrm{E(EG/GL - TiCl_2 - surface)} + \mathrm{E(HCl)}] - [\mathrm{E(EG)} + \mathrm{E(TiCl_3 - O - surface)}]$$

We now describe the set-up for the VASP calculations in each Chapter.

Alucone system (Chapter 4)

The alucone films were modelled using a hydroxylated Al_2O_3 surface taken from previous work. [32, 33] The slab model of α-Al_2O_3 (0001) was modified with trimethylaluminium (TMA) or dimethylaluminum isopropoxide (DMAI) inorganic precursors and aliphatic organic molecules (ethylene glycol, EG and glycerol, GL) or different aromatic organic molecules. The slab geometry was optimised by relaxing ionic positions, using an energy cut-off of 400 eV, and a Monkhorst-Pack k-point sampling grid of (3 × 3 × 1). The computed equilibrium lattice parameters for the TMA-EG/GL [34] and TMA-aromatic organics [35] systems are a = b = 9.614 Å, c = 25.25 Å and α = β = 90°, γ = 120°. For the DMAI-EG system the lattice parameters are a = b =19.228 Å and c = 40.627 Å and α = β = 90°, γ = 120°. Van der Waals (vdW) corrections are not required due to the strong interaction of precursors in the surface.

Titanicone system (Chapter 5)

Titanicone films were modelled on an anatase TiO_2 (101) surface with a coverage of 1 ML OH, rutile TiO_2 (110) surface with a coverage of 0.75 ML OH, and an Al_2O_3 (0001) surface at a coverage 0.50 ML OH. [32, 36] These surface models interact with titanium tetrachloride

($TiCl_4$) and tetrakis(dimethylamido)titanium ($Ti(DMA)_4$) inorganic precursors and then EG and GL organic coreactants. [37] The geometry of the structures was optimized by relaxing the ionic positions using an energy cut-off of 400 eV as well as a Monkhorst−Pack **k**-point (3 × 3 × 1). The lattice parameters are a =20.612, b = 15.164, c = 24.399 and α = β = γ = 90° for the anatase TiO_2 surface model, a =11.846, b = 13.051, c = 33.870 and α = β = γ = 90° for the rutile TiO_2 surface model and a = b=19.228, c = 40.627 and α = β = 90°, γ = 120° for the Al_2O_3 surface model. The surfaces are 2, 4 and 6 O-metal-O layers thick for anatase (101), rutile (110) and Al_2O_3 (0001). In computing the adsorption and interaction energies we also employ vdW interactions using the DFT-D3 parameterisation. [30]

Magnesicone system (Chapter 6)

A hydroxylated MgO (100) surface in a (2 × 2) surface supercell is prepared by starting from four dissociated water molecules followed by relaxation. During relaxation, three water molecules are spontaneously formed and desorb from the surface. This leaves two surface -OH groups on the MgO (100) surface which are then involved in subsequent interactions with $MgCp_2$. The lattice parameters for this surface are a = b = 8.38 Å, c = 25.98 Å, α = 89.84°, β = γ = 90.00°. The geometry of the structures was optimized using an energy cut-off of 400 eV and a Monkhorst−Pack **k**-point sampling grid of (3 × 3 × 1). [38] VdW corrections are not used for this system due to the strong interaction of precursors.

Ceria hybrid system (Chapter 6)

The ceria hybrids were modelled using a hydroxylated CeO_2 (111) surface, at a coverage of 0.38 ML OH which is modified with tris(N,N'-diisopropyl-2-dimethyl-amido-guanidinato)cerium(III) ($Ce(dpdmg)_3$) as inorganic precursor and hydroquinone (HQ) and terephthalic acid (TPA) as organic precursors. For the ceria system we use the well-known GGA+U approach to consistently describe the Ce 4f electronic states, [39] with U = 5 eV, typical of values used in the literature. For the ceria hybrid system the geometry convergence criterion for the forces was set to 1.5×10^{-2} eVÅ^{-1}. The lattice parameters for this surface model are a = 30.95 Å, b = 20.47 Å, c = 40.27 Å and α = β = 90°, γ = 120°. The CeO_2 surface is four O-Ce-O layers thick. [40] VdW corrections are not used for the ceria hybrid system.

Metallochitin system (Chapter 6)

A hydroxylated monoclinic ZrO_2 (111) surface in a (2 × 2) surface supercell was used for the modelling of alumochitin and titanochitin hybrid films. For the alumochitin films the ZrO_2

surface was modified with as TMA as metal source and N-acetyl-D-Mannosamine (ManNAc) as organic reactant while for titanochitin films it was modified with titanium isopropoxide (TTIP) as metal source and ManNAc as organic reactant. The geometry of the structures was optimized by relaxing the ionic positions, using an energy cut-off of 400 eV and a Monkhorst−Pack **k**-point sampling grid of (2 × 2 × 1). The lattice parameters for this surface model are a = b = 14.70 Å, c = 32.45 Å, α = β =90°, γ=114°. VdW corrections are not required due to the strong interaction of precursors in the surface.

All surface models used in this work are presented in **Fig 2.**

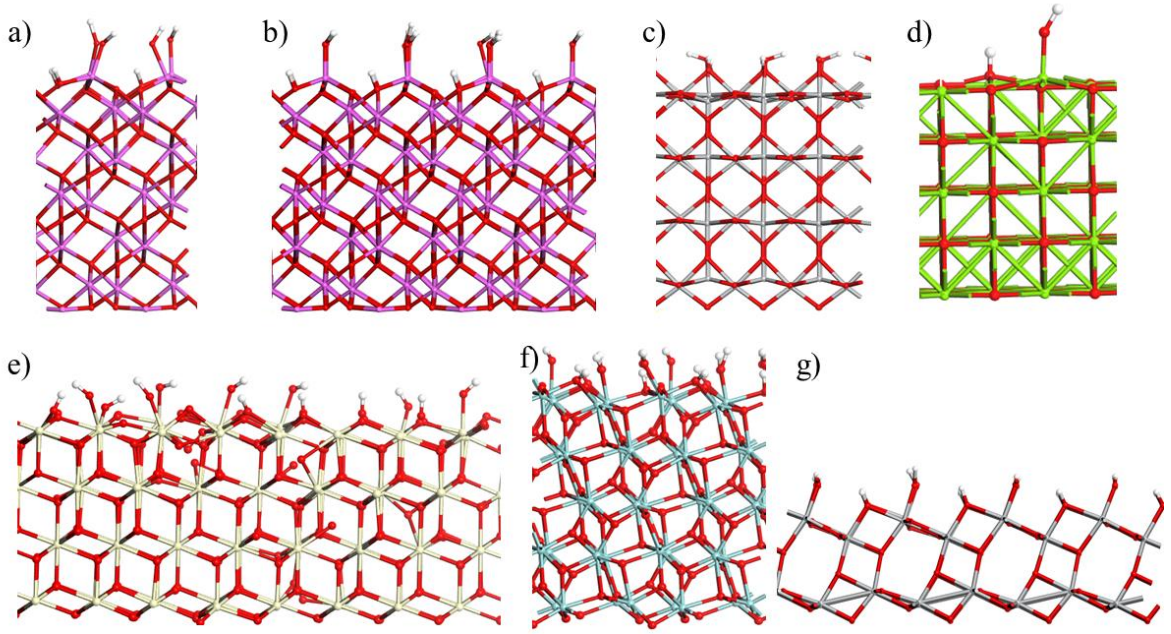


Figure 2 Atomistic structures of a) Al_2O_3 surface used in the TMA-EG/GL and TMA-aromatic organics studies, b) Al_2O_3 surface used in the DMAI-EG study, c) rutile TiO_2 surface, d) MgO surface, e) CeO_2 surface, f) ZrO_2 surface and g) anatase TiO_2 surface. Purple-Al, red-O, grey-Ti, green-Mg, creamy-Ce, cyan-Zr, white-H.

Self-healing systems (Chapter 7)

The model for the polymer is a periodic supercell composed of two parylene C chains, each with a total of six rings, **Fig. 3**. The precursors are gas phase hydrogen peroxide (H_2O_2) and trimethylindium (TMIn) for the TMIn-based vapour phase infiltration systems (VPI) system and H_2O_2 and diethylzinc (DEZ) for the DEZ-based VPI system. The geometry of the structure is optimized by relaxing the ionic positions using an energy cut-off of 550 eV. A Gamma-centred **k**-point sampling grid of (3 × 3 × 1) is used and computed equilibrium lattice

parameters are a = 41.40 Å, b = 20 Å, c = 15 Å and α = β = γ =90°. In computing E_{int} we also employ vdW interactions using the DFT-D3 parameterisation. [37]

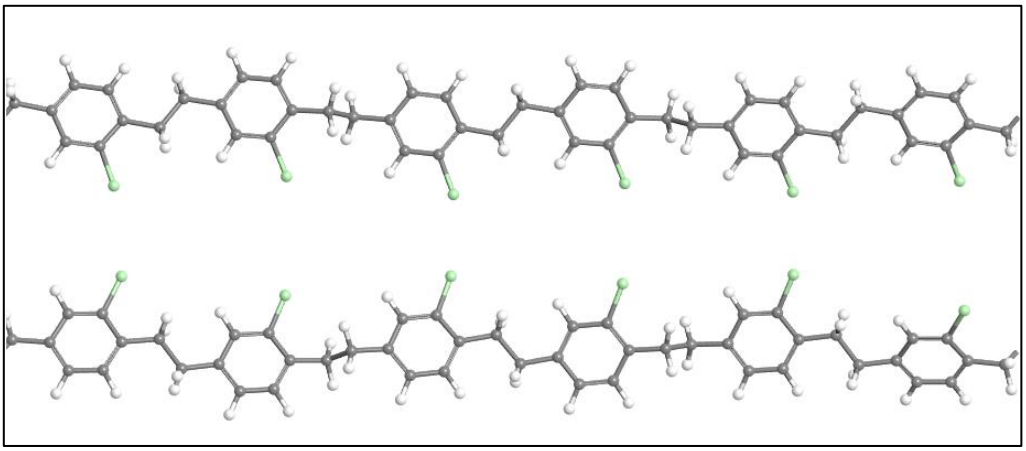


Figure 3 Optimised atomistic structure of parylene C chains. Grey-C, green-Cl, white-H.

3.2.2 Gas phase calculations

Gas phase calculations are carried out with the TURBOMOLE [13] package using the hybrid PBE0 functional, which incorporates 25% exact HF exchange, [23] and a polarized split valance basis set, denoted def-SV(P). [41]. Tests indicate that the results are similar to the larger triplet zeta TZVP basis set. Number of valence electrons used for each metal are shown in **Table 3.2.2**. A fine integration grid (m3) is used and SCF convergence criterion is set to 10^{-6} Ha. Calculations are performed in vacuum conditions at zero Kelvin and zero GPa.

Table 3.2.2 Valence electrons for each element used in Turbomole calculations.

Atomic species	Valence electrons
Cu	29
Ag	19
Ce	40
Yb	42
Y	11
Eu	35
Mg	25

PS/PMMA-Ru system (Chapter 7)

The polymethyl methacrylate (PMMA) polymer model is an oligomer that consists of three methyl methacrylate monomers and the polystyrene (PS) polymer model is an oligomer that consists of three styrene monomers, **Fig. 4.** [42]

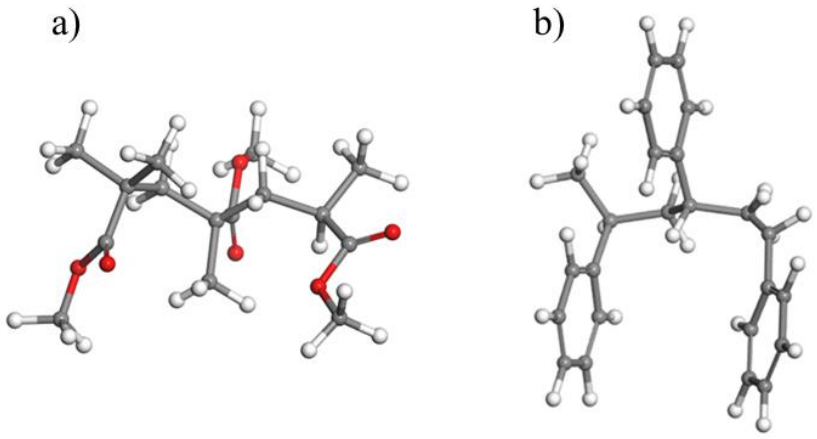


Figure 4 Optimised atomistic structure of a) PMMA three unit oligomer and b) PS three unit oligomer. Grey-C, red-O, white-H.

Precursor chemistry (Chapter 8)

To obtain an insight into the fundamental aspects of the chemistry of different metallic precursors on the molecular level, DFT was used to model the atomic structures and to simulate the reactivity of the complexes towards potential coreactants. [43-46] Interaction energies between precursor molecules and the coreactants are calculated using equation (39). Bond dissociation energies for the precursor molecules are calculated using:

$$E_{diss} = (E_L - E_{P-1L}) - E_P \qquad (40)$$

In equation (39), E_L - computed total energy of one free ligand, E_P is the computed total energy of the precursor molecule and $E_{P\text{-}1L}$ is the computed total energy of the precursor after cleaving one ligand (L). For the example of $Ce(dpdmg)_3$:

$$E_{diss} = [E(dpdmg) - E(Ce(dpdmg)_2] - [E(Ce(dpdmg)_3]$$

3.3 References

1. E. Schrödinger, *Physical review*, **1926**, 28, 1049.
2. W. Koch, M. Holthausen, A Chemist's Guide to Density Functional Theory, *Wiley*, Weinheim, Germany: **2001**, 3–18.
3. M. Born, R. Oppenheimer, *Annalen Der Physic*, **1927**, 389, 457–484.
4. C. J. Cramer, Essentials of Computational Chemistry, *Wiley*, **2003**, Minnesota, United States.
5. P. Misra, Physics of Condensed Matter, *Elsevier*, *2011*, Texas, United States.
6. A. Szabo, N. S. Ostlund, *Dover Publication*, **2012**, 231–241.
7. R. O. Jones, O. Gunnarsson, *Reviews of Modern Physics*, **1989**, 61, 689.
8. J. Oh, J. Weaver, M. Karasik, L. Chan, *Review of Scientific Instruments*, **2015**, 86, 083501.
9. P. Hohenberg, W. Kohn, *Physical Review*, **1964**, 136, B864.
10. W. Koch, M. Holthausen, A Chemist's Guide to Density Functional Theory, *Wiley*, Weinheim, Germany: **2001**, 33–40.
11. W. Kohn, L. J, Sham, *Physical Review*, **1965**, 140, A1133.
12. G. Kresse, J. Furthmuller, *Physical Review B*, **1996**, 54, 11169.
13. R. Ahlrichs, M. Bär, M. Häser, H. Horn, C. Kölmel, *Chemical Physics Letters*, **1989**, 162, 165–169.
14. W. Koch, M. Holthausen, A Chemist's Guide to Density Functional Theory, *Wiley*, Weinheim, Germany**, 2001**, 93–116.
15. F. Bloch, *Zeitschrift Fur Physic*, **1929**, 52, 555–600.
16. I. N. Levine, Quantum Chemistry, Pearson Education, *Pearson*, **2013**, New York, United States.
17. J. Simon, An Introduction to Theoretical Chemistry, *Cambridge University Press*, **2003**, Utah, United States.
18. E. Davidson, D. Feller, *Chemical Reviews*, **1986**, 86, 681–696.
19. M. Rasander, A Theoretical Perspective on the Chemical Bonding and Structure of Transition Metal Carbides and Multilayers, *Uppsala University*, **2010**, Uppsala, Sweden. https://uu.divaportal.org/smash/record.jsf?pid=diva2%3A314586&dswid=-9548. ISBN: 978-91-554-7827-8.
20. P. Blöchl, *Physical Review B*, **1994**, 50, 17953.
21. W. Koch, M. Holthausen, *Wiley*, Germany, **2001**, 65–9.
22. J.P. Perdew, Y. Wang, Y. *Physical Review B*, **1992**, 45, 13244.
23. J.P. Perdew, K. Burke, M. Ernzerhof, *Physical Review Letters*, **1996**, 77, 3865.
24. C. Lee, W. Yang, R. G. Parr, *Physical Review B*, **1988**, 37, 785.
25. H. Xiao, J. Tahir-Kheli, W. A. Goddard, *The Journal of Physical Chemistry Letters*, **2011**, 2, 212–217.
26. J. P. Perdew, W. Yang, K. Burke, Z. Yang, E. K. Gross, M. Scheffler, G.E. Scuseria, T.M Henderson, I. Y. Zhang, A. Ruzsinszky, H. Peng, J. Sun, E, Trushin, A. Görling, *Proceedings of the National Academy of Sciences*, **2017**, 114, 2801–2806.
27. S. Lany, A. Zunger, *Physical Review B*, **2008**, 78, 235104.
28. J. Perdew, E. McMullen, A. Zunger, *Physical Review A*, **1981**, 23, 2785.

29. E. Finazzi, C. Di Valentin, G. Pacchioni, A. Selloni, *The Journal of Chemical Physics*, **2008**, 129, 154113.
30. S. Grimme, J. Antony, S. Ehrlich, H. Krieg, *The Journal of Chemical Physics*, **2010**, 132, 154104.
31. G. Kresse, D. Joubert, *Physical Review B*, **1999**, 59, 1758.
32. G. R. Jenness, J. Seiter, M. K. Shukla, *Physical Chemistry*, **2018**, 20, 18850–18861.
33. G. N. Fomengia, M. Nolan, S. D. Elliott, *Physical Chemistry*, **2018**, 20, 22783–22795.
34. A. Muriqi, M. Nolan, *Dalton Transactions*, **2020**, 49, 8710–8721.
35. A. Muriqi, M. Karppinen, M. Nolan, *Dalton Transactions*, **2021**, 50, 17583–17593.
36. J. Liu, S. Saedy, R. Verma, J. Ommen, M. Nolan, *ChemRxiv*, **2020**, 1–44.
37. A. Muriqi, M. Nolan, *Beilstein Journal of Nanotechnology*, **2022**, 1240–1255.
38. J. Kint, F. Mattelaer, S. S. T. Vandenbroucke, A. Muriqi, M. M. Minjauw, M. Nisula, Ph. M. Vereecken, M. Nolan, J. Dendooven, Ch. Detavernier, *Chemistry of Materials*, **2020**, 32, 4451–4466.
39. M. Nolan, S. Grigoleit, D. C. Sayle, S. C. Parker, G. W. Watson, *Surface Science*, **2005**, 576, 217–229.
40. P. Kaur, A. Muriqi, J-L Wree, R. Ghiyasi, M. Safdar, M. Nolan, M. Karppinen, A. Devi, *Dalton Transactions*, **2022**, 51, 5603-5611.
41. A. Schäfer, H. Horn, R. Ahlrichs, *Journal of Chemical Physics*, **1992**, 97, 2571–2577.
42. N. Poonkottil, E. Solano, A. Muriqi, M. M. Minjauw, M. Filez, M. Nolan, Ch. Detavernier, J. Dendooven, *Chemistry of Materials*, **2022**, 34, 23, 10347–10360.
43. N. Boysen, B. Misimi, A. Muriqi, J-L. Wree, T. Hasselmann, D. Rogalla, T. Haeger, D. Theirich, M. Nolan, Th. Riedl, A, Devi, *Chemical Communications*, **2020**, 56, 13752–13755.
44. P. Kaur, L. Mai, A. Muriqi, D. Zanders, R. Ghiyasi, M. Safdar, N. Boysen, M. Winter, M. Nolan, M. Karppinen, A. Devi, *Chemistry—A European Journal*, **2021**, 27, 4913–4926.
45. S. M. J. Beer, N. Boysen, A. Muriqi, D. Zanders, Th. Berning, D. Rogalla, C. Bock, M. Nolan, A. Devi, *Dalton Transactions*, **2021**, 50, 12944–12956.
46. S. M. J. Beer, A. Muriqi, P. Lindner, M. Winter, D. Rogalla, M. Nolan, A. Ney, J. Debus, A. Devi, *Chemistry of Materials*, **2022**, 34, 152–164.

Chapter 4

Modelling of Al-based hybrid films

4.1 Introduction

This chapter presents the results of first principles density functional theory (DFT) studies on aluminium based hybrid inorganic-organic films grown by molecular layer deposition (MLD). In each study we determine the atomistic mechanism of aluminium based hybrid films, explore the atomic structure of the MLD reaction products, analyse the impact of different organic and inorganic precursors on the film growth and support experimental data in growth of aluminiua hybrid films.

Section 4.2 presents a first principles investigation of the molecular mechanism of the growth of hybrid thin films of aluminium alkoxides using aliphatic diols, known as ”alucones”, grown by MLD. The chemistry of the MLD process between the post trimethylaluminium (TMA, $Al(CH)_3$) pulse methyl-terminated Al_2O_3 surface with ethylene glycol (EG) and glycerol (GL) as the organic coreactant is explored in detail. Double reactions of organic molecules with the aluminium oxide (Al_2O_3) surface are explored in detail to assist the interpretation of experimental findings regarding the differences in different metalcone films grown with EG and GL. [1-5] We show that while both organic precursors react favourably with TMA fragments, EG and GL lie flat and create double reactions through the two terminal hydroxyl (OH) groups. For EG this phenomenon removes the active OH groups from the surface and growth will be less favourable while for GL the third OH group is available and growth can proceed.

Section 4.3 describes the molecular mechanism and the atomic level details of the deposition of hydroxyl (OH) and amino (NH_2) terminated aromatic molecules in hybrid aluminium organic films. We find that as a result of their stiff backbone aromatic molecules avoid the unwanted double reactions found for aliphatic molecules (EG and GL) and lead to thicker and more stable hybrid films. These also offer the advantage of allowing the facile tuning of the properties of the organic component through ring functionalisation, without impacting on the stability of the resulting films.

Due to the fact that the infiltration phenomenon of TMA into the growing film is another common practical issue in alucone film growth, in order to support experimental data, [6, 7] in

Section 4.4 we investigate the molecular mechanism of alucone films deposited with dimethylaluminum isopropoxide (DMAI, $(CH_3)_2Al(OC_3H_7)$) and EG, where DMAI is as an alternative to TMA, the size of which can avoid the unwanted infiltration processes.

4.2 Modelling of Alucone films

This work is published in the paper "***First principles study of reactions in alucone growth: the role of the organic precursor***" in Dalton Transactions. [8]



DOI: https://doi.org/10.1039/D0DT01376E

4.2.1 Results

Trimethylaluminium (TMA) terminated aluminium oxide (Al_2O_3) surface models

The hydroxylated surface of aluminium oxide (Al_2O_3) that results from the interaction with water and before the introduction of trimethylaluminium (TMA) is taken from previous studies on Al_2O_3. [9] **Fig. 1 (a)** and **(b)** show the atomic structure of Al_2O_3 surface after the TMA pulse. The adsorption of TMA on a hydroxylated Al_2O_3 surface is a Lewis acid-base process and is barrier-free in the correct orientation: electrons are donated from oxygen of surface OH groups to the aluminium centre of the gas phase TMA precursor. The adsorption energy includes contributions from formation of an Al-O bond and from associated tilting of the surface OH groups. We consider two possible terminations of Al_2O_3 after TMA pulse. The first is the dimethyl Al_2O_3 ($Al(CH_3)_2$-Al_2O_3, DMA-Al_2O_3) surface in which TMA has lost one methyl (CH_3) group, released as methane (CH_4) molecule. Aluminium of TMA binds with one oxygen from the surface with a distance 1.71 Å and the surface has two CH_3 groups remaining that can react with the organic precursor in the next pulse. The second case is the monomethyl Al_2O_3 ($Al(CH_3)$-Al_2O_3, MMA-Al_2O_3) surface where TMA has lost two CH_3 groups which have

reacted with surface protons and are released as CH_4 molecules. Aluminium of TMA binds with three oxygens from the surface with distances of 1.76 Å, 1.78 Å, and 2.0 Å. The surface therefore has one CH_3 group remaining that can react with the organic precursor in the next pulse.

In addition to these models that result from the adsorption of a single TMA precursor molecule, we have also built models in which two TMA molecules are adsorbed on Al_2O_3. The distance between the two aluminium sites in the surface with two adsorbed $Al(CH_3)_2$ species is 4.18 Å while the surface model with two adsorbed $Al(CH_3)$ shows a distance of 2.64 Å between the two aluminium sites. These structures are shown in **Fig. 1 (c)** and **(d)**. The models with two DMA or MMA surface bound species allow us to study how favourable are "double reactions" of EG and GL, i.e. those reactions where the molecule tilts so that it binds to two surface $Al(CH_3)_2$ or $Al(CH_3)$ species through the two terminal OH groups. This is compared to the "single reaction" where the reaction takes place with one of the terminal OH groups of the organic molecules.

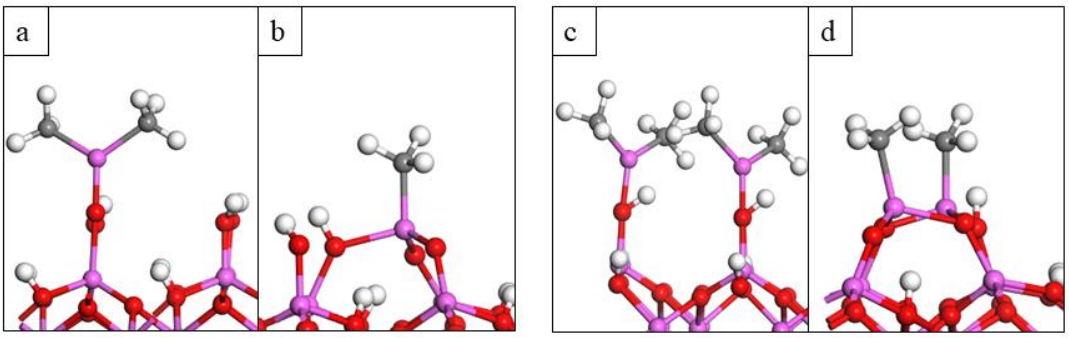


Figure 1 Optimised atomic structures of a) DMA-Al_2O_3 surface, b) MMA-Al_2O_3, c) 2DMA-Al_2O_3 surface and d) 2MMA-Al_2O_3 surface. Purple-Al, red-O, blue-N, grey-C and white-H. Figure coding is the same for all figures.

Reactions between organic precursors and MMA/DMA terminated Al_2O_3 surface

With the models of Al_2O_3 in the post TMA pulse, the interactions between the $Al(CH_3)_2$ and $Al(CH_3)$ species and the organic precursors are then investigated by analysing the formation of MLD reaction products with ethylene glycol (EG), diethylene glycol (DEG), triethylene glycol (TEG), tetraethylene glycol (FEG) and glycerol (GL). This set of organic precursors allows us to examine the influence of the chain length in the diol on the interaction between the oxygen site of the organic molecules and the aluminium site of TMA, as well as the preferred

orientation of the organic species. In addition, using GL allows us to compare a precursor with two OH groups with one with a third OH group. Optimised atomic structures of the organic alcohol molecules are shown in **Fig. 2**.

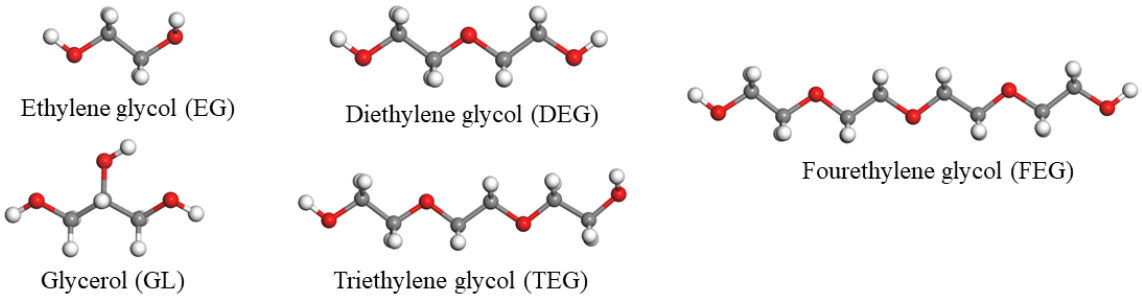
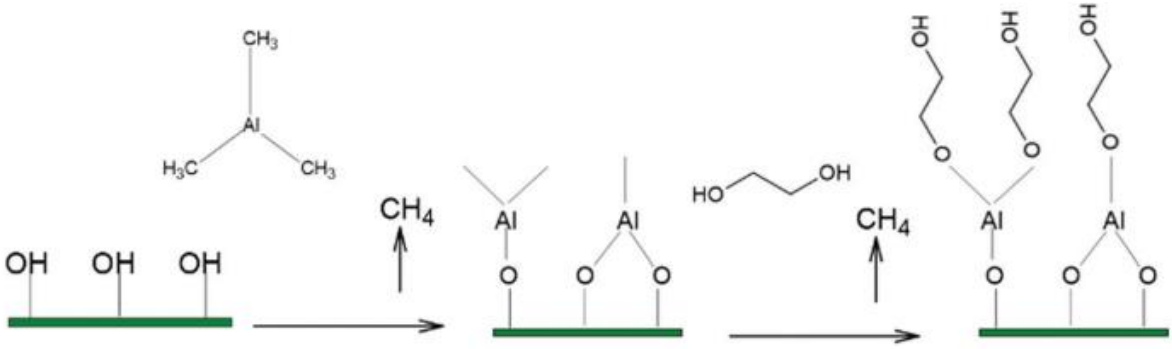


Figure 2 Structures of ethylene glycol (EG), glycerol (GL), diethylene glycol (DEG), triethylene glycol (TEG) and fourethylene glycol (FEG) after optimization by DFT.

In our first calculations, all organic precursor molecules were modelled in an upright configuration. EG, DEG, TEG and FEG molecules contain two OH groups separated by a carbon chain where the OH groups serve as reactive linkers for condensation reactions with metal sites, leading to hybrid films. In the case of DMA-Al_2O_3 and MMA-Al_2O_3 surfaces, the proton of the OH group of the organic molecule reacts with the CH_3 group of TMA, to release a CH_4 molecule. A proposed reaction mechanism for the growth of alucone films using EG is presented in **Scheme 1**. The resulting atomic structures are shown in **Fig. 3** for the DMA surface and **Fig. 4** for the MMA surface. The computed change in energy upon forming the Al-O bond between one surface bound MMA/DMA on Al_2O_3 and the organic molecule is shown in **Table 1**.



Scheme 1 Schematic illustration of alucone MLD based on the reaction between surface hydroxyl groups of Al_2O_3 with TMA and the reaction between $Al(CH_3)$ (MMA) and $Al(CH_3)_2$ (DMA) surface species with EG.

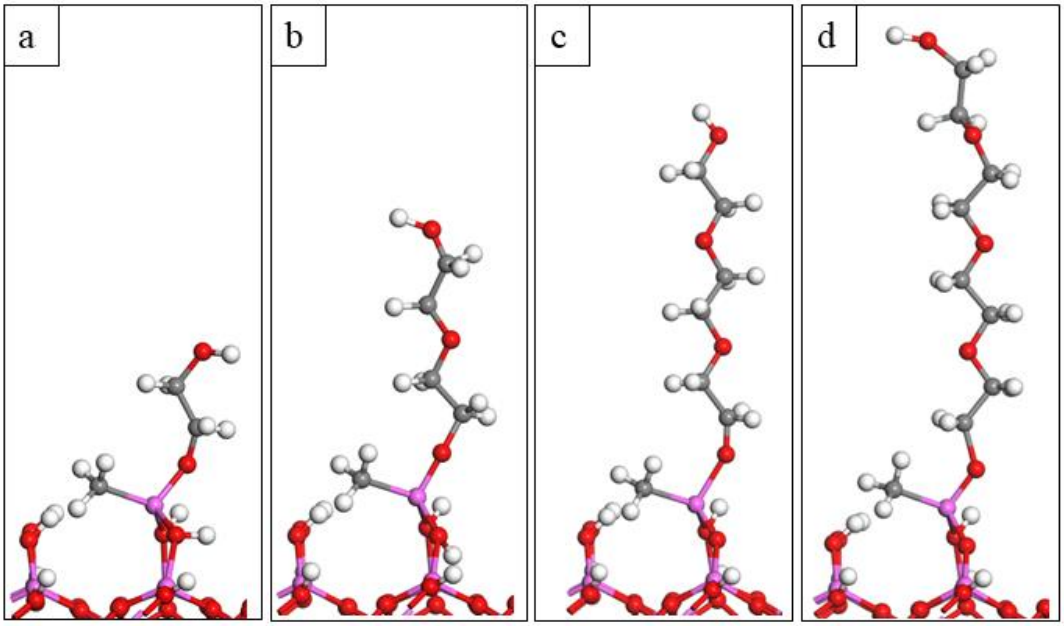


Figure 3 Optimised atomic structures of the DMA-Al_2O_3 surface after interaction with a) EG, b) DEG), c) TEG and d) FEG.

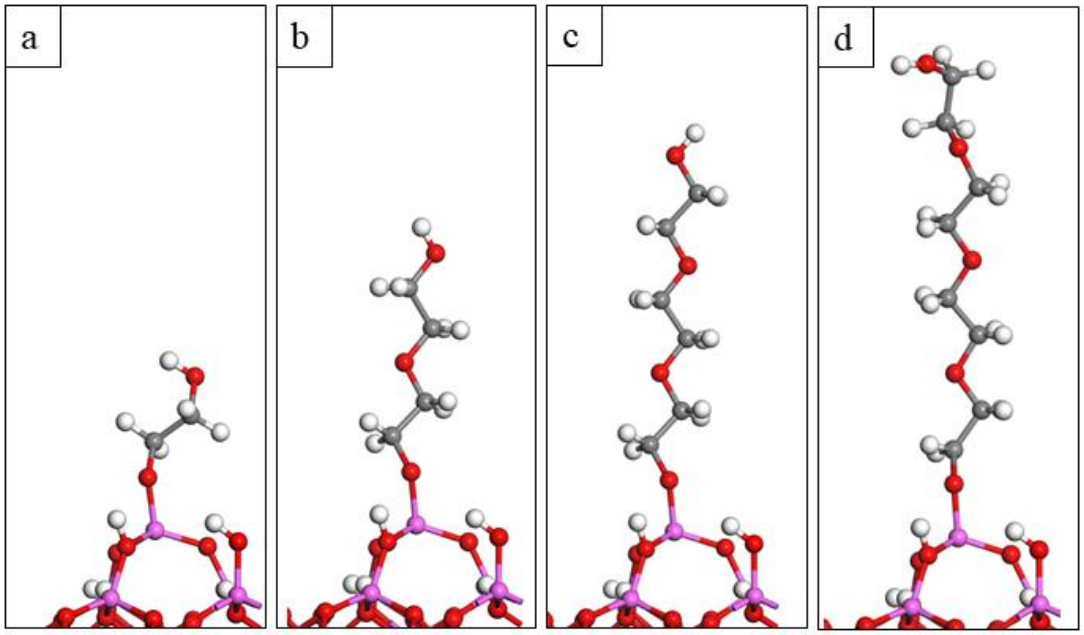


Figure 4 Optimised atomic structures of the MMA-Al_2O_3 surface after interaction with a) EG, b) DEG), c) TEG and d) FEG.

Table 1 Computed interaction energy of organic molecules on the DMA and MMA terminated Al_2O_3 surface.

Structure	**Interaction energy (eV)**
Dimethyl-Al_2O_3 – EG	-2.34
Dimethyl-Al_2O_3 – DEG	-1.82
Dimethyl-Al_2O_3 – TEG	-1.40
Dimethyl-Al_2O_3 – FEG	-1.48
Dimethyl-Al_2O_3 – GL	-2.17
Monomethyl- Al_2O_3 – EG	-1.54
Monomethyl- Al_2O_3 – DEG	-1.42
Monomethyl- Al_2O_3 – TEG	-1.48
Monomethyl- Al_2O_3 – FEG	-1.53
Monomethyl- Al_2O_3 – GL	-1.26

From **Table 1** we see that the formation of the Al-O bond between MMA/DMA and all diols, with release of CH_4, is favourable. For the DMA terminated Al_2O_3 surface, the computed energy of interaction decreases with an increase of the chain length, going from -2.34 eV for EG to -1.48 eV for FEG, where we observe that there is little difference in the energy change on going from TEG to FEG.

In contrast to the computed energies at the DMA-Al_2O_3 surface, for the MMA-Al_2O_3 surface the interaction energies do not show a strong dependence on the length of the diol, being -1.54 eV for EG and -1.53 eV for FEG. We suggest that this is due to the lack of the second CH_3 group in the MMA-Al_2O_3 structure.

We consider next the local geometry and in particular the Al-O distances between aluminium atom in DMA and MMA and the diol **(Table 2)**, as well as the Al-O distances to the surface. The Al-O distance could change when the length of the organic precursor is increased. Shorter Al-O bonds tend to be stronger, and this can affect the stability of the system.

The resulting Al-O distance between aluminium in DMA and the diols increases when the chain length of the organic precursor increases. For EG-DMA-Al_2O_3, the Al-O distance is 1.73 Å and it lengthens slightly to 1.74 Å for DEG-DMA-Al_2O_3 and to 1.75 Å for TEG-DMA-Al_2O_3. For the FEG-DMA-Al_2O_3 surface there is a decrease to 1.73 Å. However, these changes

are not particularly large and do not fully account for the wide change in interaction energy on going from EG to FEG. When we compare the C-O and C-C distances between the free gas phase molecules and the same molecules bound to DMA, we also find little change; for example, the C-O distance in the free DEG is 1.40 Å and upon forming the bond to the DMA it changes to 1.41 Å. The coordination number of aluminium can be affected by the reaction with the alcohol as well. In the DMA-Al_2O_3 surface, the aluminium is bound to one surface oxygen with an Al-O distance of 1.71 Å. When the diol is added this aluminium forms one more bond with another surface oxygen, resulting in a two coordinated aluminium site to surface oxygen atoms, with a further bond to oxygen from the diol and carbon from the CH_3 group. For EG both Al-O distances to the surface oxygens are 1.88 Å. For DEG these distances are 1.83 Å and 1.92 Å. For TEG and FEG the Al-O distances to surface oxygens are 1.73 Å and 2 Å. With the longer chains, one Al-O bond becomes shorter and one Al-O bond elongates.

Table 2 Computed Al-O distances between MMA/DMA-Al_2O_3 surface and organic molecules.

Structure	**Al-O distances (Å)**
Dimethyl- Al_2O_3 – EG	1.73
Dimethyl- Al_2O_3 – DEG	1.74
Dimethyl- Al_2O_3 – TEG	1.75
Dimethyl- Al_2O_3 – FEG	1.73
Dimethyl- Al_2O_3 – GL	1.73
Monomethyl- Al_2O_3 – EG	1.72
Monomethyl- Al_2O_3 – DEG	1.72
Monomethyl- Al_2O_3 – TEG	1.72
Monomethyl- Al_2O_3 – FEG	1.72
Monomethyl- Al_2O_3 – GL	1.73

For the MMA surface, Al-O distances to the alcohol molecules are 1.72 Å in all cases while the C-O and C-C distances are also not affected by the length of the organic molecule. Examining the atomic structure for diol interactions at the MMA-Al_2O_3 surface, the coordination of the aluminium atom does not change with adding the diol, presumably arising in part to there being no CH_3 group present. Although the coordination number does not change,

we do see some changes to the Al-O distances involving surface oxygens. Before adding the diol, the Al-O distances to the surface oxygens are 1.76 Å, 1.78 Å and 2 Å. The aluminium in MMA after adding the diol is coordinated to three surface oxygen atoms and oxygen from diol. For all diols two Al-O distances from aluminium of MMA to the surface oxygens are 1.75 Å and 1.77 Å. The distance to the third surface oxygen becomes longer, being in the range of 2.02 Å (for EG) to 2.05 Å (for FEG).

Based on the interaction energies we propose that for longer diols it will be harder to maintain an upright configuration compared to lying flat and participating in the "double reaction" where the terminal OH groups bind to the aluminium atoms. However, the chain oxygens of DEG, TEG and FEG can also serve as active sites and they can bind with other TMA molecules. These adsorbed TMA molecules interact with new molecules of DEG, TEG or FEG and form three dimensional alucone networks. [10] This highlights the complexity of alucone film growth. In the absence of chain oxygens in the organic precursor, because of the favoured double reactions that reduce the number of active sites from the surface (see the following section), we expect the growth rate to decrease when the carbon chain length is increased as found in reference [11] where the thickness of alucones grown with ethanediol, butanediol and pentanediol varied with chain length. When the carbon chain length increased, the growth rate rapidly decreased and deviated from a linear pattern; and these changes were proposed to arise from the occurrence of a large number of double reactions, which resulted in the loss of reactive surface sites.

Due to the characteristic surface reaction of MLD, we have considered the secondary reaction between DMA terminated surface and EG. The interaction energy of 2EG-DMA-Al_2O_3 was calculated relative to the model of EG-DMA-Al_2O_3. The second EG molecule was modelled in an upright configuration. Similar to the primary reaction, again the proton of the OH group of EG reacts with the CH_3 group and produces a CH_4 molecule that is released as a byproduct. The computed change in energy upon forming the new Al-O bond between one surface bound DMA on Al_2O_3 and EG is -1.72 eV confirming that the secondary reaction is favourable. The Al-O distances to EG molecules are 1.72 Å and 1.75 Å. When we compare Al-O distances with surface oxygens for 2EG-DMA-Al_2O_3 and EG-DMA-Al_2O_3 we see some changes. While Al-O distances in EG-DMA-Al_2O_3 are 1.88 Å, for 2EG-DMA-Al_2O_3 one Al-O distance decreases to 180 Å while one increases to 1.89 Å. It is reasonable that these EG species would also participate in the flat lying reaction with a neighbouring DMA, **Fig. 5**.

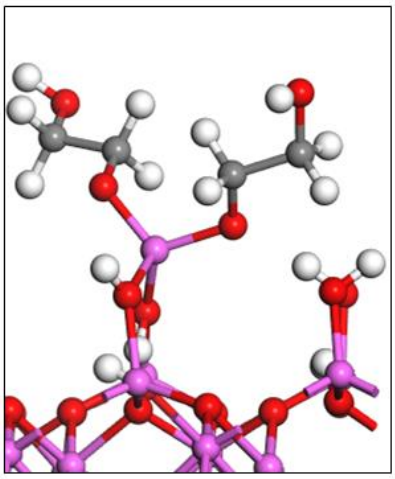


Figure 5 Optimised atomic structure of the DMA-Al_2O_3 surface after the interaction with two EG molecules.

We now consider the interaction between GL and MMA/DMA-Al_2O_3 surfaces. Again, GL was modelled in an upright configuration. On both DMA-Al_2O_3 and MMA-Al_2O_3 surfaces, the proton of the OH group of GL reacts with CH_3 to produce a free CH_4 molecule released as a byproduct while oxygen binds with the aluminium site. From the energetics in **Table 1**, we see that the formation of an Al-O bond is favourable in both cases (**Fig. 6**). However, the computed interaction energy is weaker on MMA-Al_2O_3 compared to DMA-Al_2O_3; this difference is ca. 0.9 eV.

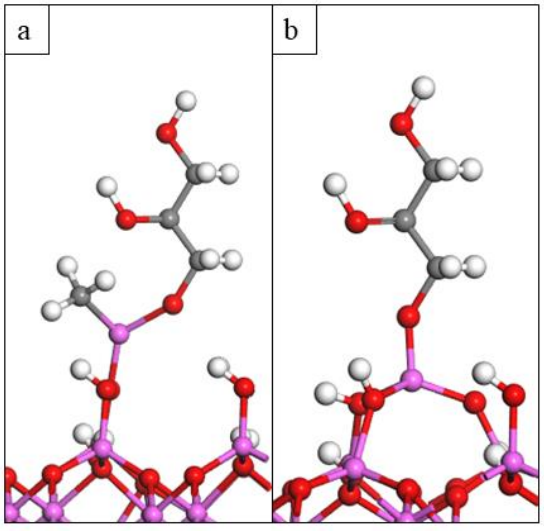


Figure 6 Optimised atomic structures of a) DMA-Al_2O_3 surface with GL and b) MMA-Al_2O_3 surface with GL.

The Al-O distances to GL are 1.73 Å for both cases. In DMA aluminium binds to two surface oxygen atoms with distances 1.88 Å and 1.90 Å. The aluminium atom in MMA binds to three surface oxygen atoms with distances 1.75 Å, 1.77 Å and 2.05 Å. The C-O and C-C distances between the gas phase molecules and the molecules bound to MMA/DMA are little changed as a result of this interaction. The C-O distance in free GL is 1.42 Å and it changes to 1.41 Å upon binding to aluminium in DMA-Al_2O_3 and 1.40 Å in MMA-Al_2O_3.

Comparison of upright and flat lying reactions of ethylene glycol (EG) and glycerol (GL) on MMA/DMA terminated Al_2O_3 surface

To examine the double reaction phenomenon of EG and GL we investigate the models of Al_2O_3 terminated with two DMA or two MMA and analyse the upright and flat lying or double reaction configurations of EG and GL. In the former, organic molecules bind to one aluminium species through one terminal oxygen site, while in the latter the molecules binds through the two terminal oxygen sites to two neighbouring aluminium sites.

Firstly, examining the geometry of the 2DMA and 2MMA terminated surfaces, the distance between the two aluminium atoms on 2DMA-Al_2O_3 is 4.18 Å and 2.64 Å on the 2MMA-Al_2O_3 surface. This geometry is geometrically favourable for the EG molecule to lie flat, with a distance of 3.69 Å between the terminal oxygen sites in EG and in this way both active terminal groups of EG will be occupied. The distance between the oxygen sites in the gas phase GL molecule, 4.98 Å, is also long enough to create double reactions with the MMA/DMA sites on the Al_2O_3 surface. However, in contrast to EG, GL has a third OH group, and this group will not be used in the binding in the flat lying configuration, so that can persist as a reactive group irrespective of how the molecule binds. This OH can then react with TMA in a subsequent metal pulse.

We compute the energy change when the organic molecules bind to one aluminium site in an upright configuration and these energies are shown in **Table 3**. The resulting atomic structures are shown in **Fig. 7 (a)** and **(b)** for DMA and **(c)** and **(d)** for MMA.

The GL molecule interacts in an upright configuration with an energy gain of -1.25 eV at both 2DMA-Al_2O_3 and 2MMA-Al_2O_3, while for EG there is a difference of 0.3 eV between interaction at DMA and MMA. However, all interactions are favourable for both molecules. The energies of the models with the flat lying precursors were calculated relative to the models with the upright EG and GL and represent an overall energy change on going from the upright

to flat configuration, **Table 3.** From this table we see that the formation of double reactions between MMA/DMA and EG and GL, together with release of CH_4 is favourable. For the DMA terminated surface we compute an energy gain of between -1.42 eV for the flat EG and -1.17 for the flat GL, while for the MMA terminated surface we compute an energy gain of -1.49 eV for the flat EG and -1.03 for the flat GL. This means that the formation of Al-O bonds through both terminal OH groups of the organic precursor is favourable and preferred for both molecules, EG and GL.

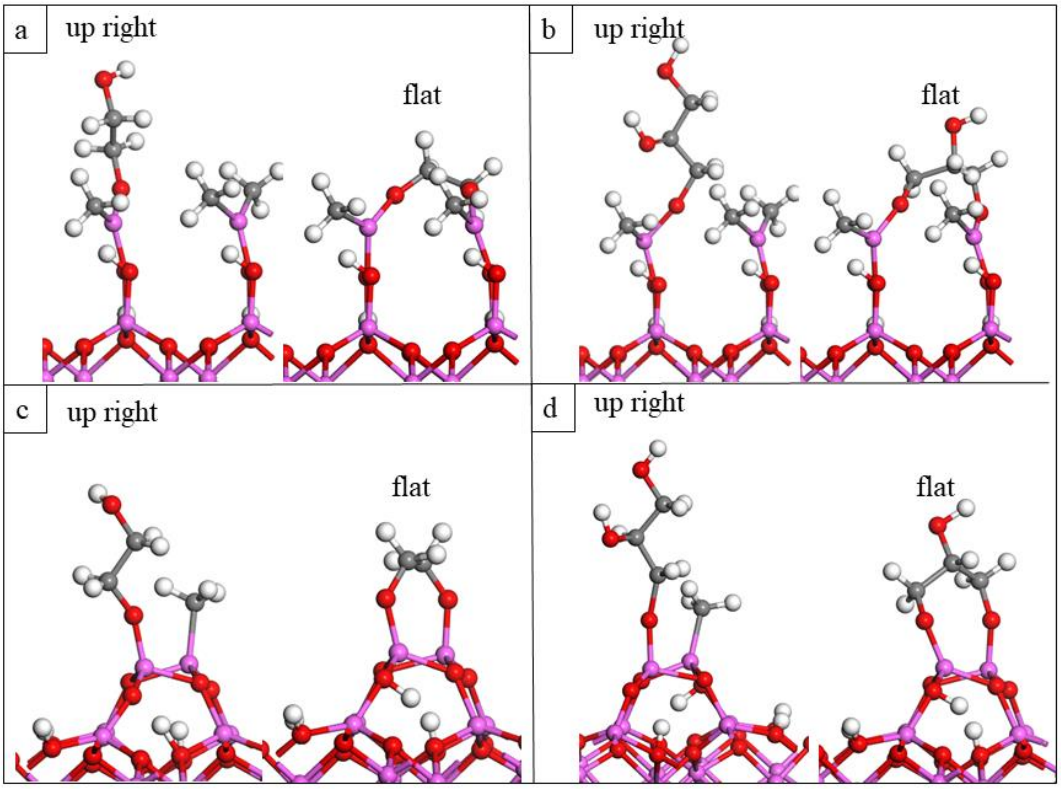


Figure 7 Optimised atomic structures of a) 2DMA-Al_2O_3 surface with the upright and flat EG, b) 2DMA-Al_2O_3 surface with the upright and flat GL, c) 2MMA-Al_2O_3 surface with the upright and flat EG and d) 2MMA-Al_2O_3 surface with the upright and flat GL

When we compare the Al-O distances between the upright models and flat lying models we see that the Al-O distances to the alcohol undergo only small changes. For EG-DMA, the Al-O distance decreases from 1.70 Å for the upright model to 1.68 Å for the flat lying model while for GL-DMA the Al-O distance decreases from 1.72 Å for the upright model to 1.71 Å for the flat lying model. For EG-MMA the Al-O distance increases from 1.68 Å for the upright to 1.70 Å for the flat lying configuration. For GL-MMA the Al-O distance is the same in both cases, 1.71 Å (**Table 4**). For the upright EG and GL on the 2DMA-Al_2O_3 surface, both Al-O distances

between aluminium of DMA and surface oxygens are 1.70 Å. For the flat lying EG and GL both Al-O distances to the surface oxygens are 1.69 Å. For the upright EG on the 2MMA surface, the distances between aluminium of MMA and surface oxygens are 1.63 Å, 1.82 Å and 2.05 Å. For the upright GL these distances are 1.74 Å, 1.93 Å and 1.99 Å. For the flat lying EG the Al-O distances are more uniform, being 1.85 Å, 1.86 Å and 1.88 Å. For the flat laying GL the distances are 1.86 Å, 1.88 Å and 1.90 Å.

Table 3 Computed interaction energy, upon formation of Al-O bonds between MMA/DMA in the upright configuration of EG and GL. The energy for the flat structures (double reactions) is the overall energy change on going from the upright to flat configuration.

Structure	**Interaction energy (eV)**
2MMA-Al_2O_3 – EG – upright	-1.18
2DMA-Al_2O_3 – EG – upright	-1.47
2MMA-Al_2O_3 – GL – upright	-1.24
2DMA-Al_2O_3 – GL– upright	-1.28
2MMA-Al_2O_3 – EG – flat	-2.67
2DMA-Al_2O_3 – EG – flat	-2.89
2MMA-Al_2O_3 – GL – flat	-2.27
2DMA-Al_2O_3 – GL– flat	-2.45

Table 4 Computed Al-O distances between MMA/DMA and EG and GL in the upright and flat lying configurations.

Structure	**Al-O distances (Å)**
2MMAl-Al_2O_3 – EG – upright	1.68
2DMAl-Al_2O_3 – EG – upright	1.7
2MMAl-Al_2O_3 – GL – upright	1.71
2DMAl-Al_2O_3 – GL– upright	1.72
2MMAl-Al_2O_3 – EG – flat	1.7
2DMAl-Al_2O_3 – EG – flat	1.68
2MMAl-Al_2O_3 – GL – flat	1.71
2DMAl-Al_2O_3 – GL– flat	1.71

Based on the energy differences, both terminal OH groups of EG and GL are able to react with surface bound DMA and MMA. For EG, no OH sites are available while with GL, the additional OH group is available for further reactions, which provides an atomistic origin for the findings of reference [1], where linear and saturated growth was obtained for GL based alucones in the temperature range of 100°C to 145°C while a decrease in growth per cycle (GPC) with increasing temperature was observed for both processes, EG and GL based alucones. The decrease was less pronounced for GL based alucones. DFT findings are also in agreement with the literature. [12, 13]

Reaction of ethylene glycol (EG) and glycerol (GL) with trimethylaluminium (TMA) in the second MLD cycle

To examine the reactivity of flat lying EG and GL with a TMA precursor molecule, we have built models where the remaining OH group of GL reacts with TMA to form a new Al-O bonds and a CH_4 molecule is released. These structures can be described as DMA-GL-MMA-Al_2O_3 and DMA-GL-DMA-Al_2O_3. For EG, we have also considered the reaction of TMA with the terminal oxygen sites that bind to Al, to assess if the reactivity of these sites towards the metal precursor persists.

For GL, the energy gain in forming an Al-O bond with TMA, together with release of CH_4, is -1.36 eV for MMA and -1.63 eV for DMA. These are similar to the energy gains when forming the Al-O bond between MMA and GL indicating that this exposed OH group is reactive to TMA and further growth will proceed. For DMA-GL-MMA-Al_2O_3 and DMA-GL-DMA-Al_2O_3 the Al-O distance from the available -OH site and aluminium of the new TMA molecule is 1.69 Å. This is little changed from the Al-O distances of 1.69 Å and 1.70 Å for aluminium in the original surface bound MMA and DMA.

The energy gain in forming an Al-O bond between EG and TMA is -0.82 eV for MMA and -1.32 eV for DMA. These are smaller than the energy gains when forming the Al-O bond between the original exposed MMA/DMA and EG and we note that the EG does not take an upright configuration but lies flat, due to the local structure around the aluminium site. For DMA-GL-MMA-Al_2O_3 and DMA-GL-DMA-Al_2O_3 we see some significant differences in the Al-O distances. The Al-O distances from the organic to the adsorbed TMA molecule are 2.0 Å for MMA-Al_2O_3 and 1.87 Å for DMA-Al_2O_3 with less uniform Al-O distances of 1.71 and 1.83 Å involving the original DMA groups. Consequently, we could expect that the growth can

proceed, but the thickness of an EG alucone film would be smaller than that of a GL alucone film and this is consistent with experimental results in [1], where saturation curves show that TMA/GL MLD process gives higher growth rates per cycle and thicker films compared to the TMA/EG MDL process. Optimised atomic structures are shown in **Fig. 8**.

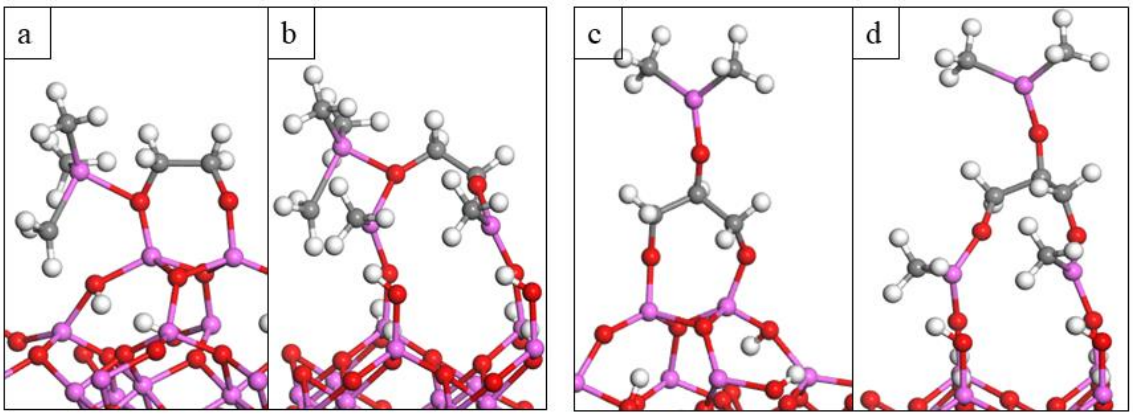
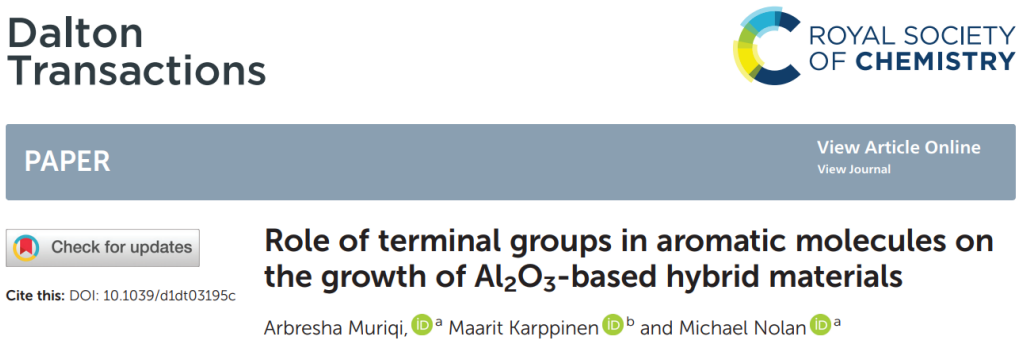


Figure 8 Optimised atomic structures of a) flat lying EG on MMA-Al_2O_3 surface with adsorption of TMA at the exposed OH site on EG, b) flat lying EG on DMA-Al_2O_3 surface with adsorption of TMA at the exposed OH site on EG, c) flat lying GL on MMA-Al_2O_3 surface with adsorption of TMA at the exposed OH site on GL and d) flat lying GL on DMA-Al_2O_3 surface with adsorption of TMA at the exposed OH site on GL.

4.3 Modelling of hybrid Al_2O_3 films using aromatic precursors

This work is published in the paper "***Role of terminal groups in aromatic molecules on the growth of Al_2O_3-based hybrid materials***" in Dalton Transactions. [14]

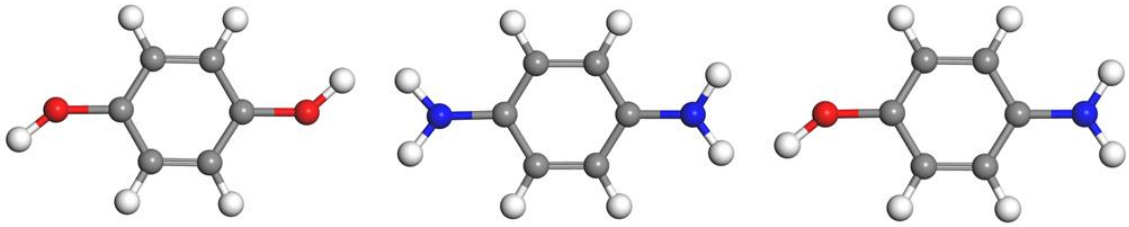


DOI: https://doi.org/10.1039/D1DT03195C

4.3.1 Results

Reactions between aromatic precursors molecules the and monomethyl (MMA) terminated aluminium oxide (Al_2O_3) surface

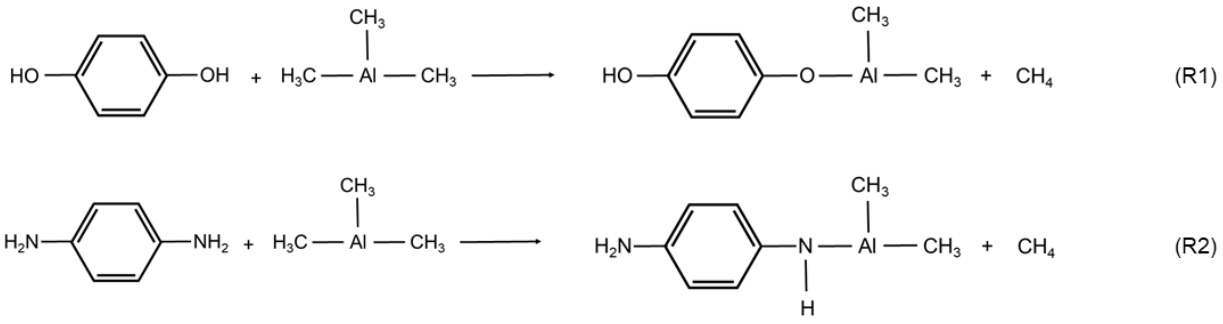
The hydroxylated aluminium oxide (Al_2O_3) surface terminated with one methyl group (MMA-Al_2O_3, Al(CH_3)-Al_2O_3) that results from the adsorption of trimethylaluminium (TMA) on the Al_2O_3 surface was taken from our previous work with alucones. [8] We performed investigations on the interactions between the post TMA pulse MMA-Al_2O_3 surface and a selection of aromatic molecules with very different chemical character and these are hydroquinone (HQ), p-phenylenediamine (PD) and 4-aminophenol (AP), **Fig. 9.** This set of aromatic molecules allows us to examine the reactivity of hydroxyl (OH) and amino (NH_2) groups towards TMA as well as the preferred orientation of the organic species. The selected aromatic molecules contain OH and NH_2 groups separated by an aromatic ring where the OH and NH_2 groups serve as reactive linkers for condensation reactions with metal sites, leading to hybrid films.



hydroquinone (HQ) | p-phenylenediamine (PD) | 4-aminophenol (AP)

Figure 9 Structures of hydroquinone (HQ), p-phenylenediamine (PD) and 4-aminophenol (AP) after optimization by DFT. Red-O, blue-N, grey-C and white-H. Figure coding is the same for all figures.

The modelling was done considering the potential proton transfer, elimination of CH_4 molecules and the formation of new Al-O and Al-N bonds. The OH and NH_2 groups have lone electron pairs with Lewis base character and can bind with the CH_3 ligands of TMA which have a strong Lewis acid character and eliminate as CH_4. The initial reactions between TMA with HQ and PD are likely to be as follows (**Scheme 2**):



Scheme 2 Schematic representation of the proposed reaction mechanism of TMA with HQ (R1) and PD (R2) in the gas phase. [15]

The AP molecule is a heterobifunctional aromatic molecule that contains both active groups, OH and NH_2. Therefore, AP can react with MMA according to R1 or R2. [15] The optimized atomic structures of the MLD products with HQ, PD and AP are shown in **Fig. 10**. In the first calculations the aromatic precursors were modelled in an upright configuration. When these aromatic molecules react with MMA adsorbed on the Al_2O_3 surface, a proton from a terminal active group (OH or NH_2) transfers to the CH_3 ligand of TMA to form a new CH_4 molecule that is released as a byproduct.

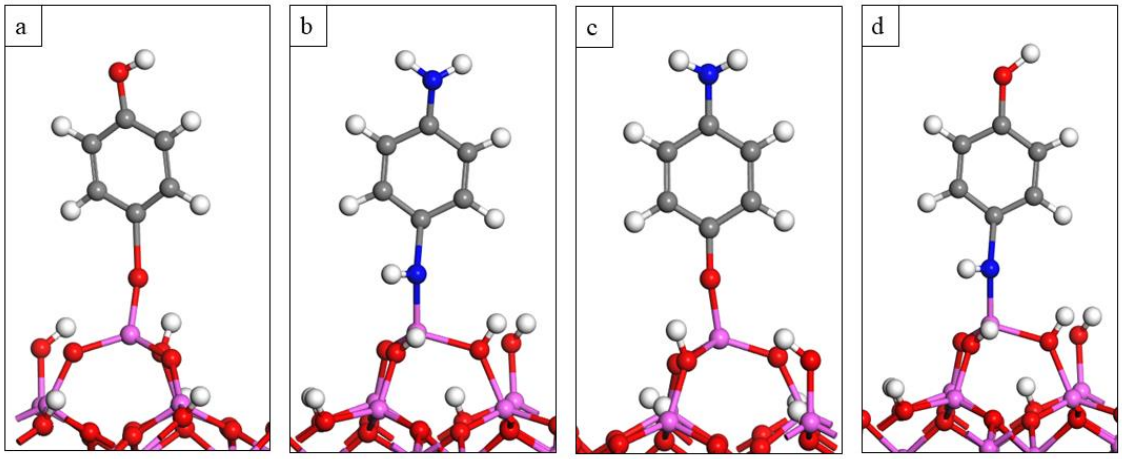


Figure 10 Optimised atomic structures of MMA-Al_2O_3 surface after interacting with a) HQ, b) PD, c) AP, Al-O bonding and d) AP, Al-N bonding.

For HQ the remaining oxygen binds to aluminium of TMA with a Al-O distance 1.73 Å, and the calculated energy change for this reaction is -1.38 eV. For PD the remaining nitrogen binds to aluminium of TMA with a Al-N distance of 1.83 Å, and the calculated energy change for this reaction is -1.12 eV. Calculated energetics show that HQ and PD molecules bind favourably with TMA on Al_2O_3 via formation of new Al-O and Al-N bonds and CH_4 elimination. However, reaction energetics suggest a higher reactivity of the OH group with TMA in comparison to the NH_2 group. Containing both active groups, OH and NH_2, AP can bind to aluminium of TMA through oxygen with a calculated Al-O distance 1.71 Å and through nitrogen with a calculated Al-N distance 1.83 Å. A higher reactivity was calculated again for the reaction with the OH group with an energy change -1.25 eV for the Al-O bonding in comparison to the NH_2 group with an energy change of -0.86 eV for the Al-N bonding (**Table 5**).

In addition to the Al-O and Al-N bonds formed with the aromatic molecules, the aluminium atom is bonded to three surface oxygen sites with distances 2.0 Å, 1.78 Å and 1.75 Å in the reaction with HQ, 1.94 Å, 1.92 Å and 1.73 Å in the reaction with PD and 2.0 Å, 1.78 Å and 1.75 Å in the reaction with AP. After the interactions with the aromatic molecules the coordination number of the aluminium atom of TMA and the Al-O distances are changed compared to the methyl terminated structure (MMA-Al_2O_3). The aluminium atom binds with two surface oxygens with Al-O distances 1.78 Å and 1.76 Å. The results of this set of calculations are consistent with the findings of the gas phase model that was used to examine the interactions between TMA and the functional groups OH, NH_2, and NO_2 in the respective

substituted phenyl molecules with DFT. [15] While that model accounts for the Al-O/Al-N bond formation, it lacks the alumina surface which is an important part of the growth chemistry. However, that study does show that the reactions between TMA and the functional groups are exothermic. It was also found that the reaction energy for TMA with NH_2 or NO_2 functional groups is considerably less favourable than with OH.

Table 5 Computed interaction energy upon formation of Al-O and Al-N bonds between MMA-Al_2O_3 and the organic molecules of interest.

Structure	**Interaction energy (eV)**
MMAl-Al_2O_3 – HQ	-1.38
MMAl-Al_2O_3 – PD	-1.12
MMAl-Al_2O_3 – AP (Al–O)	-1.25
MMAl-Al_2O_3 – AP (Al–N)	-0.86

Comparison of upright and flat lying reactions of hydroquinone (HQ), p-phenylenediamine (PD) and 4-aminophenol (AP)

To investigate the double reaction phenomenon for the aromatic molecules in more detail, we examine interactions of the Al_2O_3 surface terminated with two surface bound Al(CH_3) species (2MMA-Al_2O_3), used in our previous work, [8] with HQ, PD and AP molecules in the upright and flat lying configuration. Minimising double reactions of the organic precursor is considered an important advantage of using stiff aromatic molecules as organic precursors. [16-18] While in the upright configuration the aromatic molecules bind to aluminium sites through one active group and one CH_4 molecule is released, in the flat configuration, the aromatic molecules bind through both active groups with two neighbouring aluminium sites and two CH_4 molecules are released. MLD reaction products of TMA adsorbed at Al_2O_3 surface with the upright and flat lying HQ, PD and AP molecules are shown in **Fig. 11**. The energy change given for the double reaction is with reference to the upright structure and allows us to assess if the double reaction is thermodynamically favourable.

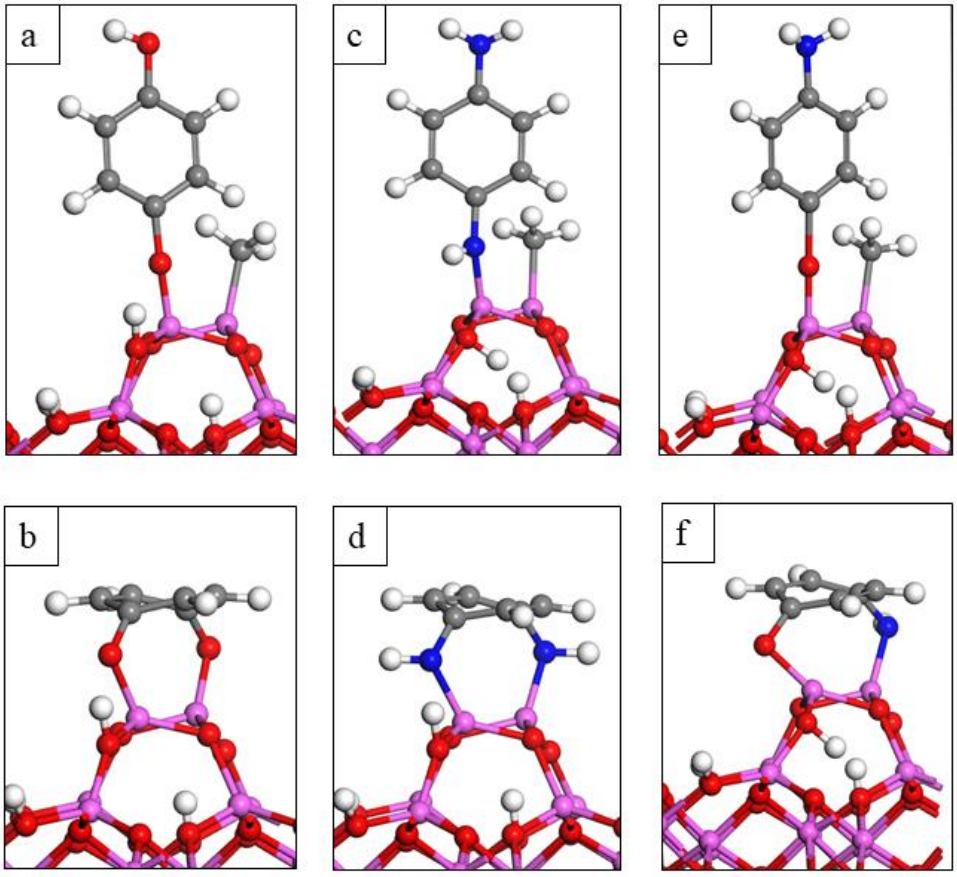


Figure 11 Optimised atomic structures of 2MMA-Al_2O_3 surface with a) upright HQ, b) flat HQ, c) upright PD, d) flat PD, (e) upright AP and (f) flat AP.

Aromatic molecules interact favourably with TMA in an upright configuration with an energy change ranging from -0.49 eV for PD to -1.69 eV for HQ. Once again the calculated energies show that the reaction is more exothermic for the formation of the Al-O bond in comparison to the formation of the Al-N bond. The energy for the double reaction of HQ on the 2MMA-Al_2O_3 surface is -0.11 eV and shows that the molecule can also lie flat and react twice with the surface. In contrast to HQ, calculated energies for the double reactions of PD and AP with TMA are endothermic and thereby not favourable. PD and AP molecules do not prefer to lie flat and react twice with aluminium sites and this might be due to the presence of NH_2 active groups for which a lower reactivity with TMA was calculated.

However, we also computed interaction energies with van der Waals forces (vdW), **Table 6**, and we find that there is generally a small impact due to including vdW interaction. However, for HQ the inclusion of the vdW interactions makes the double reactions for the HQ molecule less favourable.

Table 6 Computed interaction energy with van der Waals forces (vdW) on, upon formation of Al-O and Al-N bonds between 2MMA-Al_2O_3 in the upright configuration of HQ, PD and AP. The energy for the flat structures (double reactions) is the overall energy change on going from the upright to flat configuration.

Structure	**Interaction energy (eV)**
2MMAl-Al_2O_3 – HQ – upright	-1.42
2MMAl-Al_2O_3 – HQ – flat	0.25
2MMAl-Al_2O_3 – PD – upright	-0.38
2MMAl-Al_2O_3 – PD – flat	1.17
2MMAl-Al_2O_3 – AP – upright	-1.13
2MMAl-Al_2O_3 – AP – flat	0.35

When we compare the Al-O and Al-N distances between the upright models and flat lying models we see that the Al-O and Al-N distances to the aromatic molecule undergo small changes. For the HQ molecule bonded on the 2MMA-Al_2O_3 surface the Al-O bond is lengthened from 1.71 Å to 1.82 Å while for AP the Al-O distance is lengthen from 1.69 Å to 1.83 Å. For the PD molecule the Al-N distance is lengthen from 1.80 Å to 1.91 Å.

Based on the calculated energetics for the double reactions of aromatic molecules, HQ could react with both OH groups with TMA on the Al_2O_3 surface and form the double reactions. However, given the very small change in energy without vdW interactions, and the positive energy with inclusion of vdW interactions, we propose that the two binding modes of HQ will be competitive. Steric effects also may prevent the HQ molecule to bind in a flat configuration. For PD and AP, because of the presence of the NH_2 group, the unwanted double reactions on the surface are efficiently reduced and the molecules can self-assemble in a vertical orientation with a free -OH or -NH_2 group for the next cycle. Hence, the surface remains covered with active groups that react with TMA in the next pulse. This will lead to thicker PD and AP based aluminium organic films compared to HQ based aluminium organic films.

These findings are consistent with work on titanium oxide (TiO_2) based MLD films that are grown using HQ, PD, AP and ODA molecules as organic precursors. [16] We expect PD and AP based aluminium organic films to have the same thickness as PD and AP molecules have similar backbone lengths as well (5.5 Å and 5.6 Å).

Reaction of hydroquinone (HQ), p-phenylenediamine (PD) and 4-aminophenol (AP) with trimethylaluminium (TMA) in the second MLD cycle

Next we examine the reactivity of HQ, PD and AP molecules with a TMA precursor molecule, which takes place in the second cycle of the MLD process. After formation of Al-O and Al-N bonds and loss of CH_4, these structures can be described as DMA-HQ-MMA-Al_2O_3, DMA-PD-MMA-Al_2O_3 and DMA-AP-MMA-Al_2O_3, where DMA stands for the $Al(CH_3)_2$, present after one CH_3 elimination. During the reaction with TMA, the remaining OH and NH_2 groups of aromatic molecules react with TMA and form new Al-O or Al-N bonds and one CH_4 molecule is released.

Optimised structures for the products of the MLD reactions in the second cycle are shown in **Fig. 12**. For HQ the energy change upon forming a new Al-O bond with distance 1.70 Å, together with the release of CH_4, is -1.48 eV. Since we found that HQ can also lie flat and react with TMA via both OH groups, we also examine the reactivity of the flat lying HQ towards TMA. We consider the reaction between a terminal oxygen of HQ with TMA as shown in **Fig. 12 (b)**. The energy change in forming an Al-O bond between the flat HQ and TMA is -0.68 eV. Calculated energetics indicate that HQ in both configurations is reactive towards TMA, although less in the flat lying configuration since the terminal oxygens are bounded to aluminium sites. For PD and AP, the energy change upon forming new Al-N bonds with distance 1.80 Å, together with release of CH_4 are -0.71 eV and -0.92 eV, respectively.

When we compare the reaction energetics between the three aromatic molecules in the upright configuration with TMA, a lower reactivity of the NH_2 group with TMA in comparison to the OH group was again noted. However, the reactions between the three aromatic molecules and TMA in the second cycle of the MLD process are exothermic and this indicates that the exposed OH and NH_2 groups are reactive to TMA and further growth will proceed for HQ, PD and AP based aluminium organic films.

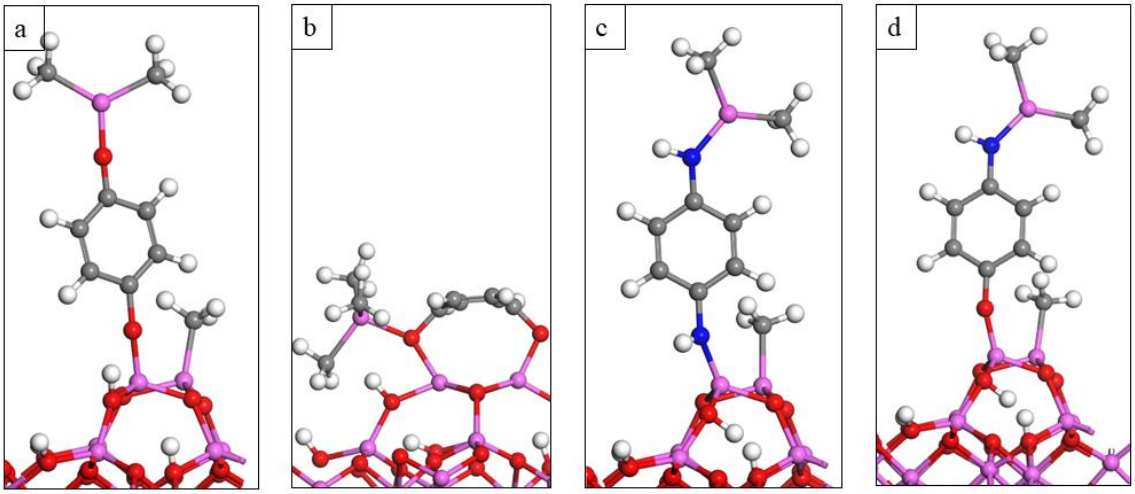


Figure 12 Optimised atomic structure of a) upright HQ with adsorption of TMA at the exposed OH site on HQ, b) flat lying HQ with adsorption of TMA at the exposed OH site on HQ, c) PD with adsorption of TMA at the exposed NH_2 site on PD and d) upright AP with adsorption of TMA at the exposed NH_2 site on AP.

The influence of phenyl functionalization

The molecules 2-methoxyhydroquinone (HQ-OCH_3), 2-methylhydroquinone (HQ-CH_3), 2-chlorhydroquinone (HQ-Cl) and 2-nitrohyrdoquinone (HQ-NO_2) were chosen to examine the role of phenyl functionalization on the interaction between the OH site of the HQ molecule and the aluminium site of TMA. This set of calculations allows us to analyse if activating groups -OCH_3, -CH_3 and deactivating groups -Cl and -NO_2 added in the structure of aromatic molecules with the purpose to tune film properties will affect the stability of the film by weakening the Al-O bond between the precursors. The substitution of the proton atom on the HQ molecule was done in the meta position and the reaction mechanism between the functionalized molecules and TMA is according to R1. Optimised structures of the functionalized HQ molecule reacting with TMA on the Al_2O_3 surface are shown on **Fig. 13**. Although activating and deactivating groups impact the stability and the reactivity of the aromatic ring in different ways, there is no significant difference in the calculated energies for four reactions of TMA with the aromatic molecules. Calculated energies are -1.21 eV for the reaction with HQ-OCH_3, -1.25 eV for the reaction with HQ-CH_3, -1.30 eV for the reaction with HQ-Cl and -1.25 eV for the reaction with HQ-NO_2. Calculated energies for the reaction between the functionalized HQ molecule with TMA on the Al_2O_3 surface do not differ much also from the calculated energy for the reaction between the unmodified HQ with TMA on Al_2O_3 surface (-1.38 eV).

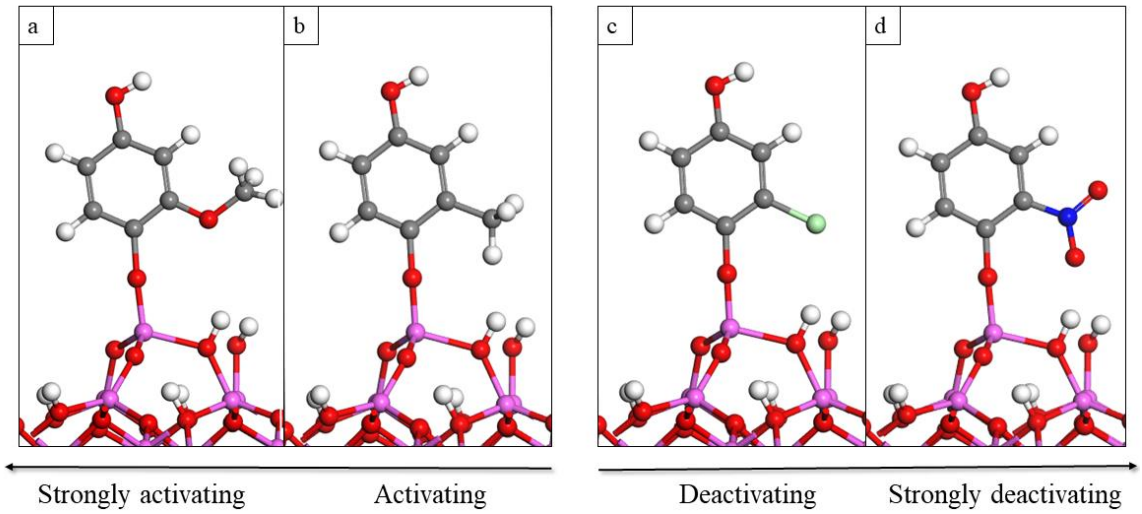


Figure 13 Optimised atomic structures of the MMA-Al_2O_3 surface after interacting with a) HQ-OCH_3, b) HQ-CH_3, c) HQ-Cl and d) HQ-NO_2.

Some small changes were observed on the Al-O bond when the aromatic molecule is modified with activating and deactivating groups. The Al-O distance for the unmodified HQ model is 1.73 Å and it decreases to 1.71 Å for HQ-OCH_3, HQ-CH_3, and HQ-Cl, while there is an increase to 1.74 Å for HQ-NO_2. The calculations show that the functionalisation of the aromatic ring can be done with the purpose to tune hybrid film properties and importantly this will not weaken the interaction between aromatic molecules and the TMA precursor nor the stability of the system. Given the possibility of the double reaction for the HQ molecule, a flat configuration of the HQ-OCH_3, HQ-CH_3, HQ-Cl and HQ-NO_2 on the 2MMA-Al_2O_3 was examined. The reaction energies are now endothermic with a calculated energy of 0.20 eV for HQ-OCH_3, 0.01 eV for HQ-CH_3, 0.11 eV for HQ-Cl and 0.29 eV for HQ-NO_2 on the 2MMA-Al_2O_3. Calculated energies indicate that phenyl functionalisation can have an impact on the configuration of the aromatic molecule by further preventing the molecule to lie flat and react twice with the surface. This promotes an upright binding mode and thicker film growth compared to an unfunctionalised phenyl ring.

We also evaluate the role of phenyl functionalization on the interaction between the NH_2 site of the PD molecule and the aluminium site of TMA. Again, the substitution of the proton atom on the PD molecule was done in the meta position while the reaction mechanism between the functionalized PD molecule and TMA is according to R2. Optimised structures of the functionalized PD molecule reacting with TMA on the Al_2O_3 surface are shown on **Fig. 14**. Calculated energies are -1.25 eV for the reaction with PD-OCH_3, -1.20 eV for the reaction with

PD-CH_3, -1.42 eV for the reaction with PD-Cl and -1.49 eV for the reaction with PD-NO_2. The calculated energies between the functionalized PD molecules and TMA on Al_2O_3 surface are more negative compared to the energy for the reaction between the unmodified PD with TMA on Al_2O_3 surface (-1.12 eV). This shows that for PD, the functionalization of the molecule can also impact the chemistry of the NH_2 group with TMA by increasing the interactions between the precursors. Small changes are also observed on the Al-N distance which increased from 1.83 Å for the unmodified PD molecule to 1.84 Å for PD-OCH_3, PD-CH_3, and PD-Cl, and 1.88 Å for PD-NO_2.

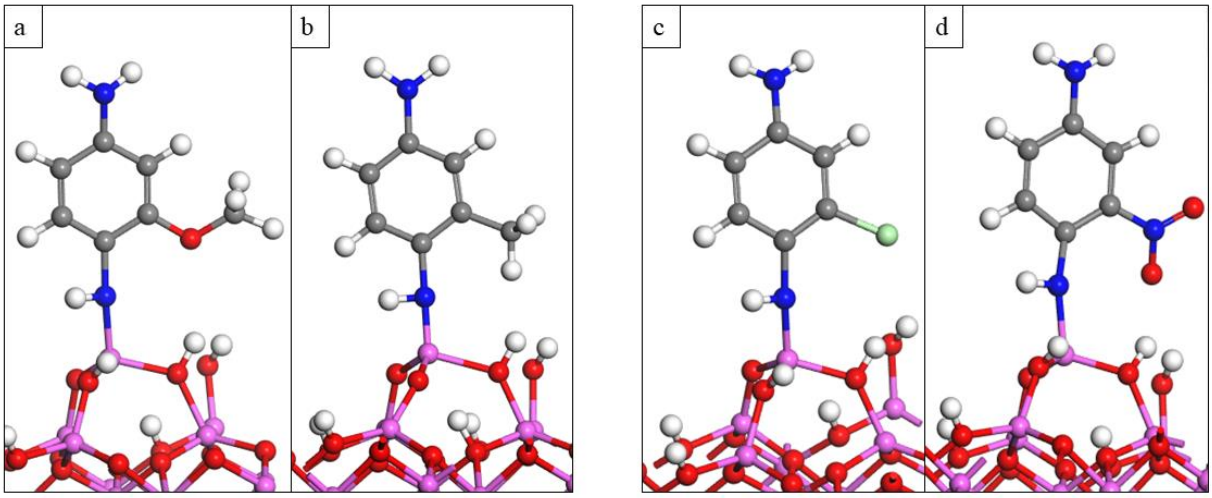


Figure 14 Optimised atomic structures of the MMA-Al_2O_3 surface after interacting with a) PD-OCH_3, b) PD-CH_3, c) PD-Cl and d) PD-NO_2.

Reactions between hydroquinone bis(2-hydroxyethyl) ether and 1,1′-biphenyl-4,4′-diamine with monomethyl (MMA) terminated aluminium oxide (Al_2O_3) surface

In our final study we examine the interactions between TMA on the Al_2O_3 and the aromatic molecules hydroquinone bis(2-hydroxyethyl)ether ($C_6H_4(OCH_2CH_2OH)_2$) and 1,1′biphenyl 4,4′-diamine (($C_6H_4NH_2)_2$). None of the selected molecules has been used so far in MLD although similar molecules to 1,1′- biphenyl-4,4′-diamine such as 4,4′-oxydianiline and 4,4′-biphenyldicarboxylic have already been used in practice. [19, 20] The hydroquinone bis(2-hydroxyethyl)ether and 1,1′-biphenyl-4,4′-diamine have been specifically selected in this study to examine the influence of the length of the organic precursor on the Al-O and Al-N interactions.

Optimised structures of the MLD reaction products with hydroquinone bis(2-hydroxyethyl)ether and 1,1′-biphenyl-4,4′-diamine are shown in **Fig. 15**. Organic molecules were modelled in the upright configuration. Hydroquinone bis(2-hydroxyethyl)ether molecule contains two hydroxyethyl chains separated by one aromatic ring where the hydroxyethyl chains participate in the reactions with the TMA. During this reaction a proton from the terminal OH group of the hydroxyethyl chain transfers to the CH_3 ligand to form a new CH_4 molecule while the remaining oxygen binds to aluminium of TMA with a Al-O distance 1.74 Å. The calculated interaction energy, -1.15 eV, confirms that this reaction is favourable. When we compare interaction energies for the reaction of TMA with HQ and with hydroquinone bis(2-hydroxyethyl)ether, we see a drop in energy from -1.38 eV to -1.15 eV. The drop in energy when the size of the aromatic molecule has increased shows that for longer aromatic molecules it may be more difficult to maintain a stable upright configuration compared to lying flat and participate in the double reaction.

The 1,1′-biphenyl-4,4′-diamine molecule contains two NH_2 groups separated by two aromatic rings. In this reaction a proton from the terminal NH_2 group transfers to the CH_3 ligand to form a new CH_4 molecule while the remaining nitrogen binds to aluminium of TMA with a Al-N distance 1.84 Å. This reaction is favourable with an interaction energy of -0.32 eV. When compared to the interaction energy for the PD bonded to TMA, this energy has decreased from -1.12 eV to -0.32 eV and again we propose that this drop in energy when the size of the aromatic molecule has increased is due to the difficulty of longer aromatic molecules to maintain in an upright configuration.

In the reactions with hydroquinone bis(2-hydroxyethyl)ether and 1,1′-biphenyl-4,4′-diamine the aluminium atom of TMA remains four coordinated. The aluminium atom is bonded to oxygen or nitrogen site of the aromatic molecule and also to three oxygen atoms on the surface with distances 2.06 Å, 1.79 Å and 1.76 Å for hydroquinone bis(2-hydroxyethyl)ether and 2.1 Å, 1.77 Å and 1.75 Å for 1,1′-biphenyl-4,4′-diamine. In conclusion, DFT calculations show that the hydroquinone bis(2-hydroxyethyl)ether molecule has potential to be used as an organic precursor for the deposition of hybrid films with MLD. The thermal properties of hydroquinone bis(2-hydroxyethyl)ether also indicate that most probably the compound would be suitable for MLD and DFT studies provide further motivation to develop an MLD process for the deposition of hybrid films using hydroquinone bis(2-hydroxyethyl) ether as organic precursor.

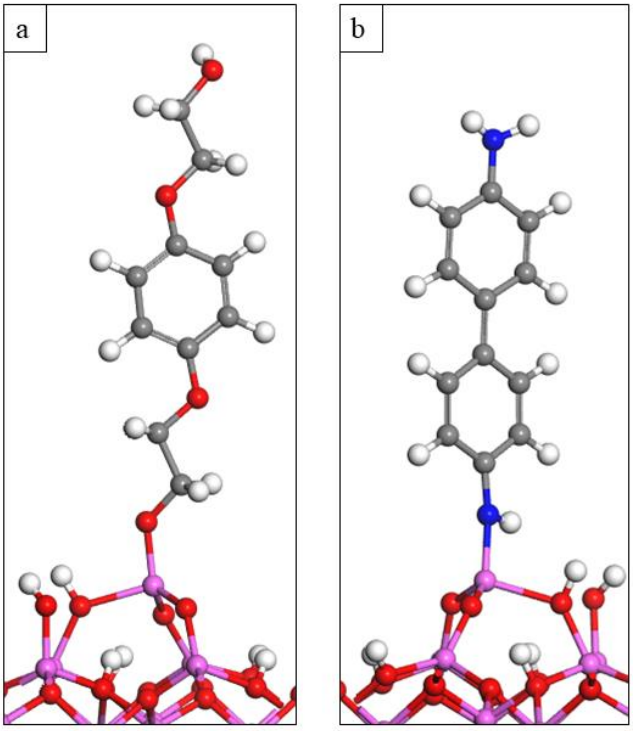


Figure 15 Optimised atomic structures of the MMA-Al_2O_3 surface after interacting with a) hydroquinone bis(2-hydroxyethyl)ether and b) 1,1'-biphenyl-4,4'-diamine.

4.4 Modelling of Alucone films grown with DMAI

4.4.1 Results

Dimethyl aluminum isopropoxide (DMAI) is a trivalent aluminium compound same as trimethyl aluminium (TMA), and as such, can be considered as a TMA molecule where one of the methyl (CH_3) ligands on each aluminium centre has been replaced by an isopropoxide (O-$CH(CH_3)_2$) group. In contrast to TMA, DMAI is non pyrophoric and offers a more stable form of dimer. The optimised atomic structures of DMAI molecules in its monomeric form and dimeric form is presented in **Fig. 16**.

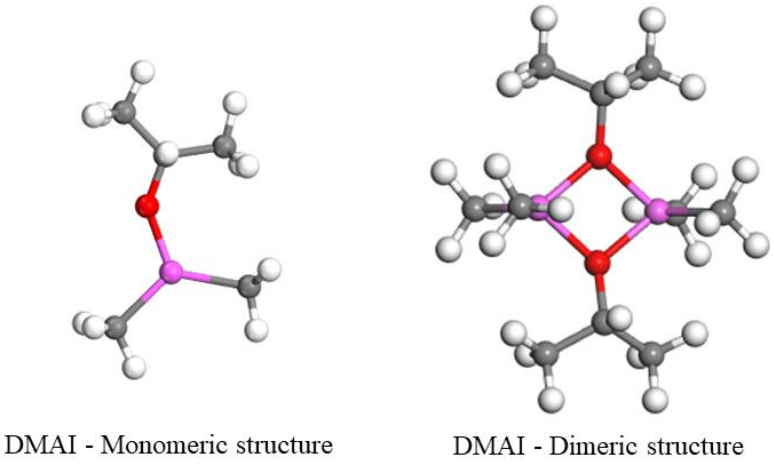


Figure 16 Structures of dimethylaluminum isopropoxide (DMAI) in the monomeric form and dimeric form after optimization by DFT. Purple-Al, red-O, grey-C and white-H. Figure coding is the same for all figures.

In our calculations we investigate the reactivity of DMAI in the dimeric form towards the hydroxylated aluminium oxide (Al_2O_3) surface taken from previous work [9] and the selected organic precursor EG. We consider two possible configurations of the DMAI molecule, the flat configuration and the upright configuration. **Fig. 17 (a)** shows the atomic structure of the hydroxylated Al_2O_3 surface after interaction with the DMAI in the flat configuration and **(b)** with the DMAI in the upright configuration. The computed adsorption energy for DMAI in the flat configuration on the hydroxylated Al_2O_3 surface is -0.47 eV. For DMAI in the upright configuration, this energy is -0.29 eV. Although the difference on the adsorption energies for the flat and upright configuration is small, calculations show that DMAI prefers to orient in a flat configuration and react with the surface via both aluminium atoms.

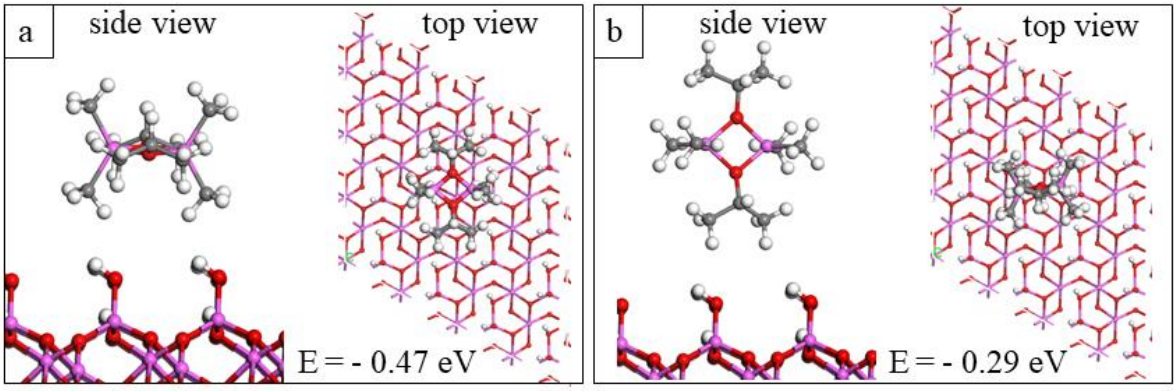


Figure 17 Optimised atomic structure of DMAI interacting with the hydroxylated Al_2O_3 surface a) in the flat configuration and b) in the upright configuration.

Results from previous experimental work show that methane (CH_4) and isopropanol (HO-$CH(CH_3)_2$) are the main products of DMAI decomposition. [21] Therefore, we consider the formation of CH_4 and HO-$CH(CH_3)_2$ as byproducts during the reactions of DMAI with the hydroxylated Al_2O_3 surface and EG. The first case involves breaking the Al-C bonds first and the release of two CH_4 molecules as byproducts. During this reaction two protons transfers from the OH surface groups to the CH_3 ligands of DMAI, one CH_3 ligand for each aluminium atom, to form two new CH_4 molecules and the remaining aluminium atoms of DMAI attach to the surface oxygens from which the proton migrate with Al-O distances 1.70 Å and 1.74 Å, **Fig 18 (a)**. The calculated energy change upon forming the new Al-O bonds and releasing the two new CH_4 molecules is -2.30 eV.

Next, we consider the loss of the two remaining CH_3 ligands in the DMAI molecule. This reaction includes the transfer of protons from the surface OH groups to the CH_3 ligands, the elimination of two new CH_4 molecules and the formation of two new Al-O bonds with distances 1.72 Å and 1.73 Å, **Fig 18 (b)**. During this reaction the structure of DMAI dimer breaks so that each aluminium atom is bonded with one O-$CH(CH_3)_2$ ligand. The calculated energy change for this reaction is 0.29 eV. This reaction leaves the surface covered with two O-$CH(CH_3)_2$ ligands that can exchange with EG molecules during the organic precursor pulse.

After the introduction of EG, two new HO-$CH(CH_3)_2$ molecules are formed when protons transfer from the OH groups of EG to the O-$CH(CH_3)_2$ ligands and new Al-O bonds with distances of 1.67 Å and 1.70 Å are formed as shown in **Fig 18 (c)**. The calculated energy change for the reaction with EG that involves also the release of two HO-$CH(CH_3)_2$ molecules is -0.08 eV, leading to an overall energy change of -2.09 eV. The energy -0.08 energy is much smaller

when compared to the energy for the loss of the CH_3 ligands and the formation of CH_4 products. It also shows that the removal of the O-$CH(CH_3)_2$ ligands and the formation of HO-$CH(CH_3)_2$ is more difficult suggesting that this might be the rate limiting step in the overall reaction. This is consistent with bond dissociation energy values for the breakage of the Al-O and Al-C bonds (512 kJ/mol and 255 kJ/mol respectively) which also shows that the Al-O bond is much stronger and thus much difficult to break. However, the overall energy for the loss of four CH_4 molecules and two O-$CH(CH_3)_2$ molecules in the reaction with EG is exothermic, -2.09 eV and thereby favourable.

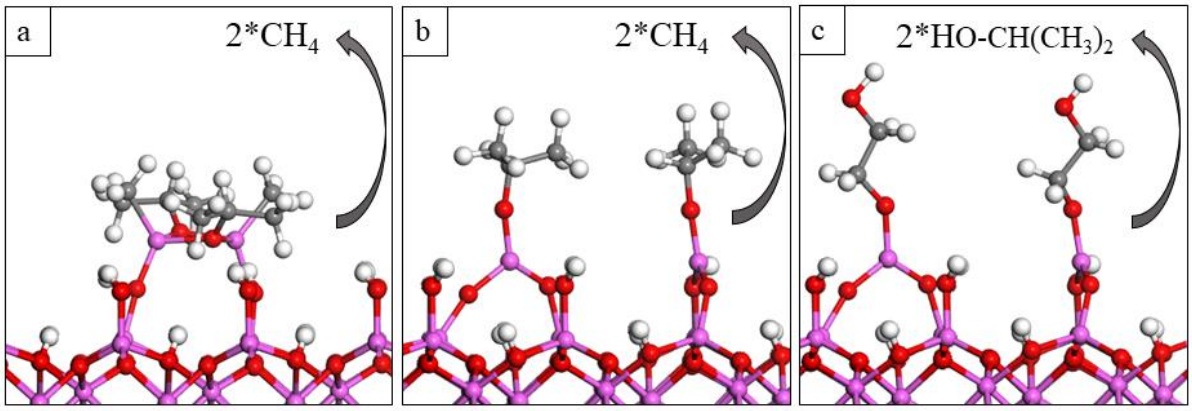


Figure 18 Optimised atomic structures of the hydroxylated Al_2O_3 surface with DMAI after a) elimination of the first two CH_3 ligands, b) elimination of the second two CH_3 ligands and c) elimination of the two O-$CH(CH_3)_2$ ligands in the reaction with EG.

In the second case we consider the loss of O-$CH(CH_3)_2$ ligands first and the formation of two free HO-$CH(CH_3)_2$ molecules as a byproducts when two protons transfer from the surface OH groups to the O-$CH(CH_3)_2$ ligands and the aluminium atoms of DMAI bind to surface oxygen with Al-O distances 1.70 Å, **Fig. 19**. The calculated energy change for this reaction is 1.59 eV. The positive energy gain shows that the loss of HO-$CH(CH_3)_2$ ligands first is not favourable. From the calculated energetics it is very clear that the preference is to remove the CH_3 ligands first which affects the surface coverage before the EG pulse.

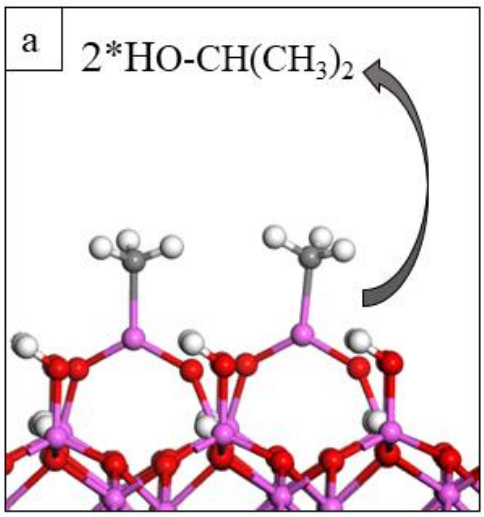


Figure 19 Optimised atomic structure of the hydroxylated Al_2O_3 surface with DMAI after elimination of two $O\text{-}CH(CH_3)_2$ ligands.

Finally, we analyse the interactions between EG and DMAI by investigating the first half reaction in the second cycle of the MLD process. During this reaction, a proton from the OH group of EG transfers to one CH_3 ligand of DMAI and forms a CH_4 molecule while the aluminium of DMAI binds to the oxygen of EG through a new Al-O bond with distance 1.73 Å. The calculated interaction energy is -1.49 eV, **Fig. 20**. The exothermic reaction shows that EG reacts favourably with DMAI in the second cycle of the MLD process and hence we expect the growth to proceed for alucone films grown with DMAI as the aluminium precursor. DFT studies show that the reactivity of DMAI towards the Al_2O_3 surface and the organic precursor EG is similar to the reactivity of TMA (adsorption energies on the Al_2O_3 surface: -0.60 eV for TMA, -0.47 eV for DMAI; interaction energies with EG: -1.54 eV for TMA, -1.59 eV for DMAI). [8, 22] In summary, the reactivity of DMAI is sufficient enough for DMAI to be involved in the MLD reactions and combined with the fact that DMAI is safer than TMA by being non pyrophoric in nature and avoids infiltration due to its stability in the dimeric form, we confirm that DMAI is a good alternative to TMA.

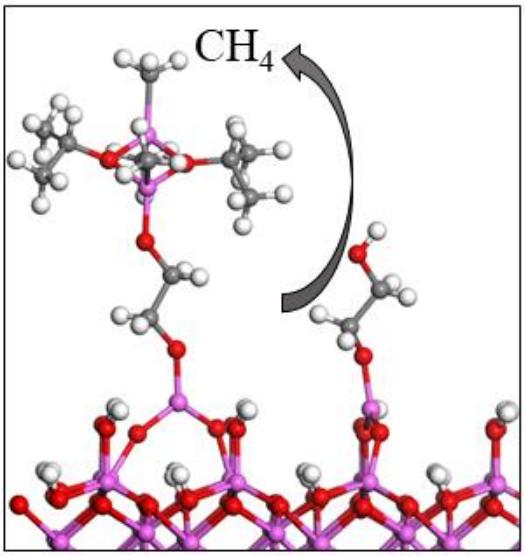


Figure 20 Optimised atomic structure of the EG on the CH_3 terminated Al_2O_3 surface with adsorption of DMAI at the exposed OH site on EG.

4.5 Conclusion

In this chapter, we have investigated the molecular mechanism of the growth of aluminium based films deposited by molecular layer deposition (MLD). Reaction energetics show that selected organic diol molecules ethylene glycol (EG), diethylene glycol (DEG), triethylene glycol (TEG) and tetraethylene glycol (FEG), which differ by the length of chain, react favourably with the TMA precursor ($Al(CH_3)_2$ (DMA) and $Al(CH_3)$ (MMA) species) on the aluminium oxide (Al_2O_3) surface via Al-O bonds. All reactions with the diols are associated with the release of methane (CH_4) byproducts. We observed a less exothermic energy for DMA-Al_2O_3 upon increasing the length of the diols which indicates that the longer the chain length the harder it is for the organic precursor to stay in an upright configuration and avoid reacting twice with both terminal hydroxyl (OH) groups with the surface. This phenomenon will reduce the number of OH groups on the surface. However, even if these molecules participate in the so called "double reactions", the chain oxygens of DEG, TEG and FEG can also serve as active, albeit less reactive, sites and they can bind with other TMA molecules in the following cycle by forming so three dimensional alucone networks as found from experimental work, [10] but with a lower growth per cycle compared to an upright bonding configuration.

DFT calculations also show that EG and GL molecules, which are the most common alcohols used in metalcone film growth, react favourably with the Al_2O_3 surface terminated with two $Al(CH_3)_2$ and $Al(CH_3)$species. EG and GL prefer to lie flat and form double reactions through the reaction of the two terminal OH groups with the surface fragments. This phenomenon removes all active OH sites for EG which makes the growth less favourable for EG based alucones. For GL the third OH group is available to react with TMA in the next cycle and therefore the growth is more favourable. We also showed that TMA in the next pulse reacts favourably with this OH from the flat GL and also with the terminal oxygen sites from EG, suggesting that the growth can proceed for both. However, the preference for flat lying EG means that the change in thickness in the reaction of EG with TMA is smaller when compared to the GL-TMA fragment, indicating that GL based alucones will grow thicker films compared to EG based alucones. This analysis shows the origin of the difference in thickness of alucone films found for EG and GL [1] and is in good agreement with experimental findings on other metalcone films grown with EG and GL [2-5] and the literature. [12, 13]

While the main issue with the aliphatic molecules is the double reaction phenomenon, DFT shows that aromatic molecules hydroquinone (HQ), p-phenylenediamine (PD) and 4-aminophenol (AP) which are terminated with hydroxy (OH) and/or amino (NH_2) groups bind more favourably in an upright configuration with TMA on Al_2O_3 surface via formation of new Al-O and Al-N bonds and CH_4 elimination. This upright configuration of the aromatic molecules will lead to thicker more flexible and more stable hybrid films. A higher reactivity of the OH group in comparison to the NH_2 group towards TMA in the hydroxylated Al_2O_3 was also calculated. Calculated energetics also show that we can modify the core of the aromatic molecules with specific chemical groups (OCH_3, CH_3, Cl, NO_2) and this will promote a more upright configuration of the molecules and increase the interactions between the aromatic and inorganic precursors. In addition, these groups can also improve particular properties of films. Hydroquinone bis(2-hydroxyethyl)ether is a new aromatic molecule that has not been used so far in any MLD processes. Calculated energetics shows that this molecule reacts favourably with TMA on a Al_2O_3 surface, and considering also the suitable thermal properties of this molecule, we suggest that hydroquinone bis(2-hydroxyethyl)ether is a promising candidate for the deposition of aluminium organic films.

Except of the double reaction phenomenon of the aliphatic molecules in aulcone film growth, another issue is the tendency of TMA to infiltrate into the growing film, which also leads to low growth rates. [6, 12, 23] Through DFT calculations we show that DMAI which is suggested as alternative aluminium precursor for TMA from experimental work, [6, 7] is sufficient reactive towards the hydroxylated Al_2O_3 substrate and the EG molecule and therefore can be used as an alternative precursor to TMA for MLD in alucone film growth.

4.6 References

1. K. Kerckhove, M. K. S. Barr, L. Santinacci, P. M. Vereecken, J. Dendooven, Ch. Detavernier, *Dalton Transactions*, **2018**, 47, 5860–5870.
2. K. Kerckhove, F. Mattelaer, J. Dendooven, Ch. Detavernier, *Dalton Transactions*, **2017**, 46, 4542–4553.
3. H. Zhu, M. H. A. Shiraz, L. Yao, K. Adair, Zh. Wang, H.Tong, X. Song, T-K. Sham, M. Arjmand, X. Song , J. Liu, *Chemical Communications*, **2020**, 56, 13221–13224.
4. K. Kerckhove, F. Mattelaer, D. Deduytsche, P. M. Vereecken, J. Dendooven, Ch. Detavernier, *Dalton Transactions*, **2016**, 45, 1176–1184.
5. J. Kint, F. Mattelaer, S. S. T. Vandenbroucke, A. Muriqi, M. M. Minjauw, M. Nisula, Ph.M. Vereecken, M. Nolan, J. Dendooven, Ch. Detavernier, *Chemistry of Materials*, **2020**, 32, 4451–4466.
6. H. Jain, P. Poodt, *Dalton Transactions*, **2021**, 50, 5807–5818.
7. H. Jain, M. Creatore, P. Poodt, *Dalton Transactions*, **2022**, 51, 7918–7927.
8. A. Muriqi, M. Nolan, *Dalton Transactions*, **2020**, 49, 8710–8721.
9. G. R. Jenness, J. Seiter, M. K. Shukla, *Physical Chemistry*, **2018**, 20, 18850–18861.
10. D. W. Choi, M. Yoo, H. M. Lee, J. Park, H. Y. Kim, J. S. Park, *ACS Applied Materials and Interfaces*, **2016**, 8, 12263–12271.
11. Y-S. Park, H. Kim, B. Cho, Ch. Lee, S-E. Choi, M. M. Sung, J. S. Lee, A*CS Applied Materials and Interfaces*, **2016**, 8, 17489–17498.
12. A. A. Dameron, D. Seghete, B. B. Burton, S. D. Davidson, A. S. Cavanagh, J. A. Bertrand, S. M. George, *Chemistry of Materials*, **2008**, 20, 3315–3326.
13. S. M. George, B. H. Lee, B. Yoon, A. I. Abdulagatov, R. A. Hall, *Journal of Nanoscience and Nanotechnology*, **2011**, 11, 7948–7955.
14. A. Muriqi, M. Karppinen, M. Nolan, *Dalton Transacions*, **2021**, 50, 17583–17593.
15. F. Yang, J. Brede, H. Ablat, M. Abadia, L. Zhang, C. Rogero, S. D. Elliott, M. Knez, *Advanced Materals Interfaces*, **2017**, 4, 1700237.
16. A. Tanskanen, P. Sundberg, M. Nolan, M. Karppinen, *Thin Solid Films*, **2021**, 736, 138896.
17. P. Sundberg, M. Karppinen, *European Journal of Inorganic Chemistry*, **2014**, 6, 968–974.
18. R. A. Nye, S. Wang, S. Uhlenbrock, J. A. Smythe, G. N. Parsons, *Dalton Transactions*, **2022**, 51, 1838–1849.
19. A. Sood, P. Sundberg, J. Malm, M. Karppinen, *Applied Surface Science*, **2011**, 257, 6435–6439.
20. J. Multia, J. Heiska, A. Khayyami, M. Karppinen, *ACS Applied Materials Interfaces*, **2020**, 12, 41557–41566.
21. S. E. Potts, G. Dingemans, C. Lachaud, and W. M. M. Kessels, *Journal of Vacuum Science & Technology A*, **2012**, 30, 021505.
22. S. D. Elliott, J. C. Greer, *Journal of Materials Chemistry*, **2004**, 14, 3246–3250.
23. D. Seghete, R. A. Hall, B. Yoon, S. M. George, *Langmuir*, **2010**, 26, 19045–19051.

Chapter 5

Modelling of Ti-based hybrid films

5.1 Introduction

In this chapter, we have used first principles density functional theory (DFT) to investigate the growth mechanism of titanium containing hybrid inorganic-organic films, fabricated via molecular layer deposition (MLD), which are known as "titanicones". We investigated in detail the chemistry between the most common titanium precursors, namely titanium tetrachloride ($TiCl_4$) and tetrakis(dimethylamido)titanium ($Ti(DMA)_4$,) with ethylene glycol (EG) and glycerol (GL) as organic precursors. We analysed the impact of the substrate on the initial MLD reactions in titanicone film growth using three different surface models: anatase and rutile titanium oxide (TiO_2), and aluminium oxide (Al_2O_3). Calculated energetics show that while $TiCl_4$ is reactive towards the anatase and rutile TiO_2 surfaces, it is not reactive towards the Al_2O_3 surface. $Ti(DMA)_4$ is reactive towards all surfaces. This is attributed to the stronger Ti-Cl bonds in $TiCl_4$ compared to Ti-N bonds in $Ti(DMA)_4$. $Ti(DMA)_4$ also shows higher reactivity to the organics compared to $TiCl_4$. Double reactions of EG and GL with the $TiCl_3$ species from $TiCl_4$ and TiDMA species from $Ti(DMA)_4$ are also explored to better understand the origin of the different thicknesses of EG based titanicone and GL based titanicone films observed in experimental work. We found that EG and GL coupled with $TiCl_4$ can orient in a flat lying configuration on anatase, while on rutile the preferred orientation is upright. When combined with $Ti(DMA)_4$, EG and GL prefer the flat lying configuration on all surfaces. This work shows that the choice of the surface and the metallic precursor has a major impact on the chemistry of titanicone films. DFT findings provide motivation to develop a low temperature rutile TiO_2/titanicone film, suggesting that the desired film growth could be achieved.

This work is published in the paper "***Role of Titanium and Organic Precursors in Molecular Layer Deposition of "Titanicone" Hybrid Materials***", in Beilstein Journal of Nanotechnology.

BEILSTEIN JOURNAL OF NANOTECHNOLOGY

Role of titanium and organic precursors in molecular layer deposition of "titanicone" hybrid materials

Arbresha Muriqi and Michael Nolan*

DOI: https://doi.org/10.3762/bjnano.13.103

5.1.1 Results

Chemical structures of the titanium tetrachloride ($TiCl_4$), tetrakis(dimethylamido)titanium ($Ti(DMA)_4$), ethylene glycol (EG) and glycerol (GL) precursors used in this study for titanicone films are presented in **Fig. 1.**

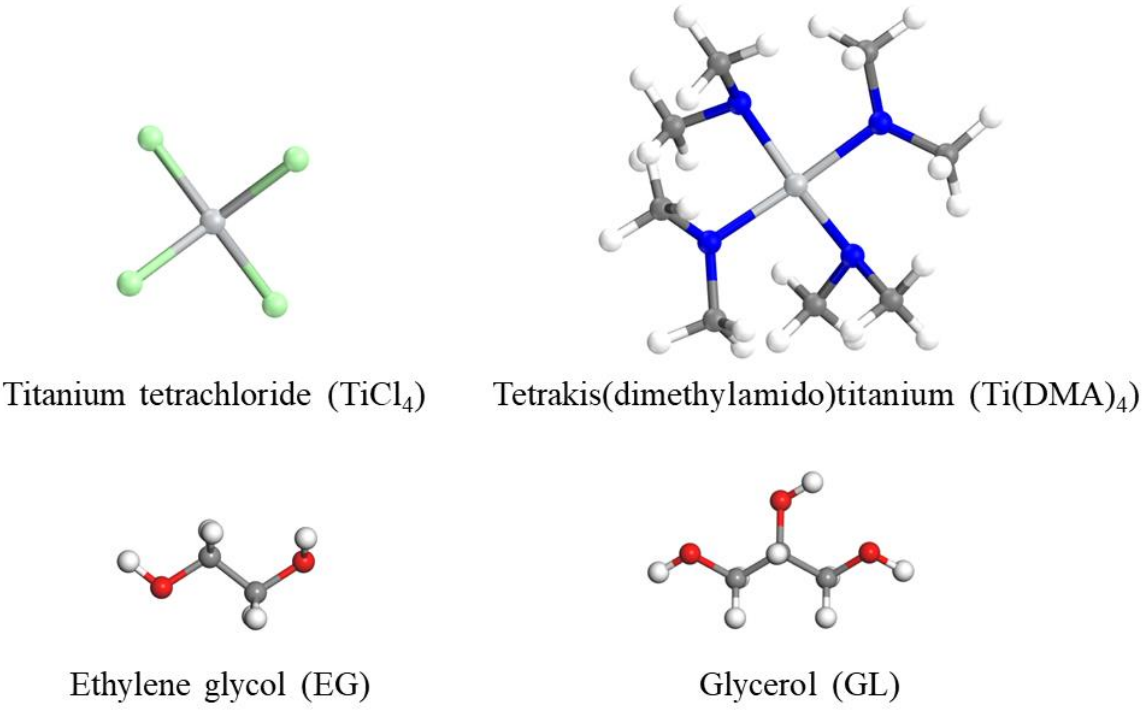


Figure 1 Molecular structure of titanium tetrachloride ($TiCl_4$), tetrakis(dimethylamido) titanium ($Ti(DMA)_4$), ethylene glycol (EG) and glycerol (GL) precursors. Light grey-Ti, green-Cl, red-O, grey-C and white-H.

Titanium tetrachloride ($TiCl_4$) terminated anatase/rutile titanium oxide (TiO_2) and aluminium oxide (Al_2O_3) surface models

As oxide/metalcone films are of high interest, we explored the feasibility of anatase TiO_2/titanicone, rutile TiO_2/titanicone and Al_2O_3/titanicone film formation. This is a common approach in modelling MLD chemistry. [1-4] We performed fundamental investigation on the interactions between the hydroxylated anatase TiO_2, hydroxylated rutile TiO_2 and hydroxylated Al_2O_3 surfaces with $TiCl_4$ and EG or GL precursors. The hydroxylated surfaces that result from the interactions with water and before the introduction of $TiCl_4$ are taken from previous studies. [5, 6]

In the first calculations we have calculated the interaction energies of the $TiCl_4$ molecule on the selected surfaces. These energies are -0.29 eV for anatase TiO_2, -0.22 eV for rutile TiO_2 and 0.87 eV for the Al_2O_3. These energies indicate that $TiCl_4$ will adsorb favourably, although with a small energy gain, on the anatase TiO_2 surface and rutile TiO_2 surface and will not adsorb on the Al_2O_3 surface. A previous study reports that TiO_2 films grow well using $TiCl_4$ and water on amorphous Al_2O_3. [7] However, in our case, the Al_2O_3 surface model we use is crystalline. It is well known that in an amorphous surface the molecular mobility is significantly higher than in any corresponding crystalline form and there is a lower coordination number for atoms in the surface which can give rise to enhanced chemical reactivity of the amorphous surface. These results show that the choice of the surface can have a major impact on the initial deposition steps.

As we find that the adsorption of $TiCl_4$ is not favourable on the Al_2O_3 surface, we continue only with the anatase and rutile TiO_2 surface models with $TiCl_4$.

Next, we investigate the first and second ligand loss reactions of $TiCl_4$, which involve the proton transfer from surface OH groups to the chlorine ligands of $TiCl_4$ to form HCl byproducts, and the formation of new Ti-O bonds between $TiCl_4$ and the surface oxygen. During the first ligand loss reaction, $TiCl_4$ forms one new Ti-O bond with the surface and one HCl molecule is released. This reaction leaves the surface covered with three chlorine ligands, $TiCl_3$-TiO_2. During the second ligand loss reaction $TiCl_4$ forms a second new Ti-O bond with the surface and a second HCl molecule is released. After this reaction the surface is left covered with two chlorine ligands, $TiCl_2$-TiO_2. The coordination number of titanium in the $TiCl_4$ molecule is four and remains unchanged during the first and second ligand loss reactions. Atomic structures of the anatase TiO_2 surface and rutile TiO_2 surface after adsorption of one

$TiCl_4$ molecule and the elimination of the first and second ligand from $TiCl_4$ are presented in **Fig. 2.** Calculated interaction and ligand loss energies of $TiCl_4$ on the anatase TiO_2 surface and rutile TiO_2 surface are presented in **Table 1.**

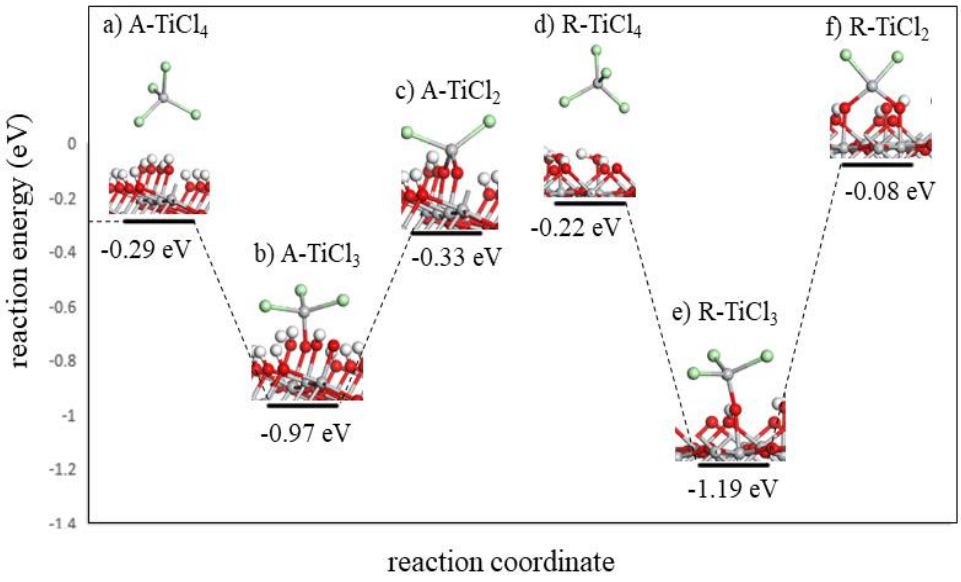


Figure 2 Plotted ligand loss reactions of $TiCl_4$ on the anatase/rutile TiO_2 surface. Optimised atomic structure of a) $TiCl_4$ interacting with anatase TiO_2 surface, b) $TiCl_3$ terminated anatase TiO_2 surface, c) $TiCl_2$ terminated anatase TiO_2 surface, d) $TiCl_4$ interacting with rutile TiO_2 surface, e) $TiCl_3$ terminated rutile TiO_2 surface and f) $TiCl_2$ terminated rutile TiO_2 surface.

Table 1 Computed adsorption and ligand loss energies of $TiCl_4$ on anatase/rutile TiO_2 surface.

Structure (Anatase)	**Interaction energy (eV)**	**Structure (Rutile)**	**Interaction energy (eV)**
$TiCl_4$	-0.29	$TiCl_4$	-0.22
$TiCl_3$	-0.97	$TiCl_3$	-1.19
$TiCl_2$	-0.33	$TiCl_2$	-0.08

Energetics for the ligand loss reactions are calculated relative to the first model of $TiCl_4$ interacting with the surface, and present an overall reaction energy. The overall energy for $TiCl_4$ to lose chlorine ligands and bind on either TiO_2 surface is negative, although there is a notable energy cost for losing the second chlorine ligand to give a surface bound $TiCl_2$. We do not explore further loss of HCl to give adsorbed TiCl since XPS analysis from previous experimental work showed that chlorine impurities are still present in the titanicone film, [8] indicating that some Ti–Cl bonds have reminded unreacted.

The length of the Ti-O bonds formed between $TiCl_4$ and both TiO_2 surfaces during the first and second ligand loss reactions is presented in **Table 2**. From **Table 2** we can see that Ti-O bonds formed between anatase TiO_2 surface and $TiCl_4$ are about 0.02-0.03 Å shorter when compared to Ti-O bonds formed between rutile TiO_2 surface and $TiCl_4$. Generally, shorter Ti-O bonds tend to be stronger, and this can also influence the stability of the system.

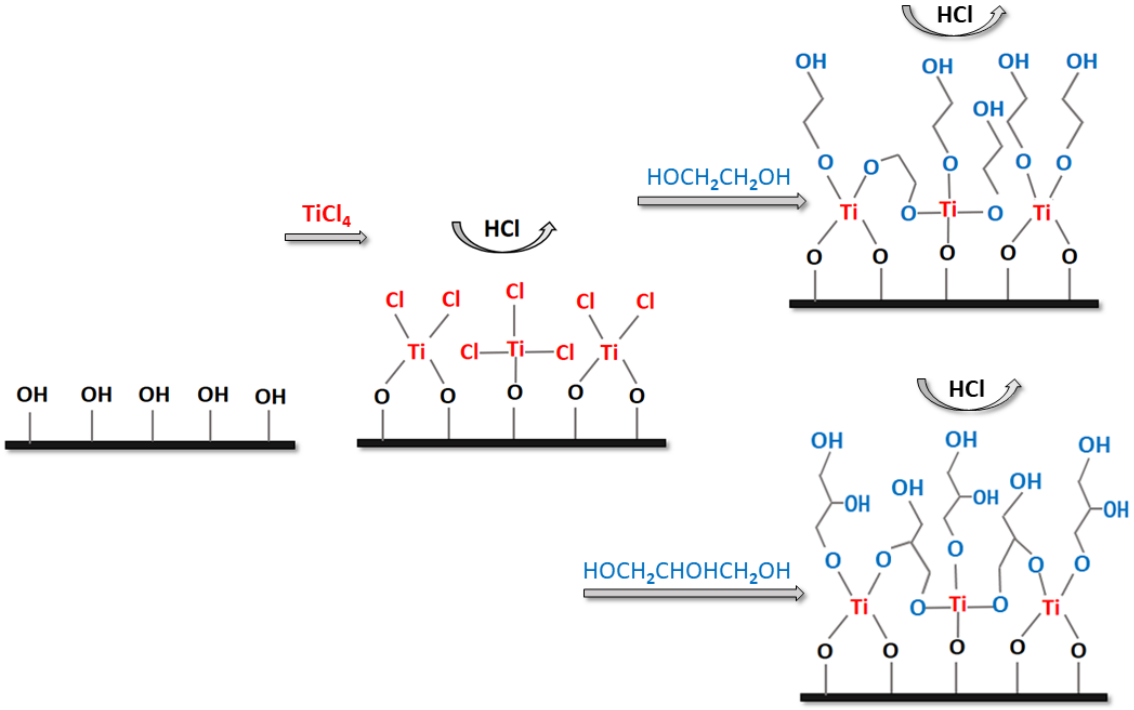
Table 2 Computed T-O distances between $TiCl_4$ and the anatase/rutile TiO_2 surface.

Structure (Anatase)	**Ti-O (Å)**	**Structure (Rutile)**	**Ti-O (Å)**
$TiCl_3$	1.72	$TiCl_3$	1.74
$TiCl_2$	1.78, 1.78	$TiCl_2$	1.78, 1.81

In addition to the surface models that result from the adsorption of a single $TiCl_4$ molecule, in order to investigate the double reaction phenomenon of EG and GL, we have also built models in which two $TiCl_4$ molecules are adsorbed on the anatase TiO_2 and rutile TiO_2 surfaces. Calculated energies for the adsorption of the second $TiCl_4$ molecule are -0.81 eV on the anatase TiO_2 surface and -0.03 eV on the rutile TiO_2 surface. This difference may arise from the higher stability of rutile TiO_2 compared to anatase. The resulting surfaces after the adsorption of the second $TiCl_4$ molecule are terminated with two $TiCl_3$ species, $2TiCl_3$-anatase and $2TiCl_3$-rutile, and the distance between the titanium atoms of the two $TiCl_3$ species is 6.0 Å on the anatase TiO_2 surface and 6.9 Å on rutile TiO_2 surface.

Reactions between organic precursors and $TiCl_2$/$TiCl_3$ terminated anatase/rutile TiO_2 surface

With these post-$TiCl_4$ pulse models of anatase TiO_2 and rutile TiO_2 available, the interactions between the $TiCl_3$-TiO_2 and $TiCl_2$-TiO_2 species and the organic precursors are investigated by analysing the formation of MLD products with EG and GL. Reactions with EG and GL involve the transfer of one proton from a terminal OH group of the organic molecule to a chlorine ligand of $TiCl_2$/$TiCl_3$ to release a HCl molecule as byproduct and form one new Ti-O bond between $TiCl_2$/$TiCl_3$ species and the organic molecules. A schematic illustration of titanicone MLD films based on the reactions between the hydroxylated surface and $TiCl_4$ and the reactions between the $TiCl_2$/$TiCl_3$ surface species with EG and GL is presented in **Scheme 1**.



Scheme 1 Schematic representation of titanicone MLD using $TiCl_4$ as inorganic precursor and EG or GL as organic precursors.

The resulting atomic structures of the MLD reaction products with EG and GL are shown in **Fig. 3**. The overall energy change for the reactions between the $TiCl_2$/$TiCl_3$ terminated anatase TiO_2 and rutile TiO_2 surfaces with EG and GL is presented in **Table 3** and these results show that the calculated energies for the reactions between the $TiCl_3$ terminated surfaces with EG and GL, associated with the release of one HCl molecule are exothermic and therefore favourable. There are also clear differences when EG and GL bind with $TiCl_3$ and $TiCl_2$ terminated TiO_2 surfaces. The calculated energies for the reactions between the $TiCl_2$ terminated surfaces with EG and GL, associated with the release of one HCl molecule, are endothermic, meaning that these reactions are not favourable. We found a similar difference for the reaction of $TiCl_2$/$TiCl_3$ with aromatic precursors. [9]

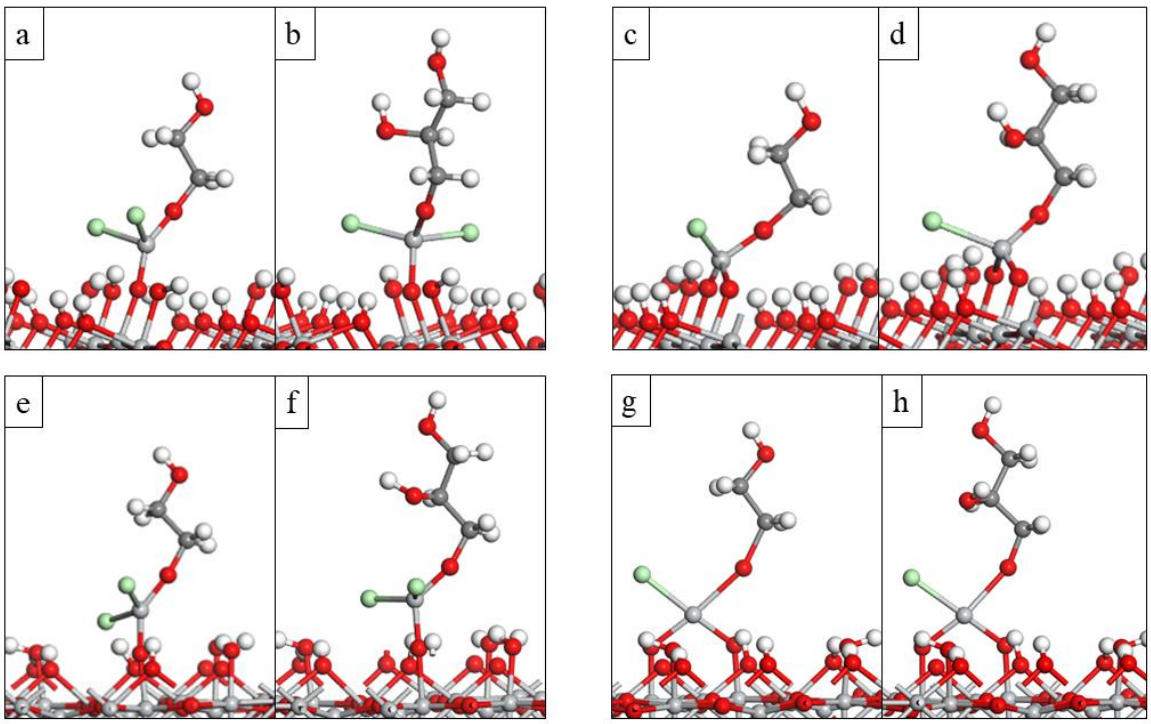


Figure 3 Optimised atomic structure of a) anatase-$TiCl_3$-EG, b) anatase-$TiCl_3$-GL, c) anatase-$TiCl_2$-EG, d) anatase-$TiCl_2$-GL, e) rutile-$TiCl_3$-EG, f) rutile-$TiCl_3$-GL, g) rutile-$TiCl_2$-EG and h) rutile-$TiCl_2$-GL.

Table 3 Computed interaction energy of EG and GL on the $TiCl_2$/$TiCl_3$ terminated anatase/rutile TiO_2 surface.

Structure (Anatase)	**Interaction energy (eV)**	**Structure (Rutile)**	**Interaction energy (eV)**
$TiCl_3$ – EG	-0.79	$TiCl_3$ – EG	-0.96
$TiCl_3$ – GL	-0.66	$TiCl_3$ – GL	-1.77
$TiCl_2$ – EG	0.08	$TiCl_2$ – EG	0.49
$TiCl_2$ – GL	0.15	$TiCl_2$ – GL	0.81

We also consider the Ti-O distances formed between the EG and GL with $TiCl_2$/$TiCl_3$ species, **Table 4,** as well as changes in the Ti-surface distances between $TiCl_3$ and $TiCl_2$ and surface oxygens after the introduction of EG and GL, **Table 5**. We notice that Ti-O bonds formed between EG and GL and the $TiCl_3$ terminated anatase TiO_2 and rutile TiO_2 surfaces are 0.02 Å shorter compared to Ti-O bonds formed between EG and GL with the $TiCl_2$ terminated anatase TiO_2 and rutile TiO_2 surfaces. Ti-O distances between $TiCl_4$ and the surface oxygens also change after the introduction of EG and GL. After the introduction of EG and GL, Ti-O bonds

to the surface are lengthen for 0.02 Å to 0.03 Å in the $TiCl_3$ terminated anatase TiO_2 and rutile TiO_2 surfaces and 0.02 Å to 0.07 Å in the $TiCl_2$ terminated anatase TiO_2 and rutile TiO_2 surfaces. As DFT results suggest that the formation of Ti-O bonds between EG and GL and the $TiCl_2$ species on the anatase TiO_2 and rutile TiO_2 surfaces is energetically unfavourable, in the next calculations we exclude the $TiCl_2$ terminated surfaces.

Table 4 Computed Ti-O distances between EG and GL and the $TiCl_2$/$TiCl_3$ terminated anatase/rutile TiO_2 surface.

Structure (Anatase)	**Ti-O (Å)**	**Structure (Rutile)**	**Ti-O (Å)**
$TiCl_3$ – EG	1.82	$TiCl_3$ – EG	1.80
$TiCl_3$ – GL	1.80	$TiCl_3$ – GL	1.80
$TiCl_2$ – EG	1.84	$TiCl_2$ – EG	1.82
$TiCl_2$ – GL	1.82	$TiCl_2$ – GL	1.82

Table 5 Computed Ti-O distances between $TiCl_2$/$TiCl_3$ species with surface oxygens after the introduction of EG and GL.

Structure (Anatase)	**Ti-O (Å)**	**Structure (Rutile)**	**Ti-O (Å)**
$TiCl_3$ – EG	1.75	$TiCl_3$ – EG	1.76
$TiCl_3$ – GL	1.75	$TiCl_3$ – GL	1.77
$TiCl_2$ – EG	1.80, 1.81	$TiCl_2$ – EG	1.82, 1.82
$TiCl_2$ – GL	1.81, 1.81	$TiCl_2$ – GL	1.83, 1.82

Comparison of upright and flat lying reactions of ethylene glycol (EG) and glycerol (GL) on $TiCl_3$ terminated anatase/rutile TiO_2 surface

Double reactions of EG and GL are investigated by examining the interactions between the TiO_2 surface terminated with $2TiCl_3$ and EG and GL in the upright configuration and in the flat configuration. In the upright configuration, EG and GL bind to titanium sites through one terminal OH group and one HCl molecule is released. In the flat configuration, EG and GL bind through two terminal OH groups with two neighbouring titanium sites and two HCl molecules are released.

Optimised atomic structures of the MLD reactions products of $TiCl_3$ terminated anatase TiO_2 and rutile TiO_2 surfaces with the upright and flat lying EG and GL are shown in **Fig. 4**. The computed energies when EG and GL bind with one titanium site in the upright configuration and with two titanium sites in the flat lying configuration are shown in **Table 6**. The calculated energy for the upright configuration of EG and GL is calculated with reference to the energy of the adsorbed $TiCl_4$ precursor on the relevant surface, while the calculated energy for the flat configuration of EG and GL is with reference to the energy of the corresponding upright structure. This allows us to asses if the double reactions of EG and GL are thermodynamically favourable when reacting with $TiCl_3$ on anatase TiO_2 and rutile TiO_2 surfaces.

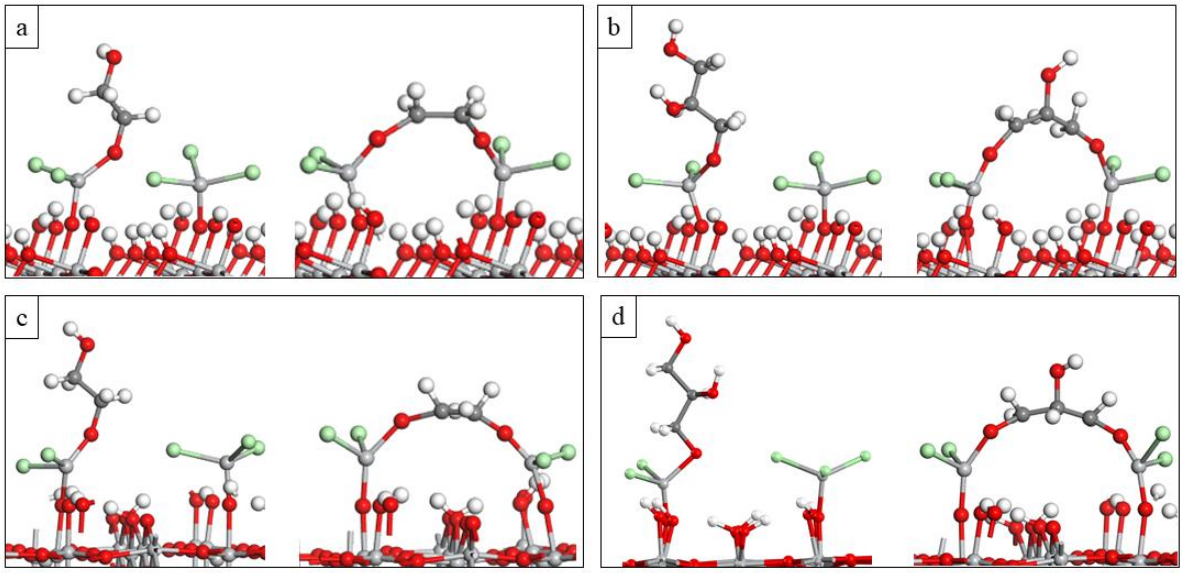


Figure 4 Optimised atomic structure of a) upright and flat EG on the anatase- $2TiCl_3$, b) upright and flat GL on the anatase-$2TiCl_3$, c) upright and flat EG on the rutile-$2TiCl_3$, d) upright and flat GL on the rutile-$2TiCl_3$.

From **Table 6** we see that the EG and GL molecules interact favourably in an upright configuration at the $2TiCl_3$ terminated anatase TiO_2 surface. However, there is a further gain in energy of -0.55 eV for EG and -0.33 eV for GL when the molecules change their configuration from upright to lying flat, and a second HCl molecule is released. These energies show that EG and GL could also undergo double reactions on the anatase TiO_2 surface, although for GL this difference in energy is smaller than for EG.

Table 6 Computed interaction energy of EG and GL in the upright configuration with the $TiCl_3$ terminated anatase/rutile TiO_2 surface. The energy change between the flat (double reaction) and upright configuration is also presented.

Structure (Anatase)	Interaction energy (eV)	Structure (Rutile)	Interaction energy (eV)
$2TiCl_3$ – EG – up	-0.72	$2TiCl_3$ – EG – up	-0.46
$2TiCl_3$ – EG –flat	-0.55	$2TiCl_3$ – EG – flat	0.34
$2TiCl_3$ – GL – up	-0.63	$2TiCl_3$ – GL – up	-0.36
$2TiCl_3$ – GL – flat	-0.33	$2TiCl_3$ – GL – flat	0.33

Similar to Al_2O_3, this phenomenon for EG will reduce the number of OH sites on the surface and this should make the growth of $TiCl_4$-EG films less favourable. However, despite the reduction of OH groups on the surface, terminal oxygen sites of the flat EG can also serve as active sites and they can bind with other $TiCl_4$ molecules in the following cycle, similar to TMA-EG alucones. [2] The GL molecule is a triol with three OH active groups, so even in the case of double reactions for GL, the third OH group is available for further reactions.

The EG and GL molecules interact also favourably in an upright configuration with the $2TiCl_3$ terminated rutile TiO_2 surface, while for their flat lying configuration the overall energy change is slightly endothermic. This shows that in a rutile surface EG and GL could prefer to orient in an upright configuration. For the $2TiCl_3$-EG model, the distance between titanium and oxygen in the Ti-O-CH_2CH_2-O fragment that is formed during one MLD cycle (EG in the upright configuration) is ~4.97 Å. This distance is similar with the achieved GPC of ~ 4.5 Å/cycle - 6 Å/cycle for $TiCl_4$-EG films in a temperature range of 100-120°C on SiO_2 membrane [10] and ~ 4.6 Å/cycle at a the temperature 90°C in Si(100) wafers. [11] We note the relatively low temperature of the titanicone deposition in references [10, 11] which may prevent the double reaction with EG.

For $TiCl_3$-GL model, the distance between titanium and oxygen in the Ti-O-$CH_2CH_2OHCH_2$-O fragment (GL in the upright configuration) is ~6.26 Å. However, the achieved GPC of $TiCl_4$-GL films in experimental work is much smaller, 2.8 Å/cycle at 130°C to 2.1 Å/cycle at 210°C when deposited in Si wafers [11] and 2.2 Å/cycle at 150°C deposited again in Si wafers in another study. [12] The distance between the surface and the available OH group of the flat GL is 4.2 Å and this distance close to the measured GPC of $TiCl_3$-GL films in experimental work. Although the lower GPC of $TiCl_4$-GL films achieved in these experimental studies is most

consistent with a flat lying orientation of GL when deposited in Si surfaces, DFT shows that the desired upright orientation of GL could be energetically favourable on a rutile TiO_2 surface and this provides motivation to develop a low temperature rutile TiO_2/$TiCl_4$-GL process where higher GPCs could be achieved. We note that the experimental data are not immediately comparable since different deposition temperatures are used, with significantly higher temperatures for the GL process compared to the EG process which may favour the flat lying configuration.

In summary, DFT calculations show that while on anatase TiO_2 the organic molecules EG and GL can orient in both configurations, upright and lying flat, in the rutile TiO_2 surface these molecules could prefer more the upright configuration, although the flat lying configuration may also be stabilised. This indicates that the surface can also have an important role on the orientation of the organic species.

The Ti-O distances to the EG and GL in the upright and flat lying configurations are presented in **Table 7**. The computed distances show that the Ti-O bond to the molecules does not change significantly when EG and GL change their configuration from upright to lying flat on the anatase TiO_2 surface (0.01 Å longer). On the other hand, on rutile, the Ti-O bonds to the organic molecules in the flat lying configuration are 0.03 Å to 0.06 Å longer compared to Ti-O bonds of these molecules in the upright configuration. The increment of these bonds when EG and GL change their configuration from upright to lying flat on the rutile TiO_2 surface also indicates the lower stability of these molecules in the flat configuration on the $TiCl_3$ terminated rutile TiO_2 surface.

Table 7 Computed Ti-O distances between EG and GL in the upright and flat laying configuration and the $TiCl_3$ terminated anatase/rutile TiO_2 surface.

Structure (Anatase)	**Ti-O distance (Å)**	**Structure (Rutile)**	**Ti-O distance (Å)**
$TiCl_3$ – EG – up	1.80	$TiCl_3$ – EG – up	1.81
$TiCl_3$ – EG – flat	1.81	$TiCl_3$ – EG – flat	1.84
$TiCl_3$ – GL – up	1.80	$TiCl_3$ – GL – up	1.82
$TiCl_3$ – GL – flat	1.81	$TiCl_3$ – GL – flat	1.88

For the upright EG and GL on the anatase TiO_2 surface, the Ti-O distance between titanium of $TiCl_4$ and the oxygen atom of the anatase TiO_2 surface is 1.77 Å. This distance decreases to 1.75 Å when EG and GL change their configuration to lying flat. For EG in the upright and flat laying configuration on the rutile TiO_2 surface the Ti-O distance between titanium of $TiCl_4$ and the oxygen atom is 1.77 Å. For GL in the upright and flat lying configuration on the rutile TiO_2 surface this distance is 1.76 Å.

Tetrakis(dimethylamido)titanium ($Ti(DMA)_4$) terminated anatase/rutile titanium oxide (TiO_2) and aluminium oxide (Al_2O_3) surface models

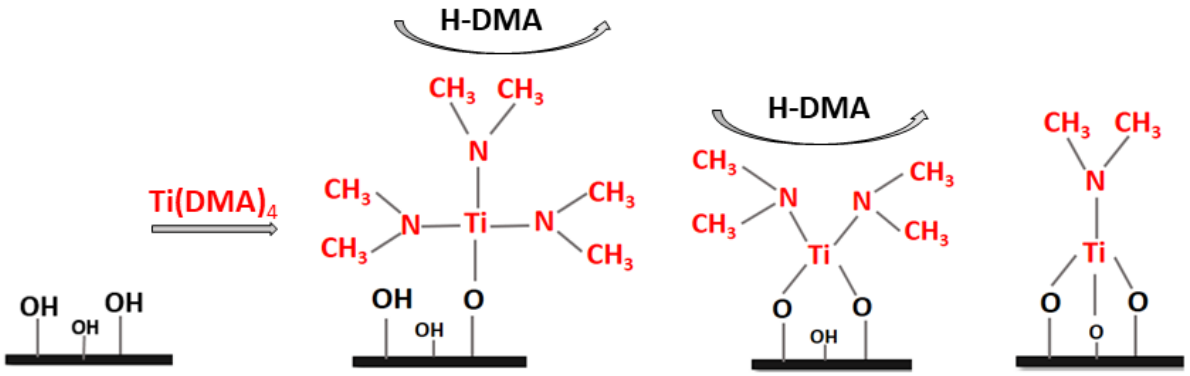
$Ti(DMA)_4$ is another titanium precursor that has been used for the deposition of TiO_2 [13] and TiN [14] ALD films and titanicone MLD film. [8] $Ti(DMA)_4$ is a metalorganic precursor containing Ti-N bonds to the organic ligands, dimethylamino DMA ($N(CH_3)_2$), and with a much larger molecular size when compared to $TiCl_4$. It offers some advantages as a precursor, including the noncorrosive nature of byproducts during ligand elimination, higher reactivity due to the weak Ti-N bonds and good thermal stability. [15]

We performed DFT calculations to study the feasibility of the growth of titanicone films using $Ti(DMA)_4$ and EG or GL as MLD precursors and to investigate the molecular mechanism behind the possible growth. The hydroxylated anatase TiO_2 surface, hydroxylated rutile TiO_2 surface and hydroxylated Al_2O_3 surface were selected as surface models.

In the first step, we calculate the reactivity of $Ti(DMA)_4$ precursor towards the selected surfaces. The calculated interaction energies on the anatase TiO_2, rutile TiO_2 and the Al_2O_3 surfaces are -0.88 eV, -0.74 eV and -1.47 eV, respectively. These energies show that $Ti(DMA)_4$ adsorbs favourably on the three oxide surfaces.

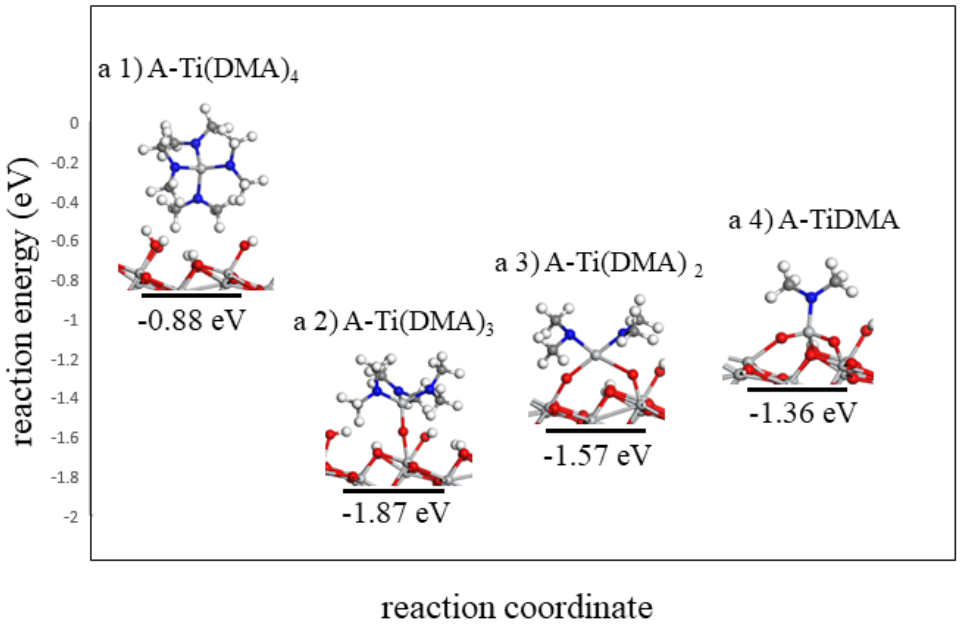
Next, the thermodynamics of the first, second and third ligand loss reactions of $Ti(DMA)_4$ precursor are examined. These reactions take place with a proton transfer from surface OH groups to the DMA ligands of $Ti(DMA)_4$ to form protonated molecules, H-DMA, released as byproducts and the formation of new Ti-O bonds between $Ti(DMA)_4$ and oxygen atoms on the surface. After the third ligand loss reaction, titanium of $Ti(DMA)_4$ is bonded to three surface oxygens and to one DMA ligand that can exchange with one organic molecule during the organic precursor pulse. The coordination number of titanium of the $Ti(DMA)_4$ molecule is

four and remains unchanged during the ligand loss reactions. The ligand loss reaction mechanism of $Ti(DMA)_4$ is presented in **Scheme 2**.



Scheme 2 Schematic representation of ligand loss reactions of tetrakis(dimethylamido) titanium ($Ti(DMA)_4$) inorganic precursor on a hydroxylated surface.

Optimized atomic structures of the anatase TiO_2, rutile TiO_2 and the Al_2O_3 surfaces interacting with $Ti(DMA)_4$ and after the elimination of the first, second and third ligand of $Ti(DMA)_4$ are presented in **Fig. 5.** The computed adsorption and ligand loss energies of $Ti(DMA)_4$ on the selected surfaces are presented in **Table 8.** The energies for the ligand loss reactions are calculated relative to the first model of $Ti(DMA)_4$ interacting with the surface, and present an overall reaction energy. Ligand loss energies show that the overall energy for $Ti(DMA)_4$ to lose DMA ligands and bind on either TiO_2 surface or Al_2O_3 surface is favourable.



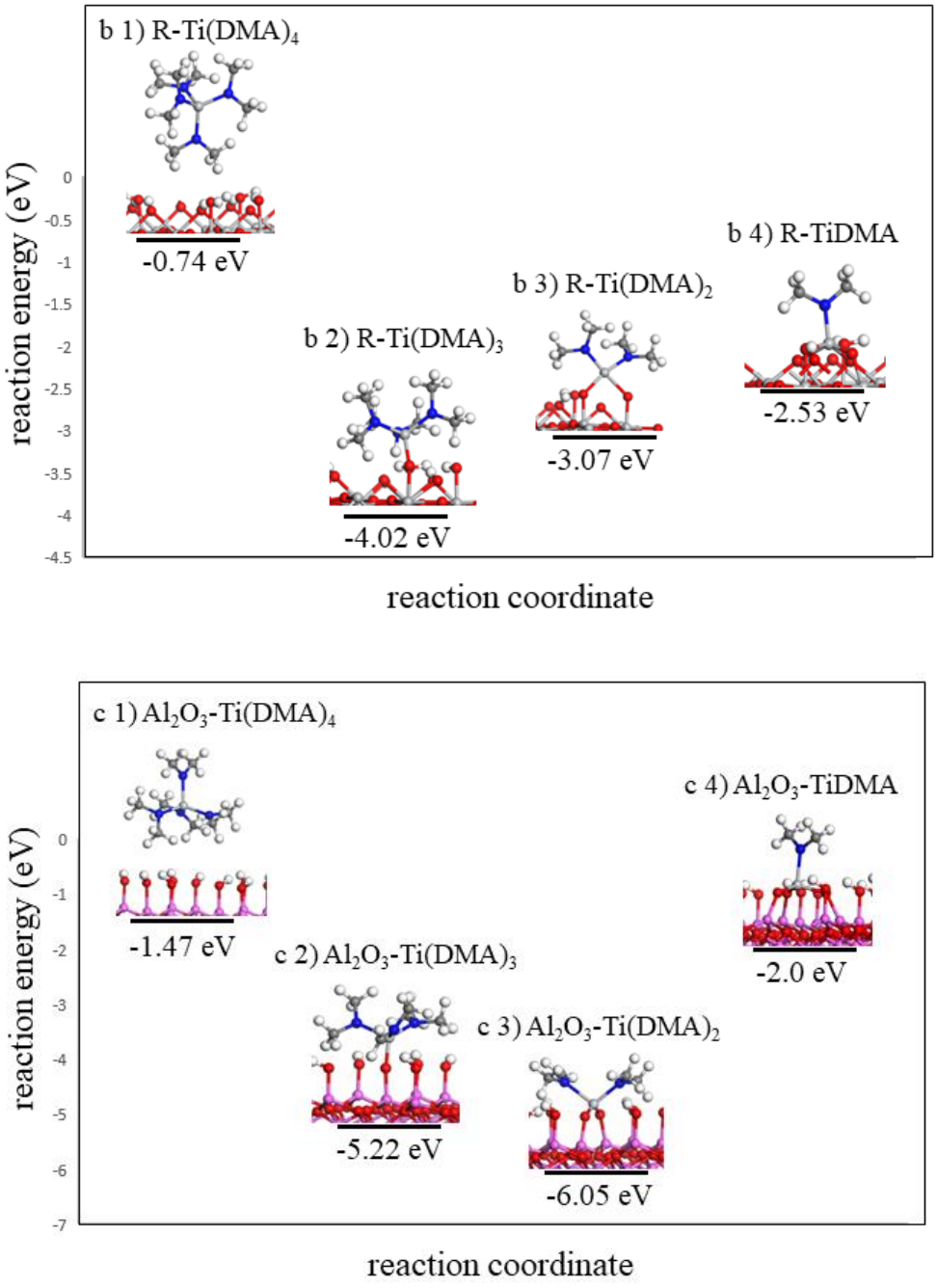


Figure 5 The plotted ligand loss reactions of $Ti(DMA)_4$ on the anatase/rutile TiO_2 surface and Al_2O_3 surface. Optimised atomic structure of a1) $Ti(DMA)_4$ interacting with the anatase TiO_2 surface, a2) $Ti(DMA)_3$ terminated anatase TiO_2 surface, a3) $Ti(DMA)_2$ terminated anatase TiO_2 surface, a4) TiDMA terminated anatase TiO_2 surface, b1) $Ti(DMA)_4$ interacting with the rutile TiO_2 surface, b2) $Ti(DMA)_3$ terminated rutile TiO_2 surface, b3) $Ti(DMA)_2$ terminated rutile TiO_2 surface, b4) TiDMA terminated rutile TiO_2 surface, c1) $Ti(DMA)_4$ interacting with the Al_2O_3 surface, c2) $Ti(DMA)_3$ terminated Al_2O_3 surface, c3) $Ti(DMA)_2$ terminated Al_2O_3 surface and c4) TiDMA terminated Al_2O_3 surface.

Table 8 Computed adsorption and ligand loss energy of $Ti(DMA)_4$ on the anatase/rutile TiO_2 surface and Al_2O_3 surface.

Structure (Anatase)	**Interaction energy (eV)**	**Structure (Rutile)**	**Interaction energy (eV)**	**Structure (Al_2O_3)**	**Interaction energy (eV)**
$Ti(DMA)_4$	-0.88	$Ti(DMA)_4$	-0.74	$Ti(DMA)_4$	-1.47
$Ti(DMA)_3$	-1.87	$Ti(DMA)_3$	-4.02	$Ti(DMA)_3$	-5.22
$Ti(DMA)_2$	-1.57	$Ti(DMA)_2$	-3.07	$Ti(DMA)_2$	-6.05
TiDMA	-1.36	TiDMA	-2.53	TiDMA	-2

When we compare these energies to those calculated for $TiCl_4$ interacting and binding on the same selected surfaces, we see that $Ti(DMA)_4$ adsorbs and binds more favourably with the surfaces as the calculated reaction energies are more negative. This is consistent with bond dissociation energy values for the breakage of the Ti-Cl and Ti-N bonds, 494 kJ/mol and 464 kJ/mol, respectively, which show that the Ti-Cl bond is stronger and thus more difficult to break.

The overall reaction energy which includes the interaction of $Ti(DMA)_4$ with the surface and the three ligand loss reactions is the largest on the rutile TiO_2 surface, -2.53 eV, which is -0.53 eV larger when compared to the Al_2O_3 surface and -1.73 eV larger when compared to the anatase TiO_2 surface. The new Ti-O bonds of $Ti(DMA)_4$ to the Al_2O_3 surface are 0.03-0.08 Å shorter, when compared to those formed between $Ti(DMA)_4$ and the anatase TiO_2 surface or rutile TiO_2 surface, **Table 9**.

Table 9 Computed Ti-O distances between $Ti(DMA)_4$ and the anatase/rutile TiO_2 and Al_2O_3 surfaces.

Structure (Anatase)	**Ti-O (Å)**	**Structure (Rutile)**	**Ti-O (Å)**	**Structure (Al_2O_3)**	**Ti-O (Å)**
$(DMA)_3$	1.91	$(DMA)_3$	1.79	$(DMA)_3$	1.73
$(DMA)_2$	1.91, 1.91	$(DMA)_2$	1.82, 1.85	$(DMA)_2$	1.79, 1.80
DMA	1.91, 1.98. 2.03	DMA	1.86, 1.86, 2.27	DMA	1.83, 1.83, 1.8

In order to investigate double reactions of EG and GL we build also the surface models after the adsorption of two $Ti(DMA)_4$ molecules. The reactions when a second $Ti(DMA)_4$ molecule

is adsorbed are associated with the release of three H-DMA molecules as byproducts and the surfaces are left covered with two TiDMA species, anatase-2TiDMA, rutile-2TiDMA and Al_2O_3-2TiDMA. Calculated energetics for the adsorption of the second $Ti(DMA)_4$ precursors are -1.05 eV for the anatase TiO_2 surface, -1.29 eV for the rutile TiO_2 surface, -2.06 eV for the Al_2O_3 surface. The distance between titanium atoms of the two TiDMA species is 7.2 Å on the anatase TiO_2 surface and rutile TiO_2 surface and 7.1 Å on the Al_2O_3 surface.

Reactions between organic precursors and TiDMA terminated anatase/rutile TiO_2 and Al_2O_3 surface

Next, we analyse MLD reactions using EG and GL as organic reactants which are modelled in both upright and flat lying configurations. Similar to the reaction between $TiCl_4$ and EG or GL, the reaction between $Ti(DMA)_4$ and EG or GL requires the transfer of one proton from the terminal OH group of the organic molecule to one DMA ligand of $Ti(DMA)_4$ to release a H-DMA molecule as a byproduct coupled with the formation of a new Ti-O bond between titanium and the organic molecule. **Fig. 6** shows the optimized atomic structures after the introduction of one EG and GL molecules and the loss of one H-DMA byproduct.

The overall energy change for the reactions between the TiDMA terminated anatase TiO_2, rutile TiO_2 and Al_2O_3 surfaces with EG and GL is presented in **Table 10**. Calculated energetics show that the Ti-O bond formation with EG and GL, with release of H-DMA, is favourable on all surfaces. The overall interaction energy is largest on anatase TiO_2 followed by rutile TiO_2.

Ti-O distances between titanium and the organic molecules are shown in **Table 11.** Ti-O bonds formed between EG and GL with the TiDMA terminated anatase TiO_2 and rutile TiO_2 surfaces are 0.06 Å to 0.08 Å shorter when compared to those formed between the EG and GL and the TiDMA terminated Al_2O_3 surface, which is consistent with the more favourable interaction energies.

We also examine the change in the Ti-O distances to the surface oxygens after the introduction of the EG and GL, and these are presented in **Table 12**. The computed Ti-O distances show that after the introduction of the EG and GL Ti-O bonds to the surface oxygens undergo negligible changes, indicating that the EG and GL will not affect the stability of the systems.

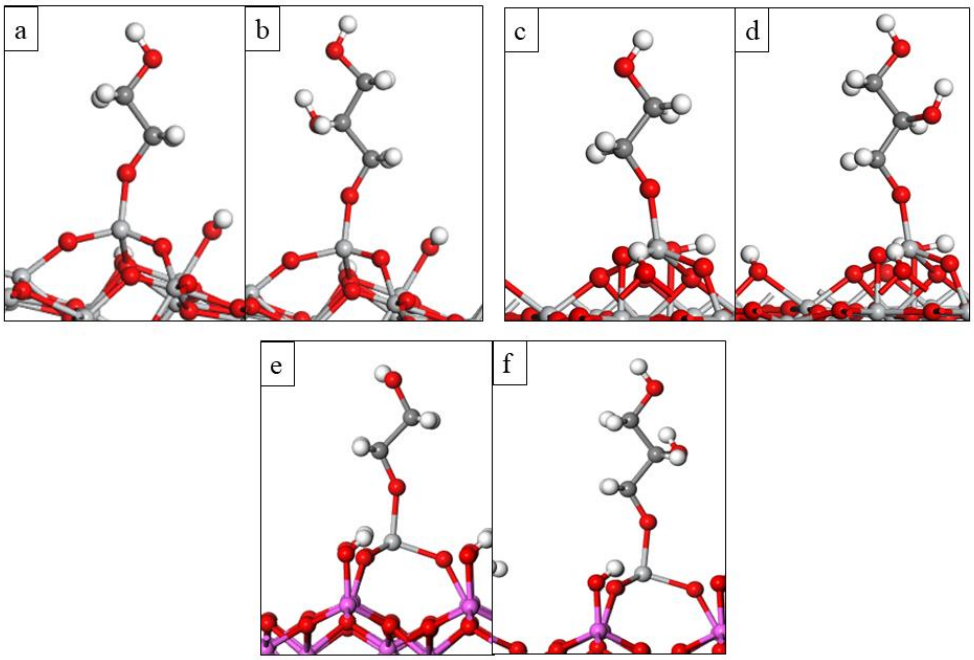


Figure 6 Optimised atomic structure of a) anatase-TiDMA-EG, b) anatase-TiDMA-GL, c) rutile-TiDMA-EG, d) rutile-TiDMA-EG, e) Al_2O_3-TiDMA-EG and f) Al_2O_3-TiDMA-GL.

Table 10 Computed interaction energy of EG and GL on the TiDMA terminated anatase/rutile TiO_2 and Al_2O_3 surfaces.

Structure (Anatase)	**Interaction energy (eV)**	**Structure (Rutile)**	**Interaction energy (eV)**	**Structure (Al_2O_3)**	**Interaction energy (eV)**
TiDMA – EG	-3.42	TiDMA – EG	-2.98	TiDMA – EG	-1.75
TiDMA – GL	-3.31	TiDMA – GL	-2.89	TiDMA – GL	-1.60

Table 11 Computed Ti-O distances between EG and GL with the TiDMA terminated anatase/rutile TiO_2 and Al_2O_3 surfaces.

Structure (Anatase)	**Ti-O (Å)**	**Structure (Rutile)**	**Ti-O (Å)**	**Structure (Al_2O_3)**	**Ti-O (Å)**
DMA – EG	1.80	DMA – EG	1.80	DMA – EG	1.86
DMA – GL	1.79	DMA – GL	1.80	DMA– GL	1.87

Table 12 Computed Ti-O distances between TiDMAT and the anatase/rutile TiO_2 and Al_2O_3 surfaces after the introduction of EG and GL.

Structure (Anatase)	**Ti-O (Å)**	**Structure (Rutile)**	**Ti-O (Å)**	**Structure (Al_2O_3)**	**Ti-O (Å)**
DMA – EG	1.90, 1.98, 2.0	DMA – EG	1.86, 1.87, 2.23	DMA – EG	1.84, 1.85, 1.85
DMA – GL	1.91, 1.98, 2.0	DMA – GL	1.86, 1.87, 2.21	DMA– GL	1.83, 1.85, 1.85

Comparison of upright and flat lying reactions of ethylene glycol (EG) and glycerol (GL) on TiDMA terminated anatase/rutile TiO_2 and Al_2O_3 surface

We investigate also the double reactions of EG and GL on the anatase-2TiDMA surface, rutile-2TiDMA surface and Al_2O_3-2DMA, where EG and GL are modelled in the upright and flat lying configurations. In the upright configuration organic molecules bind to titanium sites through one terminal OH group and one H-DMA molecule is released while in the flat configuration organic molecules bind through two terminal OH groups with two neighbouring titanium sites and two H-DMA molecules are released. **Fig. 7** shows the optimised atomic structures of the MLD reaction products of 2TiDMA terminated anatase TiO_2, rutile TiO_2 and Al_2O_3 surfaces with the upright and flat lying EG and GL. Calculated energetics for the reactions of EG and GL in the upright and flat laying configuration with the 2TiDMA terminated surfaces are shown in **Table 13**.

Calculated energetics for the reactions between upright EG and GL with the 2TiDMA terminated anatase TiO_2, rutile TiO_2 and Al_2O_3 surfaces are negative, meaning that the reactions are exothermic and therefore favourable. The energies for the reactions between the upright EG and GL and the 2TiDMA terminated anatase TiO_2, rutile TiO_2 and Al_2O_3 surfaces are calculated relative to the energy for the adsorption of two $Ti(DMA)_4$ molecules on the relevant surface. The energies for the flat configuration are calculated relative to the upright structures of EG and GL. A negative energy gain was calculated for all reactions when EG and GL change their configuration from upright to flat lying and one H-DMA molecule is released, regardless of the surface.

Calculated energetics show that while the EG and GL can bind to the titanium sites via formation of Ti-O bonds and loss of H-DMA, it is most favourable for the organic precursors to lie flat and create the double reactions through the two terminal OH groups. This phenomenon removes all active sites for EG and the growth will be less favourable while GL

has an extra OH group compared to EG which reacts with $Ti(DMA)_4$ in the next cycle and the growth proceeds.

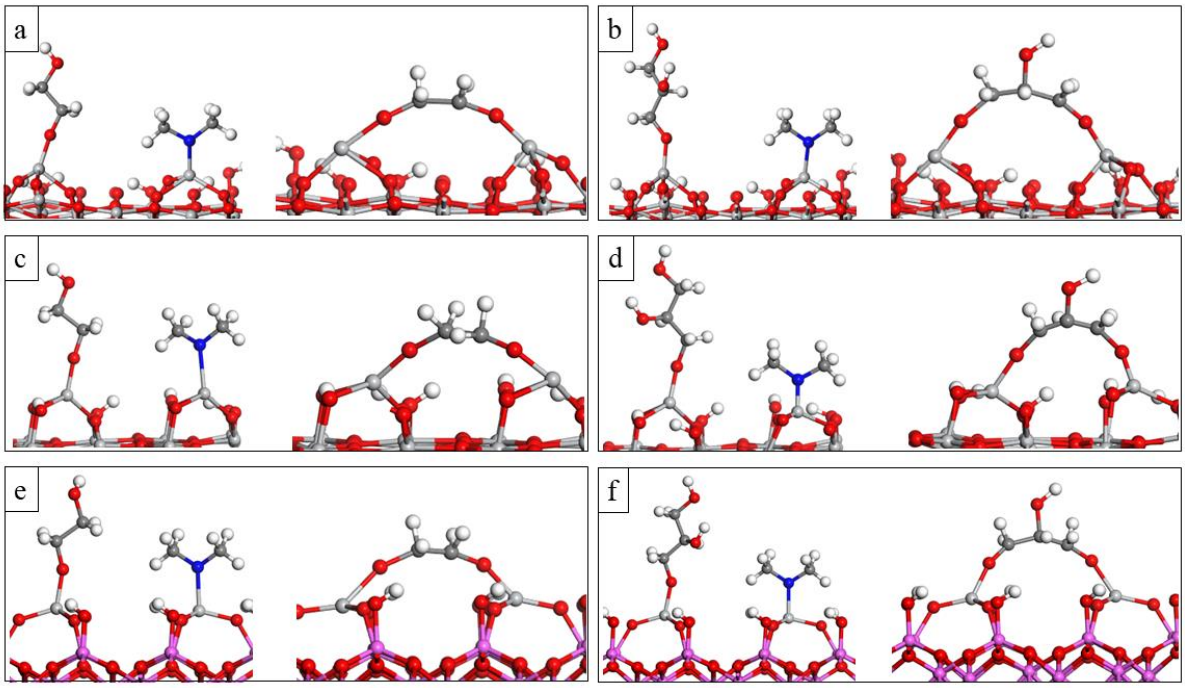


Figure 7 Optimised atomic structure of a) upright and flat EG on the anatase-2TiDMA, b) upright and flat GL on the anatase-2TiDMA, c) upright and flat EG on the rutile-2TiDMA, d) upright and flat GL on the rutile-2TiDMA, e) upright and flat EG on the Al_2O_3-2TiDMA and f) upright and flat GL on the Al_2O_3-2TiDMA.

Calculated energetics suggest that organic molecules EG and GL combined with $Ti(DMA)_4$ in a anatase TiO_2, rutile TiO_2 and Al_2O_3 surface behave similarly as when combined with $Ti(DMA)_4$ on a Si substrate. [8] Experimental data in reference [8] shows that for $Ti(DMA)_4$-EG films deposited on a Si substrate in a temperature range 80-150°C the growth starts but it stops after 5-10 cycles, and this most probably due to the favourable double reactions of EG molecules with the titanium species. For $Ti(DMA)_4$-GL films the growth proceeds even when the molecule reacts twice with the surface due to the extra OH group which reacts with $Ti(DMA)_4$ in the next cycle. However, although the growth of $Ti(DMA)_4$-GL films proceeds, these double reactions lead to small GPCs, 0.9 Å/cycle - 0.2 Å/cycle when deposited in a Si substrate in a temperature range 80-160°C. The stability and GPC of the $Ti(DMA)_4$-GL based film may also depend on the strength of interaction with GL, which is less favourable than with EG.

The Ti-O distances to the EG and GL molecules in the upright and flat lying configurations are presented in **Table 14.** The computed Ti-O bonds to the organic molecules in the anatase TiO_2 and rutile TiO_2 surfaces are lengthen from 0.05 Å to 0.25 Å when EG and GL change their configuration from upright to lying flat.

In summary, DFT calculations show that the chemistry of the organic molecules will depend on the inorganic precursor used and on the surface onto which the films are deposited. We see that EG and GL prefer to lie flat when combined with $Ti(DMA)_4$ on the anatase TiO_2, rutile TiO_2 and Al_2O_3 surfaces and with $TiCl_4$ in a anatase TiO_2 surface but they do not prefer to lie flat when combined with $TiCl_4$ on a rutile TiO_2 surface. The interactions with $TiCl_4$ precursor are also less favourable than with $Ti(DMA)_4$, partially explained by the strong Ti-Cl bond compared to Ti-N.

Table 13 Computed interaction energy of EG and GL in the upright configuration with the 2TiDMA terminated anatase/rutile TiO_2 and Al_2O_3 surfaces. The energy change between the flat (double reaction) and upright configuration is also presented.

Structure (Anatase)	**Interaction energy (eV)**	**Structure (Rutile)**	**Interaction energy (eV)**	**Structure (Al_2O_3)**	**Interaction energy (eV)**
2TiDMA – EG – up	-1.44	2TiDMA – EG – up	-1.65	2TiDMA – EG – up	-1.73
2TiDMA – EG – flat	-0.32	2TiDMA – EG – flat	-0.20	2TiDMA – EG – flat	-1.6
2TiDMA – GL – up	-1.40	2TiDMA – GL – up	-1.61	2TiDMA – GL – up	-1.81
2TiDMA – GL – flat	-0.68	2TiDMA – GL – flat	-0.90	2TiDMA – GL – flat	-1.3

Table 14 Computed Ti-O distances between EG and GL in the upright and flat laying configuration and the TiDMA terminated anatase/rutile TiO_2 and Al_2O_3 surfaces.

Structure (Anatase)	**Ti-O (Å)**	**Structure (Rutile)**	**Ti-O (Å)**	**Structure (Al_2O_3)**	**Ti-O (Å)**
DMA – EG – up	1.80	DMA – EG – up	1.79	DMA – EG – up	1.87
DMA – EG – flat	1.88	DMA – EG – flat	1.85	DMA – EG – flat	2.08
DMA – GL – up	1.79	DMA – GL – up	1.79	DMA – GL – up	1.86
DMA – GL – flat	1.86	DMA – GL – flat	1.84	DMA – GL – flat	2.11

5.2 Conclusion

In this chapter, we have used first principles density functional theory (DFT) to investigate the atomistic mechanism of the growth of titanium containing hybrid films known as "titanicones" deposited by MLD. We investigated in detail the chemistry of the MLD process between the titanium tetrachloride ($TiCl_4$) and tetrakis(dimethylamido) titanium *(*$Ti(DMA)_4$) inorganic precursors and ethylene glycol (EG) and glycerol (GL) organic molecules. We used anatase TiO_2, rutile TiO_2 and Al_2O_3 surface models. Through DFT we calculated the reactivity of $TiCl_4$ and $Ti(DMA)_4$ inorganic precursors towards the selected surfaces and towards EG and GL organic molecules and predicted the preferred orientation of these organic molecules when combined with $TiCl_4$ and $Ti(DMA)_4$ in the selected syrfaces. Calculated energetics showed that while $TiCl_4$ adsorbs and binds favourably with the anatase TiO_2 and rutile TiO_2 surfaces via Ti-O bonds and release of HCl, the adsorption on the Al_2O_3 surface is not favourable. Ligand loss reactions of $TiCl_4$ on the anatase TiO_2 and rutile TiO_2 surface are favourable, although there is a notable energy cost for losing the second chlorine ligand from surface bound $TiCl_3$. Double reactions of EG and GL molecules with $TiCl_3$ species are also closely explored. DFT findings show that these molecules can bind with $TiCl_3$ species in the anatase TiO_2 surface in the upright configuration with one terminal OH group and in the flat configuration with two terminal OH groups. In the rutile TiO_2 surface on the other hand, the preferred orientation of EG and GL molecules is upright. Therefore, we consider the rutile TiO_2 surface as a suitable surface for the growth of $TiCl_4$-EG and $TiCl_4$-GL titanicone films where the desired GPCs could be achieved. DFT calculations show that $Ti(DMA)_4$ also interacts and binds favourably with the anatase TiO_2, rutile TiO_2 and the Al_2O_3 surface via Ti-O bonds. The ligand loss reactions of $Ti(DMA)_4$ are associated with the release of H-DMA byproducts. A higher reactivity of $Ti(DMA)_4$ compared to $TiCl_4$ was calculated and this is most probably due to the stronger Ti-Cl bonds present in $TiCl_4$ compared to Ti-N bonds present in $Ti(DMA)_4$. We show that EG and GL bind favourably with titanium species of $Ti(DMA)_4$ via Ti-O bonds and release of H-DMA byproducts. However, reaction energetics indicate that these molecules can lie flat and create the unwanted double reactions through the reaction of the two terminal OH groups with the surface fragments. For EG this phenomenon removes active OH groups from the surface and the growth will be less favourable while for GL the third OH group is available and growth proceeds. This analysis supports experimental data on $Ti(DMA)_4$-EG and $Ti(DMA)_4$-GL film growth and clarifies why for the $Ti(DMA)_4$-EG process, the growth stops after 5-10 cycles while for the $Ti(DMA)_4$-GL process, the growth proceeds. [8]

5.3 References

1. J. Kint, F. Mattelaer, S. S. T. Vandenbroucke, A. Muriqi, M. M. Minjauw, M. Nisula, Ph. M. Vereecken, M. Nolan, J. Dendooven, Ch. Detavernier, *Chemictry of Materials*, **2020**, 32, 4451–4466.
2. A. Muriqi, M. Nolan, *Dalton Transactions*, **2020**, 49, 8710–8721.
3. A. Muriqi, M. Karppinen, M. Nolan, *Dalton Transactions*, **2021**, 50, 17583–17593.
4. P. Kaur, A. Muriqi, J-L Wree, R. Ghiyasi, M. Safdar, M. Nolan, M. Karppinen, A. Devi, *Dalton Transactions*, **2022**, 51**,** 5603–5611.
5. J. Liu, S. Saedy, R. Verma, J. R. Ommen, M. Nolan, *ChemRxiv*, **2020**, 1–44.
6. G. R. Jenness, J. Seiter, M. K. Shukla, *Physical Chemistry Chemical Physics*, **2018**, 20, 18850–18861.
7. S. Ali, T. Juntunen, S. Sintonen, O. M. E. Ylivaara, R. L. Puurunen, H. Lipsanen, I. Tittonen, S-P. Hannula, *Nanotechnology*, **2016**, 27, 445704.
8. K. Kerckhove, F. Mattelaer, D. Deduytsche, P. M. Vereecken, J. Dendooven, Ch. Detavernier, *Dalton Transaction*, **2016**, 45, 1176–1184.
9. A. Tanskanen, P. Sundberg, M. Nolan, M. Karppinen, *Thin Solid Films*, **2021**, 736, 138896.
10. S. Ishchuk, D. H. Taffa, O. Hazut, N. Kaynan, R. Yerushalmi, *ACS Nano*, **2012**, 6, 7263–7269.
11. A. I. Abdulagatov, R. A. Hall, J. L. Sutherland, B. H. Lee, A. S. Cavanagh, S. M. George, *Chemistry of Materials*, **2012**, 24, 2854–2863.
12. A. I. Abdulagatov, K. E. Terauds, J. J. Travis, A. S. Cavanagh, R. Raj, S. M. George, *The Journal of Physical Chemistry C*, **2013**, 117, 17442–17450.
13. Q. Xie, Y-L. Jiang, Ch. Detavernier, D. Deduytsche, R. L. V. Meirhaeghe, G-P. Ru, B-Z. Li, X-P. Qu, *Journal of Applied Physics*, **2007**, 102, 083521.
14. D. Longrie, D. Deduytsche, J. Haemers, P. F. Smet, K. Driesen, Ch. Detavernier, *ACS Applied Materials and Interfaces*, **2014**, 6, 7316–7324.
15. B. Kim, N.Lee, S. Park, T. Park, J. Songa, S. Han, H. Park, D. Lee, H. Kim, H. Jeon, *Journal of Alloys and Compounds*, **2021**, 857, 157931.

Chapter 6

Modelling of Mg, Ce and chitin-based hybrid films

6.1 Introduction

This chapter presents the results of combined experimental and computational studies on new magnesium, cerium and chitin based hybrid inorganic-organic films deposited by molecular layer deposition (MLD). The combination of computation and experimental data gives a comprehensive and cohesive analysis of the growth mechanisms of the deposited MLD films. For completeness, we also include a short discussion of the chemistry of these hybrid films. This work demonstrates the ability of density functional theory (DFT) to predict and rationalise mechanisms of deposition of hybrid materials.

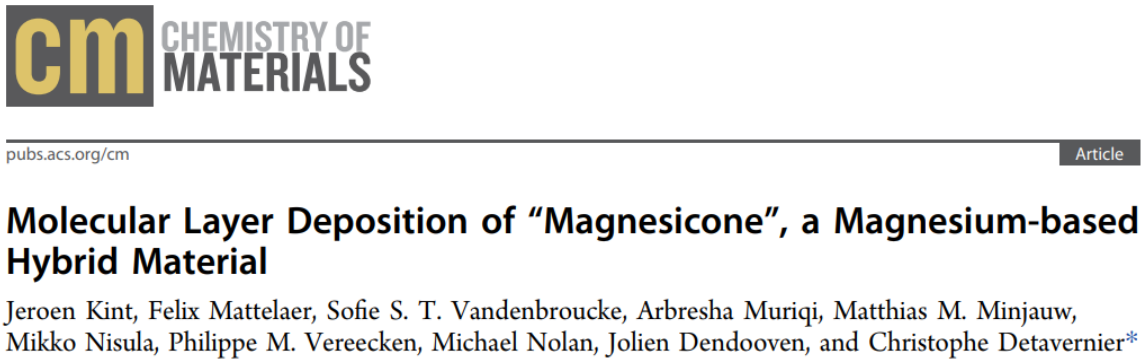
In **Section 6.2** a new type of magnesium containing MLD films is described. Using bis-(methylcyclopentadienyl)magnesium (Mg-$(MeCp)_2$) as a metal source and ethylene glycol (EG) or glycerol (GL) as organic reactants, a "magnesicone" film is deposited. My first principles DFT calculations were employed to explore in detail the reaction mechanisms, energetics and especially the role of the organic precursors EG and GL on the growth of these hybrid films.

Section 6.3 presents a new MLD processes for cerium containing hybrid thin films using the highly reactive Ce (III) guanidinate precursor, $Ce(dpdmg)_3$, as a metal source and organic reactants composed of rigid backbones, terephthalic acid (TPA) and hydroquinone (HQ) for the growth of the respective hybrid films. My DFT calculations were employed for a better understanding of the reaction mechanisms during the growth of the ceria hybrid films. DFT was also used to predict the oxidation state of cerium in the film which was further confirmed by X-ray photoelectron spectroscopy (XPS).

Section 6.4 discusses the development of an entirely new class of hybrid inorganic-organic metallochitin thin films by applying MLD. The monosaccharide N-Acetyl-D-mannosamine (ManNAc) was coupled with trimethylaluminum (TMA) or titanium tetraisopropoxide (TTIP) to obtain the respective alumochitin or titanochitin thin films. DFT calculations were employed to understand the growth mechanism of the deposited alumichitin and titanochitin MLD films.

6.2 Modelling of Magnesicone films

This work was published in the paper "***Molecular Layer Deposition of "Magnesicone", a Magnesium-based Hybrid Material***" in Chemistry of Materials. [1]



DOI: https://doi.org/10.1021/acs.chemmater.9b05116

6.2.1 Results

Magnesicone films were deposited using bis-(methylcyclopentadienyl) magnesium (Mg-$(MeCp)_2$) as metal source and ethylene glycol (EG) or glycerol (GL) as organic reactants on a oxide-covered Si substrate. **Fig. 1** shows the chemical structures of the Mg-$(MeCp)_2$, EG and GL precursors.

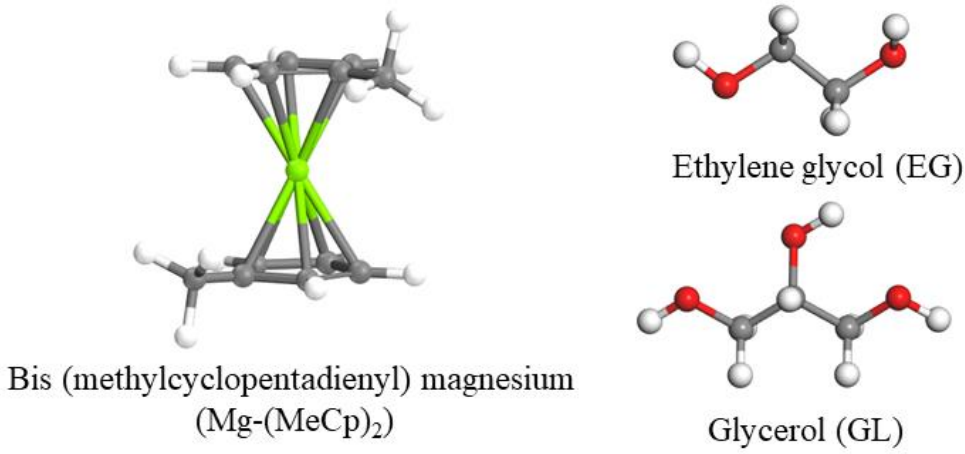


Figure 1 Molecular structure of bis (methylcyclopentadienyl) magnesium (Mg-$(MeCp)_2$), ethylene glycol (EG) and glycerol (GL) precursors. Green-Mg, red-O, grey-C, white-H.

6.2.1.1 Selected experimental results (Ghent University)

MLD process development

A standard dosage time of 10 s was chosen for the $Mg(MeCp)_2$, EG, and GL precursors. The chamber was pumped down for 60 s after every exposure to avoid CVD-type reactions. The substrate was first exposed to 100 pulses of $Mg(MeCp)_2$ in the absence of any reactant pulses and next, 100 cycles of both the magnesicone processes were given.

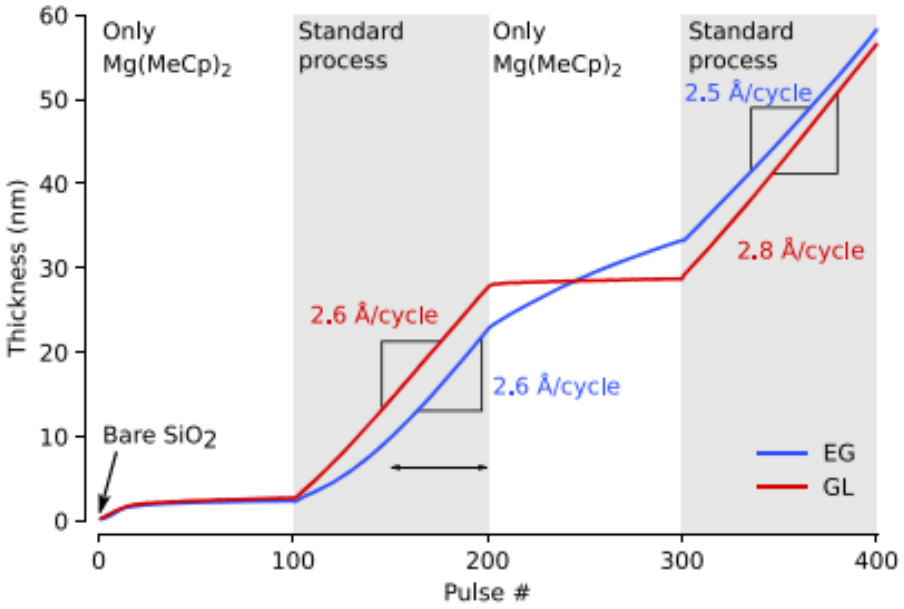


Figure 2 Growth profiles for 100 pulses $Mg(MeCp)_2$, followed by 100 cycles of the standard process, followed by 100 pulses $Mg(MeCp)_2$, followed by 100 cycles of the standard process, for both the EG and GL based process.

The EG precursor shows some growth inhibition, but after 50 cycles it reaches the GPC of 2.6 Å/cycle. The GL precursor immediately shows this GPC. Subsequently, another 100 pulses of $Mg(MeCp)_2$ without reactant were given, on the previously deposited magnesicone. As expected for a typical ALD or MLD process, the GL based process showed no additional growth. However, the EG process showed a continuous, albeit decreasing GPC. A possible explanation for this is that a reservoir-like effect, as reported earlier for ALD [2, 3] and MLD [4, 5] films involving EG (instead of water) takes place and unbound EG gets incorporated in the film during film growth, which then reacts when coming into contact with the $Mg(MeCp)_2$. When the standard process is now performed again, the growth continues as expected for both magnesicone types. This observation is presented in **Fig. 2**. For both magnesicone types, growth is observed in the investigated temperature window of 100°C to 250°C, with a

maximum in the GPC at 125°C of 2.5 Å/cycle for the EG based process and 2.8 Å/cycle for the GL based process. The GPCs at higher temperatures drop off, which is typical behaviour of MLD processes. [6-8] The decrease in GPC with increasing temperature is more pronounced for the EG based process compared to the GL based process, **Fig. 3.**

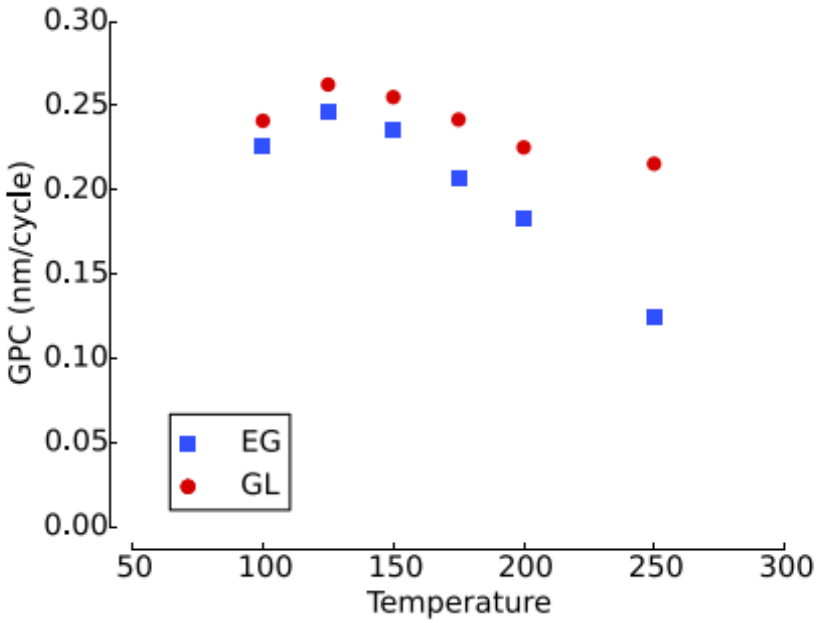


Figure 3 Temperature dependence of the growth per cycle (GPC) for both magnesicone processes between 100 and 250°C using the standard pulsing and pumping times.

In situ mass spectrometry (MS) characterisation

The reaction mechanism of the GL/$Mg(MeCp)_2$ process was investigated using in situ MS (**Fig. 4**). The most prominent indication toward unravelling the reaction mechanism are the fragments of the $Mg(MeCp)_2$ ligands, as for example the m/z = 79 related to methylcyclopentadienyl (HCpMe). These not only are detected during the $Mg(MeCp)_2$ pulses but also arise during the GL pulses, indicative of (a) chemisorption of the $Mg(MeCp)_2$ molecule on the OH surface during the $Mg(MeCp)_2$ pulse and (b) ligand exchange reactions during the GL pulses. In both cases, HCpMe release is expected and observed.

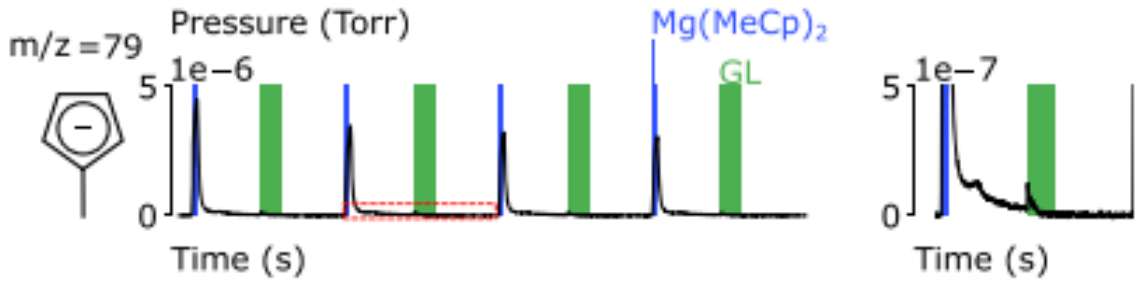


Figure 4 Mass spectrometry during the initial four cycles of a 5−60/ 20−60 GL/$Mg(MeCp)_2$ process for a mass-over-charge ratio of 79, related to methylcyclopentadienyl. The regions shaded blue represent the $Mg(MeCp)_2$ pulses, the regions shaded in green represent the GL pulses. The area highlighted by the red boxes is enlarged on the right for clarity.

X-ray reflectometry (XRR), spectroscopic ellipsometry (SE), X-ray photoelectron spectroscopy (XPS) characterisation

Both types of the magnesicone films were characterized using XRR, SE, and XPS to determine their density, optical properties and composition, respectively. The results are listed in **Table 1**. The GL films show a lower density and refractive index, which could indicate more carbon (and by extension, hydrogen) into the films. XPS shows that EG grown magnesicone contain about 43 at. % C, 12 at. % Mg, and 45 at. % O at the surface and this composition matches rather well with a 1:1 ratio of magnesium to EG precursor components into the films. A perfect magnesium alkoxide like structure would have a formula unit as $MgC_2O_2H_x$, that is, -$MgOCH_2CH_2O$- with 40 at % C, 20 at. % Mg, and 40 at. % O, which is close to the observed values. For GL grown magnesicone, about 46 at. % C, 11 at. % Mg, and 43 at. % O is found. The atomic ratios match rather well with a 3:2 ratio of magnesium to GL precursor components which is expected when balancing the charges of the reaction. This results again in the formula unit MgC_2O_2Hx, identical to the EG based films.

Table 1 Properties of Both magnesicone types deposited at 125°C

			XPS		
	density (g/cm^3)	refractive index at 632.8nm	at % C	at % Mg	at % O
EG	1.8	1.46	43	12	45
GL	1.6	1.41	46	11	43

Possible applications of magnesicone films

Two possible applications are envisioned for these magnesicone films. On the one hand, they can be used as component for self-sealing water barrier coatings in combination with a ceramic metal oxide film such as ALD Al_2O_3. For this application, three key properties were investigated. First, the desiccant properties and associated swelling of the films were evaluated, in order to slow down water transmission and act as a component of an ALD/MLD multilayer in water barrier films. From FTIR, a clear water uptake was observed in the EG grown films, associated with $MgCO_3$ formation. This water uptake was accompanied by a thickness increase of about 10%. The GL grown films on the other hand showed no carbonate formation, and a slower water uptake. In addition, the possibility to overcoat with ALD Al_2O_3 was tested on the EG based magnesicone. It was found that during initial growth the EG stored in the film reservoir reacted with the TMA precursor, potentially forming an "alucone" interface, followed by a slow Al_2O_3 ALD growth.

A second potential application is porous and lithium stable MOx frameworks, for example, as a backbone for solid composite electrolyte (SCE) films. For this application, the transformation from the hybrid magnesicone to a porous magnesium containing framework is critical. Calcining of the GL based magnesicone did not lead to porous films. Rather than carbon removal, the carbon is transformed into carbonate species, which cannot be removed by the calcination treatment. However, it was shown that by calcining the EG based magnesicone, porous MgO films could be obtained with porosities between 27.4 and 44.7%, as determined by ellipsometric porosimetry (EP). The porosity clearly depended on the ramp (both heating and cooling) rates. Slow annealing allows the porous MgO films to react with ambient moisture, leading to a lower porosity due to "clogging" of the pores and the formation of magnesium hydroxide, whereas faster annealing (≥400 °C) can cause a collapse of the pores, resulting in nonporous films. These functionally relevant tests demonstrate the potential of magnesicone films, making it a promising material for future applications.

6.2.1.2 Computational results

Based on the experimental results in **Section 6.2.1.1** and the reaction mechanisms previously elucidated in a MgO ALD process using water and magnesium bis-(ethylcyclopentadienyl) $Mg(EtCp)_2$, [9] which is chemically very similar to the $Mg(MeCp)_2$ precursor, we proposed

the following typical ligand exchange reaction mechanism for the GL process in which * denotes a surface species.

$$OH^* + Mg(MeCp)_2 \rightarrow O{-}MgCpMe^* + HCpMe \quad (1)$$

$$MgCpMe^* + HOCH_2CHOHCH_2OH \rightarrow Mg{-}OCH_2CHOHCH_2OH^* + HCpMe \quad (2)$$

$$2MgCpMe^* + HOCH_2CHOHCH_2OH \rightarrow Mg{-}OCH_2CHOHCH_2O{-}Mg^* + 2HCpMe \quad (3)$$

In analogy, a typical ligand exchange reaction mechanism for the EG process would look like this:

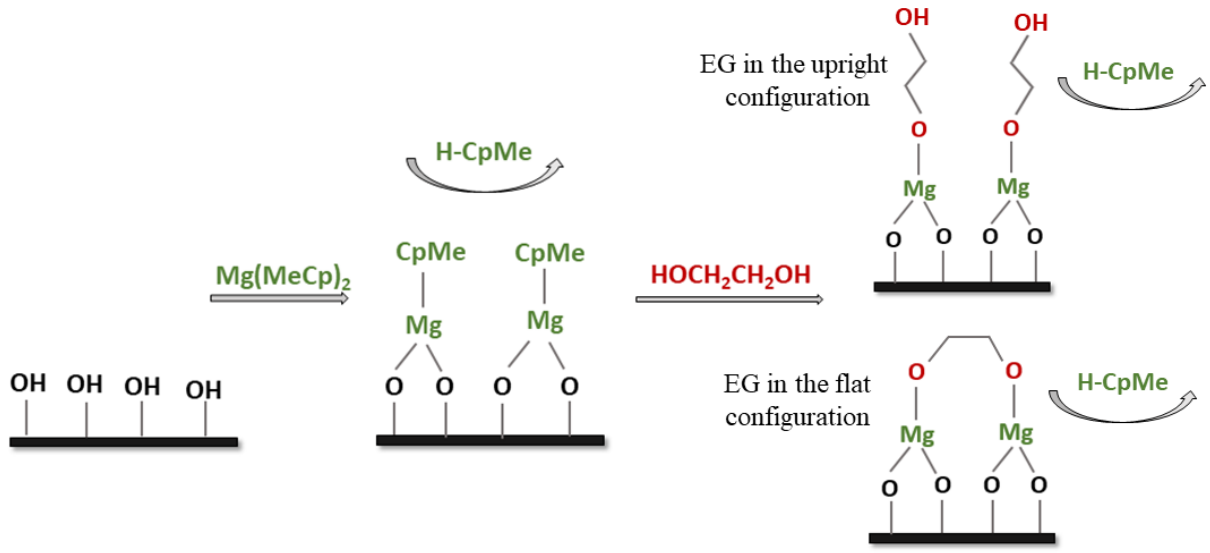
$$OH^* + Mg(MeCp)_2 \rightarrow O{-}MgCpMe^* + HCpMe \quad (4)$$

$$MgCpMe^* + HOCH_2CH_2OH \rightarrow Mg{-}OCH_2CH_2OH^* + HCpMe \quad (5)$$

For the GL process, either of the reactions 2 or 3 takes place, corresponding to either one or two of the GL OH groups reacting to the surface. In principle, bridging can also occur, for EG using both OH groups, resulting in the following reaction during the EG pulse:

$$MgCpMe^* + HOCH_2CH_2OH \rightarrow Mg{-}O\ CH_2CH_2O{-}Mg + 2HCpMe \quad (6)$$

which renders the surface non-reactive for chemisorption of precursor molecules, as no remaining OH adsorption sites are left. This has been observed for earlier MLD processes using EG. [10] Recent work shows that these nonreactive surface sites might allow absorption or adsorption of precursor molecules, introducing new reactive surface sites. [11, 12] This would eventually lead to typical linear steady state growth as observed in **Fig. 2**. As discussed previously, the EG based process displays a reservoir effect which is not seen for the GL based process. It is therefore possible that the EG based process displays a more complex reaction mechanism than the typical ligand exchange reaction mechanism proposed here. A proposed reaction mechanism for the growth of alucone films using $Mg(MeCp)_2$ and EG is presented in **Scheme 1**.



Scheme 1. Schematic illustration of magnesicone MLD based on the reaction between surface hydroxyl groups of MgO with $Mg(MeCp)_2$ and the reaction between Mg(MeCp) surface species with EG.

To explore the mechanism of magnesicone growth, DFT calculations were performed using the reaction of EG and GL at MgCp terminated hydroxylated magnesium oxide (MgO) (100) as a model system. In the DFT calculations, $Mg(Cp)_2$ is used as magnesium precursor instead of $Mg(MeCp)_2$ as the former is more computationally tractable.

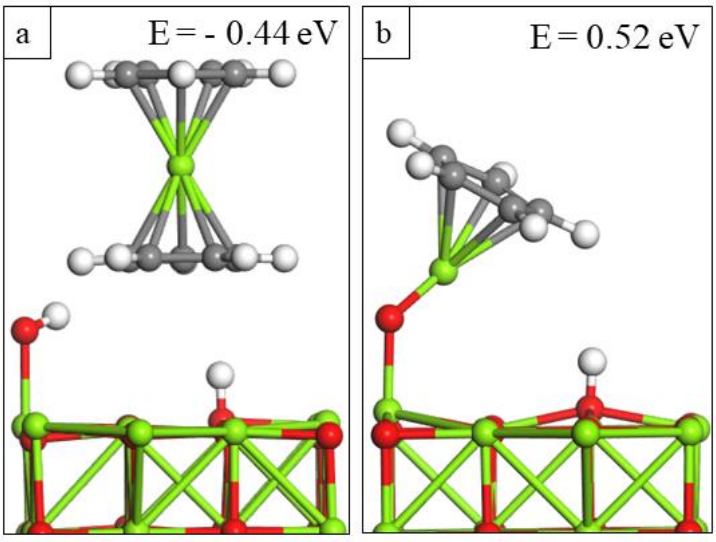


Figure 5 Optimised atomic structures of a) the hydroxylated MgO surface after adsorption of the $Mg(Cp)_2$ precursor and b) elimination of CpH.

Fig. 5 (a) shows the relaxed atomic structure after the adsorption of the $Mg(Cp)_2$ precursor. The computed adsorption energy of the $Mg(Cp)_2$ precursor is -0.44 eV, showing a moderate energy gain for the adsorption of the precursor. There is no spontaneous proton transfer to the Cp ligand. The energy cost for this process, leading to loss of CpH and formation of a new Mg-O bond is 0.52 eV. The resulting atomic structure is shown in **Fig. 5 (b),** and in this structure the Mg-O distance is 1.79 Å.

Further loss of CpH is not favourable, and the next pulse will result in exchange of a Cp ligand with the organic precursor. These calculations are consistent with the mass spectrometry results that show CpH elimination during the growth, **Fig. 4.**

Next, the MLD reactions using EG and GL as organic reactants were analysed. Energetics for the reactions with EG and GL are calculated relative to the MgCp terminated MgO surface. In the first calculation, the organic reactants were modelled in an upright configuration. **Fig. 6 (a)** shows the optimized atomic structure after the introduction of GL and associated loss of CpH. A new Mg-O bond with a distance 1.81 Å is formed and the computed energy change for this reaction is -0.43 eV, **Fig. 6 (b1).** The computed energy change for the reaction with EG in the upright configuration, which involves the formation of a new Mg-O bond with distance 1.81 Å and the release of a CpH molecule, is 0.23 eV. This positive energy means that the upright configuration is not favourable.

Given the propensity for EG to lie flat, other configurations in which the EG molecule lies flat are explored. The structure in **Fig. 6 (b2)** shows EG tilted toward the surface. This also results in an endothermic reaction with a calculated energy change of 0.28 eV. **Fig. 6 (b3)** shows EG tilted such that the terminal OH group interacts with a magnesium atom at the MgO (100) surface. The Mg-O distance to the EG molecule is 1.83 Å, while the distance from the surface to the terminal OH group is 2.2 Å. The energy change for this configuration is exothermic by -0.62 eV. The EG molecule thus prefers to orient flat to the surface, in order to interact with the MgO (100) surface.

GL molecules will thus prefer to lie in an upright position, while EG molecules prefer to lie flat on the surface. As a consequence the change in thickness for GL based process is larger than for EG based process, resulting in a thicker GL based magnesicone compared to the EG based magnesicone. This was also observed in the first 50 cycles of the magnesicone processes in **Fig. 2** where the EG process shows some growth inhibition compared to the GL process.

After these 50 cycles, the growth process becomes more complicated, possibly by the reservoir effect.

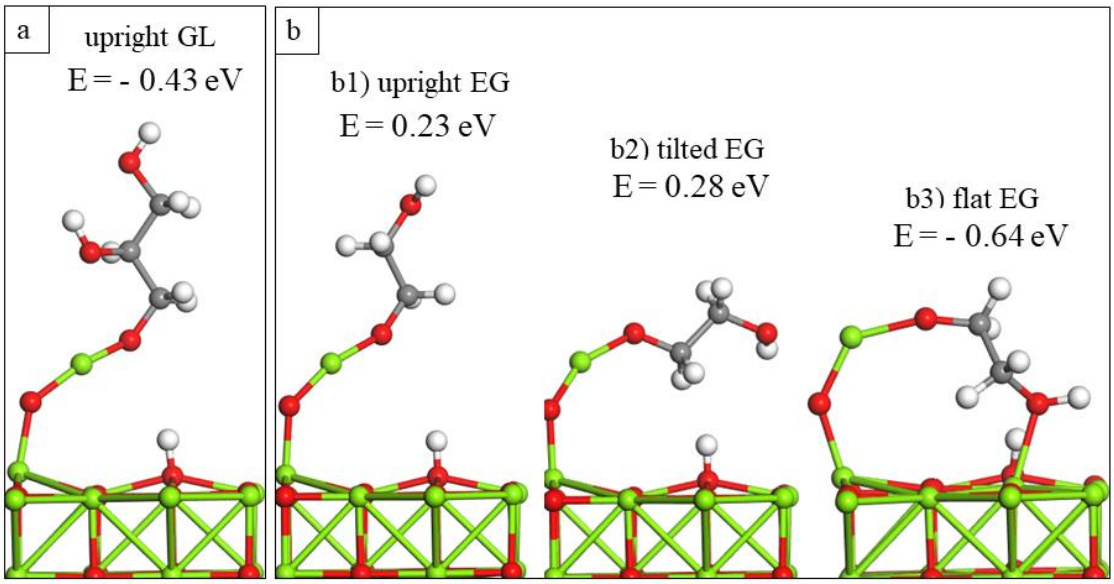


Figure 6 Optimised atomic structures reaction products of the adsorption of an a) upright GL molecule and b1) upright EG molecule, b2) tilted EG molecule and b3) flat EG molecule on a Mg(Cp)-MgO surface.

Given the possible role of this "reservoir" of EG in the growth of the EG based magnesicone film as shown in **Fig. 2** when only introducing the magnesium precursor, it was briefly investigated how EG and GL react with the MgO (100) surface. **Fig. 7** shows the optimized atomic structures of MgCp-MgO in the presence of the organic reactants adsorbed at the surface. Upon relaxation, the proton of the terminal OH group of EG is transferred such that the oxygen atom can bind with the magnesium atom of MgCp. The distance from this oxygen atom to magnesium at the surface is 1.98 Å. The energy gain in this case is -1.64 eV, which is significantly larger than the gain in energy of EG binding to magnesium from Mg(Cp) as shown in **Fig. 7 (a)**. Therefore, EG molecules could be incorporated into the growing film and remain available. In the case of GL, **Fig. 7 (b)**, the change in energy is -0.70 eV, similar to the energy gain when GL reacts with Mg(Cp). In this case, the terminal OH group remains intact, whereas the central OH group binds to magnesium of Mg(Cp) with an Mg-O distance of 2.17 Å.

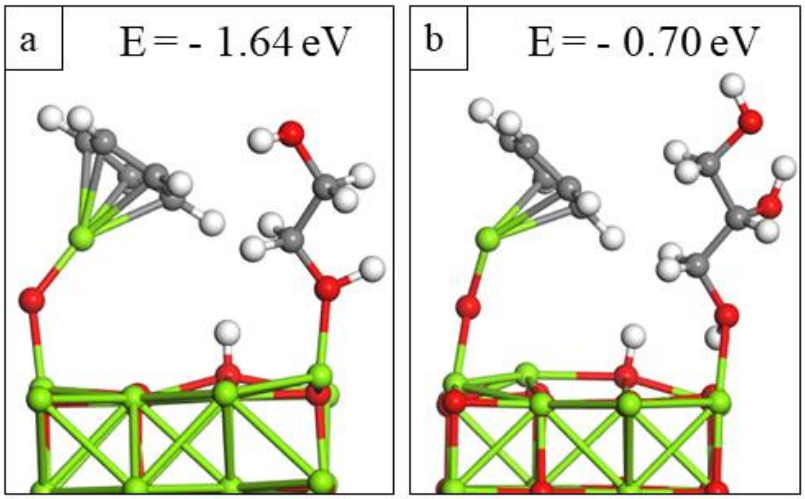


Figure 7 Optimised atomic structures of Mg(Cp)-MgO surface in the presence of a) EG adsorbed at the surface and b) GL adsorbed at the surface.

6.3 Modelling of Ceria hybrid films

This work was published in the paper "***Atomic/molecular layer deposition of cerium (III) hybrid thin films using rigid organic precursors***", in Dalton Transaction. [13]

Dalton Transactions

ROYAL SOCIETY OF CHEMISTRY

PAPER

View Article Online
View Journal | View Issue

Check for updates

Cite this: *Dalton Trans.*, 2022, **51**, 5603

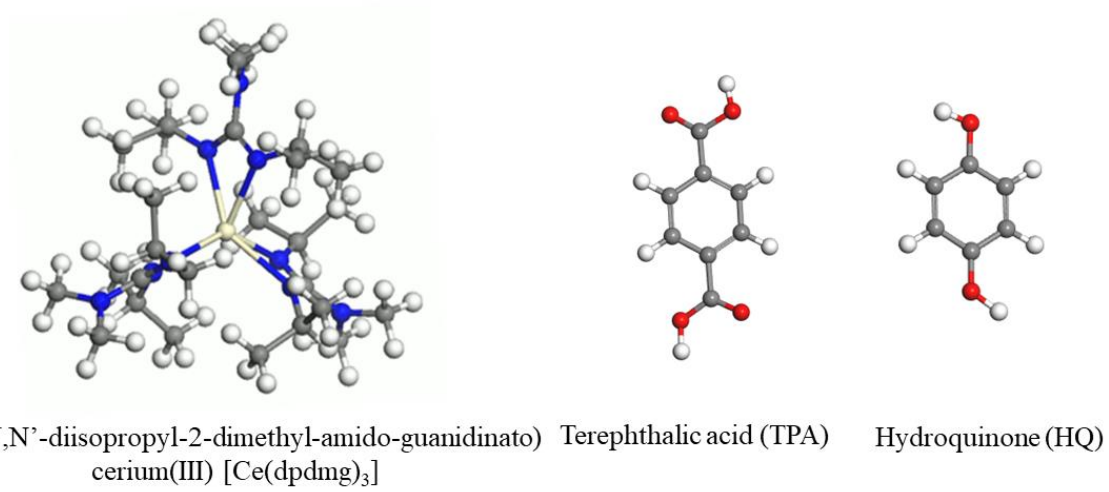
Atomic/molecular layer deposition of cerium(III) hybrid thin films using rigid organic precursors†

Parmish Kaur, [a] Arbresha Muriqi, [b] Jan-Lucas Wree, [a] Ramin Ghiyasi, [c] Muhammad Safdar, [c] Michael Nolan, [b] Maarit Karppinen [c] and Anjana Devi *[a]

DOI: https://doi.org/10.1039/D2DT00353H

6.3.1 Results

This study demonstrates for the first time the fabrication of cerium based metal-organic hybrid films using tris-(N,N'-diisopropyl-2-dimethylamido-guanidinato) Ce (III) ($Ce(dpdmg)_3$) as metal source and terephthalic acid (TPA) and hydroquinone (HQ) as organic reactants on a Si (100) substrate.



Tris(N,N'-diisopropyl-2-dimethyl-amido-guanidinato) cerium(III) [$Ce(dpdmg)_3$]

Terephthalic acid (TPA)

Hydroquinone (HQ)

Figure 8 Molecular structure of tris-(N,N'-diisopropyl-2-dimethylamido-guanidinato) cerium(III) ($Ce(dpdmg)_3$), terephthalic acid (TPA) and hydroquinone (HQ). Cream-Ce, red-O, blue-N, grey-C, white-H.

Fig. 8 shows the chemical structures of the $Ce(dpdmg)_3$, TPA and HQ precursors. In our study on cerium (Ce) precursors (**Chapter 8, Section 8.4**) we show that the selected cerium precursor to deposit ceria hybrids, $Ce(dpdmg)_3$, has a Ce +3 oxidation state and is a highly reactive and volatile precursor. $Ce(dpdmg)_3$ was successful for proof of concept deposition of ALD CeO_2 films together with water as coreactant. [14]

6.3.1.1 Selected experimental results (Ruhr University Bochum, Aalto University)

Thermal investigations of the precursors

The TGA results are shown in **Fig. 9.** Solid lines show the onset of volatilization (1% weight loss) for $Ce(dpdmg)_3$ at 90°C; at 264°C for TPA and at 139°C for HQ under atmospheric pressure. The endothermic peaks in the DSC correspond to the melting points of the precursors which are found to be 104°C for $Ce(dpdmg)_3$ and 172°C for HQ. A high residual weight of 25 % for $Ce(dpdmg)_3$ precursor was obtained which corresponds to precursor decomposition at temperatures above 270°C. From the thermal analysis studies it can be inferred that both the inorganic and organic precursors are volatile and thermally stable at given deposition temperatures and possess a compatible window for sublimation that can be beneficial MLD processing.

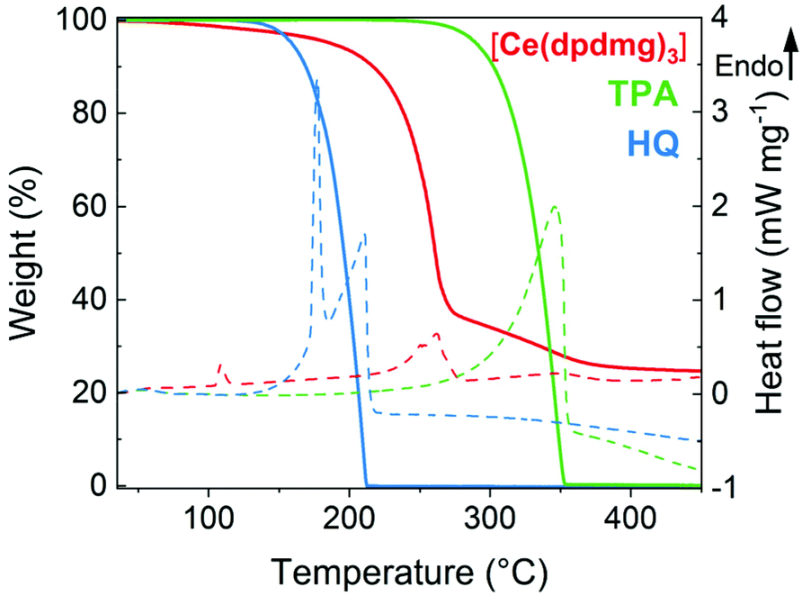


Figure 9 Thermogravimetric analysis (solid line) and differential scanning calorimetry (dashed line) of $Ce(dpdmg)_3$ in red, TPA in green and HQ in blue.

MLD process development

The films were deposited on Si (100) substrates at a deposition temperature of 200°C. Precursor saturation studies at different pulse lengths and the thickness of the films (at the applied number MLD cycles) are shown in the graphs in **Fig. 10**. The $Ce(dpdmg)_3$ and TPA precursors were kept at vaporisation temperatures of 140°C and 185°C, respectively. The TPA pulse length was varied from 2 to 10 s while all other parameters were kept constant: the $Ce(dpdmg)_3$ pulse length at 8 s, the N_2 purge length at 30 s after both precursor pulses, and the number of deposition cycles at 75. It can be seen from **Fig. 10 (a)**, that the 6 s pulse length for TPA was long enough to achieve surface saturation. The corresponding GPC was 5.94 Å/cycle.

As shown in **Fig. 10 (b)** the $Ce(dpdmg)_3$ saturation is achieved when the pulse length is 8 s or longer. The linear dependency of the film thickness on the number of MLD cycles was confirmed using the following precursor pulsing cycle: 8 s $Ce(dpdmg)_3$ / 30 s N_2 purge / 6 s TPA / 30 s N_2 purge, **Fig. 10 (c)**. From XRR, the estimated film density was found to be 2.037 g/cm^3. The temperature dependency of the GPC was also investigated for the Ce-TPA films with the GPC increasing from 4.7 Å/cycle at 190°C deposition temperature to 13.8 Å/cycle at 240°C deposition temperature.

Similarly, the growth of Ce-HQ films was investigated keeping the deposition temperature fixed at 200°C and the vaporisation temperatures of $Ce(dpdmg)_3$ and HQ at 140°C and 120°C, respectively. The HQ pulse length was varied from 6 to 12 s, maintaining all other parameters constant, $Ce(dpdmg)_3$ pulse 8 s, N_2 purge lengths 30 s, 75 cycles. A saturation behaviour was observed as shown in **Fig. 10 (d)**, at 8 s of HQ pulse having GPC of 5.06 Å/cycle. The cerium precursor pulse was varied from 8 s to 12 s, keeping all other parameters constant, HQ pulse 8 s and purge lengths 30 s. The saturation was observed at 12 s of $Ce(dpdmg)_3$, **Fig. 10 (e)**. Finally, the number of MLD cycles was varied using the optimized precursor pulsing cycle, 12 s $Ce(dpdmg)_3$ / 30 s N_2 purge / 8 s HQ / 30 s N_2 purge, to demonstrate the linearity of the film growth, **Fig. 10 (f)**. The density of the Ce-HQ films as determined by XRR was 2.302 g/cm^3.

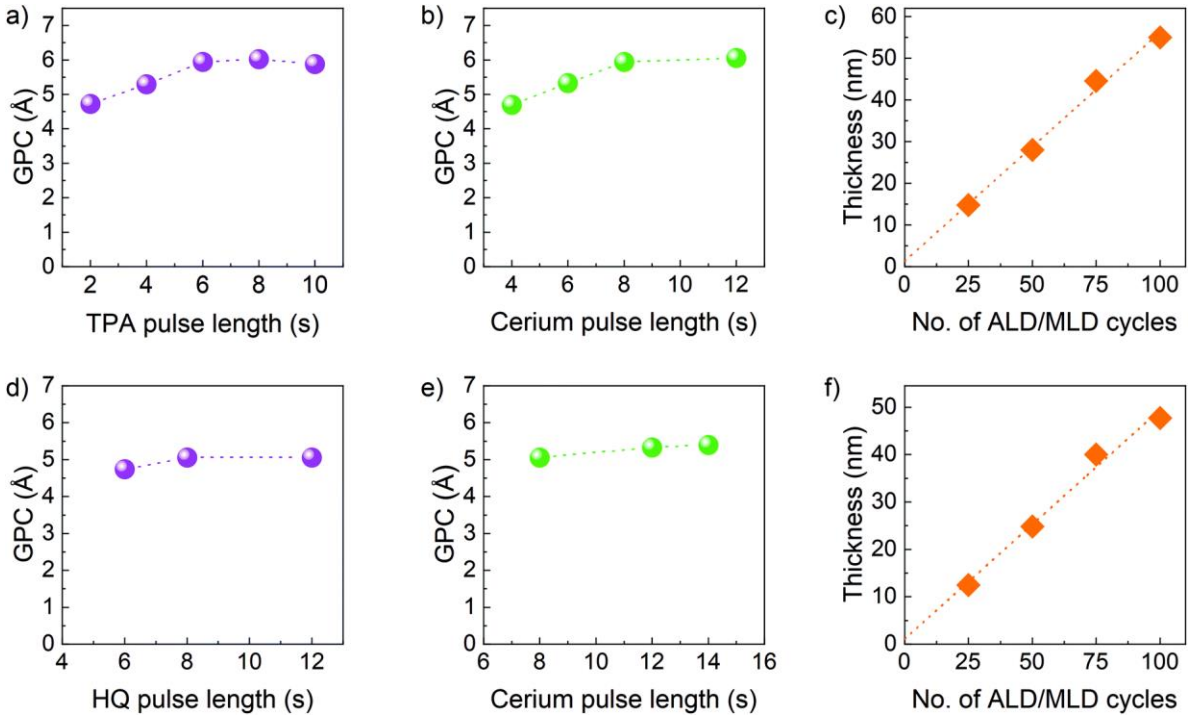


Figure 10 Precursor saturation studies by varying: a) TPA pulse length and b) $Ce(dpdmg)_3$ pulse length for Ce-TPA film growth, d) HQ pulse length and e) $Ce(dpdmg)_3$ pulse length for Ce-HQ film growth. Thickness of the film *vs.* number of applied MLD cycles for: c) Ce-TPA film and f) Ce-HQ film. The estimated error bars are smaller than the data point symbols.

X-Ray photoelectron spectroscopy (XPS) characterisation

For the compositional analysis, high-resolution spectra were measured for the C 1s, O 1s and Ce 3d core levels. The Ce 3d spectra was analysed by the method developed by Romeo *et al.* [15] and was used to fit all spin-orbital and splitting components of the Ce 3d signal, resulting in two multiplets for the cerium hybrid films (**Fig. 11 (a)** and **(d)**). The spectra clearly indicate the formation of Ce^{3+} without any signs of Ce^{4+} for both materials.

The typical signal around 916-917 eV, the fingerprint region for Ce^{4+} species, [16] was not observed (**Fig. 11 (a)** and **(d)**) and moreover, only four peaks corresponding to the pairs of spin-orbit doublets, could be fitted into the Ce 3d spectrum of both cerium hybrid films. The corresponding binding energies of the Ce-TPA films (**Fig. 11 (a)**) and the Ce-HQ films (**Fig. 11 (d)**) are in good agreement with typical values for Ce^{3+} species in literature. [15, 16] XPS analysis also confirm the successful formation of Ce-O-C bonds within Ce-TPA and Ce-HQ MLD films.

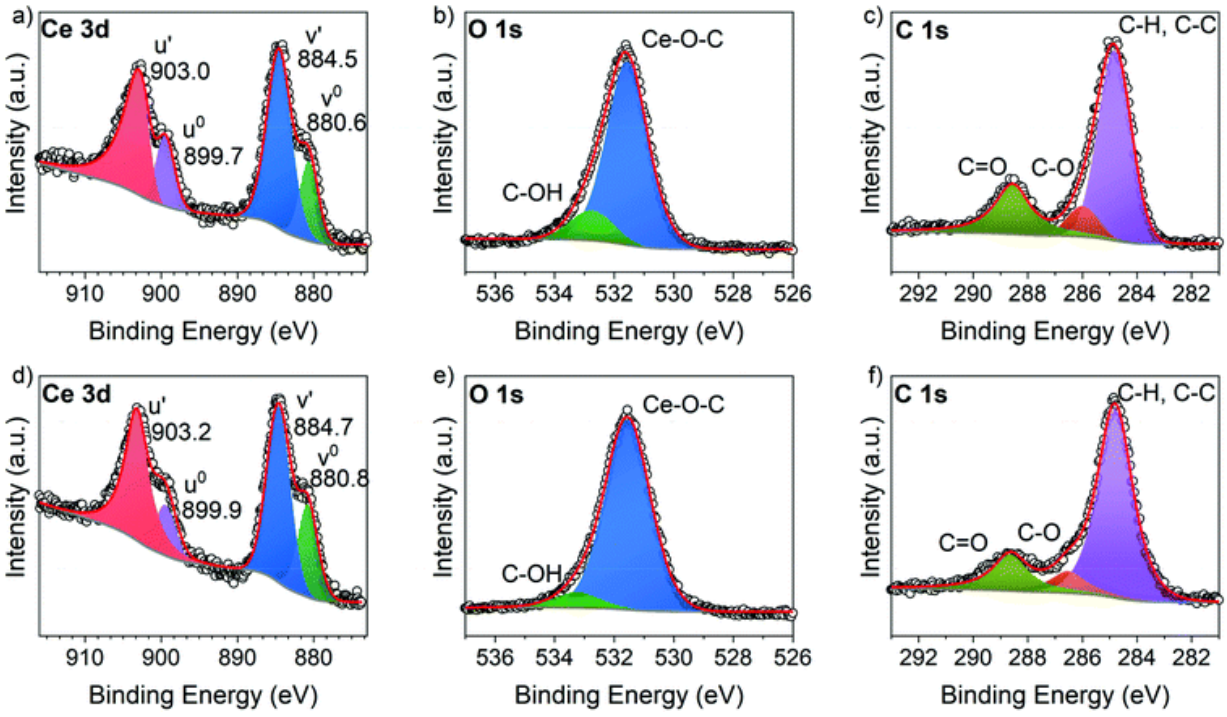


Figure 11 High resolution XPS spectra for Ce-TPA thin films deposited on Si (100) at 200°C (a) Ce 3d core level spectrum (b) O 1s spectrum (c) C 1s spectrum, and Ce-HQ thin films deposited on Si (100) (d) Ce 3d core spectrum (e) O 1s spectrum (f) C 1s spectrum; the hollow circles represent the data points and the red curve shows the total fit.

From the C 1s core level spectrum (**Fig. 11 (c)** and **(f)**) three different carbon species could be identified for both material systems, namely C-H/C-C bonds with a binding energy of 284.8 eV, C-O bonds with a binding energy of 286.6 eV and carboxylic acid functions with a binding energy of 288.6 eV. [17] The O 1s spectra of the films show both the prominent signal at 531.5 eV indicating Ce-O bonds with cerium in the oxidation state +3, (**Fig. 11 (b)** and **(e)**).

UV-visible spectroscopy

The optical properties of the Ce-TPA and Ce-HQ hybrid thin films deposited on quartz substrates were analysed by UV-vis spectroscopy, and the spectras are displayed in **Fig. 12**. The Ce-TPA film shows a prominent strong absorption maximum at 252.5 nm which corresponds to $\pi - \pi^*$ transition of the aromatic ring while the $\pi - \pi^*$ transition for the Ce-HQ film at 244.5 nm is hypsochromic shifted (blue shift) which could be due to the presence of different functional group. Another prominent peak for Ce-HQ is at 298.5 nm which can be attributed to ligand to metal charge transfer (LMCT) from O 2p to Ce 4f orbitals which is less prominent for Ce-TPA and shown by a shoulder around 298 nm.

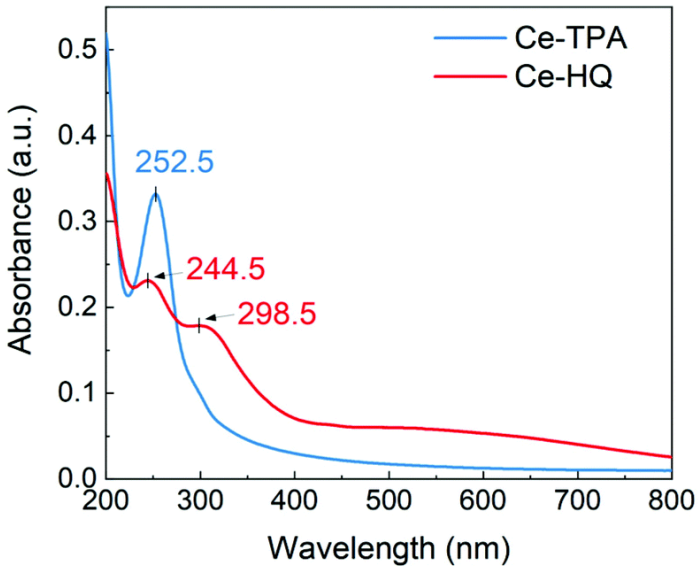


Figure 12 UV-Vis spectra of the Ce-TPA and Ce-HQ hybrid films on quartz substrate.

The Ce-TPA film is transparent i.e. >90% transmittance in the range 350 nm – 800 nm while the Ce-HQ film is >85 % transmitting above 400 nm and >90 % in the region 665 nm – 800 nm. From the above observations, the growth of Ce-TPA and Ce-HQ hybrid thin films by MLD opens new pathways for potential applications. The presence of Ce^{3+} in the films, with its $4f^1$ electronic configuration, makes it interesting to study these materials further for photo-emitting applications. The aromatic backbones act as good antennas due to their strong binding tendency towards the cerium ions and can influence the luminescent properties of the Ce^{3+} ions. [18]

6.3.1.2 Computational results

DFT methods were employed to gain deeper insights into the atomistic mechanism of the growth of cerium-organic hybrid films using TPA and HQ as organic precursors and $Ce(dpdmg)_3$ as the metal source. In the simplified model, a hydroxylated cerium oxide (CeO_2) (111) surface, with a coverage of 0.38 OH nm^{-2} formed by water dissociation at the surface is used.

Firstly, the $Ce(dpdmg)_3$ precursor was adsorbed on the hydroxylated CeO_2 surface giving a large exothermic interaction energy change of -2.84 eV, **Fig. 13 (a)**.Then the first and second ligand loss reactions of the $Ce(dpdmg)_3$ precursor when interacting with the hydroxylated CeO_2 surface were examined. During the first ligand loss reaction the cerium atom of the $Ce(dpdmg)_3$ molecule binds to the surface oxygen from which the proton migrates, with a Ce-O distance of

1.93Å. The calculated change in energy for the first ligand loss reaction is -0.52 eV, giving an overall exothermic energy change of -3.36 eV, **Fig. 13 (b)**. In the second ligand loss reaction, a second proton transfers from a surface OH group to the second dpdmg ligand to form a new H-dpdmg molecule while the cerium atom binds to the surface oxygen with an Ce-O distance of 1.95Å. The change in energy for the second ligand loss reaction is -0.58 eV, giving an overall energy gain of -3.94 eV.

The ligand lose reactions leave the surface covered with cerium bonded to one dpdmg ligand that can exchange with one organic molecule during the organic precursor pulse, **Fig. 13 (c)**. Bader charge calculations were performed to determine any change in the oxidation state of cerium atom of $Ce(dpdmg)_3$. The computed Bader charge of 9.8 electrons (a net charge of +2.2 electrons) for the cerium atom on adsorbed $Ce(dpdmg)_3$ corresponds to the Ce^{3+} oxidation state. [19]

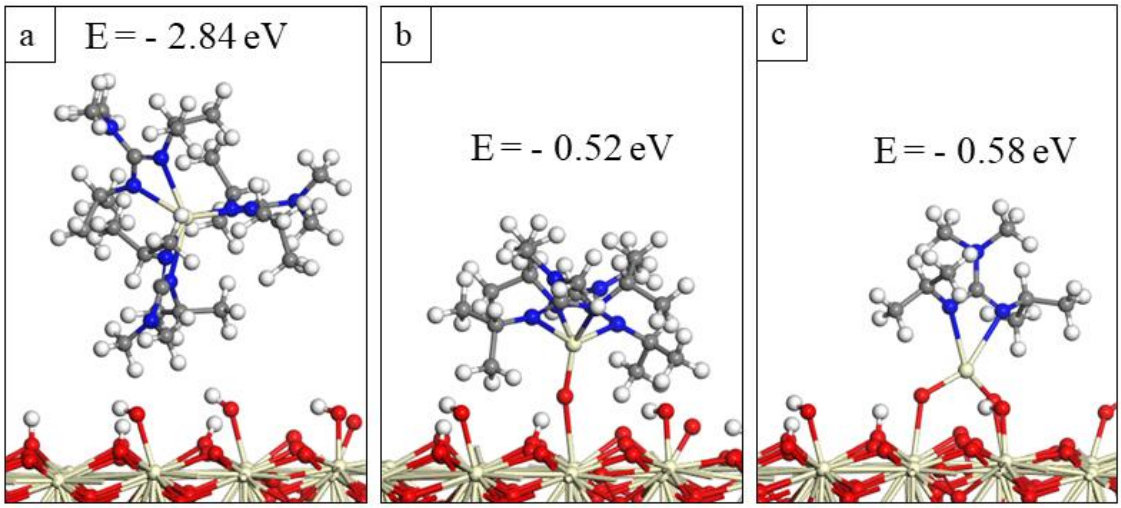


Figure 13 Atomic structure of the hydroxylated CeO_2 surface after a) adsorption of $Ce(dpdmg)_3$, b) elimination of the first dpdmg ligand and c) elimination of the second dpdmg ligand.

Next, the MLD reactions using HQ and TPA as organic reactants were analysed. **Fig. 14** shows the proposed reaction mechanism between the Ce-dpdmg terminated CeO_2 surface with TPA and HQ. During the reaction with TPA, a proton from the terminal COOH group of TPA transfers to dpdmg to release a new H-dpdmg molecule while the remaining oxygen binds to the cerium atom of the precursor, with a Ce-O distance 2.45 Å, slightly longer than typical Ce-O distance of 2.37 Å in CeO_2 (111), **Fig. 14 (a)**. The calculated interaction energy -1.96 eV calculated relative to the Ce-dpdmg terminated CeO_2 surface (**Fig. 13 (c)**) leads to an overall

energy change of -5.90 eV and confirms that this reaction is exothermic and formation of the Ce-O bond linking cerium and TPA is favourable. After interaction with the TPA, a new Ce-O bond is formed between cerium atom of the precursor with the surface oxygen. The two existing Ce-O bonds are lengthened from 1.93 Å to 1.97 Å and 1.95 to 2.00 Å while the third Ce-O bond has a distance of 2.41 Å. A Bader charge of 9.8 electrons is calculated for the cerium atom bound to TPA, again indicating that cerium remains in the Ce^{3+} oxidation state.

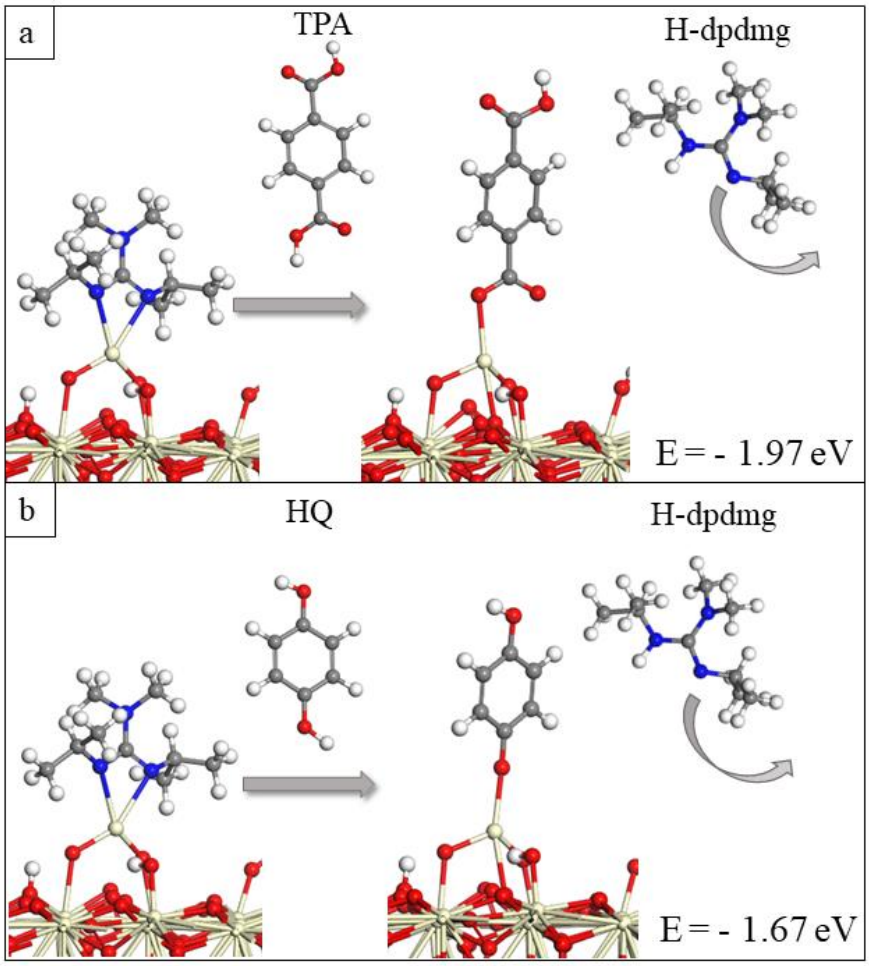


Figure 14 Schematic representation of the reaction between Cedpdmg terminated CeO_2 (111) surface with a) TPA and b) HQ.

The reaction mechanism between the Ce-dpdmg terminated CeO_2 surface with HQ is similar to that with TPA. During this reaction a proton from the terminal OH group of HQ transfers to the dpdmg ligand to form a new H-dpdmg molecule while the remaining oxygen binds to cerium site of Ce-dpdmg with a Ce-O distance 2.39 Å, shorter than that found for Ce-TPA, **Fig. 14 (b).** The calculated interaction energy -1.67 eV calculated relative to the Ce-dpdmg terminated CeO_2 surface (**Fig. 14 (c)**), leads to an overall energy change of -5.61 eV and shows

that HQ also reacts favourably with the Ce-dpdmg terminated CeO_2 surface. Again, a new bond between the cerium atom of the precursor with the surface oxygen is formed. In addition to the Ce-O bond formed with HQ, the cerium atom is bonded to three surface oxygen sites. The two existing Ce-O bonds were lengthened from 1.93 Å and 1.95 Å to 1.98 Å while the new Ce-O bond had a distance of 2.50Å. The computed Bader charge of the cerium atom that is bonded to the HQ molecule is 9.8 electrons, which indicates that the Ce^{3+} oxidation state persists.

The favourable adsorption and decomposition of $Ce(dpdmg)_3$ precursor on the CeO_2 surface and the favourable reactions with TPA and HQ aromatic molecules indicate that the formation of oxide/metal-organic films of CeO_2/Ce-TPA and CeO_2/Ce-HQ is feasible.

In summary, DFT calculations show that HQ and TPA are probably very reactive towards $Ce(dpdmg)_3$. Combined with the fact that aromatic molecules, because of their stiff backbone prevent the double reactions on the surface that hinder the film growth, the use of HQ and TPA as organic precursors is a good solution to produce thicker and more flexible films. [20-23]

6.4 Modelling of Alumochitin and Titanochitin hybrid films

6.4.1 Results on Alumochitin films

Alumochitin films were deposited using trimethylaluminum (TMA) as metal source and monosaccharide N-Acetyl-D-mannosamine (ManNAc) as organic reactant on a zirconium oxide (ZrO_2) surface. **Fig. 15** shows the chemical structures of TMA and ManNAc precursors.

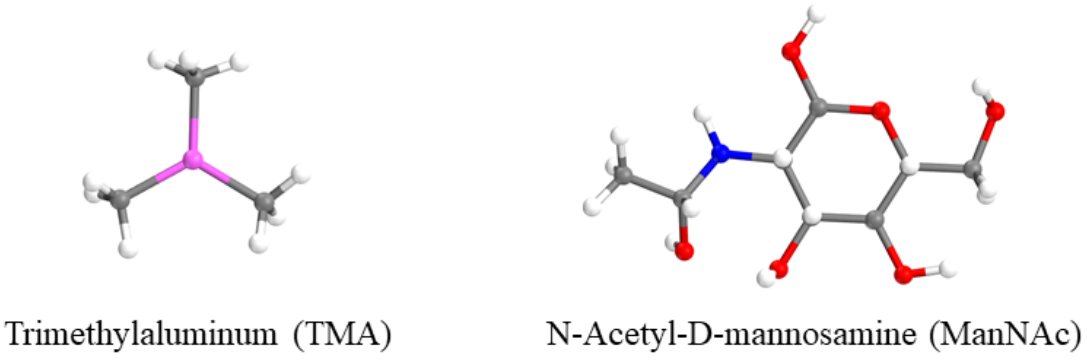


Figure 15 Molecular structure of trimethylaluminum (TMA) and N-Acetyl-D-mannosamine (ManNAc). Red-O, purple-Al, grey-C, white-H.

6.4.1.1 Selected experimental results on Alumochtin films (CIC nanoGUNE)

MLD process development

The reactor temperatures during alumochitin film growth ranged from 110°C to 125°C. The reactant pulse, exposure and purge timing are denoted as (t1, t2, t3, t4, t5, t6), where t1 is the ManNAc pulsing time, t2 is the ManNAc exposure time, t3 is the purge after the ManNAc, t4 is the TMA dose time, t5 is the TMA exposure time, t6 is the purge time after the TMA exposures. The MLD cycle timing used for the alumochitin synthesis was 6s, 5s, 25s, 0.015s, 3s, 25s, for the corresponding pulse, exposure and purge sequence of ManNAc and TMA.

Quartz crystal microbalance (QCM) characterisation

QCM was used to study the reactions between TMA and ManNAc precursors in a temperature range between 110°C and 125°C. **Fig. 16 (a)** shows the mass gain versus TMA and ManNAc exposures time. The timing sequence for the TMA exposure was (X, 20, 5, 20). The pulse duration of TMA was varied, while the purge, ManNAc pulse and ManNAc purge times were kept constant. A 1 s dose of TMA was sufficient for saturation. The timing sequence used for

ManNAc was (1, 20, X, 20). Accordingly, a 5 s dose of ManNAc was sufficient for saturation. The QCM measurements confirm that the mass increases linearly with the number of MLD cycles.

Fig. 16 (b) shows the mass gain versus time for the ManNAc/TMA MLD process in a steady state. The inset in this figure shows an expanded view of the graph from which a GPC of the hybrid film of ~20ng/cm^2 can be derived. Furthermore, a self-limiting behavior for the surface reactions of ManNAc with the chemisorbed TMA is confirmed by the QCM data.

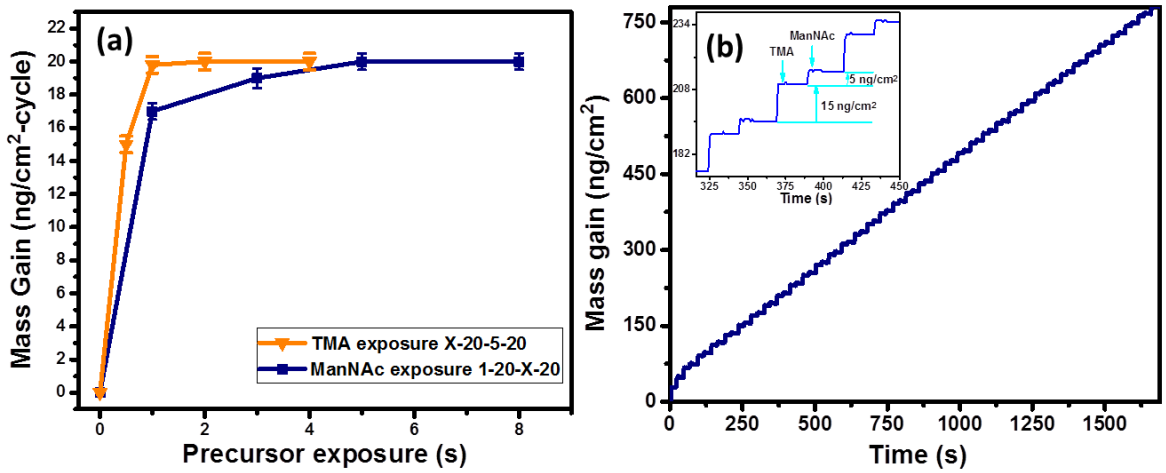


Figure 16 a) Mass gain per cycle vs. ManNAc (dark blue) or TMA (yellow) dosing times in a steady state regime at 115°C. b) Mass gain versus time for the ManNAc/TMA MLD process on a pre-deposited Al_2O_3 ALD surface at 115°C. Expanded view of the growth during four reaction cycles in a steady state at 115ºC.

X-ray reflectivity (XRR) and attenuated total reflectance FTIR (ATR-FTIR) characterisation

A GPC of 1.3 ± 0.1 Å/cycle was extracted from the film thicknesses measured XRR as a function of the number of MLD cycles (**Fig. 17 (a)**). To verify the hybrid nature of the grown alumochitin, ATR-FTIR spectra of the samples were measured and compared to those of the organic chitinoid film. The alumochitin film resembles the chitin structure with additional Al-O interactions, and therefore the major additional features in the FTIR spectra are expected in the regions of Al-O vibrations (**Fig. 17 (b)**). Indeed, the spectra of alumochitin display an additional broad Al-O absorption band at ~830 cm^{-1}, which confirms the presence of Al-O species in the film. [24] The position of the various organic FTIR bands of alumochitin were nearly identical with those of the chitinoid film.

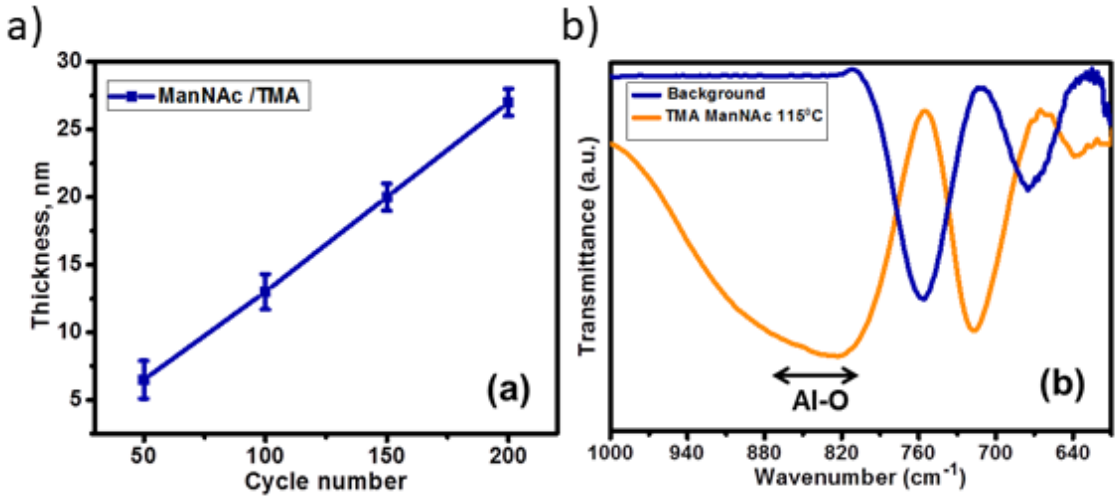


Figure 17 a) XRR measurements of thickness versus cycle number for the alumochitin growth on Si using ManNAc and TMA at 115°C. b) Expanded view of the 1000-610 cm^{-1} region of the ATR-FTIR spectrum of ManNAc/TMA.

X-ray photoelectron spectroscopy (XPS) characterisation

Fig. 18 shows the high-resolution XPS spectra of the C 1s, N 1s and Al 2p regions of the ~20 nm thick MLD film. The deconvolution of the C 1s region (**Fig. 18 (a)**) shows three main contributions with a slight difference in the carbon bonding environment between the alumochitin film and the organic chitinoid film. The three identified contributions are associated with C-C/C-H, C-O-C/ C-N and C=O species at binding energies of 284.2, 286.2 and 288.7 eV. Besides the presence of the chitin-characteristic C-C/C-H, C-N, C-O/C-O-C and C=O units, the decreased intensity of the C-O-C contribution in the alumochitin indicates the substitution of some C-O-C bonds with C-O-Al bonds.

The N 1s XPS spectrum in **Fig. 18 (b)** shows one component at the binding energy of ~400 eV, which is assigned to C-N and N-H bonds of the acetamide group, characteristic of chitin.

The Al 2p spectral region in **Fig. 18 (c)** is fitted with one component at the binding energy of 73.8 eV, which is lower in energy than the binding energies of Al-O bonds in Al_2O_3 films. [25] Together with the above mentioned decrease of the C-O-C peak in the C 1s spectra, the decrease of the binding energies of Al 2p points towards the formation of C-O-Al bonds, indicated a successful incorporation of alumina into the chitinoid network. Consequently, the XPS analyses together with ATR-FTIR confirm the hybrid nature of the alumochitin film.

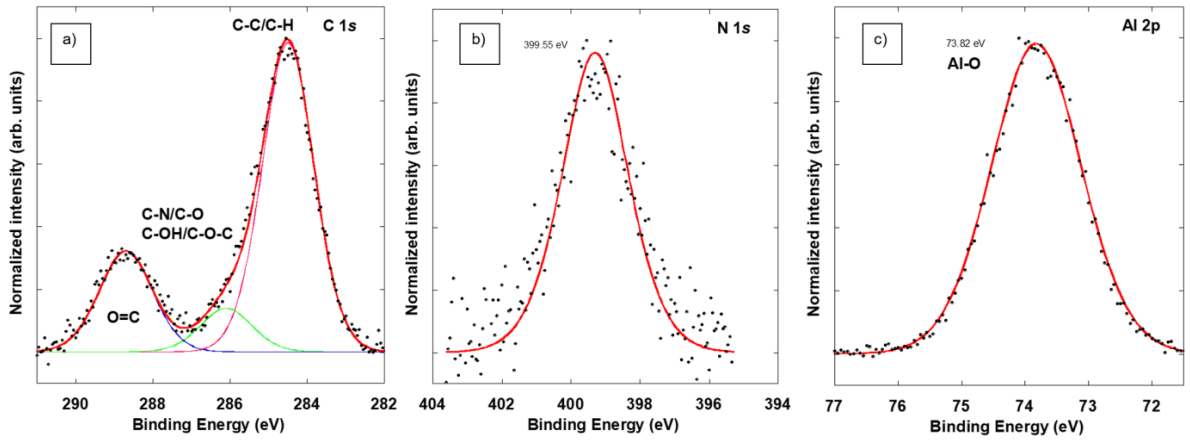


Figure 18 High-resolution XPS spectra of the ManNAc/TMA MLD sample: (a) C 1s, (b) N 1s and (c) Al 2p core-levels.

Nuclear magnetic resonance spectroscopy (NMR) characterisation

Solid state NMR spectroscopy has been used to analyze the structure of the hybrid alumochitin film. The ^{27}Al MAS solid state NMR spectrum of the alumochitin film is displayed in **Fig. 19**. The spectrum shows three aluminium coordination environments with resonances at approximately 61, 33 and 5 ppm, which are assigned to four-, five-, and six-fold coordinated aluminium, respectively.

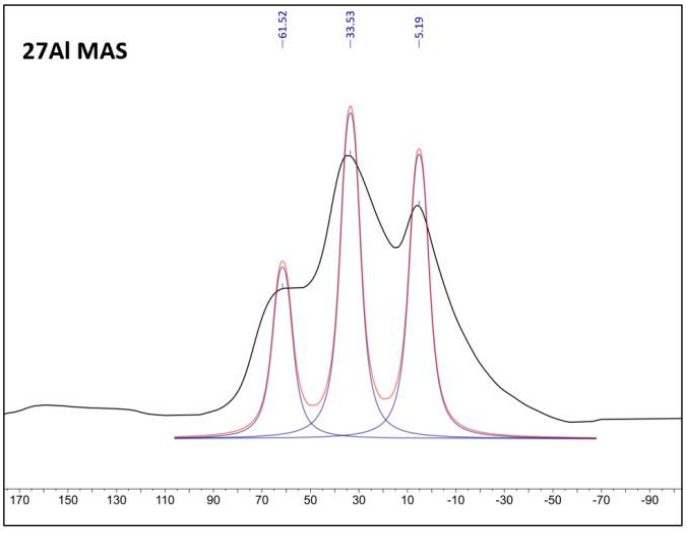
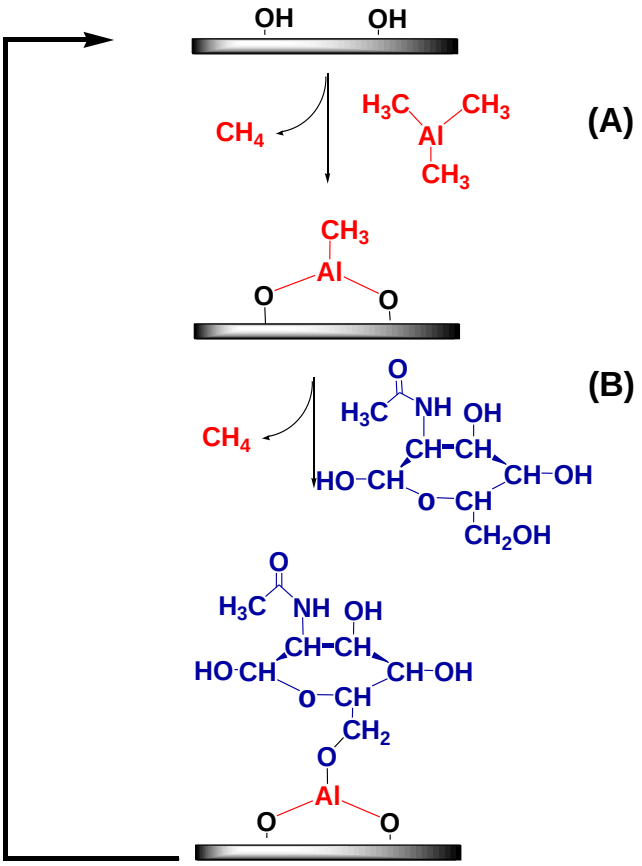


Figure 19 ^{27}Al MAS NMR solid state spectrum of a ManNAc/TMA MLD film grown on ZrO_2 substrate at 115 °C.

6.4.1.2 Computational results on Alumochitin films

The detailed mechanism of the deposition of alumochitin films was studied with the aid of first principles density functional theory (DFT) calculations by computing the reaction energetics for the relevant MLD products. A hydroxylated monoclinic ZrO_2 (111) surface in a (2 × 2) surface supercell was used for MLD modelling. This surface was modified with TMA as metal source and ManNAc as organic reactant. The proposed reaction mechanism for the MLD process of alumochitin is depicted in **Scheme 2**.



Scheme 2 Schematic illustration of alumochitin MLD based on the reaction between surface hydroxyl groups with TMA and the reaction between TMA and ManNAc.

In the first step of our calculations one TMA molecule was adsorbed on the hydroxylated ZrO_2 surface. Aluminum attaches to the surface through an oxygen bridge by forming Lewis acid-base adducts with a gain in energy -1.40 eV for the elimination of one CH_3 ligand and formation of the dimethyl terminated ZrO_2 surface ($(CH_3)_2$-Al-ZrO_2). There is a further gain in energy of -0.40 eV for the elimination of the second CH_3 ligand, leading to an overall energy of -1.80 eV

for the elimination of two CH_3 ligands and the formation of the monomethyl terminated ZrO_2 surface (CH_3-Al-ZrO_2).

While the computed energies show that both $(CH_3)_2$-Al-ZrO_2 and CH_3-Al-ZrO_2 formation are exothermic, we continue the modelling work with the CH_3-Al-ZrO_2 surface, in which aluminium is three coordinated, with Al-O distances of 1.69 Å and 1.76 Å to the surface oxygen sites and Al-C distance of 1.94 Å.

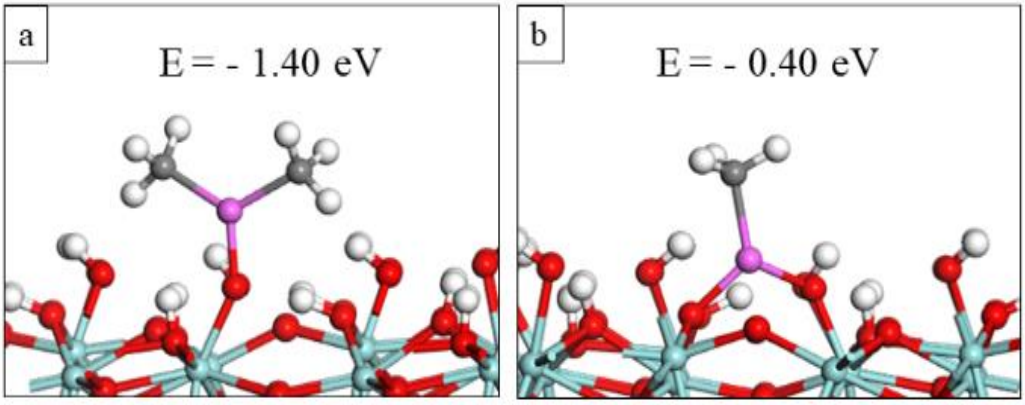


Figure 20 Atomic structure of (a) dimethyl-Al-ZrO_2 (Al$(CH_3)_2$-ZrO_2) and (b) monomethyl-Al-ZrO_2 (Al-CH_3-ZrO_2).

The interactions between the Al(CH_3) species on the ZrO_2 surface and the organic reactant are then investigated by analysing the formation of MLD reaction product with ManNAc, **Fig. 21**.

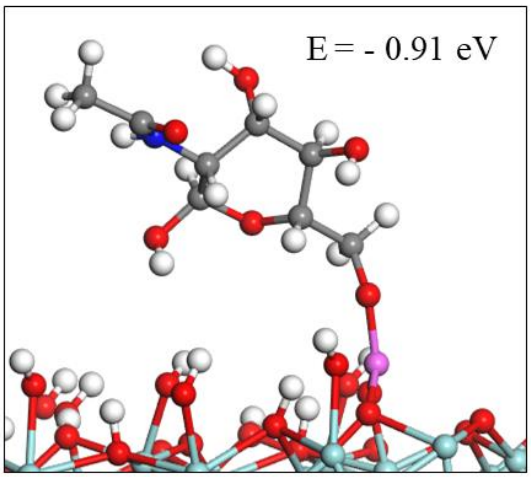


Figure 21 Atomic structure of MLD reaction product of the interaction of the MMA-ZrO_2 surface with ManNAc.

During the ManNAc pulse, a proton from an OH group of ManNAc transfers to the CH_3 ligand to form another CH_4 molecule, while the remaining oxygen binds to the aluminium atom of TMA with an Al-O distance of 1.69 Å. The second half reaction has a further energy gain of -0.91 eV which leads to an overall reaction energy -2.71 eV, and is thus thermodynamically favorable. OH groups of ManNAc regenerate the species needed to react with the next TMA in the following cycle. In this structure, the TMA aluminium atom is tri-coordinated with Al-O distances of 1.69 Å and 1.74 Å to the surface oxygen sites and an Al-O distance of 1.69 Å to the ManNAc oxygen.

The second MLD cycle proceeds through the same pathway as the first cycle. We analyzed three different options for the next TMA interacting at ManNAc: two unidentate reactions and a bidentate reaction (**Fig. 22**).

In the first model, **Fig. 22 (a)**, TMA loses one CH_3 ligand, released as a CH_4 byproduct, which is product of the proton transfer reaction from ManNAc to the CH_3 ligand of TMA. Aluminium binds with the oxygen site, labeled number 1, through a new Al-O bond with a distance of 1.73 Å. The calculated energy is -3.42 eV.

In the second model, **Fig. 22 (b)**, TMA binds with ManNaAc through oxygen in the position labeled number 2 with an Al-O distance of 1.72 Å and again one CH_4 molecule is released as byproduct. The calculated energy is -2.63 eV.

In the third model, **Fig. 22 (c)**, TMA binds to ManNAc through two oxygens of the organic molecule, indicated as 1 and 2, and two new Al-O bonds are formed with distances 1.73 Å and 1.72 Å while two CH_4 molecules are released. The calculated interaction energy for this reaction is -4.96 eV, showing that the bidentate, two-ligand elimination reaction is the most probable.

Fig. 23. The proton of the OH group of ManNAc transfers to the CH_3 ligand of TMA and form a CH_4 molecule that is released as a byproduct while the remaining oxygen of ManNAc binds to the aluminium atom of TMA with an Al-O distance of 1.65 Å. The interaction energy upon forming the Al-O bond is -1.10 eV and was calculated relative to the MLD reaction product in **Fig. 22 (c)**. The exothermic energy for this reaction further demonstrates the strong interactions between TMA and ManNAc precursors. Therefore, these DFT studies show that the proposed reaction mechanism for formation of this hybrid alumochitin material is energetically favourable.

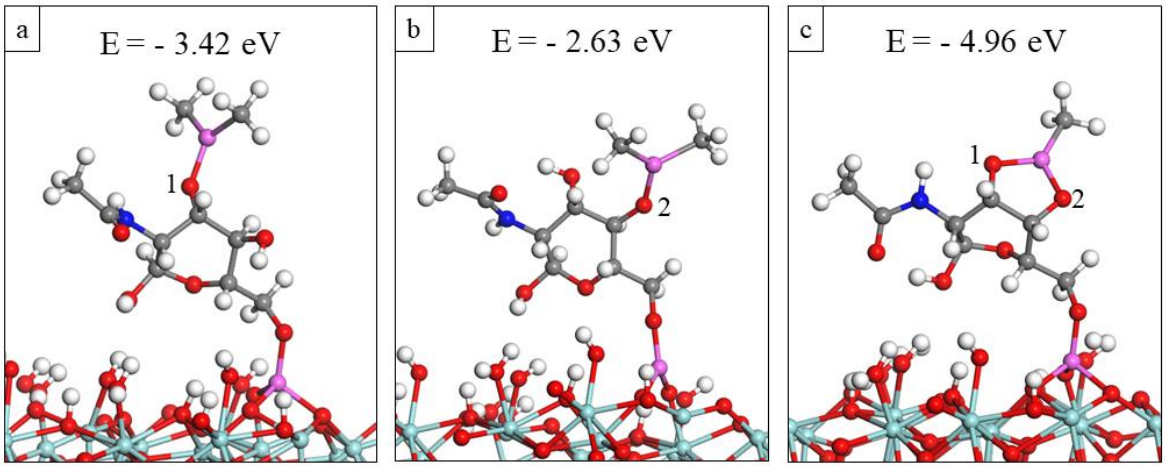


Figure 22 Atomic structure of ManNAc on the MMA-ZrO_2 surface with adsorption of TMA at the a) exposed OH number 1, b) exposed OH number 2 and c) exposed OH number 1 and 2.

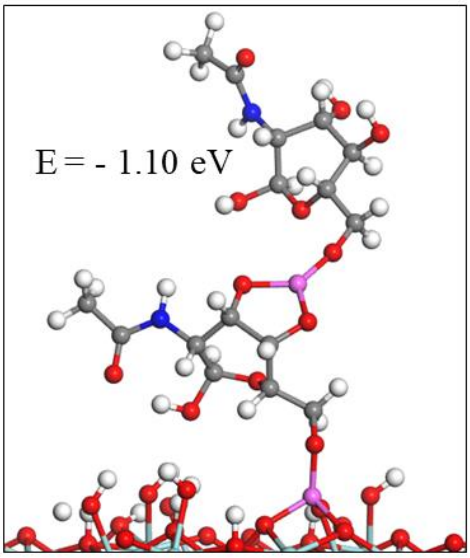


Figure 23 Atomic structure of MLD reaction product of the interaction of the MMA-ZrO_2 surface with ManNAc in the second cycle

6.4.2 Results on Titanochitin films

Titanochitin films were deposited using titanium isopropoxide (TTIP) as metal source and monosaccharide N-Acetyl-D-mannosamine (ManNAc) as organic reactant on a ZrO_2 surface. **Fig. 24** shows the chemical structures of the TMA and ManNAc precursors.

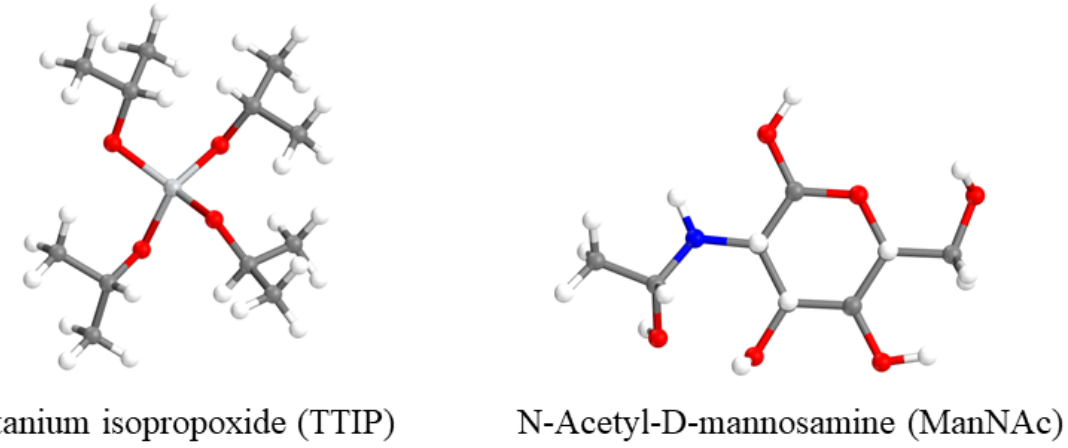


Figure 24 Molecular structure of titanium isopropoxide (TTIP) and N-Acetyl-D-mannosamine (ManNAc). Red-O, light grey-Ti, grey-C, white-H.

6.4.2.1 Selected experimental results on Titanochtin films (CIC nanoGUNE)

MLD process development

Prior to use, precursors were handled and filled into airtight cylinders in a glovebox because of their sensitivity to air and moisture. The ManNAc and TTIP precursor bubblers were heated to 100°C and 70°C, respectively, to obtain sufficient vapor pressure. The titanochitin MLD cycle consisted of pulse (6 s, 5 s, 30 s, 1 s, 4 s, 30 s) for the corresponding pulse, exposure, and purge sequence of ManNAc and TTIP.

X-ray reflectivity (XRR) and attenuated total reflectance FTIR (ATR-FTIR) characterisation

Fig. 25 (a) shows a linear correlation of the film thickness and the number of reaction cycles and an average GPC of ~1.0 Å/cycle at 115°C as derived from XRR analysis. A typical FTIR spectrum of titanochitin coated ZrO_2 is shown is **Fig. 25 (b)**. The spectrum is referenced to neat ZrO_2 powder. The spectrum exhibits a broad band at ~3400 cm^{-1} originating from O-H present in the MaNAc and Ti-OH surface hydroxyl groups. At wavenumbers 2928 cm^{-1} and 2869 cm^{-1}, together with a smaller absorption at 1253 cm^{-1}, stretching vibrations of CH_2 groups from the

MaNAc molecule can be found. The most intense absorption bands at 1604 cm^{-1} and 1537 cm^{-1} are amide I (stretching vibrations of the C=O and C-N groups) and amide II (N-H bending, C-N and the C-C stretching vibrations) bands. These two peaks clearly show the presence of the acetamide group of ManNAc, the main functional group of chitin, even after the growth process. Absorbance features are also present at 1320–1450 cm^{-1} region and are assigned to CH_x (x=1,3) bending modes originating from the ManNAc molecule. The strong features at 1020 cm^{-1} and 1120 cm^{-1} correspond to the symmetric and asymmetric C-O stretching modes of MaNAc ring, as well as to the formation of the Ti-O-C bonds. The strong peak at 1166 cm^{-1} can be linked to the C-C bonds in MaNAc and potentially some unreacted isopropoxy groups of TTIP. The band at ~ 850 cm^{-1} indicates the formation of a Ti-O bond. [6, 9, 19, 26-28] The presence of both the carbon related and the titanium related groups absorptions prove the presence of a hybrid titanium-organic MLD film.

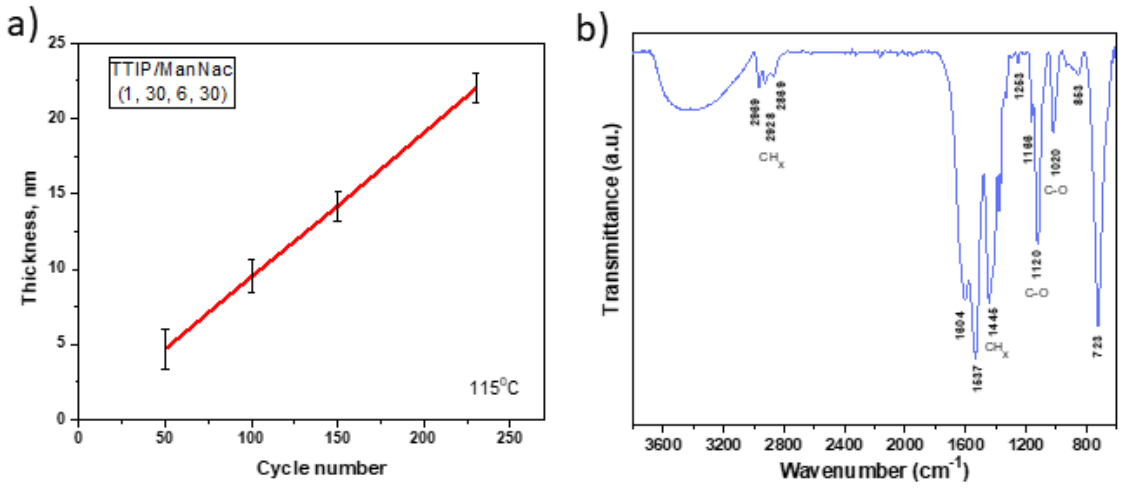


Figure 25 a) Film thickness (from XRR) versus cycle number of titanochitin grown on Si (100) wafers at 115°C. b) A typical ATR-FTIR spectrum of titanochitin, deposited at 115 ºC.

X-ray photoelectron spectroscopy (XPS) characterisation

The expected elements (Ti, C, N and O) appear in the spectrum and the resulting C 1s, N 1s, and Ti 2p XPS spectra are shown in **Fig. 26**. The spectra were deconvoluted into sets of mixed Gaussian−Lorentzian functions with a Shirley background subtraction.

The C 1s XPS spectrum of titanochitin in **Fig. 26 (a)** shows several components originating from carbon in different bonding states. We obtained the best fit after deconvolution into three contributions originating from C−C/C−H, C-O/C-N/C-O-C/C-OH, and C=O (surface contamination) at binding energies of 284.5, 285.9 and 288.4 eV, respectively.

The deconvoluted N 1s spectrum in **Fig. 26 (b)** shows a major peak at ~400 eV and two minor contributions at about 401.6 and 397.5 eV. The dominant presence of nitrogen in one chemical state, which corresponds to the –$NHCOCH_3$ group of ManNAc, confirms that the MLD process does not cleave the acetyl group. An additional, less intense peak has been observed at 397.5 eV. This component has a binding energy corresponding to reported energies of nitrogen in O-Ti-N and Ti-N bonds and further proves the hybrid nature of the film with likely a very minor amount of TTIP potentially bound to the nitrogen of the acetamide group of mannosamine. [29- 31] The Ti 2p spectrum in **Fig. 26 (c)** shows a doublet with binding energies of 464.1 and 458.3 eV, corresponding to the core level binding energies of $Ti2p_{3/2}$ and $Ti2p_{1/2}$, consistent with the Ti-O type bonding scheme of TiO_2 (Ti^{4+}). [32] The titanium core level region shows that no titanium is solely bound to N, but rather that titanium may have mixed oxygen and nitrogen bonds.

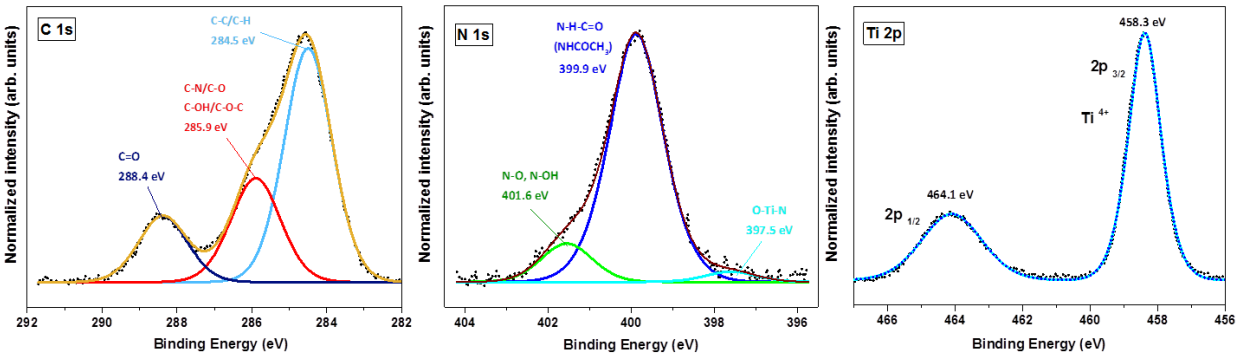
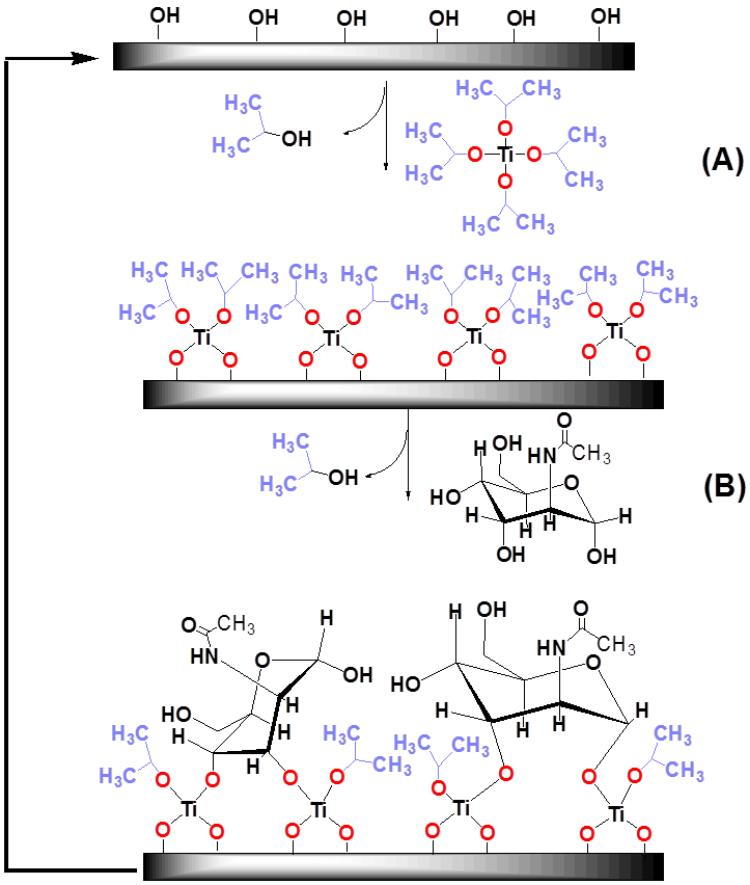


Figure 26 High-resolution XPS spectra of the titanochitin film: a) C 1s, b) N 1s and c) Ti 2p core-levels.

6.4.2.2 Computational results on Titanochitin films

We explored the mechanism of titanochitin thin film formation through DFT calculations using the reaction between TTIP and ManNAc at the hydroxylated ZrO_2 surface as a model system. The proposed reaction mechanism for the MLD process of titanochitin is depicted in **Scheme 3**.



Scheme 3 Schematic illustration of titanochitin MLD based on the reaction between surface hydroxyl groups with TTIP and the reaction between TTIP and ManNAc.

Fig. 27 (a) shows the optimised atomic structure of the hydroxylated ZrO_2 surface after interaction with TTIP from the TTIP pulse in MLD. An exothermic reaction with an energy of - 2.6 eV was calculated when TTIP interacts with hydroxylated ZrO_2. TTIP binds to the surface through the ligand loss reactions which include proton transfer from the surface OH groups to isopropoxy ligands (O-^{i}Pr, O-$CH(CH_3)_2$) to form isopropanol molecules (HO-^{i}Pr, HO-$CH(CH_3)_2$) as byproducts. Specifically, the energy gain for the individual ligand loss reactions are 0.03 eV for the first O-^{i}Pr ligand **Fig. 27 (b)**, 0.50 eV for the second O-^{i}Pr ligand **Fig. 27 (c)** and 0.55 eV for the third O-^{i}Pr ligand **Fig. 27 (d)**, therefore, leading to an overall energy of -1.52 eV for the loss of three O-^{i}Pr ligands and the formation of monoisopropoxy ZrO_2 (iPr-O-Ti-ZrO_2). Following this, titanium binds to the surface with three new Ti-O bonds with lengths 2.05 Å, 1.81 Å, and 1.82 Å. After the TTIP pulse, the surface is left covered with one O-$CH(CH_3)_2$ ligand and the next pulse will result in exchange of the ligand with the ManNAc molecule.

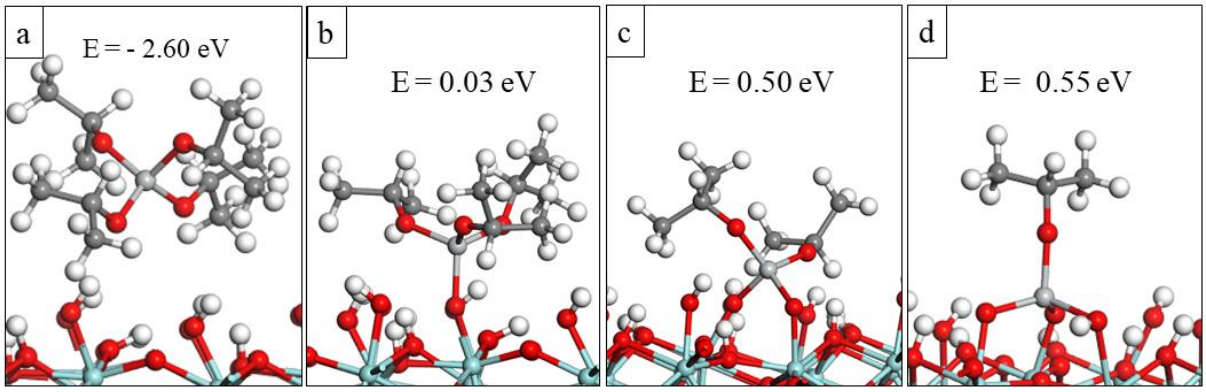


Figure 27 Optimised atomic structure of a) TTIP interacting with the hydroxylated ZrO_2 surface, b) elimination of the first O-$CH(CH_3)_2$ ligand, c) elimination of the second O-$CH(CH_3)_2$ ligand and d) elimination of the third O-$CH(CH_3)_2$ ligand. Cyan-Zr.

Next, the MLD reaction using ManNAc as organic reactant was analysed. **Fig. 28 (a)** shows the atomic structure of the Ti-O-$CH(CH_3)_2$ terminated ZrO_2 surface after ManNAc pulse. During this reaction a side proton from an OH group of ManNAc transfers to the O-^{i}Pr ligand to form a new HO-^{i}Pr molecule and the remaining oxygen binds to titanium with a Ti-O distance 1.84 Å. The calculated energy for this reaction is -1.24 eV and leads to an overall reaction energy -2.76 eV, and confirms that this reaction is also favorable. For the second cycle of the MLD process, the remaining OH groups of ManNAc react with TTIP, and form two new Ti–O bonds with distances 2.0 Å and two HO-^{i}Pr molecules are released. Calculated energy for this reaction is -1.08 eV.

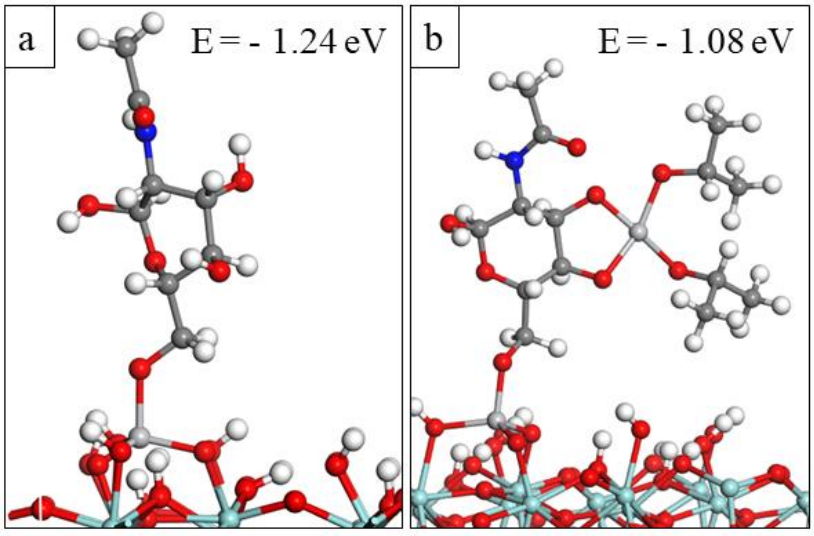


Figure 28 Optimised atomic structure of the reaction product of a) the interaction of the ZrO_2-Ti-O-$CH(CH_3)_2$ surface with ManNAc and b) ManNAc on the ZrO_2-Ti-O-$CH(CH_3)_2$ surface with adsorption of TTIP.

The exothermic reaction shows that ManNAc reacts favourably with TTIP in the second cycle of the MLD process and consequently we expect growth to proceed for titanochitin MLD thin films. The proposed reaction mechanism between TTIP and ManNAc that leads to the formation of the hybrid titanochitin material is energetically favourable.

6.4.3 Antibacterial activity of Alumochitin and Titanochitin MLD films

The main purpose of the growth of biomimetic chitinoid films is the generation of antimicrobial activity, which is intrinsic to the natural chitin. The antimicrobial activity of the alumochitin and titanochitin MLD films was evaluated against Gram-positive (Staphylococcus aureus, *S. aureus*) and Gram-negative (*Escherichia coli, E.Coli*) bacteria. The bacterial adhesion and proliferation was compared on glass substrates, covered with either of the metallochitins by MLD and with the corresponding ceramic (TiO_2 and Al_2O_3) by ALD. Coverslips coated with crystalline nanocellulose served as control samples. The resulting confocal microscopy images of *S. aureus and E. coli* bacterial biofilms for each substrate after 24h of exposure are shown in **Fig. 29.**

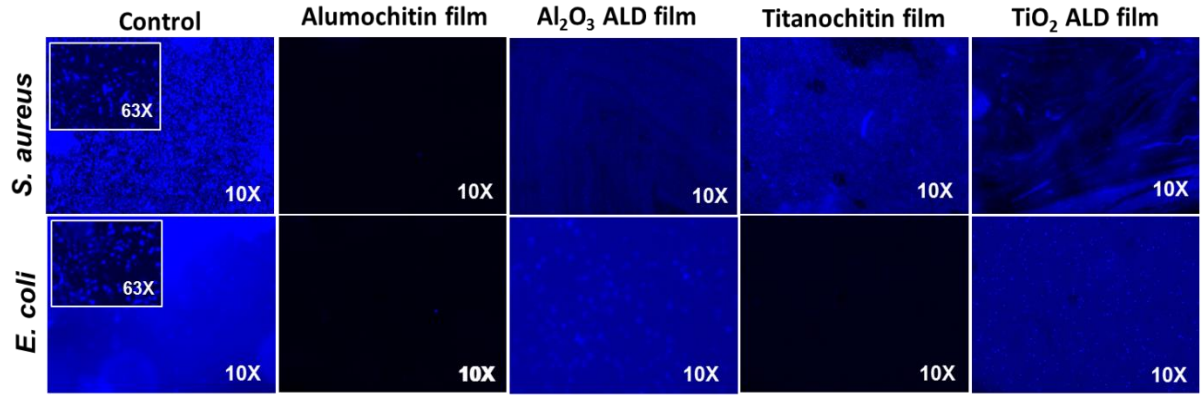


Figure 29 Confocal microscopy images of S. aureus and E. coli bacterial biofilms on the indicated substrates after 24h of exposure. Original magnification 10x (scale bar = 10 μm). Crystalline nanocellulose film was used as a control. Bacteria were stained with 4′,6-diamidino-2-phenylindole (DAPI) (blue).

Both types of bacteria grow and proliferate on the control samples with a crystalline nanocellulose film. Coverslips coated with the alumochitin film prevent the attachment of both types of bacterial strains, clearly demonstrating a very efficient antibacterial activity. The corresponding inorganic alumina film showed the opposite result, allowing proliferation of both types of bacteria. Similar to the alumochitin, the substrates coated with titanochitin

inhibited the formation of an *E. coli* biofilm. However, *S. aureus* biofilm formation was observed on titanochitin coated coverslips, suggesting a great difference in the bacterial inhibition mechanisms of the two metallochitins. For titanium oxide substrates, both *S. aureus and E. coli* attach and proliferate on its surface.

6.5 Conclusion

In this chapter we investigated new types of magnesium (Mg), cerium (Ce) and chitin $(C_8H_{13}O_5N)_n$ based hybrid MLD films. A combination of experimental data and theoretical data was done to better understand the deposition reaction mechanism of the new deposited MLD films.

Magnesicone films

A novel MLD process to deposit magnesium containing hybrid thin films, or "magnesicones", using bis-(methylcyclopentadienyl) magnesium ($Mg(MeCp)_2$) and ethylene glycol (EG) or glycerol (GL) is reported. Saturated growth could be achieved at 2 to 3 Å/cycle using relatively short precursor pulses (10 s) in a wide temperature window from 100 to 250°C for both chemistries. Growth profiles of EG based magnesicone films and GL based magnesicone films show that while thicker films are deposited with GL, for EG the reservoir like effect takes place where unbound EG gets incorporated in the film during film growth, which then reacts when coming into contact with the $Mg(MeCp)_2$ during the $Mg(MeCp)_2$ pulse, showing so additional growth. To determine film composition, both films were characterised with XPS and it was found that EG and GL magnesicone films contain about 43 and 46 at. % carbon, respectively.

We performed DFT calculations to investigate the molecular mechanism of the growth of EG magnesicone and GL magnesicone films grown by MLD and to understand the experimental results regarding the effect of the organic species on film growth. DFT calculations were carried out using the reaction of EG and GL at MgCp terminated MgO (100) as a model system. Interaction energies of EG and GL calculated by DFT, presented some clear differences in reaction mechanism. While the ligand elimination process is favorable for both organic precursors, GL species prefer to lie in an upright configuration and EG prefers to orient in a flat configuration and interacts at the MgO (100) surface. Therefore, the GL based magnesicone will grow thicker compared to the EG based magnesicone as observed for the standard MLD process before the "reservoir" effect complicates the growth. We found that the reservoir of incorporated EG molecules in the growing film is plausible as the energy gained from the interactions between EG and the MgO surface is found to be larger compared to the energy gained from the ligand exchange process. The water absorption and accompanying swelling of the deposited films, as well as their stability with respect to the TMA-H_2O process provided proof of concept of their applicability as water barrier layers for flexible electronics.

Ceria hybrid films

Thin films of the cerium based hybrid materials were successfully grown using the Ce (III) guanidinate precursor, $Ce(dpdmg)_3$, as a source of cerium along with terephthalic acid (TPA) and hydroquinone (HQ) as the organic linkers. Aromatic molecules like TPA and HQ have proven to be a good solution to produce thicker and more flexible films as due to their stiff backbone they avoid the unwanted double reactions. [20-22] Thermal studies of precursors showed that the precursors are sufficiently volatile and thermally stable at given deposition temperatures. A GPC of 5.94 Å/cycle was achieved with TPA at 200°C while HQ gives a GPC of 4.7 Å/cycle at 190 °C.

We used DFT calculations to explore in more detail surface and precursor chemistry in ceria hybrid film growth using the reactions of TPA and HQ at Ce(dpdmg) terminated CeO_2 (111) as a model system. DFT shows that $Ce(dpdmg)_3$ interacts and binds favourably with the CeO_2 surface. The oxidation state of cerium atom of the adsorbed $Ce(dpdmg)_3$ molecules is Ce^{3+} and does not change during the ligand lose reactions. DFT calculations also predicted the reactivity of TPA and HQ precursors towards the chemisorbed $Ce(dpdmg)_3$ inorganic precursor to be favourable and the charge of the cerium atom of $Ce(dpdmg)_3$ after the reaction with the these organic molecules to be still +3, which was also confirmed by XPS. In summary, DFT calculations indicate that the formation of oxide/metal-organic films of CeO_2/Ce-TPA and CeO_2/Ce-HQ is energetically feasible.

The deposited films were found to be highly UV absorbing. Hence, we envision that these films could find future application as promising redox active materials and/or UV absorbing materials.

Alumochitin films and Titanochitin films

New processes for growing natural chitin based hybrid films with MLD were developed. The processes rely on sequential depositions of trimethylaluminium (TMA) and N-acetyl-D-Mannosamine (ManNAc) to deposit alumochitin hybrid films and titanium isopropoxide (TTIP) and ManNAc to deposit titanochitin hybrid films. The alumochitin films grew linearly with the number of reaction cycles with a GPC of 1.3 ± 0.1 Å at 115°C while the average GPC of titanochitin films was 1.0 Å/cycle.

DFT calculation were performed to investigate in detail the growth mechanisms of hybrid alumochitin and titanochitin hybrid films. A hydroxylated ZrO_2 (111) surface was used to

model both MLD films. For alumochitin films the ZrO_2 surface was modified with TMA and ManNAc while for titanochitin films this surface was modified with TTIP and ManNAc.

Reaction energetics calculated with DFT show that the proposed reaction mechanism for alumochitin and titanochitin films are favourable. TMA adsorbs on the hydroxylated ZrO_2 surface most likely through the elimination of two CH_3 ligands. Calculations show that ManNAc will bind favourably to the $Al(CH_3)$-terminated ZrO_2, via formation of Al-O bonds and CH_4 elimination. The exothermic interaction energies between TMA and ManNAc observed for the reactions in the first and second cycle of the MLD process confirm the strong interactions between the two precursors promoting formation of the alumochitin hybrid material.

TTIP adsorbs on the hydroxylated ZrO_2 surface through the elimination of three $O\text{-}CH(CH_3)_2$ ligands and will bind favourably with ManNAc via formation of Ti-O bonds and $HO\text{-}CH(CH_3)_2$ elimination. The reaction between ManNAc and TTIP in the second cycle of the MLD process is also energetically favourable and therefore we expect growth to proceed for titanochitin MLD thin films. Alumichitin and titanochitin films were testes for their antibacterial activity. While titanochitin films demonstrated antibacterial activity only towards the gram negative *E. coli* biofilm, alumochitin films demonstrated antibacterial activity towards the gram negative *E. coli and* gram positive *S. aureus* biofilms.

6.6 References

1. J. Kint, F. Mattelaer, S. S. T. Vandenbroucke, A. Muriqi, M. M. Minjauw, M. Nisula, Ph.M. Vereecken, M. Nolan, J. Dendooven, Ch. Detavernier, *Chemistry of Materials*, **2020**, 32, 4451–4466.
2. D. J. Comstock, J. W. Elam, *Journal of Physical Chemistry C*, **2013**, 117, 1677–1683.
3. E. Østreng, H. H. Sønsteby, T. Sajavaara, O. Nilsen, H. Fjellvåg, *Journal of Materials Chemistry C*, **2013**, 1, 4283–4290.
4. O. Nilsen, K. Klepper, H. Nielsen, H. Fjellvaåg, *ECS Transactions*, **2008**, 16, 3–14, 2008.
5. D. Seghete, R. A. Hall, B. Yoon, S. M. George, *Langmuir*, **2010**, 26, 19045–19051.
6. P. Sundberg, M. Karppinen, "*Beilstein Journal of Nanotechnology*, **2014**, 5, 1104–1136.
7. S. M. George, B. H. Lee, B. Yoon, A. I. Abdulagatov, R. A. Hall, *Journal of Nanoscience and Nanotechnology*, **2011**, 11, 7948–7955.
8. A. A. Dameron, D. Seghete, B. B. Burton, S. D. Davidson, A. S. Cavanagh, J. A. Bertrand, S. M. George, *Chemistry of Materials*, **2008**, 20, 3315–3326.
9. B. B. Burton, D. N. Goldstein, and S. M. George, *Journal of Physical Chemistry C*, **2009**, 113, 1939–1946.
10. K. Kerckhove, F. Mattelaer, D. Deduytsche, P. M. Vereecken, J. Dendooven, Ch. Detavernier, *Dalton Transactions*, **2016**, 45, 1176–1184.
11. D. S. Bergsman, R. G. Closser, and S. F. Bent, *Chemistry of Materials*, **2018**, 30, 5087–5097.
12. L. Ju, V. Vemuri, and N. C. Strandwitz, *Journal of Vacuum Science & Technology A*, **2019**, 37, 030909.
13. P. Kaur, A. Muriqi, J-L Wree, R. Ghiyasi, M. Safdar, M. Nolan, M. Karppinen, A. Devi, *Dalton Trans*actions, **2022**, 51, 5603–5611.
14. P. Kaur, L. Mai, A. Muriqi, D. Zanders, R. Ghiyasi, M. Safdar, N. Boysen, M. Winter, M. Nolan, M. Karppinen, A. Devi, *Chemistry–A European Journal*, **2021**, 27, 4913–4926.
15. M. Romeo, K. Bak, J. El Fallah, F. Le Normand, L. Hilaire, *Surface and Interface Analysis*, **1993**, 20, 508–512.
16. E. Bêche, P. Charvin, D. Perarnau, S. Abanades, G. Flamant, *Surface and Interface Analysis*, **2008**, 40, 264–267.
17. T. L. Barr and S. Seal, *Journal of Vacuum Science & Technology A*, **1995**, 13, 1239–1246.
18. A. Farahmand Kateshali, S. Gholizadeh Dogaheh, J. Soleimannejad, A. J. Blake, *Coordination Chemistry Reviews*, **2020**, 419, 213392.
19. S. Rhatigan, M. Nolan, *Journal of Materials Chemistry A*, **2018**, 6, 9139–9152.
20. A. Muriqi, M. Karppinen, M. Nolan, *Dalton Transactions*, **2021**, 50, 17583–17593.
21. P. Sundberg and M. Karppinen, *European Journal of Inorganic Chemistry*, **2014**, 968–974.
22. A. Tanskanen, P. Sundberg, M. Nolan, M. Karppinen, *Thin Solid Films*, **2021**, 736, 138896.
23. R. A. Nye, S. Wang, S. Uhlenbrock, J. A. Smythe, G. N. Parsons, *Dalton Transactions*, **2022**, 51, 1838–1849.
24. J. W. Dumont, S. M. George, *Journal of Physical Chemistry C*, **2015**, 119, 14603–14612.
25. K. H. Yoon, H. Kim, Y. E. Koo Lee, N. K. Shrestha, M. M. Sung, *RSC Advances*, **2017**, 7, 5601–5609.
26. V. R. Rai, S. Agarwal, *Journal of Physical Chemistry C*, **2009**, 113, 12962–12965.

27. S. Wang, C. Wang, H. Wang, X. Chen, S. Wang, *Polymer Degradation and Stability*, **2015**, 114, 105–114.
28. V. R. Anderson, A. S. Cavanagh, A. I. Abdulagatov, Z. M. Gibbs, S. M. George, *Journal of Vacuum Science & Technology A*, **2014**, 32, 01A114.
29. Y-Q. Cao, X-R. Zhao, J. Chen, W. Zhang, M. Li, L. Zhu, X-J. Zhang, D. Wu, A-D. Li, *Scientific Reports*, **2018**, 8, 1–9.
30. N. C. Saha, H. G. Tompkins, *Journal of Applied Physics*, **1992**, 72, 3072–3079.
31. N. Jiang, H. J. Zhang, S. N. Bao, Y. G. Shen, Z. F. Zhou, *Physica B: Condensed Matter*, **2004**, 352, 118–126.
32. T. Jia, F. Fu, D. Yu, J. Cao, G. Sun, *Applied Surface Science*, **2018**, 430, 438–447.

Chapter 7

Modelling of VPI processes

7.1 Introduction

In this chapter we discuss the results of our computational studies and related experiments with collaborators on vapour phase infiltration (VPI) processes. In both studies my density functional theory (DFT) calculations were employed to investigate diffusion phenomena of MLD precursors into polymeric substrates with the VPI technique and to understand the chemical interactions of the precursors with the polymers.

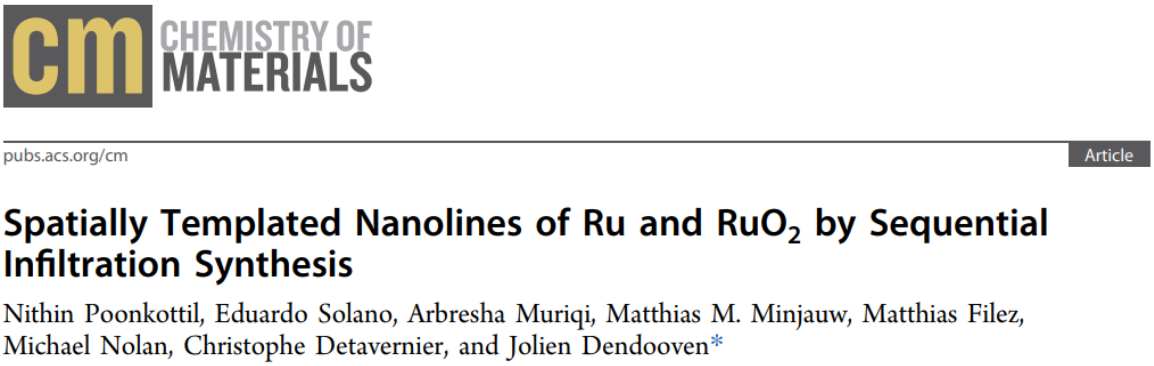
In **Section 7.2** we use DFT calculations to predict the infiltration of ruthenium oxide (RuO_4) into polystyrene-block-polymethyl methacrylate (PS-b-PMMA) templates by comparing the interactions of RuO_4 with PS and PMMA oligomers. A selective infiltration of RuO_4 into one of the polymers is important for the fabrication of nm-scale ruthenium lines which are a candidate in future interconnects. DFT shows that the PS-RuO_4 interaction is favourable, with a calculated interaction energy of -1.65 eV, suggesting that the infiltration of RuO_4 into PS can occur. The calculated energetics also show that hydrogen is a suitable coreactant to reduce the infiltrated RuO_4 molecules to metallic Ru. For PMMA-RuO_4 the calculated interaction energy of -0.05 eV indicates an unfavourable interaction, which is an indication that RuO_4 may not infiltrate into the PMMA polymer and the polymer will maintain its original properties. The RuO_4/PS-b-PMMA VPI process with H_2O_2 as coreactant was experimentally developed and *in situ* techniques prove that RuO_4 interacts selectively and strongly with the aromatic C = C and C−H groups in PS, leaving the PMMA domains inert, which is consistent with DFT data.

Section 7.3 discuses VPI hybrid materials with self-healing properties, specifically parylene C/indium oxide (In_2O_3) and parylene C/zinc oxide (ZnO) hybrid films. We have employed DFT studies to investigate the possible chemical reactions during the infiltration of parylene C polymer with trimethylindium (TMIn) and peroxide (H_2O_2) for In_2O_3 based films and with diethylzinc (DEZ) and H_2O_2 for ZnO based films. DFT indicates that metal hydroxides (M-OH) species are formed during both processes which can bind to the aliphatic and aromatic carbons of the polymer. The increase of the concentration of H_2O_2 leads to the formation of additional species such as indium chloride ($InCl_3$) and phenol rings for the In_2O_3 based process

and phenol rings for the ZnO based process which have also been observed in experimental work.

7.2 Modelling of Ru VPI films

This work is published in the paper "***Ruthenium and Ruthenium Dioxide Nanostructures via Sequential Infiltration Synthesis in Self-assembled Block co-polymer Thin Films***" in Chemistry of Materials. [1]



DOI: https://doi.org/10.1021/acs.chemmater.2c01866

7.2.1 Results

Three different polymers were studied for the ruthenium sequential infiltration synthesis (SIS) system, polystyrene (PS) and polymethyl methacrylate (PMMA) homopolymers and polystyrene-block-polymethyl methacrylate (PS-b-PMMA) di-block copolymer thin films. The combination of PS and PMMA polymers in a self-assembled manner leads to the formation of PS-b-PMMA block copolymer, **Fig. 1**.

In our DFT work we compare the interactions of RuO_4 as ruthenium source with PMMA and PS oligomers and this is enough to understand the infiltration of RuO_4 in the PS-b-PMMA block copolymer.

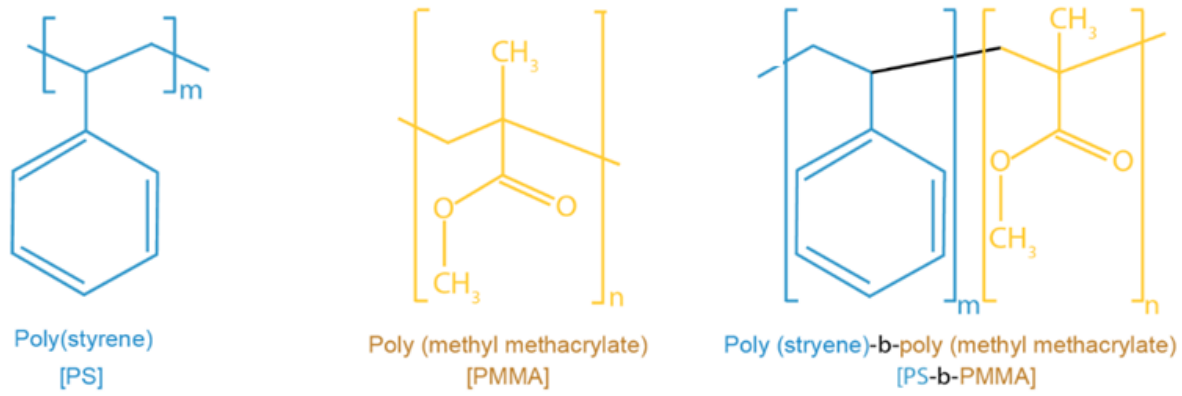


Figure 1 Molecular structure of polystyrene (PS) homopolymer, polymethyl methacrylate (PMMA) homopolymer and polystyrene-block-polymethyl methacrylate (PS-b-PMMA) di-block copolymer.

7.2.1.1 Computational results

Density functional theory (DFT) calculations were performed to predict infiltration of RuO_4 precursor into the PMMA and PS polymers during the VPI process by comparing the interactions of RuO_4 with PS and PMMA oligomers. Our PMMA and PS models are oligomers that consist of three methyl methacrylate monomers and three styrene monomers, respectively. We use these simplified models of PMMA and PS polymers and one single RuO_4 molecule since this is enough to investigate the key interaction between RuO_4 molecules and PMMA and PS polymers in the infiltration process. PMMA is a homopolymer that contains of two side groups attached to the alkyl chain, a methyl group, and an ester functional group while PS is a homopolymer that contains a hydrocarbon chain with a side benzene group. The main difference between these two polymers is the presence of functional groups in PMMA and their absence in PS.

Fig. 2 shows the relaxed atomic structure of PMMA oligomer after the interaction with one RuO_4 molecule. We have considered two different interaction sites for RuO_4 with PMMA. In the first model the RuO_4 molecule was placed between the monomer units and near the methoxy group while in the second model the RuO_4 molecule was placed near the methyl group. The optimised atomic structures show that no new bonds are formed between PMMA and RuO_4. The calculated interaction energies for the first model (**Fig. 2 (a)**) and the second model (**Fig. 2 (b)**) are 0.27 eV and -0.05 eV, respectively and these show an unfavourable interaction between RuO_4 and PMMA. Therefore we expect that the chemical groups associated with PMMA are not effected during the RuO_4 pulse (**Section 7.2.1.2).** The lack of

interaction between RuO_4 and PMMA indicates that RuO_4 will not infiltrate into PMMA. However, the low solubility and/or low diffusivity of RuO_4 in PMMA also can play a role in this apparent lack of infiltration. [2]

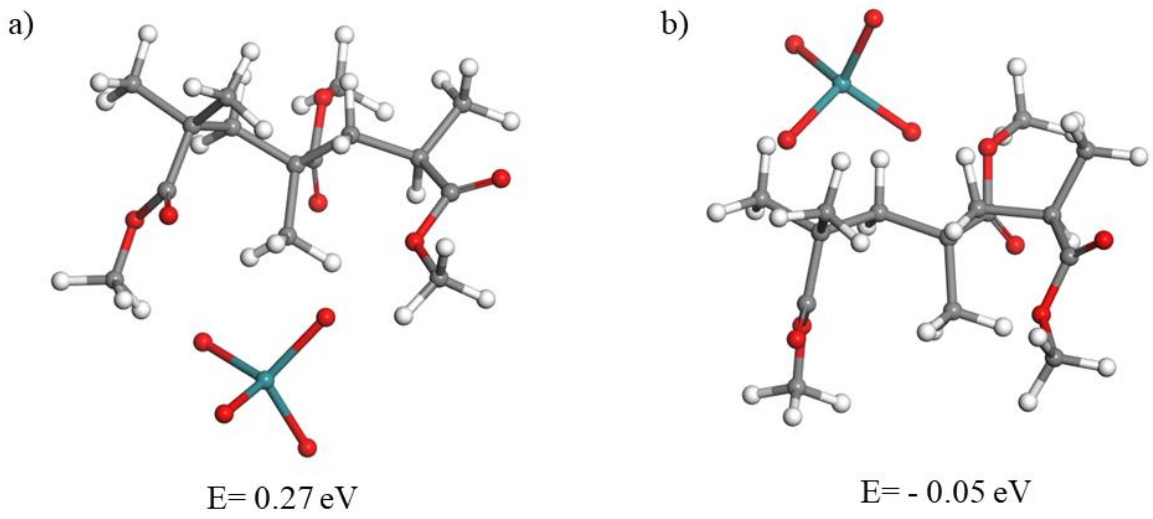


Figure 2 Optimised atomistic structure of RuO_4 located near the a) methoxy group of PMMA and b) methyl group of PMMA. Cyan-Ru, red-O, grey-C, white-H.

On the other hand, the calculated interaction energy of -1.65 eV for RuO_4 with PS indicates an exothermic interaction, and therefore a favourable interaction between RuO_4 and PS. The optimised atomic structure of PS after the interaction with one RuO_4 molecule presented in **Fig. 3 (a)**, shows that RuO_4 binds to the aromatic carbon atoms of PS by forming two new O-C bonds with distances of 1.44 Å and 1.42 Å. After binding with RuO_4, the C = C distance of these carbon atoms increases from 1.39 Å in PS to 1.52 Å, which removes the aromatic character of the ring. Based on the calculated energies, during the RuO_4/PS-b-PMMA VPI process we expect a strong and selective interaction of RuO_4 with the aromatic C = C groups in PS, leaving the PMMA domains inert.

Given the interaction of RuO_4 with PS, we next investigate the interactions between RuO_4-PS and hydrogen (coreactant) by expanding the RuO_4-PS model to include one hydrogen molecule. **Fig. 3 (b)** depicts the optimised atomic structure of RuO_4-PS after the incorporation of one hydrogen molecule. The hydrogen molecule binds with one oxygen atom of RuO_4 with a H-O distance 1.11 Å. The overall calculated energy change for this reaction is -1.70 eV. In the next step we consider the formation of one water molecule. The optimised atomic structure of this reaction product is presented in **Fig. 3 (c)**. This reaction involves the dissociation of the

hydrogen molecule and the binding of the hydrogen atoms with one oxygen atom of RuO_4 to form a water molecule while the existing Ru-O bond is lengthened from 1.65 Å to 2.13 Å. The calculated energy gain for this reaction is -1.44 eV relative to the model in **Fig. 3 (b)**, leading to an overall energy change of -3.14 eV. The final step of hydrogen and RuO_4-PS involves breaking the Ru-O distance and the release of a water molecule. The optimised atomic structure of this reaction product is presented in **Fig. 3 (d)** and the calculated energy cast to release one water molecule is 0.03 eV relative to the model in **Fig. 3 (c)**, leading to an overall energy change of -3.11 eV. The negative energies calculated for the reactions of RuO_4-PS with hydrogen indicate that hydrogen coreactant is able to reduce the RuO_4 molecules infiltrated into the PS polymer, which will yield metallic Ru. Therefore we predict that the RuO_4-PS-b-PMMA VPI process with hydrogen as coreactant will successfully enable the fabrication of nm-scale ruthenium lines.

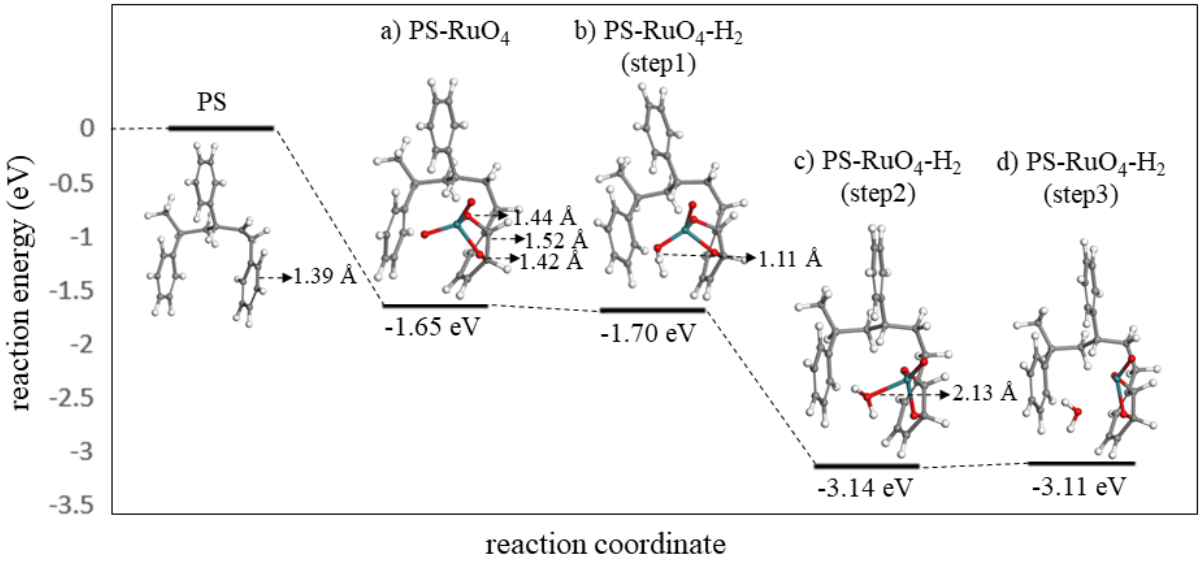


Figure 3 Optimised atomistic structures of a) PS interacting with RuO_4, b) PS interacting with RuO_4 and H_2, c) PS interacting with RuO_4 and H_2-H_2O formation and d) PS interacting with RuO_4 and H_2-H_2O release.

7.2.1.2 Selected experimental results (Ghent University)

SIS process development

The SIS technique is a variant of the VPI technique, with the only difference being in the process parameters. Nevertheless, the atomic-scale processes are the same for both techniques. The ruthenium SIS process relies on a previously developed rutheniumALD process using

RuO_4 as the ruthenium precursor, and hydrogen gas as the coreactant. [3] For the ruthenium SIS, the working substrate temperature was chosen to be 120°C as this temperature is above the glass transition temperature of both PS (100°C) and PMMA (105°C) homopolymers to ensure maximum free volume of these polymers. All polymers were prepared by spin coating and then transferred to the ALD chamber. Then these polymers were exposed to RuO_4 at a pressure of ca. 2 mbar and hydrogen gas at a pressure of ca. 5 mbar in a cyclic manner. An overview of the developed SIS process for ruthenium is depicted in **Fig. 4**.

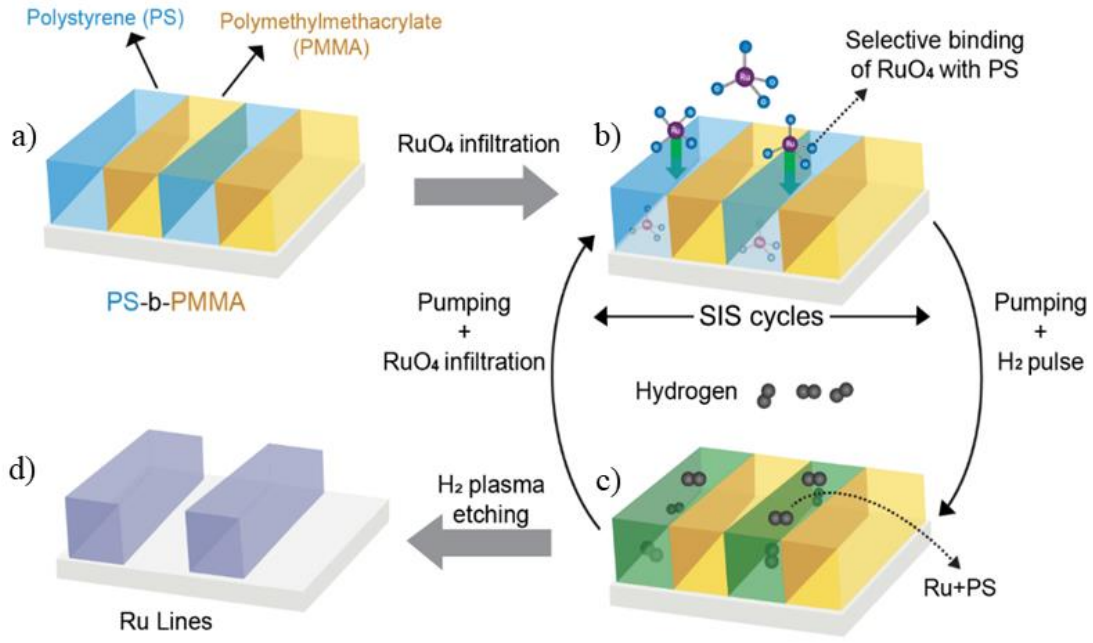


Figure 4 Simplified illustration of the ruthenium SIS process. a) Starting PS-b-PMMA template containing both PS and PMMA domains. b) Selective RuO_4 infiltration into PS domains. c) Chemical modification of the PS domain followed by hydrogen pulse to form metallic ruthenium inside PS domains. d) A hydrogen plasma etch step to remove the BCP template to generate ruthenium nanopatterns on the substrate surface.

In situ spectroscopic ellipsometry (SE) and X-ray photoelectron spectroscopy (XPS) characterisations

The infiltration process was monitored *in situ* using SE to observe the changes in the psi (Ψ) value as this can be used as an identification of the selectivity. [4] As shown in **Fig. 5 (a)**, on PS the Ψ value changes from the very first cycle, but on the other hand it remains unchanged on PMMA films even after 200 cycles. This in turn indicates the selective reaction of the RuO_4 precursor with PS compared to PMMA, opening up opportunities for selective infiltration of

the PS component in PS-b-PMMA di-block copolymer, satisfying the necessary conditions for block copolymer (BCP) based lithography, as stated before.

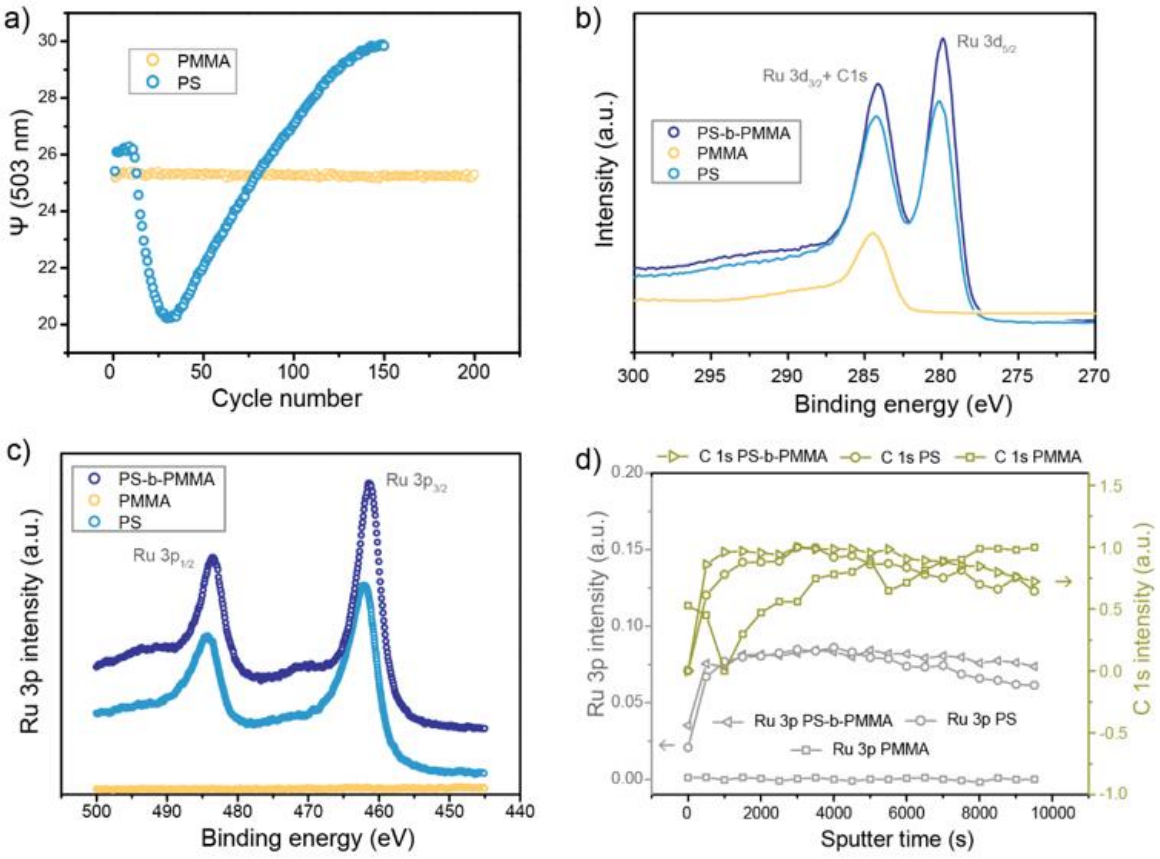


Figure 5 a) *In situ* ellipsometry data on PS and PMMA homopolymers during the ruthenium SIS experiments. *Ex situ* XPS after 30 SIS cycles, b) Ru 3d peaks on PS, PMMA and PS-b-PMMA, c) Ru 3p peaks and d) XPS depth profile for C1s and Ru 3p intensities on the polymers after 30 SIS cycles.

The selectivity was further corroborated using XPS, after 30 cycles. The Ru 3d XPS region is presented in **Fig. 5 (b)**. On PMMA, no Ru $3d_{5/2}$ peak is present, but in PS and PS-b-PMMA this feature is present. The selective infiltration of RuO_4 with PS is also revealed by the Ru 3p peaks in **Fig. 5 (c)**. PS and PS-b-PMMA gave rise to Ru 3p peaks after the SIS process, whereas no Ru 3p peak could be observed on PMMA. To confirm the ruthenium infiltration into the free volume (bulk) of the polymers, XPS depth profiling (**Fig. 5 (d)**) was performed. The Ru 3p intensity on both PS and PS-b-PMMA tends to follow the same trend as C 1s peak in these polymers, which indicates the binding of ruthenium with the carbon in the polymer and clear infiltration of ruthenium into the bulk of the polymer, in agreement with the in SE and DFT data. In short, excellent selective infiltration of RuO_4 molecules into PS could be achieved.

In situ Fourier-transform infrared (FTIR) spectroscopy characterisation

The PS and PMMA spectra (referenced to the blank Si substrate) are provided in **Fig. 6 (a)** and **(b)** for easy comparison. After the RuO_4 pulses, as evident from **Fig. 6 (a)**, negative features appear around 3026 cm^{-1}, 3063 cm^{-1}, and 3082 cm^{-1}, which reveal the interaction and subsequent consumption of aromatic CH groups by the RuO_4 molecules. Another set of negative features, that appear around 1602 cm^{-1}, 1584 cm^{-1}, 1493 cm^{-1}, and 1452 cm^{-1} correspond to aromatic C=C/C-C stretching. The other weak features that get consumed are around 2926 cm^{-1}, 2847 cm^{-1} (asymmetric, symmetric stretching of methylene, $-CH_2$, respectively), and the out of plane CH bending at ca. 698 cm^{-1}. The interaction and consumption of aromatic C-H and C=C groups by RuO_4 even after just one RuO_4 pulse, is clear from the *in situ* FTIR data. FTIR measurements are in a very good agreement with the DFT data which also show that RuO_4 removes the aromatic character of the rings of the PS oligomer (**Fig. 3**), through the interaction with the C=C bond in the ring.

On the other hand, the blanket PMMA spectrum (**Fig. 6 (b)**) indicates the typical feature expected for the C=O group at 1730 cm^{-1} as the major peak. The spectrum after 5 RuO_4 pulses and even after 30 RuO_4 pulses did not lead to significant changes compared to the pristine PMMA spectrum, indicating the absence of (significant) interaction of RuO_4 with PMMA related groups, in agreement with DFT, SE and XPS data presented earlier.

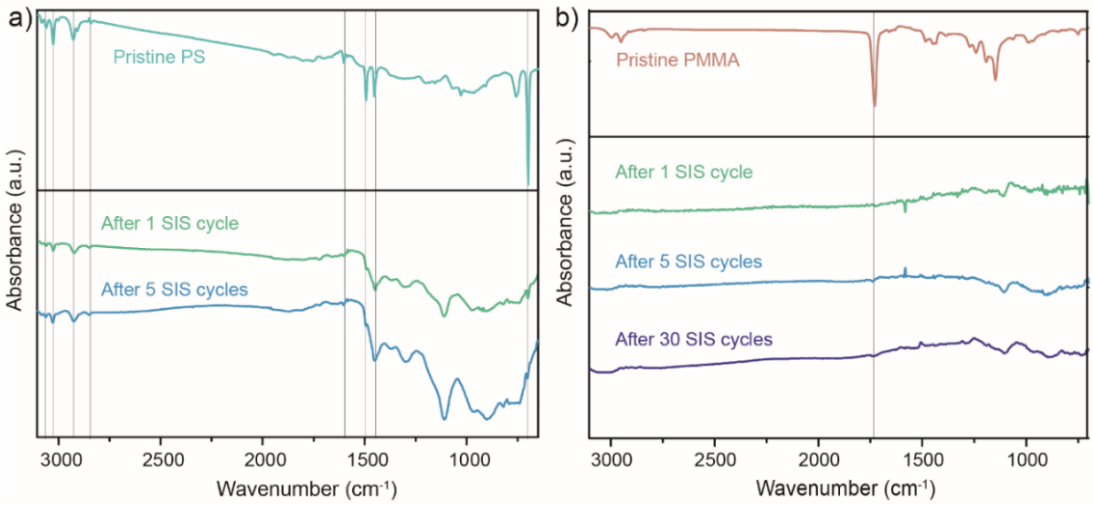
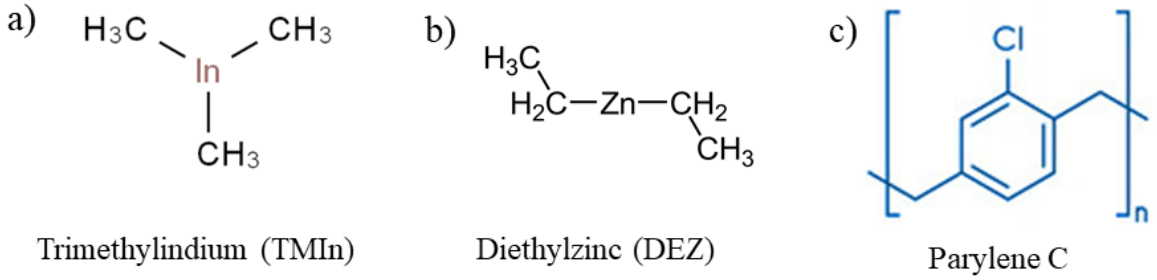


Figure 6 *In situ* FTIR data during RuO_4 infiltration on a) PS and b) PMMA blanket homopolymers. The reference spectra of the polymer films are shown on top of the graphs. The *in situ* spectra during the SIS process were recorded, and then subtracted from the spectrum recorded for the corresponding polymer film on Si to obtain difference spectra.

7.3 Modelling of In_2O_3 and ZnO VPI films

7.3.1 Results on In_2O_3 VPI process

The metalorganics employed for the indium oxide infiltration and zinc oxide infiltration are trimethylindium (TMI) and diethylzinc (DEZ). **Fig. 7** shows the chemical structures of the TMIn and DEZ precursors and a monomer of parylene C.



Trimethylindium (TMIn) Diethylzinc (DEZ) Parylene C

Figure 7 Molecular structure of trimethylindium (TMIn) and diethylzinc (DEZ) precursors and parylene C polymer.

7.3.1.1 Computational results on In_2O_3 VPI films

Density functional theory (DFT) calculations are performed to investigate the possible chemical reactions during the infiltration process of parylene C with TMIn and H_2O_2 that enables the growth of metal oxides within polymer volumes. The model for the parylene C polymer is a periodic supercell composed of two parylene C chains, each with a total of six rings.

In the first step of our calculations, the TMIn molecule was placed between two parylene C chains and the structure was allowed to relax. **Fig**. **8 (a)** shows the atomic structure of the parylene C chains infiltrated with TMIn into the polymer. The moderate calculated interaction energy of -0.52 eV indicates infiltration of the precursor rather than formation of a bond between TMIn and the polymer, which is also clear from the optimised atomic structure shown in **Fig. 8 (a).**

Next, we investigated the interactions between infiltrated TMIn and H_2O_2 by examining the possible reactions when H_2O_2 molecules are added in the system. We found two possible reactions after the introduction of H_2O_2.

The first reaction involves the transfer of two hydrogen atoms from the polymer chain to the methyl (CH_3) ligands of TMIn to release two methann (CH_4) molecules as byproducts, while

In-CH_3 binds to the aliphatic carbon atom of the polymer chain from which the hydrogen atoms were transferred; this C-In distance is 2.12 Å. The remaining CH_3 ligand of TMIn can interact with the H_2O_2 molecule to release a new methanol (CH_3OH) byproduct and this reaction produces a hydroxyl group that binds with indium to form C-In-OH species, with an In-O distance of 2.04 Å and an In-C distance of 2.12 Å. The calculated In-O bond in In-OH is shorter when compared to the calculated In-O bond in In_2O_3 in a previous study, that was found to be 2.11 Å. [5] In-OH is the usual product that is formed when TMIn is exposed to a coreactant such as water or H_2O_2, where the intercalated precursor is irreversibly converted to the oxide/hydroxide form. [6] The calculated energy for this reaction is -1.89 eV, giving a total energy gain of -2.41 eV relative to the free precursors and parylene C. The optimised structure of the reaction product is presented in **Fig**. **8 (b)**.

In the second reaction we consider the formation of byproducts ethane (CH_3CH_3), from two CH_3 ligands of TMIn and CH_3OH upon interaction with H_2O_2.This reaction produces a free OH group that binds to indium to form In-OH, similar to the first reaction. In contrast to the first reaction, here the In-OH adduct remains infiltrated between the two parylene C chains, **Fig. 8 (c)**. The calculated energy for this reaction is -4.20 eV, giving a total reaction energy of -4.72 eV. Calculations show that the second reaction is more favourable and therefore we continue our modelling work with the product from the second reaction.

We also analyse the possible reactions when the concentration of H_2O_2 is increased. This is done by expanding the model system presented in **Fig. 8 (c)** to include a second H_2O_2 molecule. We found that when a second H_2O_2 molecule is added in this system, two more reactions can occur. The first reaction favourably causes the formation of $In(OH)_3$ with a calculated energy of -3.3 eV, **Fig. 8 (d).** The second reaction causes the formation of $InCl_3$ and phenol species, as a result of the exchange of chlorine atoms of parylene C with hydroxyl groups from $In(OH)_3$ and the calculated energy for this reaction is -5.6 eV, **Fig. 8 (e)**. Therefore, the DFT results show that when the concentration of H_2O_2 is increased, the formation of $InCl_3$ species and phenol groups is the most favourable reaction.

In conclusion, based on our DFT calculations we propose that TMIn will favourably infiltrate into the parylene C polymer during the VPI process but will not bind to the polymer until the H_2O_2 coreactant is introduced. The H_2O_2 coreactant will also promote the formation of $In(OH)_3$ and $InCl_3$ species. The formation of these species can be the explanation of the increased

indium, oxygen and chlorine intensities in the FIB-patterned area from the energy dispersive X-ray (EDX) analysis as reported in an earlier study. [7]

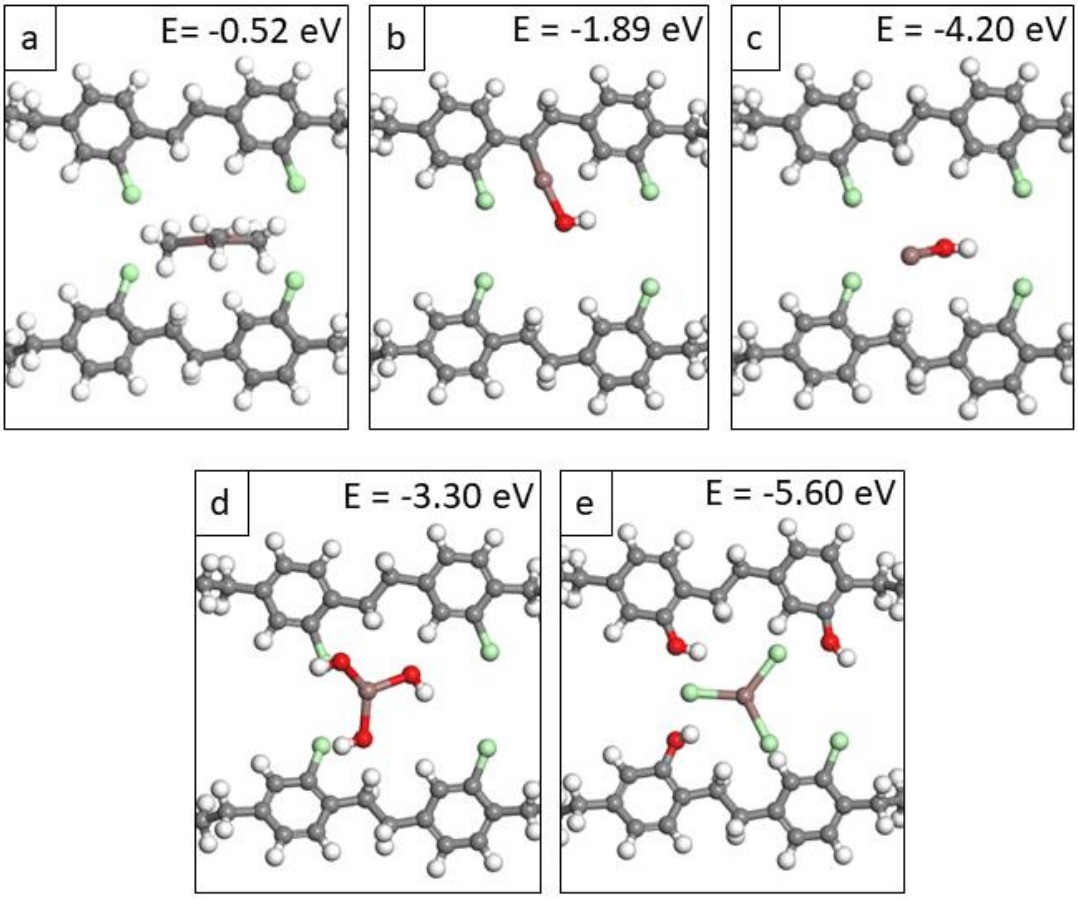


Figure 8 Optimized structures of parylene C infiltrated with a) TMIn, b) TMIn and H_2O_2; C-In-OH formation, c) TMIn and H_2O_2; In-OH formation, d) TMIn and two H_2O_2; $In(OH)_3$ formation and e) TMIn and two H_2O_2; $In(Cl)_3$ and phenol formation. Lilac-In, green-Cl, red-O, grey-C, white-H.

7.3.1.2 Selected experimental results on In_2O_3 VPI films (CIC nanoGUNE)

VPI process development

Indium oxide infiltration was performed by VPI of trimethylindium (TMIn) and 30 % hydrogen peroxide (H_2O_2). First, TMIn was pulsed for 0.4 s to the ALD reactor and left in the chamber for additional 30 s to let the precursor infiltrate the polymeric substrate. It was followed by 60 s of purging time to evacuate an unreacted precursor and byproducts. The same steps were performed for H_2O_2 thus finishing one cycle. The total number of cycles was 150. The reactor temperature was varied between 135 and 210^{o}C.

X-ray photoelectron spectroscopy (XPS) and energy dispersive X-ray (EDX) spectroscopy

Chemical state of the parylene C/In_2O_3 hybrid was studied with XPS (**Fig. 9 (a)**). For parylene C infiltrated with TMIn, Cl 2p was best fitted with two spin-orbit split peaks. This indicated that chlorine was present in two different chemical states. Chlorine bonded to polymer chain has the energy of ~200 eV, while doublet at lower binding energy indicates the metal chloride. The atomic percentage of the indium chloride was as high as 88% near the surface and it steadily dropped with the increase of the etching depth.

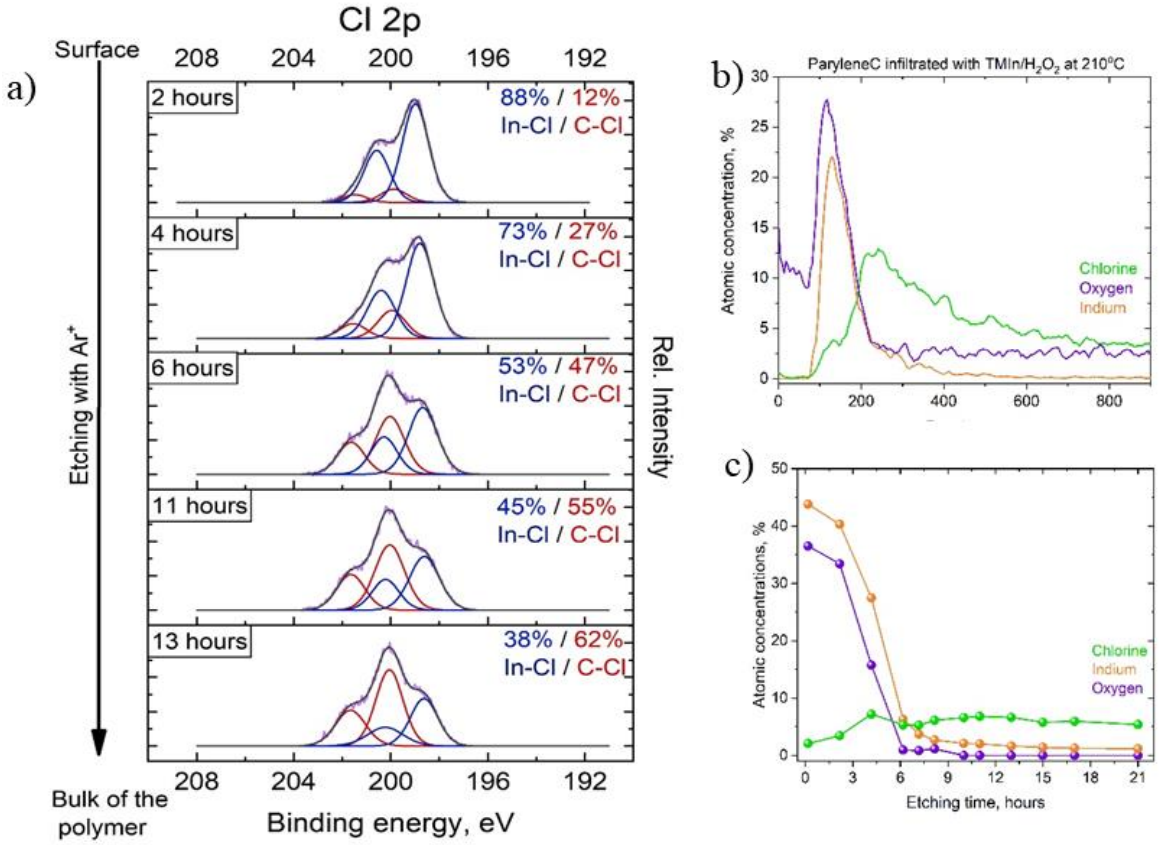


Figure 9 a) XPS depth profile of Cl 2p doublet, b) EDX depth profile and c) atomic concentrations after different etching times calculated from XPS data.

EDX from lamellae was used to estimate the thickness of the hybrid layer (**Fig. 9 (b)**). The thickness of the hybrid was about 150 nm. However, a signal of 2-3 atomic percent was present to 300 nm. Interestingly, there was an increase of chlorine on the interface of parylene C and the hybrid layer, which indicates the mobility of chlorine. Elemental composition was also

studied by XPS as presented in **Fig. 9 (c)**. From the very top layer the formation of parylene C/In_2O_3 hybrid was observed, as there was a signal of C, Cl, In, and O simultaneously.

In situ Fourier-transform infrared (FTIR) spectroscopy

Further measurements were performed with FTIR to corroborate XPS data. **Fig. 10 (a)** shows that for parylene C/In_2O_3 additional free OH groups at 3550-3370 cm^{-1} were observed. Besides, there was a small new peak at 1132 cm^{-1} which could be attributed to phenol formation (**Fig. 10 (b)**). This implies that chlorine on the aryl ring of the polymer was substituted with the OH group, found favourable by DFT. Moreover, there was an indication of another peak appearing around 1093 cm^{-1} which could be linked to a C-O formation. This is consistent with DFT findings which also show the formation of phenol species as a rresult of the exchange of chlorine atoms of parylene C with OH groups of $In(OH)_3$ species (**Fig. 8).** All peaks in the region attributed to C-Cl bands at 800-650 remained, except one not intensive peak at 791 cm^{-1}. This indicated that a part of the chlorine was cut from the polymer chain and reacted with TMIn.

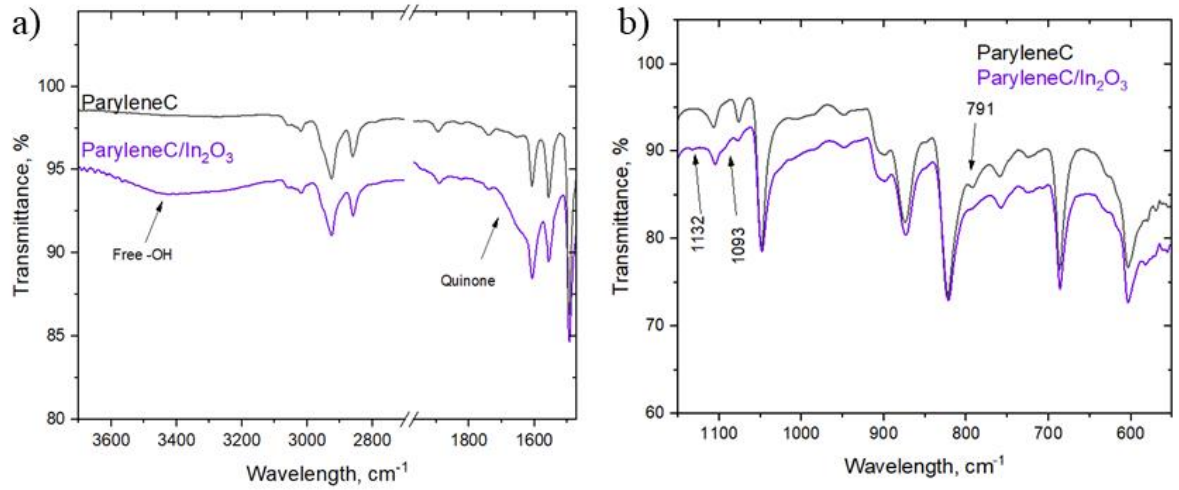


Figure 10 ATR-FTIR spectra of parylene C and parylene C/In_2O_3 of different regions: a) 3700-1530 cm^{-1} and b) 1150-550 cm^{-1}.

Self-healing properties

In discussing the experimental results from our collaborators, we can use the results from reference [7]. The cross-section of the samples was done by focused ion beam (FIB) exposing the underlying hybrid material to the environment (**Fig. 11 (a)**). The EDX maps showed

increased intensities of the carbon and chlorine signals from the exposed parylene C and decreased intensities of indium and oxygen signals in the FIB-patterned area (**Fig. 11 (c)**). After FIB-sputtering of the MeO thin film, the hybrid parylene C/In_xO_y was exposed to air for 5 min. The SEM images show a spherical feature that completely covered the exposed area (**Fig. 11 (b)**). The EDX maps of that region confirm that the spherical neoformation consists of indium and oxygen (**Fig. 11 (d)**). A chlorine signal was also present in the grown feature, albeit lower than that of the surrounding surface. Importantly, the EDX scan of the newly formed feature does not show the presence of carbon. Obviously, upon encountering ambient air the defect healed slowly by migration of the entrapped inorganic material.

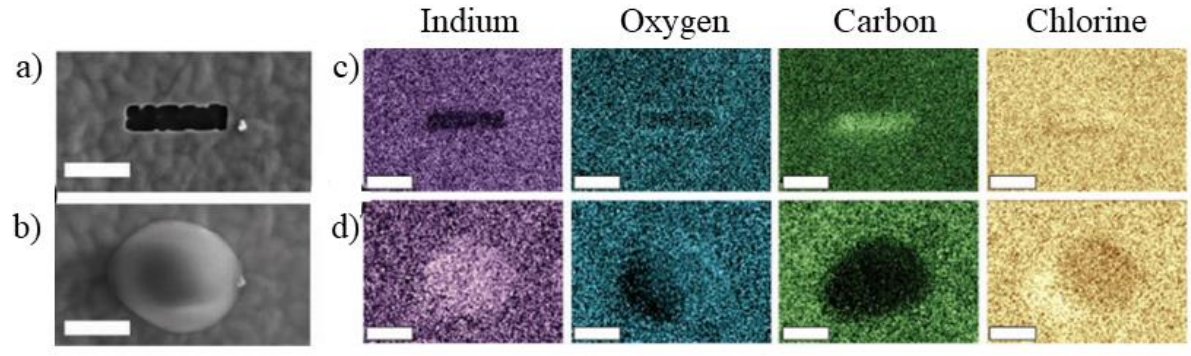


Figure 11 SEM images of the FIB-etched surface of the Parylene C/InxOy hybrid sample a) before exposure to air and b) after exposure to air. Color-coded EDX maps of In, O, C, and Cl c) before exposure to air and d) after exposure to air.

7.3.2 Results on ZnO VPI process

7.3.2.1 Computational results on ZnO VPI films

The growth mechanism of DEZ based parylene C films was investigated through DFT calculations. **Fig. 12 (a)** shows the atomic structure of the parylene C chains infiltrated with DEZ. The calculated incorporation energy of -0.59 eV shows that even DEZ is a larger molecule, it still infiltrates favourably within polymer chains and similar to TMIn, does not bind to the polymer. The calculated energy for the infiltration of DEZ is larger when compared to energy for the infiltration of TMIn (-0.52 eV); this because as a larger molecule, DEZ has stronger vdW interactions with the polymer and this increases the interaction energy.

Next, we analysed the possible reactions upon introduction of H_2O_2 and found that during the H_2O_2 pulse three reactions can occur.

The first reaction involves the transfer of one proton from the polymer chain to the ethyl (CH_3CH_2) ligand of the DEZ molecule to form a new ethane (CH_3CH_3) molecule that is released as byproduct while the remaining Zn-CH_2CH_3 binds to the aliphatic carbon atom of the polymer chain from which the proton atom is transferred. Upon interaction with H_2O_2, the remaining CH_3CH_2 ligand is released in form of ethanol (CH_3CH_2OH) and the hydroxyl group produced from this reaction binds to zinc to form a C-Zn-OH product with C-Zn and Zn-O distances 1.97Å and 1.78 Å, respectively. The calculated energy for this reaction is -3.26 eV, giving a total energy gain of -3.85eV. The optimised structure of the reaction product is presented in **Fig. 12 (b).**

The second reaction involves the transfer of one chlorine atom from the polymer ring to the CH_3CH_2 ligand of DEZ, releasing ethyl chloride (CH_3CH_2Cl) byproduct and the formation of CH_3CH_2OH byproduct and Zn-OH adduct from the interaction with H_2O_2. The Zn-OH adduct binds to the aromatic carbon atom from which the chlorine atom was transferred, with a C-Zn distance 1.91 Å, **Fig. 12 (c)**. The calculated energy for this reaction is -3.39 eV and gives a total energy of -3.98 eV. The elimination of CH_3CH_2 ligands as e CH_3CH_3 and the formation of Zn-OH was also observed in a previous study, where Kevlar was infiltrated with DEZ and H_2O. [8]

In the third reaction we consider the formation of the byproduct butane ($CH_3CH_2CH_2CH_3$) from the two CH_3CH_2 ligands of DEZ and the formation of $Zn(OH)_2$ from the interactions with H_2O_2 that remains infiltrated between the polymer chains, **Fig. 12 (d)**. Calculated energy for this reaction -4.68 eV, gives a total energy of -5.27 eV. DFT calculations indicate that Zn-O bonds are formed but not Zn-Cl bonds and this is consistent with experimental findings, where no Zn-Cl species are present in the XPS. Calculations also show that the formation of $Zn(OH)_2$, that remains infiltrated between polymer chains, is very favourable.

Finally, we explore the possible reactions when a second H_2O_2 molecule is added to the system. To check if the formation of phenol species is favourable during this reaction, we consider the reaction product presented in **Fig. 12 (c)** as reactant. We found that when a second H_2O_2 molecule is added to the system, it can dissociate, by forming two hydroxyl groups, where one hydroxyl group exchanges Zn-OH from the polymer to form a phenol specie and the other

hydroxyl binds to Zn-OH to form $Zn(OH)_2$, **Fig. 12 (e)**. The calculated energy, -3.84 eV indicates that the formation of $Zn(OH)_2$ and phenol species is favourable.

Based on our DFT calculations, during the Parylene C/ZnO VPI process we expect DEZ to infiltrate favourably into the parylene C polymer. Upon the interaction with H_2O_2, Zn-OH species can be formed and can bind with aromatic and aliphatic carbons of the polymer, and also $Zn(OH)_2$ species which remain infiltrated in between the polymer chains.

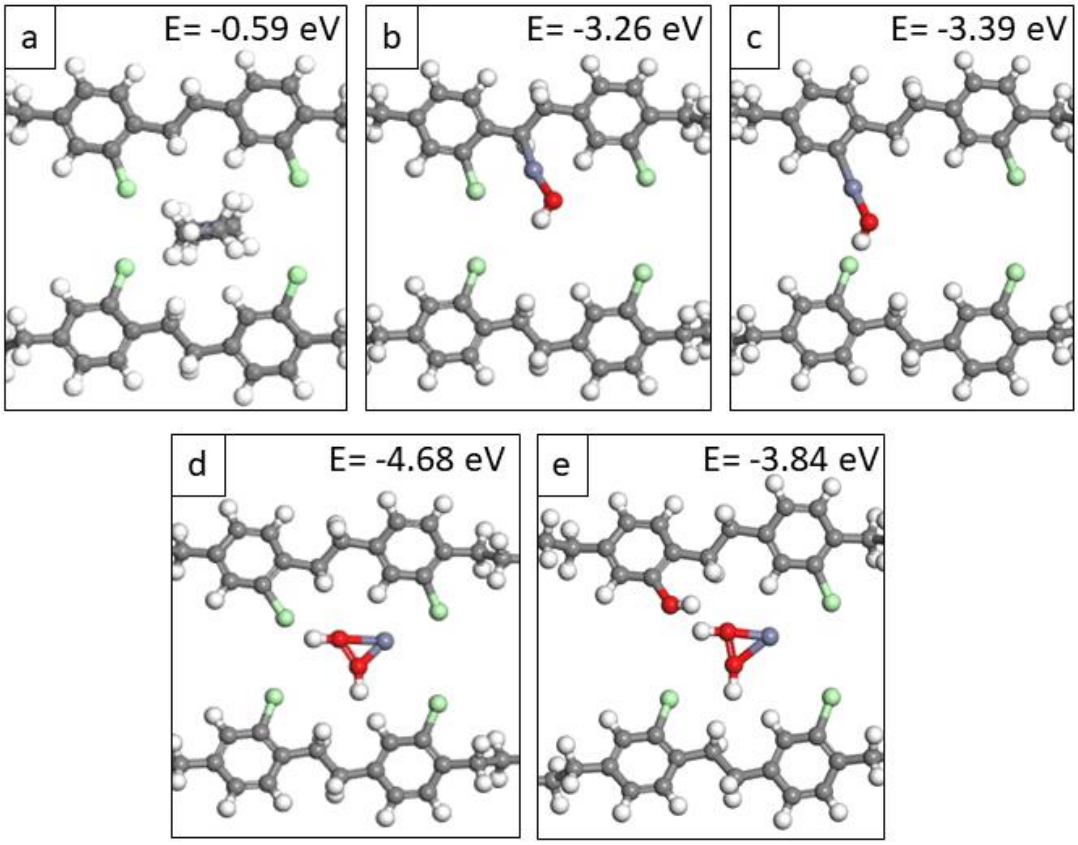


Figure 12 Optimized structures of parylene C infiltrated with a) DEZ, b) DEZ and H_2O_2; C-Zn-OH formation, c) DEZ and H_2O_2; ring bounded C-In-OH, d) DEZ and H_2O_2; $Zn(OH)_2$ formation and e) DEZ and two H_2O_2; $Zn(OH)_2$ and phenol formation. Purple-Zn, green-Cl, red-O, grey-C, white-H.

7.3.2.2 Selected experimental results on ZnO VPI films (CIC nanoGUNE)

VPI process development

To produce parylene C/ZnO hybrids, the parylene C substrate was consequentially exposed to diethylzinc (DEZ) and 30% solution of H_2O_2 by VPI. The first 50 cycles had the following pulsing /exposure / purging sequence: 0.2s / 100s / 10s for DEZ and 0.4s / 5s / 15s H_2O_2. It was

further followed by an additional 20 ALD cycles to seal off the modified polymer with a thicker film of ZnO. The infiltration temperature varied and was 100, 150, or 210°C.

X-ray photoelectron spectroscopy (XPS) and energy dispersive X-ray (EDX) spectroscopy

To check whether the healing of the parylene C/ZnO was linked to the zinc chlorine formation, the evolution of the chlorine 2p peak with the etching depth by XPS was measured (**Fig. 13 (a)**). However, in contrast to TMIn infiltration, there was only one chlorine doublet, with the binding energy of 200 eV. This was attributed to the chlorine bonded to organic carbon, or chlorine bonded to aryl ring in our case. The chlorine 2p signal was best modelled with only one chlorine doublet even after 19 hours of etching. This proves that there was no zinc chloride formation, and therefore, DEZ did not interact with the chlorine. EDX analysis proved that the material which filled the rupture consisted of zinc and oxygen. Moreover, the carbon signal barely changed, but the chlorine signal had an increase in the damaged area. It could be explained by the thinner or less dense newly grown layer, **Fig. 13 (b).** Elemental composition was also studied by XPS as presented in **Fig. 13 (c)**.

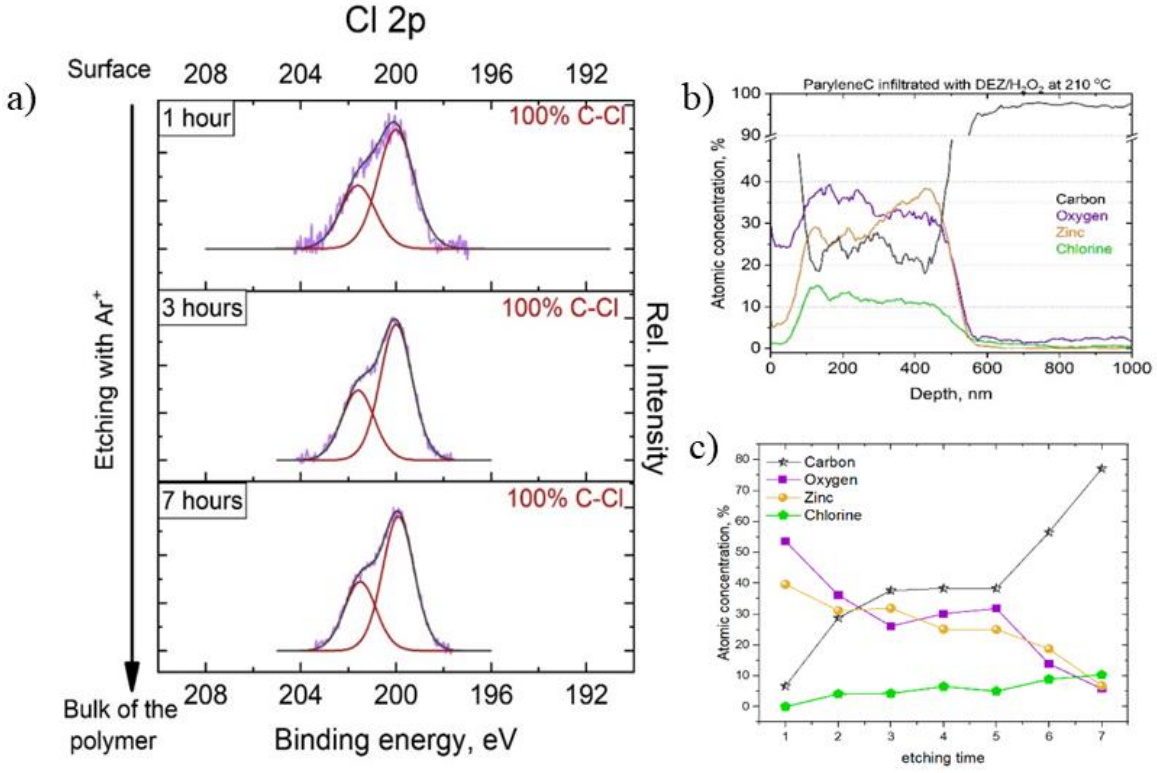


Figure 13 Parylene C infiltrated with DEZ/H_2O_2 at 210°C: a) XPS depth profile of Cl 2p doublet, b) EDX depth profile, c) atomic concentrations after different etching times calculated from XPS data.

In situ Fourier-transform infrared (FTIR) spectroscopy

FTIR was measured in order to see the possible modifications in the chemical bonding upon infiltration of DEZ and H_2O_2 (**Fig. 14**). Again, no significant differences occurred in the spectra. An important factor is that the infiltrated area of the parylene C was less than half a micron, while during FTIR measurements a signal is collected from a deeper region down to three microns. The contribution of the modified polymer by VPI was much smaller than that of the parylene C itself, and therefore, hardly distinguishable and difficult to compare with DFT data. However, we can observe free OH groups at 3550-3370 cm^{-1}.They are missing in the poly-para-xylylene polymers and they indicated the possible formation of metal oxides and hydroxides in the bulk of the polymer. Moreover, in the fingerprint region, there was the formation of an additional peak at 511 cm^{-1} which was absent for uncoated polymer and polymer coated with ZnO (not shown here). This peak was attributed to the Zn-O vibrations in the polymer. In contrast to the FTIR measurements for the TMIn infiltration into the parylene C, here we do not see any peaks that indicate the formation of phenol or zinc chloride.

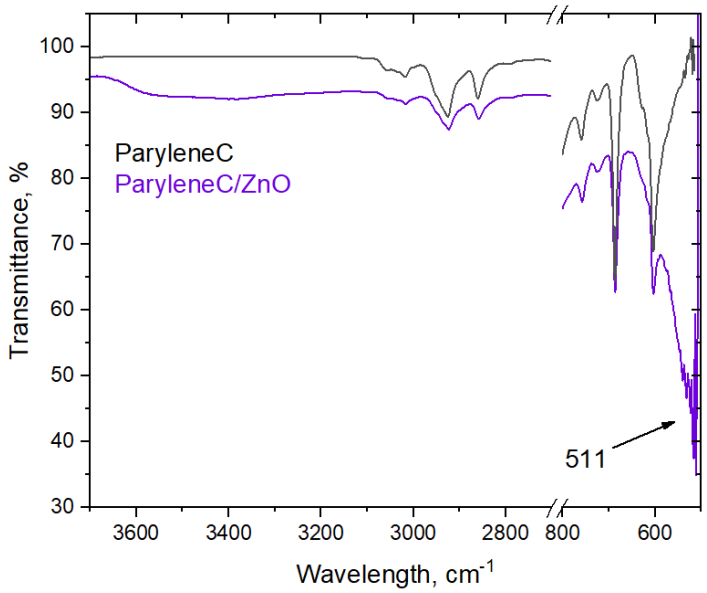


Figure 14 ATR-FTIR spectra of bare parylene C and parylene C infiltrated with ZnO.

Self-healing properties

A defect in the shape of letter "N" was written into the ZnO film by FIB (**Fig**. **15 (a)**), which upon exposure to air healed within 5 min (**Fig. 15 (b)**). TEM investigations revealed that the new formed material consists of zinc oxide with 6.6 ± 0.2 at % admixture of chlorine and 3.3 ± 0.2 at % of carbon. Interestingly, this newly formed zinc oxide was not stoichiometric having

a Zn:O ratio of ≈2.5:1. A further interesting observation is that a depletion zone that surrounded the letter N formed where the oxygen and zinc signal intensities decreased and the carbon signal intensity increased, thereby indicating a lateral diffusion of the infiltrate toward the induced defect site (**Fig. 15 (c)**).

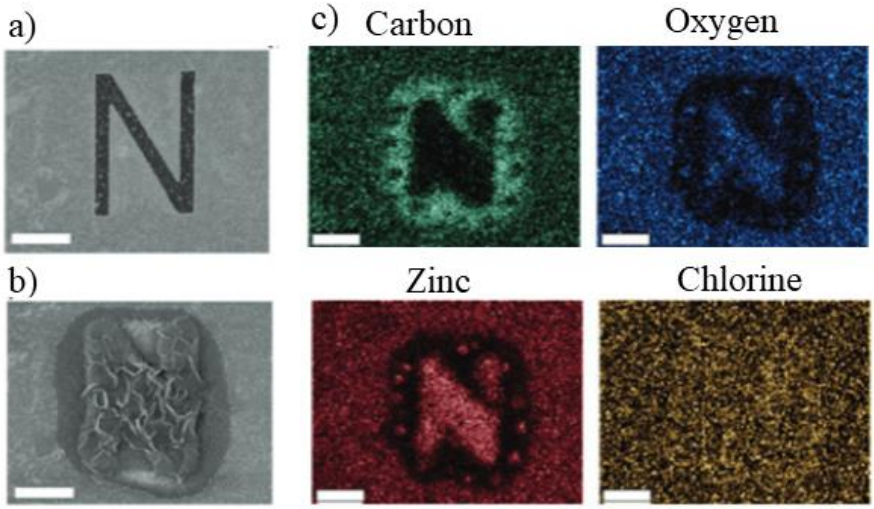


Figure 15 Healing of selectively FIB-etched patterns on the surface of Parylene C/ZnO a) before exposure to air b) after exposure to air. c) EDX maps of the mended Parylene C/ZnO hybrid structure shown in b).

7.4 Conclusion

Ruthenium SIS films

We employed density functional theory (DFT) calculations to compare the interactions of ruthenium oxide (RuO_4) precursor with polymethyl methacrylate (PMMA) and polystyrene (PS) oligomers and predict the possible reactions during the vapour phase infiltration (VPI) process that uses RuO_4, hydrogen as coreactant and the PS-b-PMMA co-block polymer. DFT calculations indicated an unfavourable interaction between RuO_4 and PMMA. We assume that this lack of interaction can impact the infiltration of RuO_4 into PMMA by making it unfeasible.

On the other hand, exothermic reaction energetics were calculated for the RuO_4-PS-H_2 process, indicating that the RuO_4-PS interaction is favourable and that hydrogen is able to reduce the RuO_4 molecules infiltrated into the PS polymer, which can lead to the formation of metallic Ru. Therefore, DFT findings suggest that the formation of nm-scale ruthenium lines is possible through a VPI process with RuO_4, hydrogen coreactant and PS-b-PMMA co-block polymer, where RuO_4 will infiltrate into PS but not into PMMA.

This VPI procedure for ruthenium metal nanostructures was successfully established in experimental work. Selective infiltration of RuO_4 within PS homopolymer films was demonstrated, whereas no reaction was observed with PMMA thin films. Self-assembled PS-b-PMMA films were then used to create ruthenium nanostructures that mimicked the reactive PS component.

Self-healing VPI materials

Enabling self-healing of materials is very important for saving energy and resources in different emerging applications. We have used DFT studies to gain a better understanding of the possible chemical reactions during the deposition of parylene C/indium oxide (In_2O_3) and parylene C/ zinc oxide (ZnO) VPI materials, which exhibit self-healing properties. [7] The In_2O_3 based process uses trimethylindium (TMIn) as inorganic precursor and the ZnO based process used diethylzinc (DEZ) as inorganic precursor. H_2O_2 is used as coreactant for both processes.

For the In_2O_3 based process DFT shows that TMIn precursor infiltrates favourably in the parylene C polymer. The reactions between TMIn and H_2O_2 can lead to the formation In-OH species that can bind to the aliphatic and aromatic carbons, and to the formation of $In(OH)_3$, $InCl_3$ and phenol species when the concentration of H_2O_2 is increased. This VPI process was developed experimentally as well. XPS and FTIR techniques indicate that the interaction of

TMIn with parylene C polymer leads to the formation of indium chloride and phenol species which is consistent with DFT data.

For the ZnO based process we show that DEZ also infiltrates into the parylene C polymer with a larger interaction energy compared to TMIn which is attributed to the stronger vdW interactions of DEZ with the polymer due to its larger size. The reactions between DEZ and H_2O_2 lead to the formation Zn-OH products which can bind to the aromatic and aliphatic carbons of the polymer, or $Zn(OH)_2$ molecules which remain infiltrated in between of the polymer chains. We also found that with increasing the concentration of H_2O_2 molecules the formation of phenol species is possible. The parylene C/ZnO VPI process was also developed experimentally. During the deposition of this material the formation of the metal oxide and hydroxides in the bulk of the polymer was believed to occur. XPS analysis shows there is no sign of the zinc chloride products meaning that DEZ did not interact with the chlorine, which was also seen from DFT.

7.5 References

1. N. Poonkottil, E. Solano, A. Muriqi, M. M. Minjauw, M. Filez, M. Nolan, Ch. Detavernier, J. Dendooven, *Chemistry of Materials*, **2022**, 34, 24.
2. C. Z. Leng, M. D. Losego, *Materials Horizons*, **2017**, 4, 747–771.
3. M. M. Minjauw, J. Dendooven, B. Capon, M. Schaekers, Ch. Detavernier, *Journal of Materials Chemistry C*, **2015**, 3, 132–137.
4. M. M. Minjauw, H. Rijckaert, I. V. Driessche, Ch. Detavernier, J. Dendooven, *Chemistry of Materials*, **2019**, 31, 1491–1499.
5. S. Lin, D. Xie, *Chinese Journal of Chemistry*, **2012**, 30, 2036–2040.
6. A. D. Taggart, N. Jeon, V. Rozyyev, E. Karapetrova, N. J. Zaluzec, R. Z. Waldman, S. B. Darling, J. W. Elam, A. B. F. Martinson, *The Journal of Physical Chemistry*, **2021**, 125, 21191– 21198.
7. O. Yurkevich, E. Modin, I. Šarić, M. Petravić, M. Knez, *Advanced Materials*, **2022**, 34, 1–9.
8. I. Azpitarte, A. Zuzuarregui, H. Ablat, L. Ruiz-Rubio, A. López-Ortega, S. D. Elliott, M. Knez, *Chemistry of Materials*, **2017**, 29, 10068–10074.

Chapter 8

Precursor chemistry

8.1 Introduction

This chapter presents the results of six combined experimental and computational studies on new organometallic precursors. In each of the studies in this chapter, my density functional theory (DFT) calculations allowed a rapid screening, to understand in detail the geometry and reactivity of new precursors and to theoretically predict which precursors would be convenient for deposition processes. The most promising precursors were used for the deposition of metal oxides, metals and hybrid materials. This shows the power and utility of DFT calculations in precursor chemistry.

In **Section 8.2** DFT calculations were used to investigate the geometry and reactivity of copper and silver carbene stabilized precursors towards hydrogen and water as potential coreactants. The synthesis and characterization of the copper precursor and its application as a precursor for the deposition of copper thin films via spatial plasma-enhanced atomic layer deposition (APP-ALD) at atmospheric pressure is also demonstrated.

Section 8.3 discusses DFT findings on four new organosilicon amide NHC copper precursors. The substitution pattern of these precursors was systematically varied within the NHC backbone and also within the organosilicon backbone. With DFT we determined the structure and reactivity of these precursors using simple thermodynamics for precursor decomposition. We also predicted precursor reactivity towards potential ALD coreactants, namely hydrogen and water.

In **Section 8.4** an insight into the geometry and of cerium and ytterbium precursors with amidinate and guanidinate ligands was gained through DFT calculations. Reactivity of precursors was predicted by simulating the reactions with the potential ALD coreactants oxygen and water. All precursors were synthesized and thoroughly characterized. The deposition of cerium oxide (CeO_2) thin films via ALD using cerium guanidinate precursor and water is demonstrated as well.

In **Section 8.5** DFT studies give theoretical insights into the geometry of a series of closely related yttrium precursors comprising formamidinate ligands. We explored the impact of

different ligand moieties on precursor reactivity by simulating reactions of precursors with water, which was targeted as a coreactant for the deposition of yttrium oxide (Y_2O_3), and by comparing the resulting interaction energies. The synthesis, characterisation and deposition of Y_2O_3 thin films via ALD is also discussed.

In **Section 8.6** DFT studies were used to determine the structure and stability of new europium precursors with formamidinate, amidinate and guanidinate ligands and evaluate their reactivity toward elemental sulfur and oxygen as potential chemical vapour deposition (CVD) coreactants. The reason of evaluating the interactions with sulfur is that sulfur would simplify the CVD process in terms of additional safety measures that need to be considered if highly toxic hydrogen sulphide (H_2S) is used as a sulfur source. We discuss also precursor synthesis, characterisation and the growth of high quality cubic europium sulphide (EuS) films via CVD process.

Finally, in **Section 8.7** a series of six homoleptic all nitrogen coordinated manganese precursors using formamidinate, amidinate and guanidinate ligands and two oxygen/nitrogen mixed coordinated ketoiminate precursors were investigated with DFT. We investigated precursor geometry and simulated the reactivity of manganese precursors towards oxygen and water to gain further insights in the applicability of these precursors as CVD or ALD precursor. Precursor synthesis and characterisation is also discussed.

8.2 Copper and Silver precursors

This work is published in the paper "***A carbene stabilized precursor for the spatial atomic layer deposition of copper thin films***", in Chemical Communications. [1]

ChemComm

ROYAL SOCIETY OF CHEMISTRY

COMMUNICATION

View Article Online
View Journal | View Issue

Check for updates

Cite this: *Chem. Commun.*, 2020, **56**, 13752

Received 26th August 2020,
Accepted 7th October 2020

DOI: 10.1039/d0cc05781a

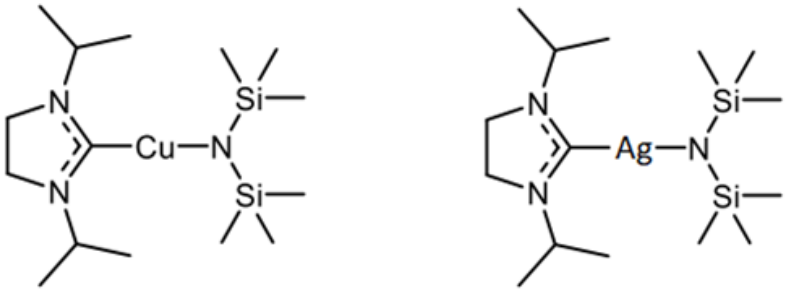
A carbene stabilized precursor for the spatial atomic layer deposition of copper thin films†

Nils Boysen, [a] Bujamin Misimi,[b] Arbresha Muriqi, [c] Jan-Lucas Wree, [a] Tim Hasselmann,[b] Detlef Rogalla, [d] Tobias Haeger,[b] Detlef Theirich,[b] Michael Nolan, [ef] Thomas Riedl [*b] and Anjana Devi [*a]

DOI: https://doi.org/10.1039/D0CC05781A

8.2.1 Results

In this study a carbene stabilized precursor, 1,3-di-iso-propyl-imidazolin-2-ylidene copper(I) N-di-trimethyl-silanamide, Cu(tBuNHC)(hmds), was compared to its analogue 1,3-di-iso-propyl-imidazolin-2-ylidene silver(I) N-di-trimethyl-silanamide, Ag(tBuNHC)(hmds). **Fig. 1** shows the chemical structures of the precursors.



[Cu(tBuNHC)(hmds)] [Ag(tBuNHC)(hmds)]

Figure 1 Molecular structure of Cu(tBuNHC)(hmds) and Ag(tBuNHC)(hmds) precursor.

8.2.1.1 Computational results

The geometries of the precursors were determined by DFT calculations (**Fig. 2 (a)**) which show that Cu(tBuNHC)(hmds) has shorter Me-C and Me-N bond lengths (1.92 Å and 1.88 Å) compared to Ag(tBuNHC)(hmds) (2.11 Å and 2.08 Å). The bonding angles around M at N-Me-C are 179.3° for Cu(tBuNHC)(hmds) and 179.1° for Ag(tBuNHC)(hmds).

The bond dissociation energy defined as the energy for the removal of the hmds ligand was computed for Ag(tBuNHC)(hmds) and Cu(tBuNHC)(hmds). For the Ag(tBuNHC)(hmds) precursor, the bond dissociation energy is 341.31 kJ/mol while for Cu(tBuNHC)(hmds) this energy is 446.33 kJ/mol. The lower bond dissociation energy of Ag(tBuNHC)(hmds) confirms the higher reactivity of the Ag-N bond in Ag(tBuNHC)(hmds) compared to Cu-N bond in Cu(tBuNHC)(hmds). DFT results indicate the presence of stronger Cu-C/Cu-N interactions in Cu(tBuNHC)(hmds) which effectively shield the highly reactive copper nucleus leading to a monomeric compound as desired for its application in ALD.

We used DFT calculations to further understand the precursor chemistry at molecular level and get an insight into the reactivity of the precursors. To assess their reactivity, we have built models of Cu(tBuNHC)(hmds) and Ag(tBuNHC)(hmds) precursors in presence of hydrogen, as hydrogen was the target ALD coreactant. The hydrogen molecule was placed at a distance of 1.70 Å from the metals and the structures were allowed to relax. The optimised atomic structure of Cu(tBuNHC)(hmds) in **Fig. 2 (b)** shows that the hydrogen molecule does not react with the copper precursor. In contrast to Cu(tBuNHC)(hmds), the Ag(tBuNHC)(hmds) precursor reacts with hydrogen where the Ag-N bond breaks and the and new Ag-H and N-H bonds with distances 1.16 Å and 1.03 Å are formed. The computed interaction energy upon forming the Ag-H and N-H bonds is -0.27 eV. These calculations confirm the higher reactivity of silver precursor compared to copper precursor towards hydrogen.

Precursor models were developed to include also the interaction with one water molecule so the reactivity of precursors for experimental conditions could be investigated. **Fig. 2 (c)** shows the optimized structures of the precursors after the interaction with one water molecule. When one water molecule interacts with Cu(tBuNHC)(hmds) and Ag(tBuNHC)(hmds), it preferably binds to the central metal atom and dissociates. For Cu(tBuNHC)(hmds) one hydroxyl group of water binds to copper with a distance 1.98 Å and the remaining proton binds to nitrogen with a distance 1.03 Å. In presence of water the Cu-N bond lengths from 1.88 Å to 2.18 Å showing the incipient breaking of the Cu-N bond. The calculated interaction energy between

Cu(tBuNHC)(hmds) and water is -0.57 eV. For Ag(tBuNHC)(hmds) the hydroxyl group of water binds to silver with a distance 2.03 Å and the remaining proton binds to nitrogen with a distance 1.05 Å. In presence of water the Ag-N bond breaks completely releasing a protoniated hmds (H-hmds) and the Ag-C bond is 1.08 Å. The calculated interaction energy between Ag(tBuNHC)(hmds) and water is -0.84 eV.

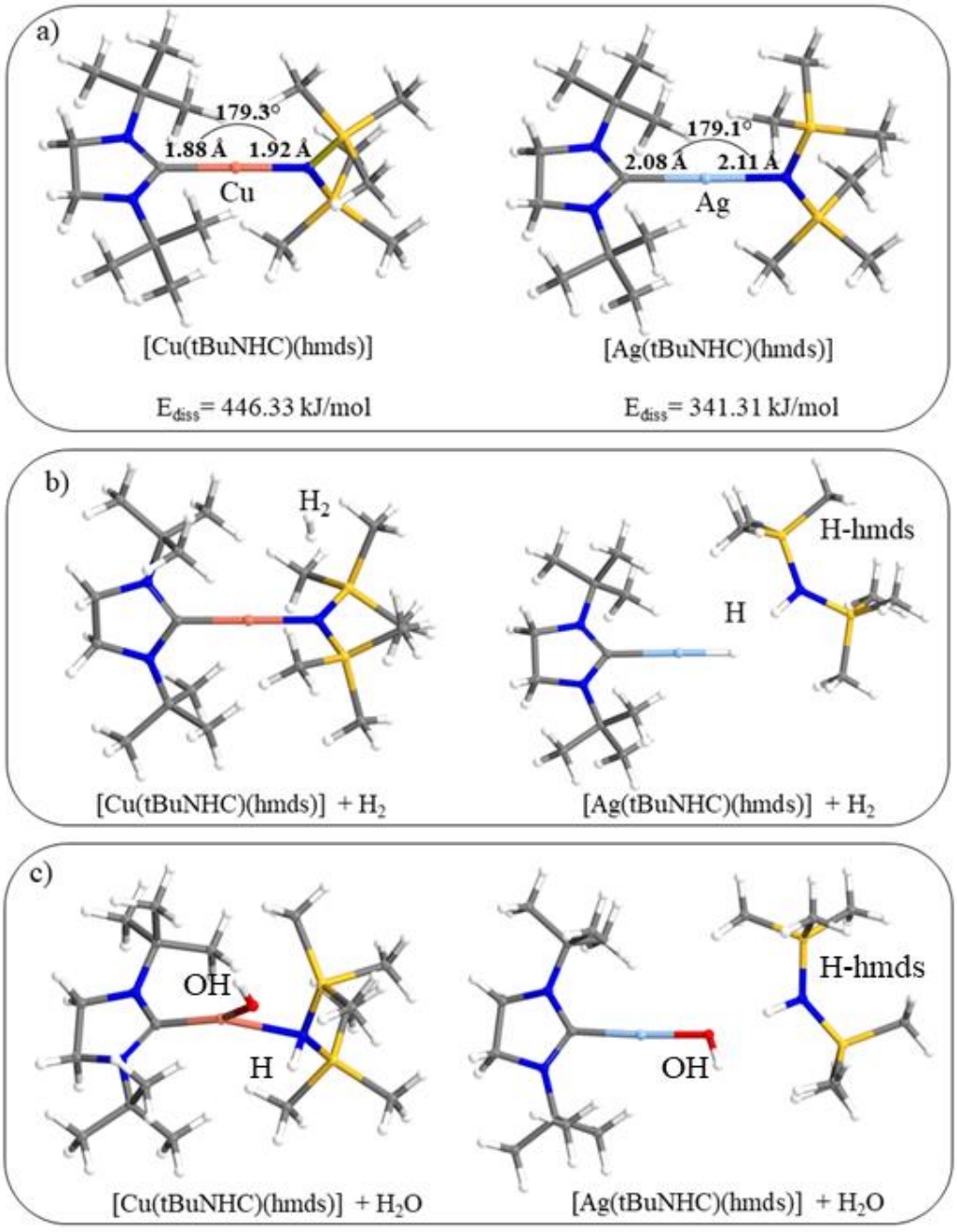
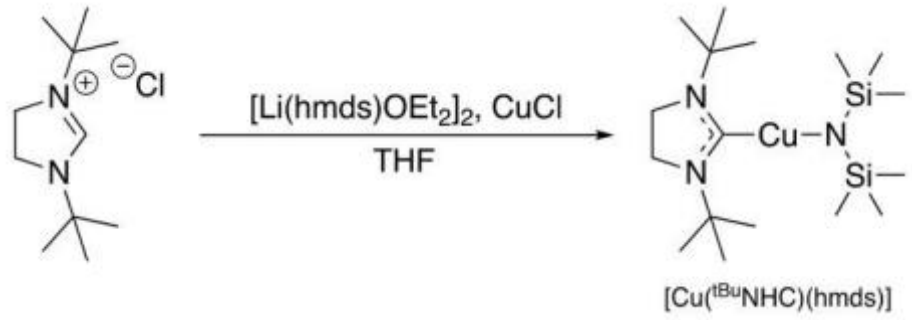


Figure 2 Optimised atomic structures of a) Cu(tBuNHC)(hmds) and Ag(tBuNHC)(hmds), b) Cu(tBuNHC)(hmds) and Ag(tBuNHC)(hmds) after incorporation of hydrogen and c) Cu(tBuNHC)(hmds) and Ag(tBuNHC)(hmds) after incorporation of water. Brown-Cu, light blue-Ag, blue-N, yellow-Si, grey-C, red-O, white-H.

8.2.1.2 Selected experimental results (Ruhr University Bochum)

Precursor synthesis

The Cu(tBuNHC)(hmds)] precursor was synthesized by modifying the procedure reported earlier. [2] A substantial improvement was achieved in terms of reducing the reaction steps necessary to obtain the product and scalability of the synthesis (**Scheme 1**). The spectroscopic purity and structural integrity of the precursor is confirmed by ^{1}H- and ^{13}C-NMR spectroscopy and is in accordance with the already reported values.



Scheme 1 Reaction pathway for the one-pot synthesis of Cu(tBuNHC)(hmds).

Single crystal X-ray diffractometers (SC-XRD) characterisation

The Cu(tBuNHC)(hmds) precursor crystallizes in monomeric state. Findings from SC-XRD showed a linear coordination of the NHC and amide (hmds) ligands around the copper nucleus highlighted by a C-Cu-N angle of 178.1° as typically seen for monomeric linear NHC copper (I) precursor. [3] Compared to the directly related silver precursor, Ag(tBuNHC)(hmds), the molecular structure is nearly identical, but due to the significantly larger mono-cationic radius of silver (1.89 Å vs. 1.73 Å), [4] the bond lengths of Ag-N (2.07 Å) and Ag-C (2.09 Å) are longer than for Cu-N (1.86 Å) and Cu-C (1.90 Å) in the solid crystalline state.

Thermal investigations of the precursors

TGA results of Cu(tBuNHC)(hmds) and Ag(tBuNHC)(hmds) are presented in **Fig. 3**. The Cu(tBuNHC)(hmds) precursor features a single step evaporation behaviour with an onset of evaporation at 110°C and a residual mass of 2.4 %. Interestingly, the parent Ag(tBuNHC)(hmds) precursor features a very similar onset of evaporation at 133°C, but a

significantly higher residual mass of 20.2 %, which could be attributed to a substantial thermal decomposition at higher temperatures. The longer and thus weaker Ag-C and Ag-N bonds in Ag(tBuNHC)(hmds) might generally explain its lower thermal stability compared to Cu(tBuNHC)(hmds), but the nearly identical molecular structure explain the close onset of evaporation points due to similar intermolecular van der Waals (vdW) interactions.

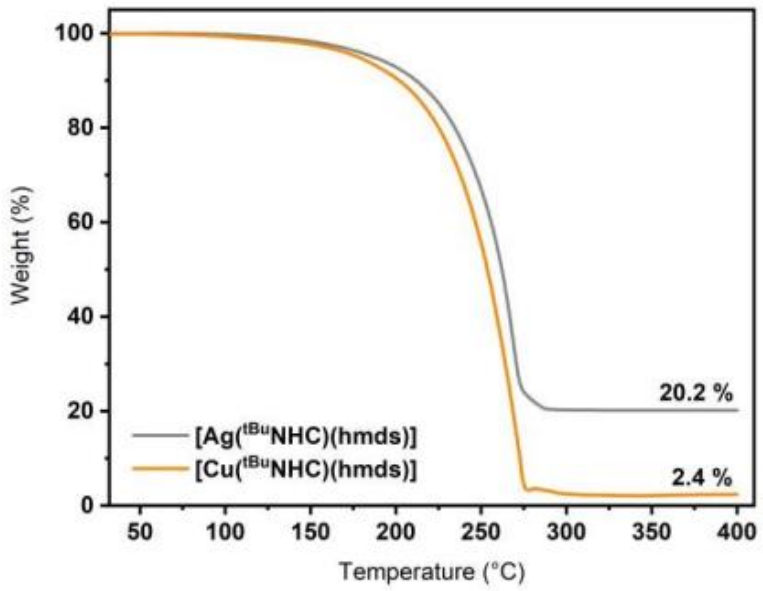


Figure 3 Thermogravimetric analysis curves of Cu(tBuNHC)(hmds) (yellow) and Ag(tBuNHC)(hmds) (grey) for comparison.

APP-ALD process development for copper multilayers

Cu(tBuNHC)(hmds) was applied as a precursor in an APP-ALD process for the deposition of copper metal layers. The substrate and precursor temperature was kept at 100°C and a borosilicate glass was used as substrate material. **Fig. 4** shows the copper atom coverage (atoms/area) as determined by Rutherford backscattering spectrometry (RBS) vs. number of ALD cycles. A GPC of 0.23 Å/cycle was achieved with Cu(tBuNHC)(hmds) as a metal precursor. For comparison, Ag(tBuNHC)(hmds) was also applied as a precursor in an APP-ALD process where a GPC of 0.76 Å/cycle was achieved, which is more than twice that of the copper process. The lower GPC of the films deposited with Cu(tBuNHC)(hmds) precursor may be related to different reactivity on the substrate surface because of the shorter and thus stronger N-Cu-C bonds, as discussed above.

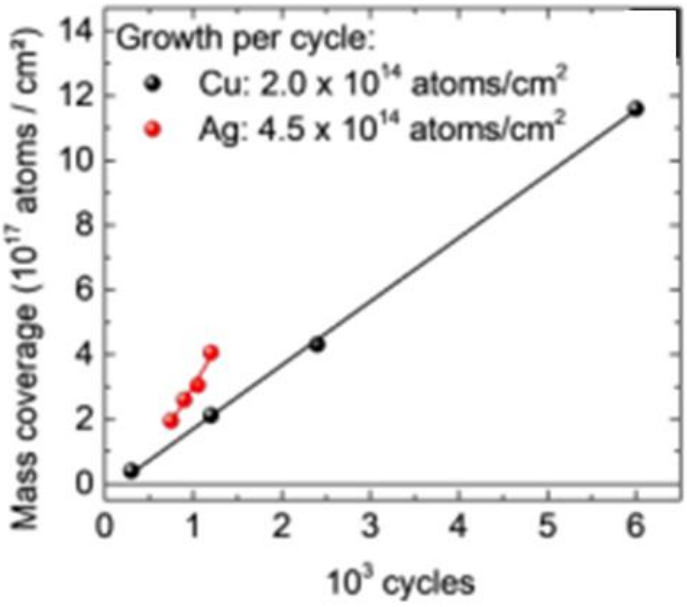


Figure 4 Atom coverage as determined by RBS vs. number of ALD cycles for Cu and Ag.

X-ray photoelectron spectroscopy (XPS) characterization

XPS revealed that all potential contaminants related to the copper precursor, i.e. Si, N or C, were below the detection limit of the measurement (< 0.5 at. %) (**Fig. 5 (a)**). The core level spectrum of Cu_2p indicates the predominant presence of Cu(0) with only some trace amounts of oxidized copper (e.g. CuO), **Fig. 5 (b)**. [5, 6]

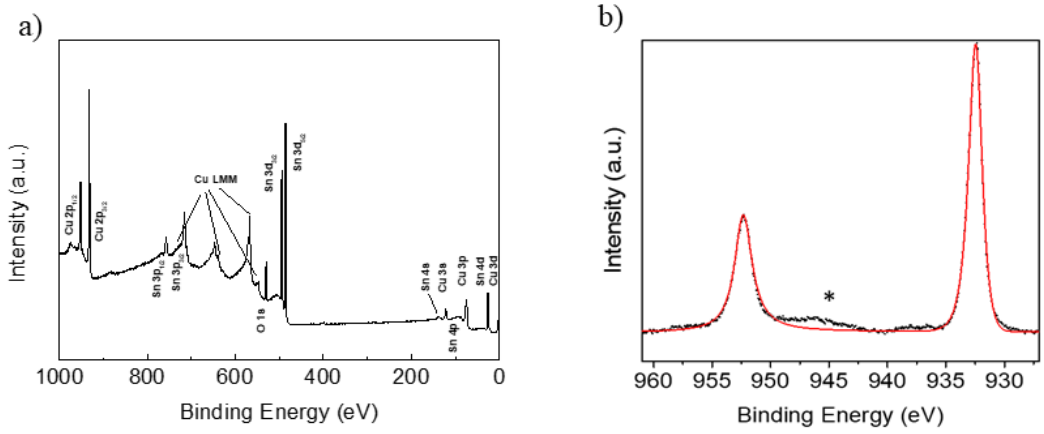


Figure 5 a) XPS survey spectra of the copper layer after 6 min sputtering at 1kV with Ar^+ ions. b) XPS spectra of the core level spectra of Cu_2p.

8.3 Copper precursors

8.3.1 Results

Four different copper precursors, namely, 1,3-di-tert-butyl-imidazolin-2-ylidene copper (I) N-(tert-butyl)-1,1,1-trimethyl-silanamide, (tBuNHC)Cu(TBTMSA), 1,3-di-tert-butyl-imidazolin-2-ylidene copper (I) N-(sec-butyl)-1,1,1-trimethyl-silanamide, (tBuNHC)Cu(SBTMSA), 1,3-di-iso-propyl-imidazolin-2-ylidene copper (I) N-(tert-butyl)-1,1,1-trimethyl-silanamide, (iPrNHC)Cu(TBTMSA), 1,3-di-iso-propyl-imidazolin-2-ylidene copper (I) N-(sec-butyl)-1,1,1-trimethyl-silanamide, (iPrNHC)Cu(SBTMSA) were synthesised and investigated. **Fig. 6** shows the chemical structures of the precursors.

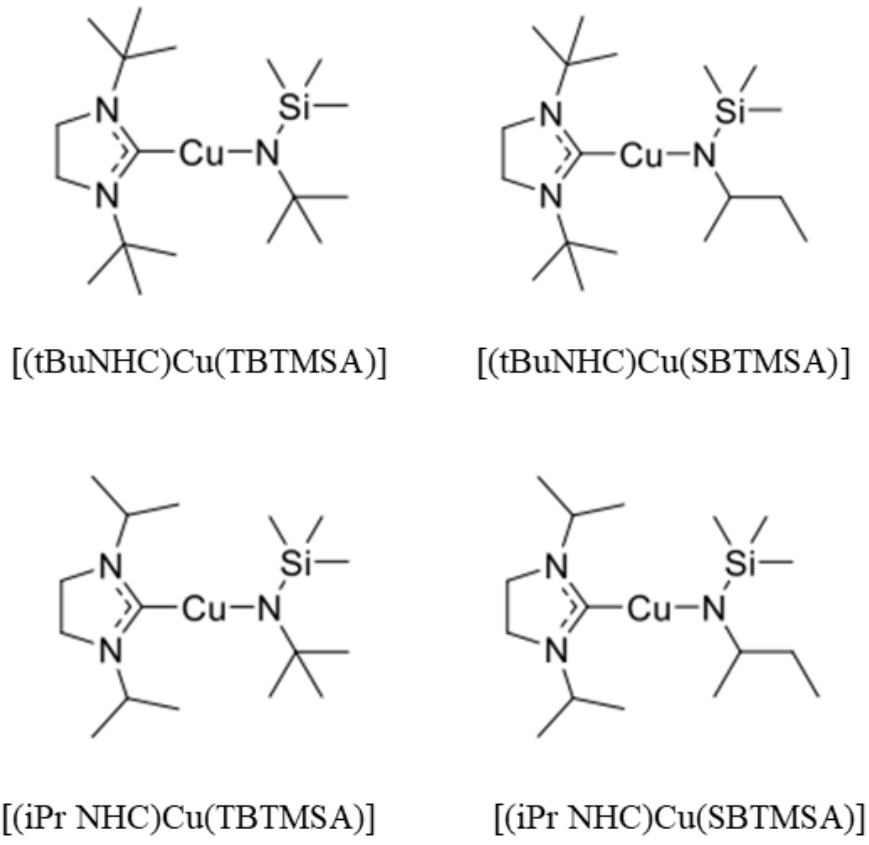


Figure 6 Molecular structure of (tBuNHC)Cu(TBTMSA), (tBuNHC)Cu(SBTMSA), (iPrNHC)Cu(TBTMSA) and (iPrNHC)Cu(SBTMSA) precursor.

8.3.1.1 Computational results

The structures of all precursors were studied for their gas phase chemistry using quantum chemical calculations for a more detailed understanding of the structure-property relationship.

In the first set of the calculations copper precursors were modelled as isolated molecules in vacuum, with the relaxed atomic structures shown in **Fig. 7.** The C-Cu-N distances and C-Cu-N angles of the optimized structures are given in **Table 1**. The C-Cu distance is 0.02 Å longer for (tBuNHC)Cu(TBTMSA) and (tBuNHC)Cu(SBTMSA) compared to (iPrNHC)Cu(TBTMSA) and (iPrNHC)Cu(SBTMSA) while the Cu-N distance is the longest for (tBuNHC)Cu(TBTMSA) precursor and it is 0.03 Å longer compared to Cu-N distance for (iPrNHC)Cu(SBTMSA) for which this distance is the shortest. The C-Cu-N angles are 177.9° for (tBuNHC)Cu(TBTMSA), 178.4° for (tBuNHC)Cu(SBTMSA), 178.5° for (iPrNHC)Cu(TBTMSA) and 177.4° for (iPrNHC)Cu(SBTMSA).

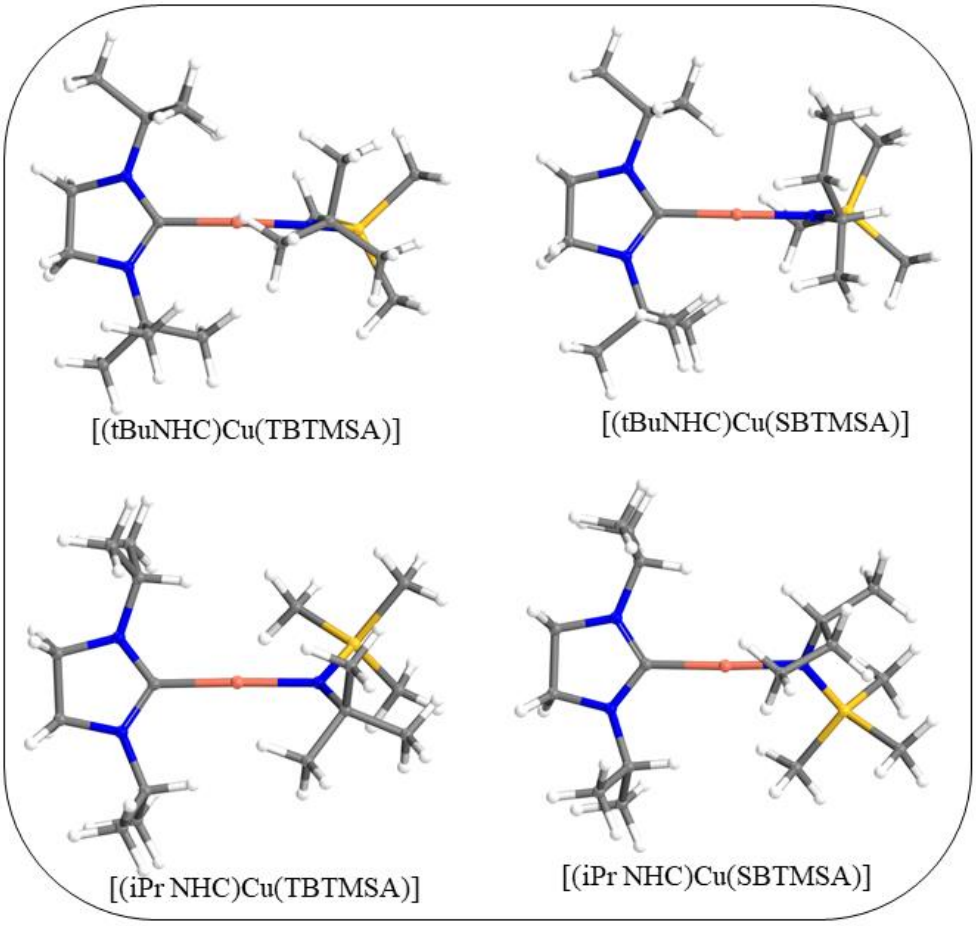


Figure 7 Optimised atomic structures of (tBuNHC)Cu(TBTMSA), (tBuNHC)Cu(SBTMSA), (iPrNHC)Cu(TBTMSA) and (iPrNHC)Cu(SBTMSA) precursors. Brown-Cu, blue-N, yellow-Si, grey-C, white-H.

Table 1 C-Cu-N distances and C-Cu-N angles of precursors in vacuum conditions.

Structure	Cu-C	Cu-N	C-Cu-N
(tBuNHC)Cu(TBTMSA)	1.93 Å	1.89 Å	177.9 °
(tBuNHC)Cu(SBTMSA)	1.93 Å	1.87 Å	178.4 °
(iPrNHC)Cu(TBTMSA)	1.91 Å	1.87 Å	178.5 °
(iPrNHC)Cu(SBTMSA)	1.91 Å	1.86 Å	177.4 °

We expanded our model to include hydrogen and water interacting with the precursors to better account for typical experimental conditions and to simulate the reactivity of precursors toward potential these coreactants.

For interactions with hydrogen, the models are prepared so that the hydrogen molecule was placed at a distance of 1.70 Å from the metal site and the structures were allowed to relax. We found that the hydrogen molecule does not react with the copper precursors and therefore we consider hydrogen as an inconvenient coreactant for the studied copper precursors.

Fig. 8 shows the relaxed atomic structures of copper precursors after interaction with one water molecule. For these models one water molecule was placed at a distance 2.50 Å from the metal site and the structures were allowed to relax under no constraints. Optimised structures show and the negative calculated reaction energetic of -1.11 eV for (tBuNHC)Cu(TBTMSA), -0.84 eV for (iPrNHC)Cu(SBTMSA), -1.14 eV for (iPrNHC)Cu(TBTMSA) and -0.76 eV for (iPrNHC)Cu(SBTMSA) show that all molecules react favorably with water. In the reaction of copper precursors with water, the water molecule dissociates, while the Cu-N bond dissociates and the hydroxyl group of water binds to copper, while the proton of water binds to nitrogen of amide backbone, releasing the ligand. The Cu-OH distance is typical of the Cu-O bond in copper oxides, being 1.82 Å for (tBuNHC)Cu(TBTMSA) and (iPrNHC)Cu(TBTMSA), 1.85 Å for (tBuNHC)Cu(SBTMSA) and 1.86 Å for (iPrNHC)Cu(SBTMSA).

The Cu-C bond remains unaffected by the water molecule and this is in agreement with previous work. [7] The results in reference [7] demonstrate the preparation of a Cu-NHC-Cl precursor by using Cu_2O and the imidazolium chloride. In this reaction, Cu_2O acts as a base, deprotonates the imidazolium chloride and forms Cu-NHC-Cl precursor together with water. This reaction would not be possible if the Cu-C bond would be reactive towards water.

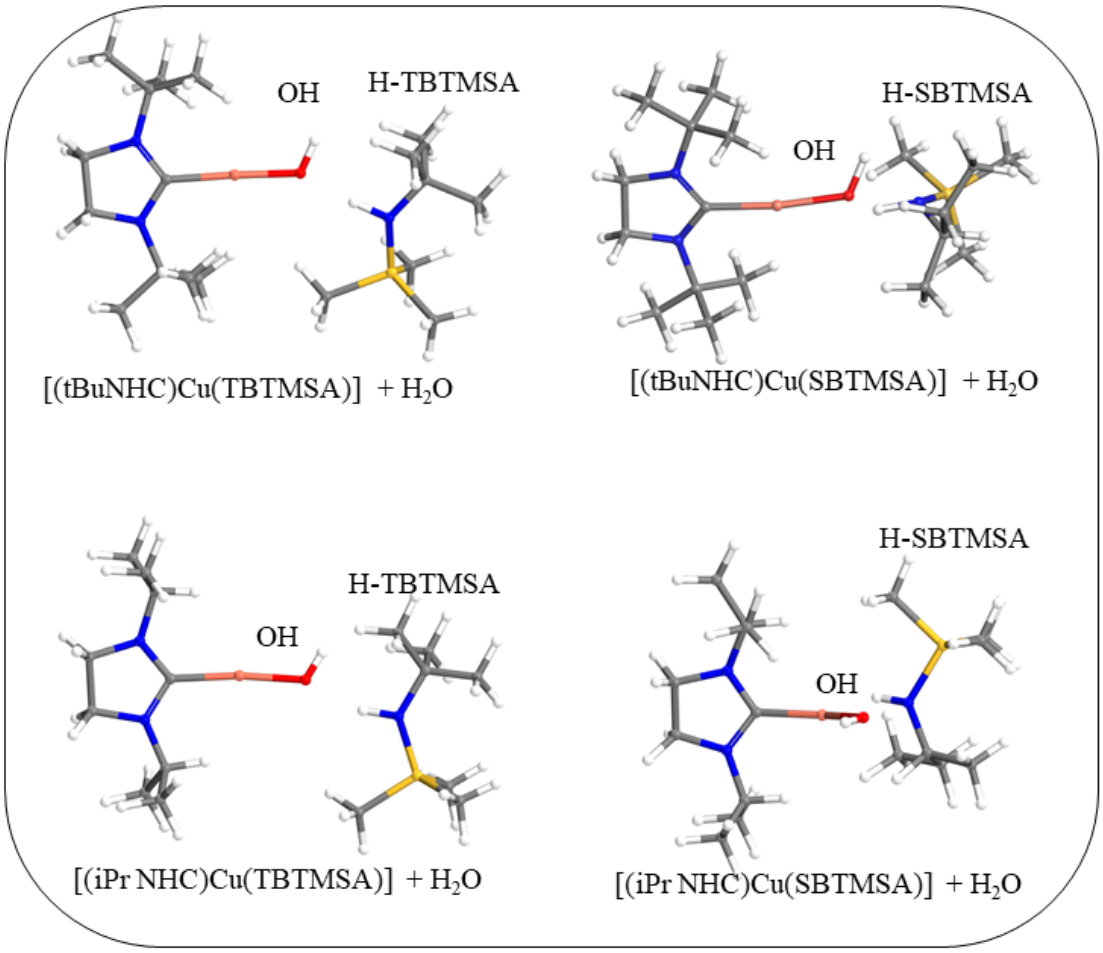


Figure 8 Optimised atomic structures of (tBuNHC)Cu(TBTMSA), (tBuNHC)Cu(SBTMSA), (iPrNHC)Cu(TBTMSA) and (iPrNHC)Cu(SBTMSA) after incorporating one water molecule.

Experimental work from our collages (not included in this thesis) suggested that (tBuNHC)Cu(SBTMSA) is the best precursor for proof-of-principle MOCVD deposition as it was successful with oxygen as coreactant for the formation of Cu_2O whiskers on Si(100) substrates. Therefore, in the final study we explore the interactions between (tBuNHC)Cu(SBTMSA) and oxygen to support the experimental findings of this study.

We have built two different models for the interaction with oxygen. In the first model the oxygen molecule was placed near the Cu-C bond while in the second model the oxygen molecule was placed near the Cu-N bond. This was done to explore which bond is more sensitive to oxygen. **Fig. 9** shows the optimised atomic structures after the interaction of (tBuNHC)Cu(SBTMSA) with oxygen. For the first model shown in **Fig. 9 (a)**, the oxygen molecule breaks the Cu-C bond and inserts in the precursor molecule by forming a Cu-O-O-C bridge. The Cu-O, O-O and O-C distances are 1.88 Å, 1.47 Å and 1.29 Å respectively. The

interaction energy for this reaction is -0.51 eV. In the second model, oxygen promotes the dissociation of the Cu-N bond and inserts into the precursor forming a Cu-O-O-N bridge. The Cu-O, O-O and O-N distances are 1.87 Å, 1.42 Å and 1.41 Å, respectively, and the interaction energy for this model is -0.20 eV.

Optimized structures and interaction energies show that the oxygen molecule interacts with (tBuNHC)Cu(SBTMSA) favorably and both Cu-C and Cu-N bonds are sensitive to oxygen. However, when we compare interaction energies for both reactions, we see that interaction energy for the reaction with the Cu-C bond is more negative and therefore we anticipate the Cu-C bond to be more sensitive to oxygen compared to the Cu-N. This is justified by the fact that stable NHCs possess a lone pair of valence electrons and an accessible vacant p orbital, which makes them reactive in reactions with small molecules like oxygen, serving as good s-electron-donors and p-electron-acceptors. Our finding that precursors can react with water and oxygen explain why such stable NHCs are sensitive to air. [7]

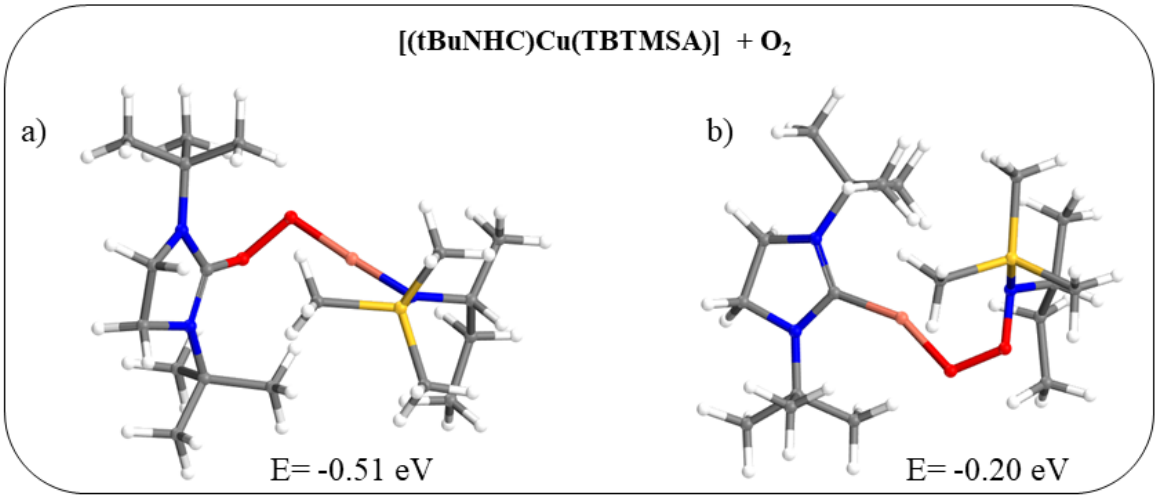


Figure 9 Optimised atomic structures of (tBuNHC)Cu(TBTMSA) after incorporating one oxygen molecule; a) the reaction with the Cu-C bond, b) the reaction with the Cu-N.

8.4 Cerium and Ytterbium precursors

This work is published in the paper "***Rational Development of Guanidinate and Amidinate Based Cerium and Ytterbium Complexes as Atomic Layer Deposition Precursors: Synthesis, Modelling, and Application***", in Chemistry-A European Journal. [8]

Chemistry–A European Journal | Full Paper doi.org/10.1002/chem.202003907 | Chemistry Europe European Chemical Societies Publishing

Precursor Chemistry



Rational Development of Guanidinate and Amidinate Based Cerium and Ytterbium Complexes as Atomic Layer Deposition Precursors: Synthesis, Modeling, and Application

Parmish Kaur,[a] Lukas Mai,[a] Arbresha Muriqi,[b] David Zanders,[a] Ramin Ghiyasi,[c] Muhammad Safdar,[c] Nils Boysen,[a] Manuela Winter,[a] Michael Nolan,[b] Maarit Karppinen,[c] and Anjana Devi*[a]

DOI: https://doi.org/10.1002/chem.202003907

8.4.1 Results

Five different precursors of cerium and two different precursors of ytterbium, namely, tris(N,N'-diisopropyl-2-dimethylamido-guanidinato) cerium (III), $Ce(dpdmg)_3$ **1**, tris(N,N'-butylethyl-2-dimethylamido-guanidinato) cerium (III), $Ce(bedmg)_3$ **2**, tris(N,N'-diisopropyl-2-diethylamido-guanidinato) cerium (III), $Ce(dpdeg)_3$ **3**, tris(N,N'-diisopropyl-acetamidinato) cerium (III), $Ce(dpamd)_3$ **4**, tris(N,N'-butylethyl-acetamidinato) cerium (III), $Ce(beamd)_3$ **5**, tris(N,N'-diisopropyl-2-dimethylamido-guanidinato) ytterbium (III), $Yb(dpdmg)_3$ **6**, tris(N,N'-diisopropyl-acetamidinato) ytterbium (III), $Yb(dpamd)_3$ **7** were synthesized. **Fig. 10** shows the chemical structures of $Ce(dpdmg)_3$ **1,** $Ce(dpamd)_3$ **4,** $Yb(dpdmg)_3$ **6** and $Yb(dpamd)_3$ **7** precursors, on which we focus in this study.

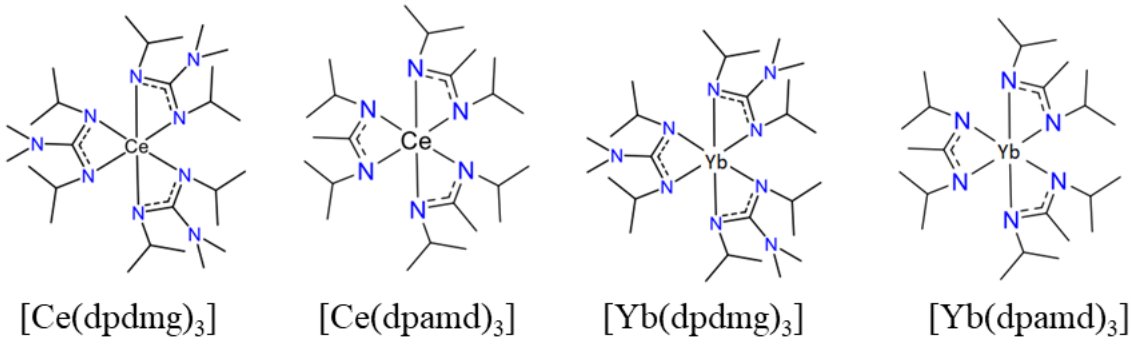


Figure 10 Molecular structure of $Ce(dpdmg)_3$, $Ce(dpamd)_3$, $Yb(dpdmg)_3$ and $Yb(dpamd)_3$ precursor.

8.4.1.1 Computational results

To obtain an insight into the fundamental aspects of the chemistry of the precursors on the molecular level, DFT was used to model the atomic structures and to simulate the reactivity of selected precursors towards potential coreactants. In the first set of calculations, the selected precursors $Ce(dpdmg)_3$,$Ce(dpamd)_3$, $Yb(dpdmg)_3$ and $Yb(dpamd)_3$ were modelled as isolated molecules in vacuum at zero Kelvin (K) and zero Giga Pascal (GPa), with the relaxed atomic structures shown in **Fig. 11 (a).** The Me-N bond lengths and bite angles (N-Me-N) of the optimized precursor structures are given in **Table 2** and **Table 3,** respectively. Me-N distances are longer for $Ce(dpdmg)_3$ and $Yb(dpdmg)_3$ compared to $Ce(dpamd)_3$ and $Yb(dpamd)_3$, as shown in **Table 2**, while Ce-N distances are longer than the corresponding Yb-N distances. The computed Ce-N distances in $Ce(dpdmg)_3$ and $Ce(dpamd)_3$ precursors range from 2.50 Å to 2.52 Å, and 2.48 Å to 2.52 Å , respectively. For $Yb(dpdmg)_3$ and $Yb(dpamd)_3$, Yb-N distances range from 2.34 Å to 2.35 Å, and 2.31 Å to 2.35 Å.

Table 2 M-N distances of precursors in vacuum conditions.

$Ce(dpdmg)_3$	**$Ce(dpamd)_3$**	**$Yb(dpdmg)_3$**	**$Yb(dpamd)_3$**
2.51 Å	2.48 Å	2.36 Å	2.34 Å
2.52 Å	2.53 Å	2.36 Å	2.33 Å
2.51 Å	2.51 Å	2.35 Å	2.34 Å
2.50 Å	2.48 Å	2.34 Å	2.32 Å
2.51 Å	2.49 Å	2.35 Å	2.35 Å
2.51 Å	2.51 Å	2.35 Å	2.34 Å

A previous study shows that there is a specific relationship between the radius (M^{3+}) and the N-Me-N bite angles, where the bite angles decrease with increasing the radius. [9] Calculated bite angles of cerium precursors (cerium radius 1.01 Å) and ytterbium precursors (ytterbium radius 0.86 Å) shown in **Table 3** indicate a smaller bite angle for larger rare-earth ion center and match this observation. Bite angles usually give us information about the geometry distortion.

Table 3 N-M-N bite angle of the precursors from DFT.

$Ce(dpdmg)_3$	**$Ce(dpamd)_3$**	**$Yb(dpdmg)_3$**	**$Yb(dpamd)_3$**
53.6°	53.9°	57.5°	57.3°
53.7°	53.9°	57.5°	57.5°
53.8°	53.5°	57.5°	57.7°

The bond dissociation energy defined as the energy for the removal of the first ligand, is computed for all precursors. Based on bond dissociation energies, as shown in **Table 4**, it is anticipated that $Ce(dpdmg)_3$ will be more stable compared to $Ce(dpamd)_3$ under vacuum conditions. It is to be noted that, under thermal conditions other reactions or decomposition pathways can also occur; for example, for guanidinates, the carbodiimide deinsertion [10] can also take place which has not been taken into consideration on the DFT study. For the ytterbium precursors, the trend is the same, although the difference is less significant. Taking into consideration the bond dissociation energies, $Yb(dpdmg)_3$ and $Yb(dpamd)_3$ would have similar stability under vacuum conditions.

Table 4 Computed bond dissociation energies to lose the first ligand from the precursors E^{ligand} ($kJmol^{-1}$) in vacuum and in models of interaction with oxygen and water.

	In vacuum **$kJmol^{-1}$**	**In the presence of a O_2 molecule ($kJmol^{-1}$)**	**In the presence of a H_2O molecule ($kJmol^{-1}$)**
$Ce(dpdmg)_3$	626.37	69.02	85.92
$Ce(dpamd)_3$	405.13	85.38	104.20
$Yb(dpdmg)_3$	373.25	332.74	68.56
$Yb(dpamd)_3$	352.40	336.29	90.73

Based on the bond dissociation energies and the overall trend described above, the stability and potential reactivity of these precursors is not necessarily correlated to the bonding properties

within their molecular structure. We would expect that precursors with the shorter Me-N bonds would be less reactive; however, this is not apparent from the data in **Table 2** and **Table 4**.

Keeping this in mind, we expanded the model system of the precursors to include the interaction with one oxygen and one water molecule and investigate the reactivity again at zero K and zero GPa.

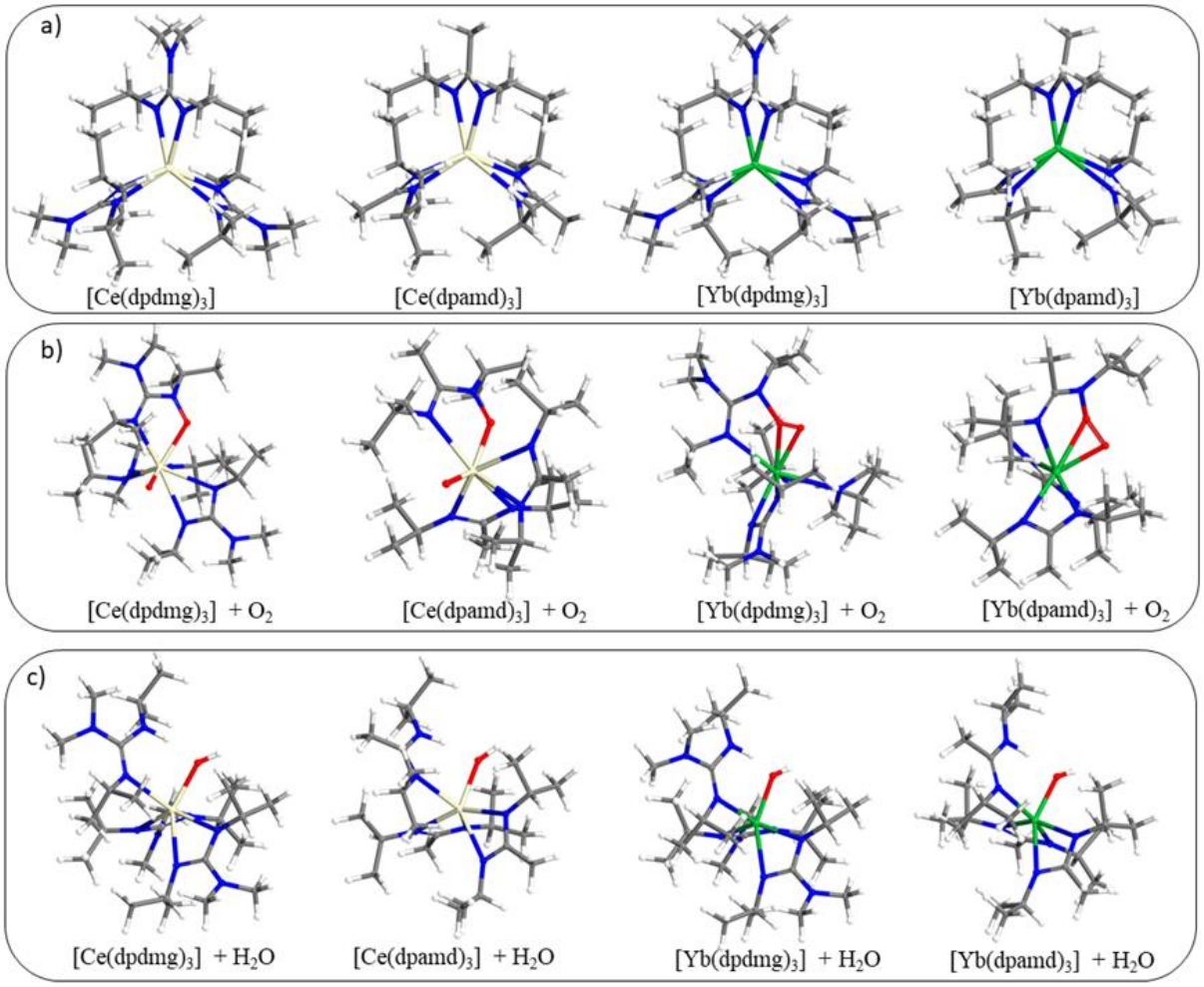


Figure 11 Optimised atomistic structures of $Ce(dpdmg)_3$, $Ce(dpamd)_3$, $Yb(dpdmg)_3$ and $Yb(dpamd)_3$ a) in vacuum condition, b) after incorporating one oxygen molecule and c) after incorporating one water molecule. Cream-Ce, green-Yb, blue-N, grey-C, red-O, white-H.

An oxygen molecule is placed at 2.50Å from the metal centre in its gas phase geometry and the structure was allowed to relax. **Fig. 11 (b)** shows the relaxed atomic structure of the precursors after the incorporation of the oxygen molecule and demonstrates that the interaction with oxygen depends on the metal centre. Cerium promotes the breaking of the O=O bond in both precursors, which is typical for Ce^{3+} species. [11, 12] For the precursors $Ce(dpdmg)_3$ and

$Ce(dpamd)_3$ one oxygen atom inserts into the original Ce-N bond creating new Ce-O and O-N bonds while the second oxygen atom binds with the cerium centre for both the precursors forming an oxo-ligand. Calculated reaction energies are -0.10 eV for $Ce(dpdmg)_3$ and -1.01 for $Ce(dpamd)_3$.

In contrast to cerium, ytterbium does not break the O=O bond. Instead, in the precursors $Yb(dpdmg)_3$ and $Yb(dpamd)_3$, the oxygen molecule forces its way to close proximity to the metal centre and forms a tricycle with ytterbium while one Yb-N bond is cleaved, which again results in a 7-fold coordination sphere. One of the oxygen atoms forms an O-N bond with the non-metal coordinated N. The O-O bond length is in the range of 1.45 Å to 1.46 Å which is characteristic of a peroxide species. Calculated reaction energies are -0.19 eV for $Yb(dpdmg)_3$ and -0.10 for $Ce(dpamd)_3$. **Table 5** shows the M-O, O-N, and M-N bonds in the presence of oxygen.

Table 5 M-O, O-N, O-O and M-N distances of precursors after the incorporation of oxygen.

	$Ce(dpdmg)_3$	**$Ce(dpamd)_3$**	**$Yb(dpdmg)_3$**	**$Yb(dpamd)_3$**
Ce-N	2.71 Å	2.73 Å	2.54 Å	2.41 Å
Ce-N	2.53 Å	2.78 Å	2.30 Å	2.33 Å
Ce-N	2.77 Å	2.64 Å	2.40 Å	2.30 Å
Ce-N	2.61 Å	2.48 Å	2.42 Å	2.39 Å
Ce-N	2.61 Å	2.59 Å	2.32 Å	2.53 Å
Ce-O1	2.32 Å	2.29 Å	2.83 Å	2.38 Å
O1-N	1.35 Å	1.34 Å	1.45 Å	1.46 Å
Ce-O2	1.82 Å	1.82 Å	2.15 Å	2.16 Å

According to bond dissociation energies shown in **Table 4**, $Ce(dpdmg)_3$ would be more reactive compared to $Ce(dpamd)_3$ with oxygen. For the ytterbium precursors, the difference in bond dissociation energies is almost negligible and slightly changed from the gas phase precursor. This suggests that the reactivity of the ytterbium containing precursors is little affected by the nature of the ligand regarding the interaction with oxygen.

Fig. 11 (c) shows the optimized structures of the precursors after the interaction with one water molecule. When one water molecule interacts with the precursors, it preferably binds to the central cerium and ytterbium atom and dissociates. The hyrdoxyl group of water binds to the Me, and the remaining proton binds to nitrogen upon Me-N bond breakage. Calculated reaction

energies of -1.90 eV for $Ce(dpdmg)_3$, -1.02 eV for $Ce(dpamd)_3$, -1.14 for $Yb(dpdmg)_3$ and -1.19 eV for $Yb(dpamd)_3$ prove the favourable interaction of all precursors with water.

Table 6 shows the Me-OH and Me-N bonds in the presence of water. Once the water molecule has reacted with the metal centre, dissociation of the semi-protonated, solely one-fold bonded ligand is identified as a preferential dissociation pathway. Based on the computed bond dissociation energies, $Ce(dpdmg)_3$ is expected to be more reactive compared to $Ce(dpamd)_3$ and $Yb(dpdmg)_3$ would be more reactive compared to $Yb(dpamd)_3$. Thus, the reactivity of all these precursors can be strongly influenced by the interaction with oxygen or water molecules.

Table 6 M-O, O-N, O-O and M-N distances of precursors after the incorporation of water.

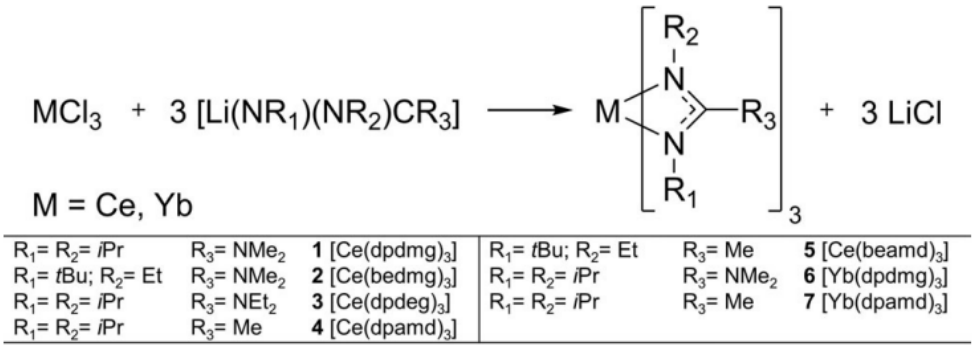
	$Ce(dpdmg)_3$	**$Ce(dpamd)_3$**	**$Yb(dpdmg)_3$**	**$Yb(dpamd)_3$**
Ce-N	2.70 Å	2.55 Å	2.42 Å	2.52 Å
Ce-N	2.48 Å	2.51 Å	2.32 Å	2.34 Å
Ce-N	2.61 Å	2.68 Å	2.58 Å	2.38 Å
Ce-N	2.56 Å	2.61 Å	2.39 Å	2.40 Å
Ce-N	2.51 Å	2.45 Å	2.34 Å	2.33 Å
Ce-OH	2.23 Å	2.22 Å	2.11 Å	2.10 Å

This study shows that these precursors are potential candidates for ALD precursors. Interestingly, the bond dissociation energy for the cerium precursors $Ce(dpdmg)_3$ and $Ce(dpamd)_3$ is found to be less in the presence of an oxygen molecule than in the vicinity of a water molecule which suggests that the elemental oxygen could be an interesting coreagent for ALD with cerium precursors.

8.4.1.2 Selected experimental results (Ruhr University Bochum, Aalto University)

Precursor synthesis

The synthesis of all the precursors was achieved by a salt metathesis reaction of the anhydrous metal chloride MCl_3 (M= Ce, Yb) and three equivalents of the respective lithium (Li) salts of the ligand $[Li(NR_1)(NR_2)C(R_3)]$ (R_1=iPr, tBu; R_2=iPr, Et; R_3= Me, NMe_2, NEt_2) as shown in **Scheme 2**.



Scheme 2 General reaction scheme for the synthesis of homoleptic rare earth guanidinate and amidinate precursors.

Nuclear magnetic resonance (NMR) characterisation

All the precursors are paramagnetic in nature (one unpaired electron in Ce^{3+} and one in Yb^{3+}), necessitating large chemical shift ranges (ppm) for the measurement of ^{1}HNMR spectra of the cerium precursors. For the ytterbium precursors, the recording of the spectra failed due to significant paramagnetic shifts.

^{1}HNMR was measured for the cerium precursors in C_6D_6, the chemical shift peaks were found to be broad in the range 10 ppm to 11 ppm and the intensity was significantly reduced. However, the integration of the peaks matched with the number of hydrogen atoms present in the precursors (**Fig. 12**).

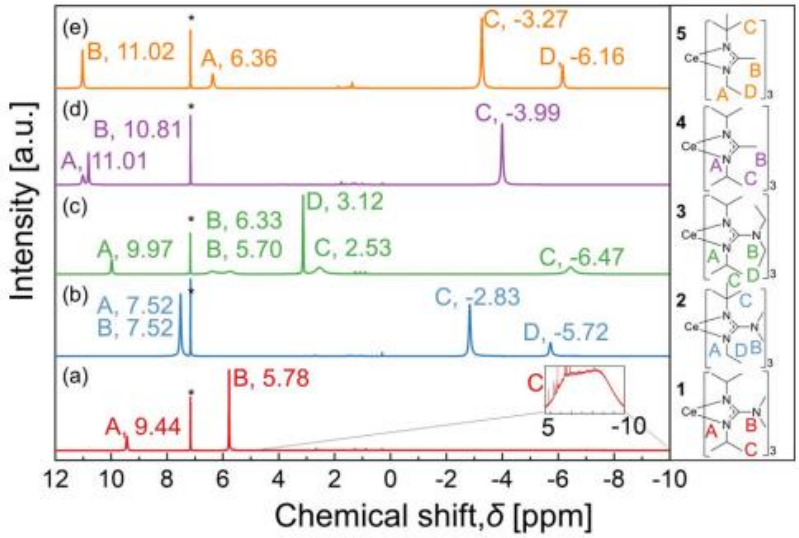


Figure 12 ^{1}H NMR spectra of the cerium precursors in C6D6. (*C_6D_6, 7.16 ppm).

Electron-impact mass spectrometry (EI-MS) characterisation

EI-MS analysis was carried out to confirm the formation of the target precursor, analyse the fragmentation pattern, and to get an insight into the structural features of the metal-organic precursors. The selected peaks of the EI-MS spectra with assigned fragments are listed in **Table 7**.

For all the precursors, the respective molecular ion peaks (ML_3^+) with expected mass to charge ratios (m/z) and considerable relative intensities of 14.8% for **1**, 9.4% for **2**, 46.8 % for **3**, 38.8 % for **4**, 44.6% for **5**, 2.0% for **6**, 7.0% for **7** were found. Peaks at higher m/z ratios than the molecular ion peak were not observed under experimental conditions, which suggests that all the precursors can exist as monomers in the gas phase. For all the precursors, the fragments from cleavage of one ligand (ML_2^+), or of two ligands (ML^+) species, as well as the ligand L^+ itself, were detected. Interestingly, for all amidinate precursors, the fragment with the highest intensity (100%) was the ML_2^+ fragment. The guanidinates seem to decompose into smaller fragments, indicated by the peak with 100% intensity which is observed for fragments associated with the organic ligands and their decomposition fragments.

Table 7 Overview of m/z (relative intensity %) of selected possible fragments observed for precursors 1-7 detected from EI-MS.

Fragments	$[Ce(dpdmg)_3]$ **1**	$[Ce(bedmg)_3]$ **2**	$[Ce(dpdeg)_3]$ **3**	$[Ce(dpamd)_3]$ **4**	$[Ce(beamd)_3]$ **5**	$[Yb(dpdmg)_3]$ **6**	$[Yb(dpamd)_3]$ **7**
ML_3^+	650.5 (14.8%)	650.5 (9.4%)	734.5 (46.8%)	563.4 (38.8%)	563.4 (44.6%)	684.8 (2.0%)	597.5 (7.0%)
ML_2^+	480.3 (35.4%)	480.3 (13.7%)	536.3 (40.8%)	422.2 (100%)	422.2 (100%)	513.4 (92.5%)	455.4 (100%)
ML^+	311.4 (13.2%)	311.4 (15.9%)	337.1 (49.4%)	280.1 (3.4%)	280.1 (5.9%)	342.2 (94.2%)	313.2 (28.9%)
ML^+-(*i*Pr/*t*Bu)	267.1 (6.0%)	253.1 (9.0%)	–	–	–	301.1 (36.2%)	–
ML^+-($2CH_2CH_2$)	–	–	282.1 (48.4%)	–	–	–	–
L^+	171.2 (5.8%)	171.2 (1.8%)	199.3 (5.8%)	142.2 (17.5%)	142.2 (18.8%)	170.2 (25.0%)	142.2 (28.6%)
*i*PrNC$^+$	69.1 (100%)	–	69.1 (91.0%)	–	–	69.1 (100%)	–
EtNC$^+$	–	57.0 (100%)	–	–	–	–	–
*t*BuNC$^+$	–	83.0 (60.3%)	–	–	–	–	–
*i*Pr$^+$	43.1 (75.6%)	43.1 (19.6%)	43.1 (100%)	43.1 (10.1%)	43.1 (10.2%)	43.1 (94.3%)	43.1 (21.8%)

Thermal investigations of the precursors

The weight loss of the precursors as a function of temperature in the range of 358 C - 400 C is shown in **Fig. 13**. This study exemplifies how systematic variation of substituents on the side chains and backbones of the employed amidinate and guanidinate ligands can be used to tune the thermal properties of the precursors. The thermal properties of precursors having the same molecular mass and an identical composition, namely **1**, **2**, and **4**, **5**, differ noticeably. Due to the large asymmetry in its structure, precursor **5** has the lowest melting point of all the precursors and precursor **2** possesses a lower melting point than **1**. On the other hand, the higher asymmetry in the molecular structure can lead to lower thermal stability and it was additionally found that the thermal stability and volatility of the amidinates is higher than the one of the guanidinates. Interestingly, the cerium guanidinate **1** is melting at a lower temperature than the isostructural ytterbium precursor **6**. Besides, the cerium precursors **1–5** are more volatile than ytterbium precursors **6** and **7** while exhibiting less thermal resilience.

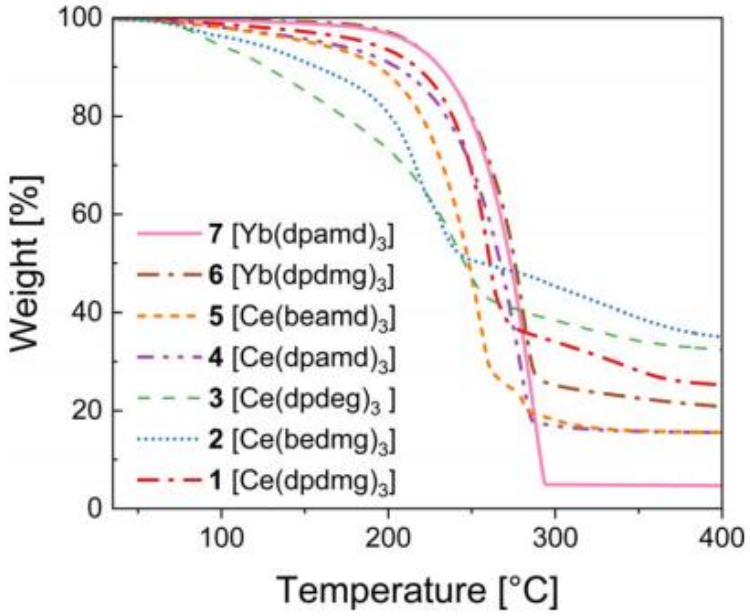


Figure 13 Thermogravimetric analysis of all cerium and ytterbium precursors.

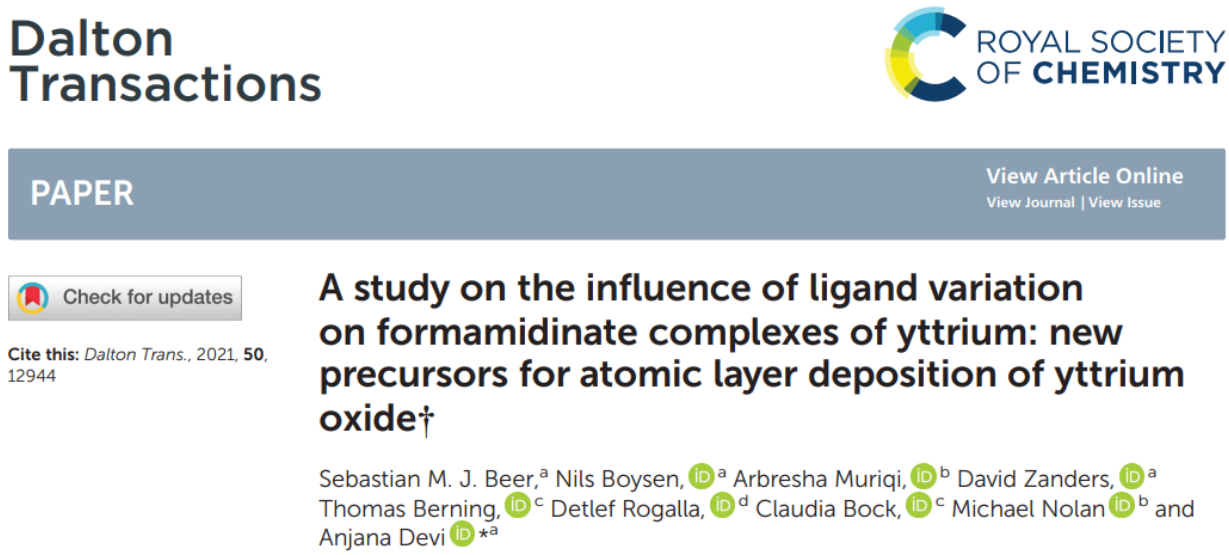
ALD process development for cerium oxide (CeO_2) thin films

Proof-of-principle ALD experiments on Si(100) substrates was performed using $Ce(dpdmg)_3$ as metal source and water as coreactant. $Ce(dpdmg)_3$ was chosen as representative case, as it was found to be very reactive towards water in on our DFT calculations (**Section 8.4.1.1**).

The sublimation temperature for $Ce(dpdmg)_3$ is set 140°C and water was maintained at room temperature. The applied pulse purge sequence at the deposition temperature 160°C was $Ce(dpdmg)_3$ precursor pulse (8 s)/N_2 purge (30 s)/H_2O pulse (3 s)/N_2 purge (30 s), which led to polycrystalline CeO_2 films with a GPC of 2.1 Å/cycle. The co-existence of Ce^{3+} and Ce^{4+} oxidation states in the films was evidenced from XPS analysis. UV/Vis analysis showed the direct allowed and indirect allowed bandgaps and hence these films could find scope for potential optical and catalytic applications.

8.5 Yttrium precursors

This work is published in the paper "***A study on the influence of ligand variation on formamidinate complexes of yttrium: New precursors for atomic layer deposition of yttrium oxide***", in Dalton Transactions. [13]



DOI: https://doi.org/10.1039/D1DT01634B

8.5.1 Results

In this study, the synthesis and characterization of a series of new homoleptic yttrium tris-formamidinate precursors tris(N,N′di-tert-butyl-2-formamidinato) yttrium (III), Y(tBu_2-famd)$_3$ **1,** tris(N-ethyl,N′-tert-butyl-2-formamidinato) yttrium (III), Y(Et-tBu-famd)$_3$ **3** and tris(N,N′-di-cyclohexyl-2-formamidinato) yttrium (III) Y(Cy_2-famd)$_3$ **4** is done and compared with the precursor tris(N,N′-di-isopropyl-2-formamidinato) yttrium (III) Y(iPr_2-famd)$_3$ **2**, which was recently implemented in a water-assisted thermal ALD process for yttrium oxide (Y_2O_3) thin films. [14] Precursor structures are shown in **Fig. 14**.

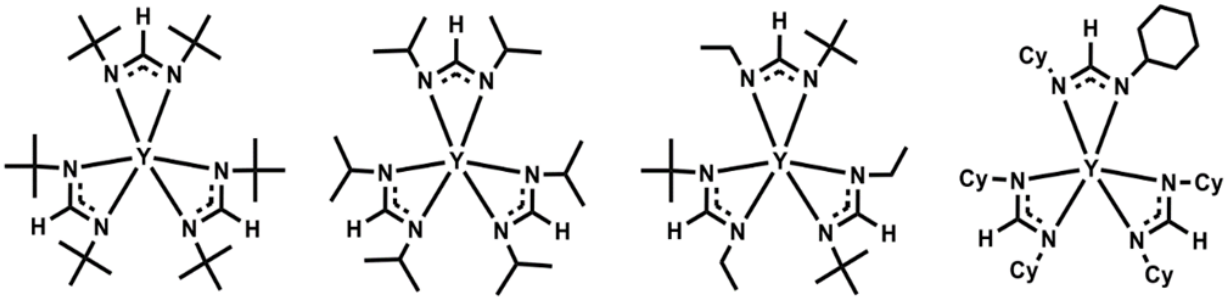


Figure 14 Molecular structure of $Y(tBu_2\text{-famd})_3$, $Y(iPr_2\text{-famd})_3$, $Y(Et\text{-}tBu\text{-famd})_3$ and $Y(Cy_2\text{-famd})_3$ precursor.

8.5.1.1 Computational results

DFT calculations of all four precursors $Y(tBu_2\text{-famd})_3$, $Y(iPr_2\text{- famd})_3$, $Y(Et\text{-}tBu\text{-famd})_3$, and $Y(Cy_2\text{-famd})_3$, were performed to gain insight into the molecular structure, the stability in the gas phase and the chemical reactivity towards water as an ALD coreactant. Since the single crystal structure determination was not successful, optimized stable atomic structures were calculated in 0 K and 0 GPa conditions using DFT, and these are presented **Fig. 15 (a)**. The corresponding M-N bond lengths and N-Y-N bite angles are presented in **Table 8** and **Table 9**, respectively. All precursors exhibit a six-fold coordination of the yttrium metal center with bite angles around 57°, indicating a prismatic coordination sphere. However, the distortion of the prism (=ligands) of 28.92° for $Y(tBu\text{-famd})_3$, 22.54° for $Y(iPr\text{-famd})_3$, 26.58° for $Y(Et\text{-}tBu\text{-famd})_3$ and 24.38° for $Y(Cy\text{-famd})_3$ deviates from the ideal value of 0° or 90°. Thus, the coordination geometry is best described as distorted prismatic, which is in accordance with single-crystal analysis of structurally related yttrium tris-guanidinates. [15] Furthermore, the influence of the steric demands of the side-chains on the overall structure of the precursor can be seen by comparing the trend in the degree of distortion showing tBu > (Et-tBu) > Cy > iPr, which follows the trend of the steric demands of the side chains.

The highest occupied molecular orbital (HOMO) and lowest unoccupied molecular orbital (LUMO) energy gap serves as one figure of merit for the stability of precursors. A large gap indicates a high stability and chemical robustness in the gas phase, [16] which is a key requirement of precursor used in ALD. The magnitude of the HOMO–LUMO energy gap ($E_{HOMO}–E_{LUMO}$) was estimated to be +5.86 eV for $Y(tBu_2\text{-famd})_3$, +5.93 eV for $Y(iPr_2\text{-famd})_3$, +5.94 eV for $Y(Et\text{-}tBu\text{-famd})_3$, and +5.84 eV for $Y(Cy_2\text{-famd})_3$. The largest difference in the

computed HOMO-LUMO gaps is only 0.13 eV which indicates that by this measure, there is very little difference in stability between the four precursors.

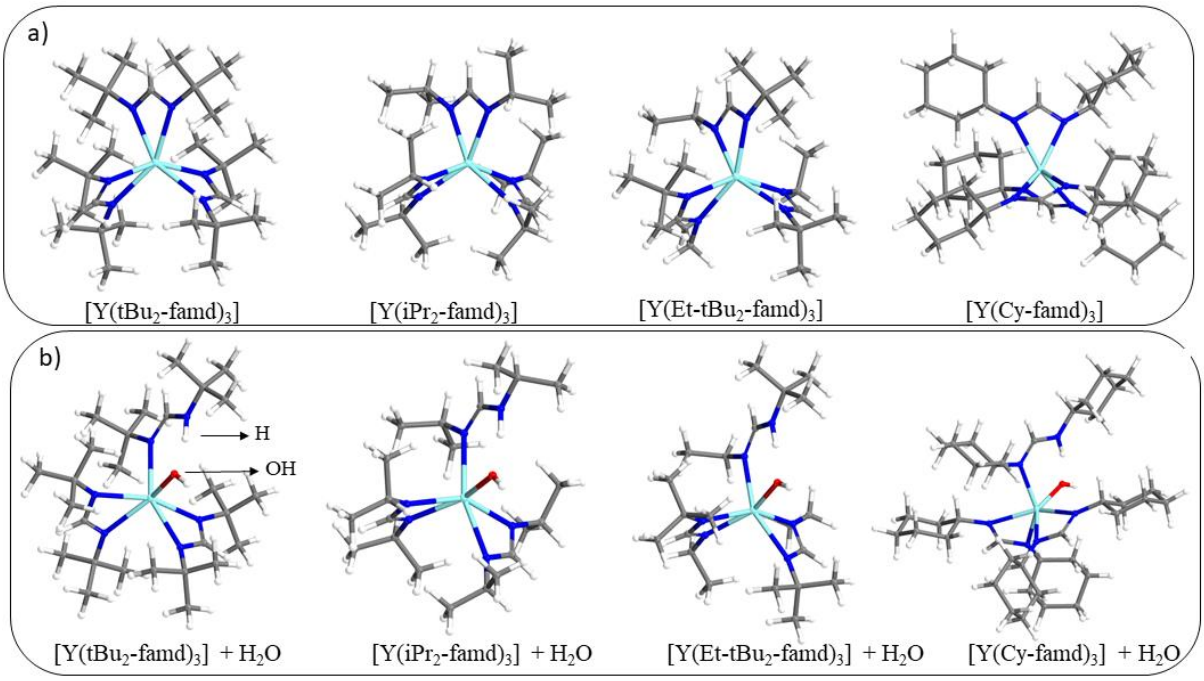


Figure 15 Optimised atomistic structures of $Y(tBu_2\text{-famd})_3$, $Y(iPr_2\text{-famd})_3$, Y(Et-tBu-famd)$_3$, and $Y(Cy_2\text{-famd})_3$ (a) in vacuum condition and (b) after incorporating one oxygen molecule. Cyan-Y, blue-N, grey-C, red-O, white-H.

Table 8 M-N distances of precursors in vacuum conditions.

Y(tBu-famd)$_3$	**Y(iPr-famd)$_3$**	**Y(Et-tBu-famd)$_3$**	**Y(Cy-famd)$_3$**
2.40 Å	2.37 Å	2.38 Å	2.39 Å
2.39 Å	2.38 Å	2.38 Å	2.39 Å
2.40 Å	2.38 Å	2.38 Å	2.36 Å
2.39 Å	2.39 Å	2.39 Å	2.41 Å
2.39 Å	2.39 Å	2.38 Å	2.38 Å
2.39 Å	2.39 Å	2.39 Å	2.39 Å

Table 9 N-M-N bite angle of the precursors from DFT.

Y(tBu-famd)$_3$	**Y(iPr-famd)$_3$**	**Y(Et-tBu-famd)$_3$**	**Y(Cy-famd)$_3$**
56.9°	57.1°	57.0°	57.0°
56.9°	57.0°	57.0°	56.8°
56.9°	58.0°	57.0°	56.9°

Furthermore, the bond dissociation energies for the cleavage of one ligand moiety in the gas phase were computed, obtaining values ranging from 493.59 kJ/mol for $Y(tBu_2\text{-famd})_3$, 488.34 kJ/mol for $Y(iPr_2\text{-famd})_3$, 493.59 kJ/mol for $Y(Et\text{-}tBu\text{-famd})_3$ and 472.58 kJ/mol for $Y(Cy_2\text{-famd})_3$. This similarity shows that all precursors tend to feature a comparable dissociation behavior, although precursor $Y(Cy_2\text{-famd})_3$ shows a slightly lower stability. In fact, the trend observed from the DFT gas phase stability partially reflects the findings from EI-MS, where $Y(Cy_2\text{-famd})_3$ exhibited a lower stability in the gas phase.

For a first prediction of the suitability of the precursor yttrium precursors for water-assisted ALD, the precursors interact with one equivalent of water in the gas phase, as depicted in **Fig. 15 (b**). Although ALD surface chemistries are far more complex in nature, this straight forward DFT approach has been demonstrated to serve as a valuable tool, enabling the screening of potential precursor chemistries. [17-19] Calculated structures show that the water molecule reacts favorably with all precursors and dissociates. The hydroxyl group bonds to the central yttrium atom with a Y-OH distance of 2.15 Å and the remaining proton binds to an nitrogen atom of the ligand, which then detaches from the yttrium site. In the presence of water, the remaining Y-N bonds are lengthened from the unmodified precursors, as shown in **Table 10.**

The calculated interaction energies show that all precursors interact favorably with water, obtaining values of -1.19 eV, -1.41 eV, -1.41 eV and -1.49 eV for $Y(tBu_2\text{-famd})_3$, $Y(iPr_2\text{-famd})_3$, $Y(Et\text{-}tBu\text{-famd})_3$ and $Y(Cy\text{-famd})_3$, respectively. Interestingly, the lowest reactivity was calculated for $Y(tBu_2\text{-famd})_3$ which might be best explained by the higher shielding of the yttrium metal center by the tBu groups compared to the other precursors. Nevertheless, the energy difference compared to the other precursors is small and thus indicates a sufficient reactivity for ALD of Y_2O_3 using water as coreactant.

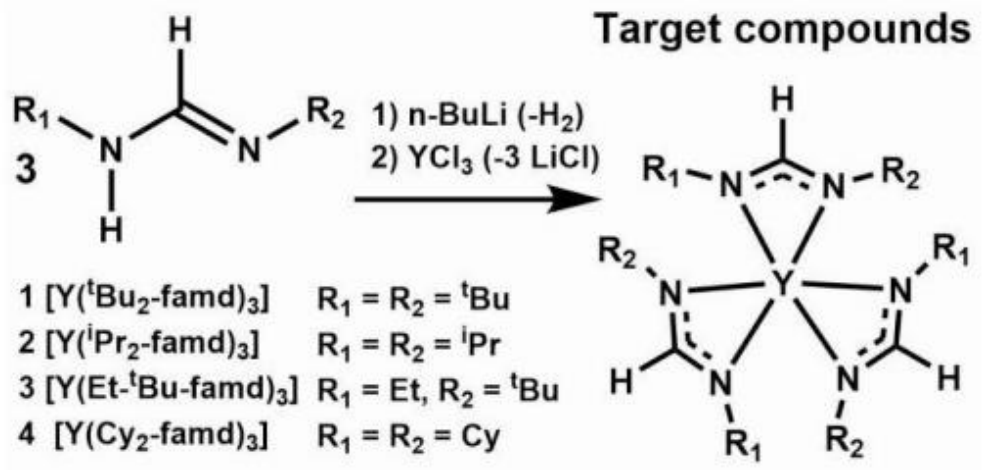
Table 10 M-O, O-N, O-O and M-N distances of precursors after the incorporation of water.

	$Y(tBu\text{-famd})_3$	**$Y(iPr\text{-famd})_3$**	**$Y(Et\text{-}tBu\text{-famd})_3$**	**$Y(Cy\text{-famd})_3$**
Y-N	2.45 Å	2.45 Å	2.38 Å	2.38 Å
Y-N	2.40 Å	2.36 Å	2.41 Å	2.43 Å
Y-N	2.39 Å	2.39 Å	2.43 Å	2.41 Å
Y-N	2.44 Å	2.43 Å	2.39 Å	2.41 Å
Y-N	2.53 Å	2.53 Å	2.47 Å	2.46 Å
Y-OH	2.15 Å	2.15 Å	2.15 Å	2.15 Å

8.5.1.2 Selected experimental results (Ruhr University Bochum)

Precursor synthesis

As shown in **Scheme 3**, the target yttrium precursors were synthesized from a salt metathesis reaction between YCl_3 and the respective lithiated ligands.



Scheme 3 Synthetic approaches for the formation of the target precursorss $Y(tBu_2\text{-famd})_3$, $Y(iPr_2\text{-famd})_3$, Y(Et-tBu-famd)$_3$, and $Y(Cy_2\text{-famd})_3$ precursors.

Nuclear magnetic resonance (NMR) characterisation

^{1}HNMR measurements of the formamidine ligands and target precursors are shown in **Fig. 16**. The peaks of the protonated ligands were consistent with literature reports [20, 21] and are in line with the obtained spectra for the yttrium precursors, thus confirming the successful synthetic approach.

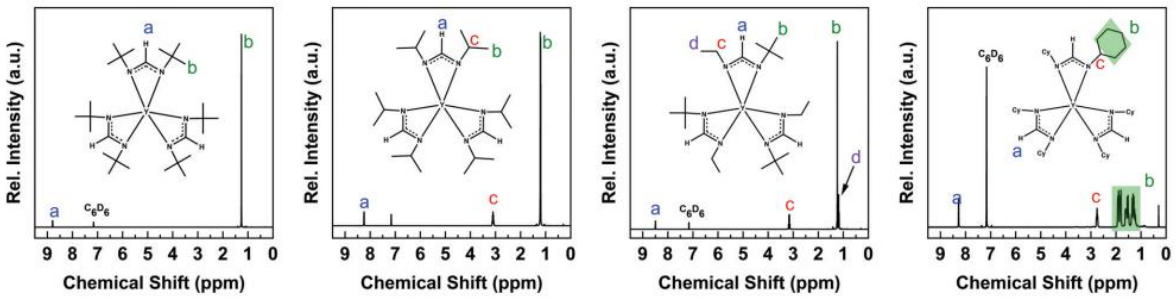


Figure 16 ^{1}H-NMR spectra of $Y(tBu_2\text{-famd})_3$, $Y(iPr_2\text{-famd})_3$, Y(Et-tBu-famd)$_3$, and $Y(Cy_2\text{-famd})_3$ precursors.

Electron-impact mass spectrometry (EI-MS) characterisation

For all the target precursors, the respective molecular ion peaks $[Y(L)_3]^{\cdot+}$ (L = ligand) "a" were identified as the peaks with the highest m/z ratios. Moreover, due to the absence of higher m/z peaks, it can be assumed that the precursors remain monomeric in the gas phase under electron ionization.

Precursors $Y(tBu_2\text{-famd})_3$, $Y(iPr_2\text{-famd})_3$ and $Y(Et\text{-}tBu\text{-famd})_3$ tend to undergo similar fragmentation pathways by the successive cleavage of the alkyl moieties and forming the relatively stable $[Y(L)_2]^{\cdot+}$ intermediates before cleaving another ligand which results in the formation of $[Y(L)]^{\cdot+}$ (signal f). In comparison to $Y(tBu_2\text{-famd})_3$, $Y(iPr_2\text{-famd})_3$ and $Y(Et\text{-}tBu\text{-famd})_3$, $Y(Cy_2\text{-famd})_3$ show a lower stability under the harsh EI-MS ionization conditions as seen from the fragments with low intensities (< 0.6 %) assignable to the molecular ion peak $[Y(L)_3]^{\cdot+}$ and $[Y(L)_2]^{\cdot+}$. The first fragment with notable stability (intensity 31.46 %) is represented by the ligand $[L]^{\cdot+}$ (signal g), which readily undergoes facile cleavage followed by successive fragmentation of the cyclohexyl rings as seen by several low m/z fragments with high intensities. This indicates a relatively lower stability of the Cy groups under EI-MS conditions compared to the tBu or iPr groups.

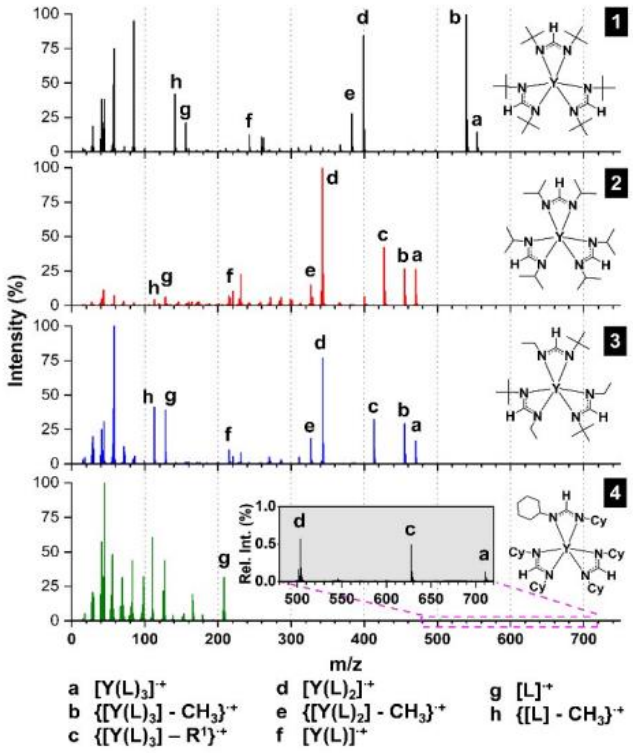


Figure 17 EI-MS (70 eV) of $Y(tBu_2\text{-famd})_3$, $Y(iPr_2\text{-famd})_3$, $Y(Et\text{-}tBu\text{-famd})_3$ and $Y(Cy_2\text{-famd})_3$. Characteristic fragments are depicted from a-h in the graphs.

Thermal investigations of the precursors

Precursors Y(tBu$_2$-famd)$_3$ and Y(iPr$_2$-famd)$_3$ exhibit an one-step volatilization behavior with step temperatures of around 253°C and 205°C, graphically estimated using a tangential method, characterizing Y(iPr$_2$-famd)$_3$ as the most volatile precursor among the series. This difference can partly be explained by the higher molecular mass of Y(tBu$_2$-famd)$_3$ (approximately 18 %).

In contrast to the one-step volatilization behavior of Y(tBu$_2$-famd)$_3$ and Y(iPr$_2$-famd)$_3$, precursors Y(Et-tBu-famd)$_3$ and Y(Cy$_2$-famd)$_3$ show multiple steps, indicating decomposition events upon heating. This results in the formation of stable intermediates, which evaporate at elevated temperatures. A notable example on the impact of molecular structure on thermal stability of a precursor is showcased focusing on Y(iPr$_2$-famd)$_3$ and Y(Et-tBu-famd)$_3$. The asymmetry in the ligand sphere of Y(Et-tBu-famd)$_3$ seems to lower the thermal stability depicted by the presence of a second step occurring at T > 230°C compared to Y(iPr$_2$-famd)$_3$, although both precursors feature the same molecular weight of 470.5 Da.

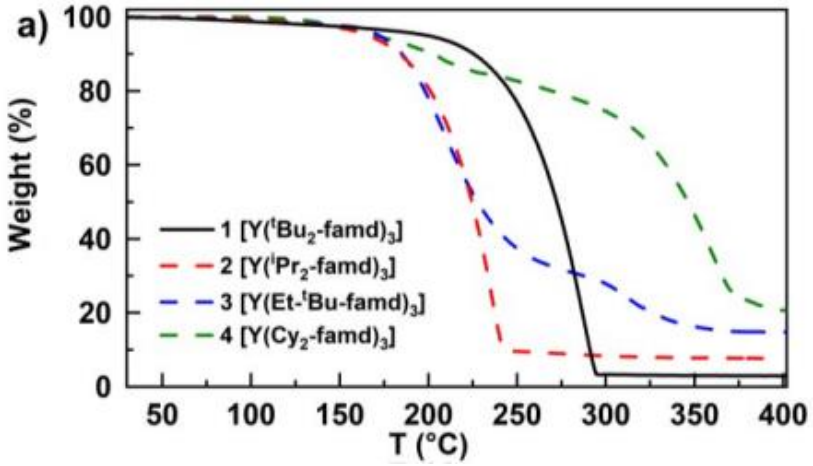


Fig. 18 Thermogravimetric analysis of all yttrium precursors.

ALD process development for yttrium oxide (Y_2O_3) thin films

As Y(tBu$_2$-famd)$_3$ was found to possess enhanced thermal stability, to demonstrate its the suitability for ALD of Y_2O_3, a thorough process optimization of a thermal ALD process with water as coreactant was carried out. Films deposited with Y(tBu$_2$-famd)$_3$ are directly compared with films deposited with the analogous Y(iPr$_2$-famd)$_3$ precursor. The depositions were performed on 2-inch Si(100) substrates with the precursor heated at 150°C and the substrate temperature.

With a 6 s of $Y(tBu_2\text{-famd})_3$ precursor pulse, with 20 s precursor purge and 0.5 s of water pulse the surface is saturated leading to a constant GPC of around 0.67 Å. Interestingly, the analogous $Y(iPr_2\text{-famd})_3$ yields to a GPC of 1.36 Å, which indicates a lower surface coverage of $Y(tBu_2\text{-famd})_3$ for each monolayer, potentially reasoned by the higher steric demand of the tBu vs. the iPr groups, blocking active surface sites.

8.6 Europium precursors

This work is published in the paper "***Ferromagnetic Europium Sulfide Thin Films: Influence of Precursors on Magneto-Optical Properties***", in Chemistry of Materials. [22]

CHEMISTRY OF MATERIALS

pubs.acs.org/cm Article

Ferromagnetic Europium Sulfide Thin Films: Influence of Precursors on Magneto-Optical Properties

Sebastian M. J. Beer, Arbresha Muriqi, Patrick Lindner, Manuela Winter, Detlef Rogalla, Michael Nolan, Andreas Ney, Jörg Debus, and Anjana Devi*

DOI: https://doi.org/10.1021/acs.chemmater.1c02958

8.6.1 Results

Three new europium containing precursors bearing amidinate and guanidinate ligand types, namely, tris(N,N′-diisopropyl-2-formamidinato) europium (III), $Eu(dpfamd)_3$ **1**, tris(N,N′-diisopropyl-2-acetamidinato) europium (III), $Eu(dpamd)_3$ **2**, and tris(N,N′-diisopropyl-2-dimethylamido-guanidinate) europium (III), $Eu(dpdmg)_3$ **3** were synthesised and characterised. Precursor structures are shown in **Fig. 19**.

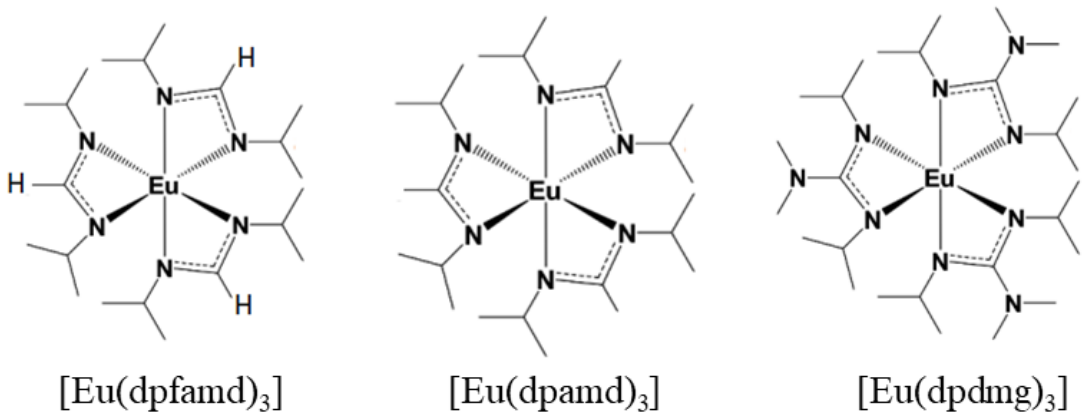


Figure 19 Molecular structure of $Eu(dpfamd)_3$, $Eu(dpamd)_3$ and $Eu(dpdmg)_3$ precursor.

8.6.1.1 Computational results

DFT methods were employed to predict the precursor stability using simple thermodynamics for precursor decomposition and to determine the precursor reactivity by simulating the chemical reactions with sulfur and oxygen as potential coreactants for CVD.

First, we have investigated the geometry of europim precursors in vacuum conditions. Optimised atomic structures are presented in **Fig. 20 (a)**. The computed Eu-N bond lengths, the mean N-Eu-N bidentate ligand angles, and the N-C-N backbone angles of the three europium precursors are presented in **Table 11**. The obtained structural characteristics of $Eu(dpdmg)_3$ exhibit Eu-N bond lengths of 2.40-2.42 Å, an average N-C-N backbone angle of 115°, and an N-Eu-N angle of 55.3°. Similar values are obtained for $Eu(dpamd)_3$, whereas the N-C-N angle of $Eu(dpfamd)_3$ is calculated to be larger (120°), possibly originating from the smaller steric demand of the endocyclic function (-H), which creates less steric repulsion on the iPr functions.

The bond strength, characterized by the bond dissociation energy representing the loss of the first ligand moiety, was calculated for the three precursors, obtaining values of 309.81 kJ/mol, 236.29 kJ/mol, and 273.05 kJ/mol for precursors $Eu(dpfamd)_3$, $Eu(dpamd)_3$, and $Eu(dpdmg)_3$, respectively. Due to the higher dissociation energies of $Eu(dpfamd)_3$ and $Eu(dpdmg)_3$, stronger Eu-N bonds and thus a higher precursor stability can be assumed. This is in line with DFT calculations on analogous indium [23] and ytterbium [8] amidinates and guanidinates. Notably, for the bond dissociation enthalpy calculations, solely simple ligand cleavage was assumed, and more complex reactions such as deinsertion reactions, as known from the guanidinates, were not taken into account. [10]

Chemical reactions with sulfur were simulated in the gas phase, which allowed us to understand the behaviour of precursors towards S_8 during sulphide based CVD processes. S_2 and S_4 were selected as coreactants in the gas phase models, functioning as simple models. Notably, elemental sulfur primarily exists in the octasulfur S_8 allotrope as the thermodynamically most stable phase. However, upon evaporation, smaller chains and rings of Sx ($x = 3-7$) and S_2 are formed in the gas phase, which supports our approach to use simple sulfur molecule for this study. [24]

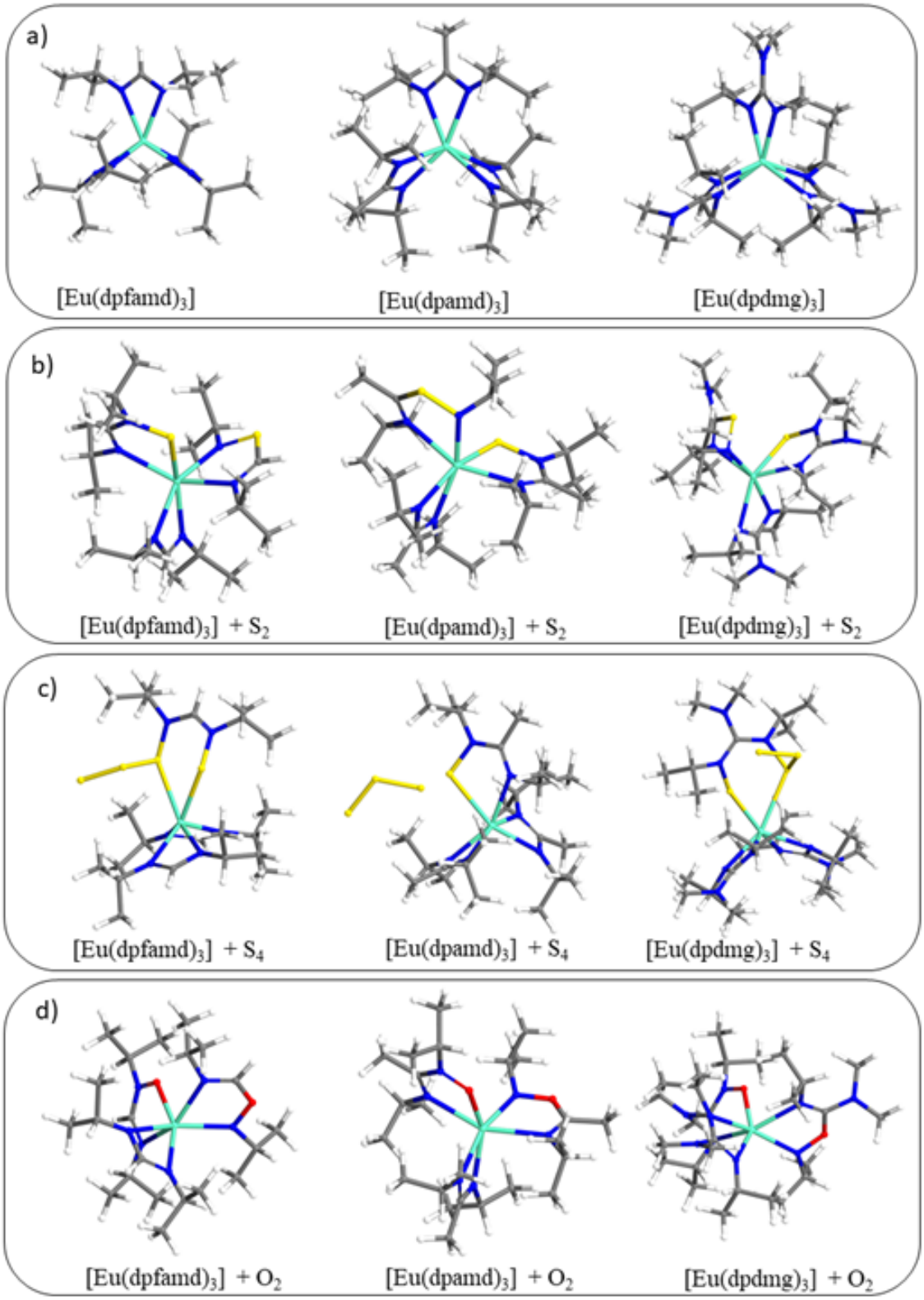


Figure 20 Optimised atomistic structures of $Eu(dpfamd)_3$, $Eu(dpamd)_3$ and $Eu(dpdmg)_3$ a) in vacuum condition, b) after incorporating one sulfur molecule in S_2 form, c) after incorporating one sulfur molecule in S_4 form and d) after incorporating one oxygen molecule. Light blue-Eu, blue-N, grey-C, yellow-S, red-O, white-H.

Table 11 Eu-N bond lengths (Å), N-Eu-N ligand angle (°), and N-C-N backbone angle (°) of $Eu(dpfamd)_3$, $Eu(dpamd)_3$ and $Eu(dpdmg)_3$ from optimized DFT structures.

	$Eu(dpfamd)_3$	**$Eu(dpamd)_3$**	**$Eu(dpdmg)_3$**
		Bond lengths (Å)	
Eu-N	2.41	2.44	2.42
Eu-N	2.42	2.42	2.41
Eu-N	2.41	2.42	2.41
Eu-N	2.42	2.41	2.41
Eu-N	2.42	2.41	2.42
Eu-N	2.42	2.40	2.42
		Bite angle (°)	
N-Eu-N	56.2	55	55.4
N-Eu-N	56.3	55.4	55.3
N-Eu-N	56.2	55.3	55.2
		Angle (°)	
N-C-N	119.8	115.8	115.3
N-C-N	120.3	115.4	114.8
N-C-N	119.8	115.9	114.8

This assumption simplifies the calculations and allows a reasonable approach for first-principles analysis of the precursor reactivity. S_2 and S_4 were positioned 2.5 Å away from the precursor molecules, and the structures were allowed to relax. Reaction products with S_2 are displayed in **Fig. 20 (b).** It is visible that the reaction of the individual europium precursors with S_2 causes a dissociation of the S-S double bond, and one S atom inserts into the cleaved Eu-N bond and forms an Eu-S bond. The second S atom inserts into an N-C bond of the endocyclic N-C-N backbone, thereby forming new N-S and S-C bonds. Geometry data are presented in **Table 12**. The calculated interaction energies were calculated to be -1.22 eV, -1.30 eV, and -0.48 eV for interaction of S_2 with $Eu(dpfamd)_3$, $Eu(dpamd)_3$, and $Eu(dpdmg)_3$, respectively.

Table 12 Eu-N, Eu-O, N-O and O-C distances of precursors after the incorporation of sulfur in form of S_2.

	Eu(dpfamd)$_3$	**Eu(dpamd)$_3$**	**Eu(dpdmg)$_3$**
Eu-N	2.52 Å	2.51 Å	2.39 Å
Eu-N	2.38 Å	2.59 Å	2.50 Å
Eu-N	2.50 Å	2.33 Å	2.36 Å
Eu-N	2.47 Å	2.47 Å	2.43 Å
Eu-N	2.45 Å	2.45 Å	2.49 Å
Eu-S1	2.79 Å	2.79 Å	2.75 Å
N-S2	1.67 Å	1.67 Å	1.68 Å
S2-C	1.69 Å	1.69 Å	2.72 Å

Reaction products with S_4 (**Fig. 20 (c)**) show that the europium precursors also react favorably, thereby promoting the breaking of S-S bonds, where S atoms insert into the cleaved Eu-N bonds to form new Eu-S and S-N bonds, similar to the reactions with S_2. The interaction energies were calculated to be -0.10 eV, -0.59 eV, and -0.21 eV for Eu(dpfamd)$_3$, Eu(dpamd)$_3$, and Eu(dpdmg)$_3$, respectively. The respective geometry data are presented in **Table 13**.

Table 13 Eu-N, Eu-O, N-O and O-C distances of precursors after the incorporation of sulfur in form of S_4.

	Eu(dpfamd)$_3$	**Eu(dpamd)$_3$**	**Eu(dpdmd)$_3$**	
Eu-N	2.38 Å	2.38 Å	Eu-N	2.38 Å
Eu-N	2.42 Å	2.45 Å	Eu-N	2.37 Å
Eu-N	2.44 Å	2.44 Å	Eu-N	2.4 Å
Eu-N	2.39 Å	2.39 Å	Eu-N	2.4 Å
Eu-S1	2.85 Å	2.84 Å	Eu-N	2.48 Å
S1-N	1.74 Å	1.75 Å	Eu-S1	2.85 Å
Eu-S2	3.01 Å	3.06 Å	S2-N	1.72 Å
S2-N	1.71 Å	1.72 Å		

Similarly, to the reaction of the precursors with S_2, the reaction toward oxygen was predicted, to allow statements on the suitability of the europium precursors for oxide-based CVD processes (**Fig. 20 (d)**). The calculated interaction energies for the reactions with oxygen were found to be -1.03 eV for Eu(dpfamd)$_3$, -1.36 eV for Eu(dpamd)$_3$, and -0.57 eV Eu(dpdmg)$_3$, indicating a higher overall reactivity for Eu(dpamd)$_3$ under the given experimental conditions.

Geometry data are presented in **Table 14**. The modelled chemistry is similar to DFT calculations of other metal precursor reacting with oxygen (**Section 8.4.1.1*)***. [8]

This observation leads to the assumption that all three precursors react favorably with oxygen in a similar fashion observed for S_2. Certainly, the applied model is simple, but the similar trend and energy values between the precursor reaction and S_2 versus oxygen predict a high compatibility of elemental sulfur as a coreactant in CVD for EuS and further Eu_2O_3.

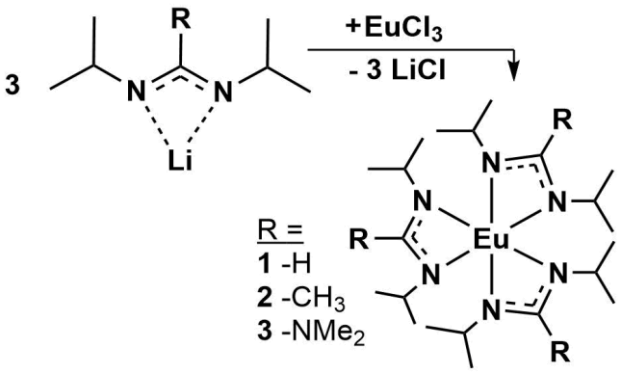
Table 14 Eu-N, Eu-O, N-O and O-C distances of precursors after the incorporation of sulfur in form of oxygen.

	Eu(dpfamd)$_3$	**Eu(dpamd)$_3$**	**Eu(dpdmg)$_3$**
Eu-N	2.37 Å	2.33 Å	2.38 Å
Eu-N	2.50 Å	2.54 Å	2.52 Å
Eu-N	2.55 Å	2.50 Å	2.47 Å
Eu-N	2.47 Å	2.40 Å	2.45 Å
Eu-N	2.44 Å	2.56 Å	2.47 Å
Eu-O	2.26 Å	2.22 Å	2.25 Å
N-O	1.41 Å	1.42 Å	1.42 Å
O-C	1.29 Å	1.31 Å	1.31 Å

8.6.1.2 Selected experimental results (Ruhr University Bochum)

Precursor synthesis

The synthesis followed a salt metathesis reaction of lithiated ligands as shown in **Scheme 4**. [15, 21, 25]



Scheme 4 Reaction pathway for the synthesis of Eu(dpfamd)$_3$, Eu(dpamd)$_3$, and Eu(dpdmg)$_3$.

Nuclear magnetic resonance (NMR) characterisation

All three europium precursors were analysed by means of ^{1}HNMR spectroscopy (**Fig. 21**) to obtain structural information of the synthesized precursors. Although Eu^{3+} is paramagnetic and features rather unusual isotropic shifts in ^{1}HNMR, [26] all peaks could be assigned and match the expected integrals.

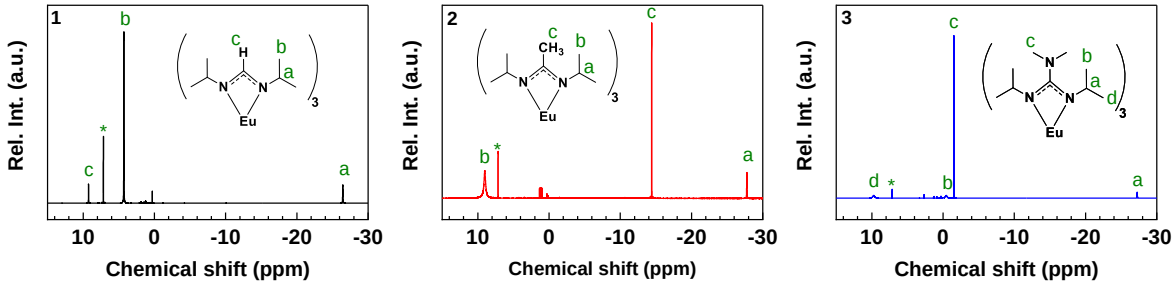


Figure 21 ^{1}H-NMR spectra (in C_6D_6) of $Eu(dpfamd)_3$, $Eu(dpamd)_3$, and $Eu(dpdmg)_3$.

Electron-impact mass spectrometry (EI-MS) characterisation

The respective EI-MS spectra are shown in **Fig. 22**. The molecular ion peak $[M]^{+\bullet}$ is detected, although being extremely low in intensity with 0.7% (577.4 m/z) for $Eu(dpfamd)_3$, 0.1% (663.2 m/z) for $Eu(dpamd)_3$, and 0.6% (533.6 m/z) for $Eu(dpdmg)_3$, respectively. In comparison, the $[Eu(L)_2]^{+\bullet}$ fragments appear to be more stable under EI-MS conditions, as evidenced by the high intensities (>55%) for all precursors.

Interestingly, peaks at higher m/z ratios than $[M]^{+\bullet}$ were detected. Even though the intensities of these peaks are rather low with 5.5% (1), 5.5% (2), and 1.0% (3), they could be assigned to oligomeric species probably from reactions of the precursor fragments. However, the general fragmentation pattern postulated from the EI-MS data is comparable with findings from previous studies on structurally analogous precursors. [24, 27, 28] All precursors undergo facile cleavage of ligand moieties, forming the fragment $[Eu(L)]^{+\bullet}$ at 278.1 m/z ($Eu(dpfamd)_3$), 292.1 m/z ($Eu(dpamd)_3$), and 321.1 m/z ($Eu(dpdmg)_3$), respectively, assignable to the respective base peak (100% intensity). Additionally, the lone intact ligand fragments $[L]^{+\bullet}$ were detected at 128.3 m/z (4.8%, $Eu(dpfamd)_3$), 141.2 m/z (40.7%, $Eu(dpamd)_3$), and 170.2 m/z (67.6%, $Eu(dpdmg)_3$), indicating a certain stability of the ligand skeleton.

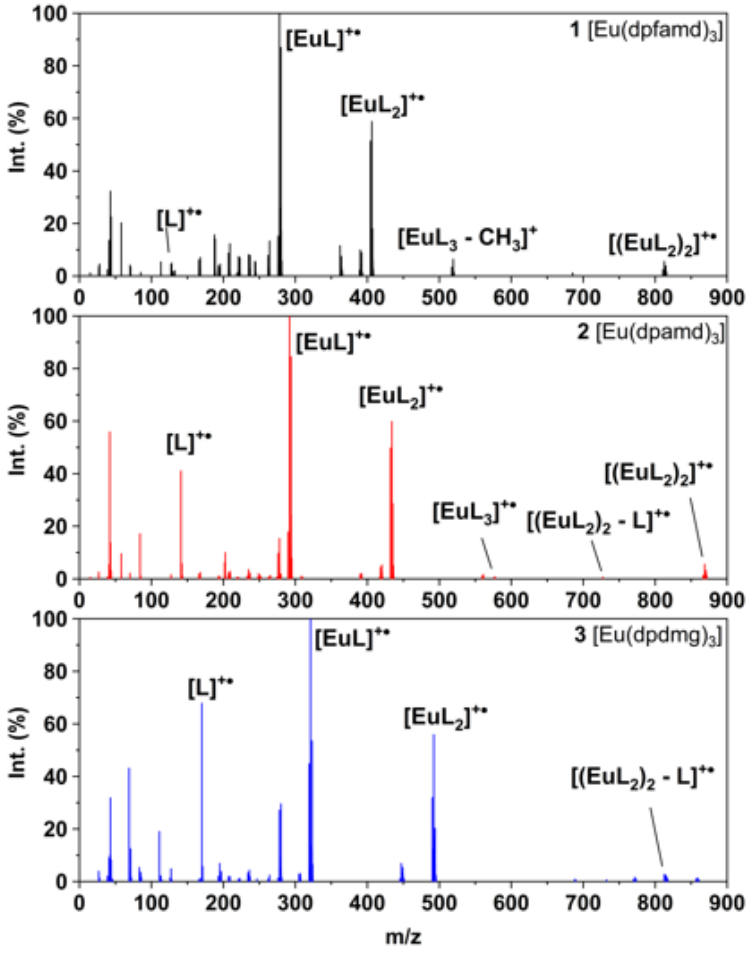


Figure 22 EI-MS (70 eV) of $Eu(dpfamd)_3$, $Eu(dpamd)_3$, and $Eu(dpdmg)_3$ with characteristic fragments assigned.

Thermal investigations of the precursors

TGA measurements of the three precursors, $Eu(dpfamd)_3$, $Eu(dpamd)_3$, and $Eu(dpdmg)_3$, are performed (**Fig. 23**), to gain insights into their physicochemical properties. Focusing on the TG curve of $Eu(dpfamd)_3$, the onset of volatilization temperature ($T_{onset,1\%}$) estimated from 1% mass loss of the precursor during the measurement is 74°C. Together with the single step occurring at 195°C graphically estimated using tangents (T_{step}) and an apparent rest mass of 3.1%, evaporation dominates during the heating of this compound.

Compared to this, $Eu(dpamd)_3$ and $Eu(dpdmg)_3$ show a lower volatility, indicated by the higher $T_{onset,1\%}$ of 79 and 94°C and T_{step} of 227 and 241°C, respectively. Furthermore, the thermal stability of these precursors seems to be lower, since residual masses of 11.4 and 30.7% are obtained, indicating evaporation of the precursors with decomposition events taking place

simultaneously upon heating. Especially for $Eu(dpdmg)_3$, a distinct second evaporation step detected at around 280°C indicates the formation of involatile byproducts, which tend to evaporate or partly decompose further during the heating process.

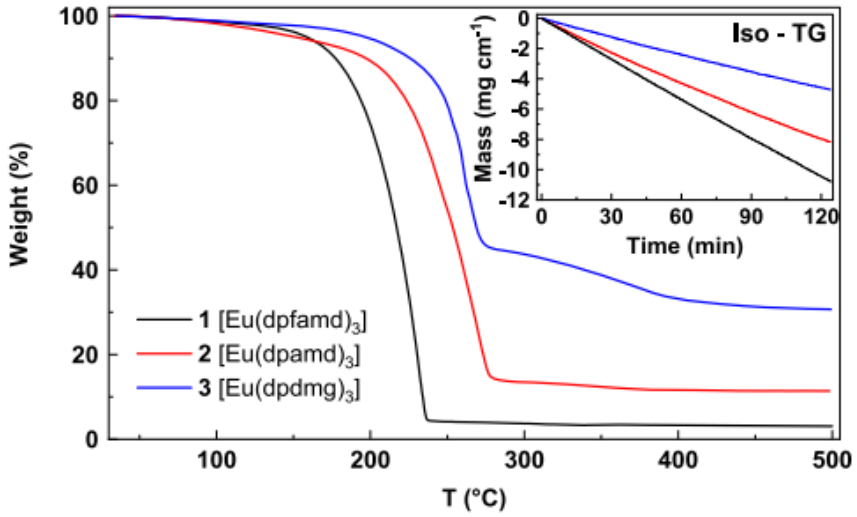


Figure 23 TG analysis of $Eu(dpfamd)_3$ (black), $Eu(dpamd)_3$ (red), and $Eu(dpdmg)_3$ (blue). The isothermal TG at 120°C is shown as an inset.

CVD process development for europium sulphide (EuS) thin films

Based on the data inferred from thermal analysis that revealed adequate volatility, and thermal stability of precursors and the identification of high reactivity toward elemental sulfur species derived from DFT analysis (**Section 8.6.1.1)**, the suitability of the three precursors for their application in CVD of EuS is assumed.

EuS thin films were successfully deposited using all three europium precursors as metal source and sulfur as a coreactant. The deposition was done on a Si(100) substrate in a moderate temperature range (400−700°C). The as-deposited thin films were analysed in terms of the structure, composition, and morphology, revealing highly oriented polycrystalline and stoichiometric EuS films. UV/vis measurements yielded a band gap of around 1.6 eV, and Raman spectroscopy exhibited a coupling between the phonons and electron spin systems of EuS. These findings, together with the soft ferromagnetic character of the films derived from semiconducting quantum interference device measurements, signify the potential of CVD grown EuS for future technological applications.

8.7 Manganese precursors

8.7.1 Results

A series of six homoleptic all nitrogen coordinated manganese (II) precursors namely, di(N,N′-diisopropyl-2-formamidinato) manganese, ($Mn(iPr_2\text{-}famd)_2$, di(N,N′-ditertbutil-2-formamidinato) manganese, ($Mn(tBu_2\text{-}famd)_2$, di(N,N′-diisopropyl-2-amidinato) manganese, ($Mn(iPr_2\text{-}amd)_2$, di(N,N′-ditertbutil-2-amidinato) manganese, ($Mn(tBu_2\text{-}amd)_2$, di(N,N′-diisopropyl-2-guanidinato) manganese, ($Mn(iPr_2\text{-}dmg)_2$, di(N,N′-ditertbutil-2-guanidinato) manganese, ($Mn(tBu_2\text{-}dmg)_2$ were synthesized, characterised and investigated through DFT calculations. The chemical structure of the investigated precursors is shown in **Fig. 24**.

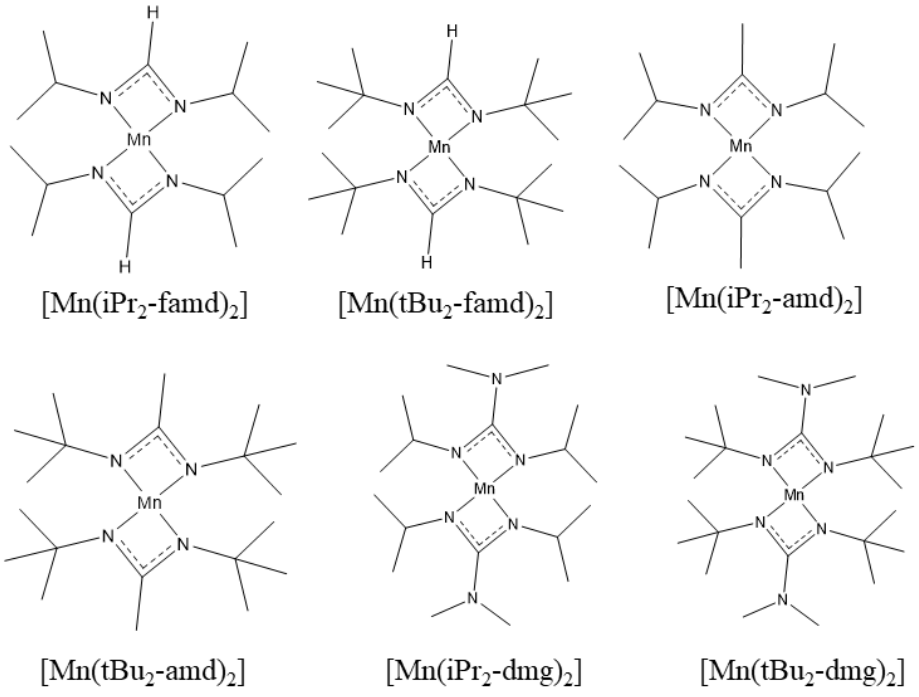


Figure 24 Molecular structure of $Mn(iPr_2famd)_2$, $Mn(tBu_2famd)_2$, $Mn(iPr_2amd)_2$, $Mn(tBu_2amd)_2$, $Mn(iPr_2dmg)_2$, $Mn(tBu_2dmg)_2$ precursors.

8.7.1.1 Computational results

The first step of the DFT studies was to evaluate the stability of the manganese precursors in the dimeric form and monomeric form. Therefore, we have modelled all precursor molecules in the monomeric form and dimeric form and calculated their bond dissociation energies, where a higher bond dissociation energy indicates a higher stability. Calculated bond dissociation

energies are presented in **Table 15**. The energy cost to remove one non-bridging ligand is higher for the manganese precursor monomers than manganese precursor dimers, indicating a higher stability of manganese precursors in the monomeric form.

Table 15 Computed bond dissociation energies to lose the first non-bridging ligand from the precursors E^{ligand} ($kJmol^{-1}$) in vacuum.

	Bond dissociation energy (kj/mol)	
	Monomer	**Dimer**
$Mn(iPr_2\text{-famd})_2$	467.33	372.81
$Mn(tBu_2\text{-famd})_2$	431.62	364.94
$Mn(iPr_2\text{-amd})_2$	480.46	417.45
$Mn(tBu_2\text{-amd})_2$	490.96	315.05
$Mn(iPr_2\text{-dmg})_2$	485.71	441.08
$Mn(tBu_2\text{-dmg})_2$	506.71	343.93

Optimised atomic structures of dimeric manganese precursors are presented in **Fig. 25**. As shown in this figure, manganese precursor dimers consist of two manganese atoms, two non-bridging ligands and two bridging ligands. For non-bridging ligands nitrogen ligand atoms are bonded to the same manganese atom and for bridging ligands the nitrogen atoms are bonded to both manganese atoms of the precursors.

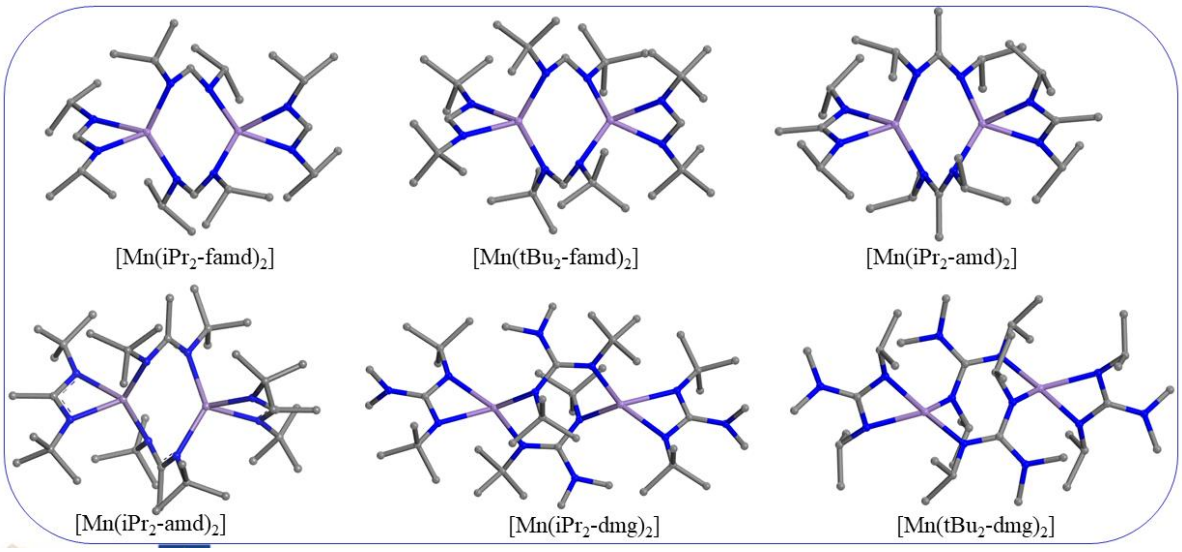


Figure 25 Optimised atomistic structures of $Mn(iPr_2famd)_2$, $Mn(tBu_2famd)_2$, $Mn(iPr_2amd)_2$, $Mn(tBu_2amd)_2$, $Mn(iPr_2dmg)_2$, $Mn(tBu_2dmg)_2$ precursors in the dimeric form in vacuum condition. Purple-Mn, blue-N, grey-C, white-H.

To get more insights into the stability of manganese precursor dimers, we have investigated in detail their geometry. **Table 16** shows the calculated Mn-N bonds to the non-bridging and bridging ligands. From **Table 16** we see that all manganese precursors have similar Mn-N distances, ranging from 2.15 Å to 2.22 Å for the non-bridging ligands and 2.13 Å to 2.15 Å for bridging ligands. A shorter Me-N bond suggests a higher stability, therefore, we expect the bridging ligands with longer Mn-N distansed to be more reactive. N-Mn-N bite angles of non-bridging ligands of all precursors are shown in **Table 17**.

Table 16 M-N distances to the non-bridging and bridging ligands of precursors in vacuum conditions.

non-bridging	**bridging**	**non-bridging**	**bridging**	**non-bridging**	**bridging**
Mn(iPr$_2$-famd)$_2$		**Mn(iPr$_2$-amd)$_2$**		**Mn(iPr$_2$-dmg)$_2$**	
2.17 Å	2.14 Å	2.17 Å	2.14 Å	2.19 Å	2.13 Å
2.19 Å	2.13 Å	2.15 Å	2.15 Å	2.16 Å	2.14 Å
2.19 Å	2.14 Å	2.15 Å	2.15 Å	2.16 Å	2.14 Å
2.20 Å	2.15 Å	2.17 Å	2.14 Å	2.19 Å	2.13 Å
Mn(tBu$_2$-famd)$_2$		**Mn(tBu$_2$-amd)$_2$**		**Mn(tBu$_2$-dmg)$_2$**	
2.17 Å	2.14 Å	2.18 Å	2.15 Å	2.19 Å	2.13 Å
2.19 Å	2.13 Å	2.20 Å	2.13 Å	2.16 Å	2.14 Å
2.19 Å	2.14 Å	2.19 Å	2.12 Å	2.16 Å	2.14 Å
2.22 Å	2.15 Å	2.21 Å	2.15 Å	2.19 Å	2.13 Å

Table 17 N-M-N bite angle of the precursors from DFT.

	N-Mn-N bite angle	
Mn(iPr$_2$-famd)$_2$	62.2 °	62.1 °
Mn(iPr$_2$-famd)$_2$	62.2 °	62.1 °
Mn(iPr$_2$-amd)$_2$	62.3 °	62.3 °
Mn(tBu$_2$-amd)$_2$	63.1 °	63.1 °
Mn(iPr$_2$-dmg)$_2$	62.4 °	62.4 °
Mn(tBu$_2$-dmg)$_2$	62.1 °	62.1 °

We also investigate the geometry of two ß-ketoimate precursors, namely [Mn(ipki)$_2$] and Mn(tBuki)$_2$]. **Fig. 26** shows the optimised structures of both ß-ketoimate precursors and **Table 18** shows their Mn-N, Mn-O distances and N-Mn-O angles. From **Table 18** we see that both precursors consist of Mn-O bonds of same length, 2.02 Å while Mn-N bonds are 0.04 Å longer

for $Mn(tBuki)_2$ compared to $Mn(ipki)_2$. Also N-Mn-O angles are larger for $Mn(tBuki)_2$ compared to $Mn(ipki)_2$. Same as for nitrogen coordinated precursors, to predict the stability we calculated bond dissociation energies of precursors and these are 527.72 kj/mol for $Mn(ipki)_2$ and 658.99 kj/mol for $Mn(tBuki)_2$. Calculated bond dissociation energy suggest e higher stability for $Mn(tBuki)_2$ and in general a higher stability of mixed O-/N-coordinated manganese precursors in comparison to all nitrogen coordinated precursors.

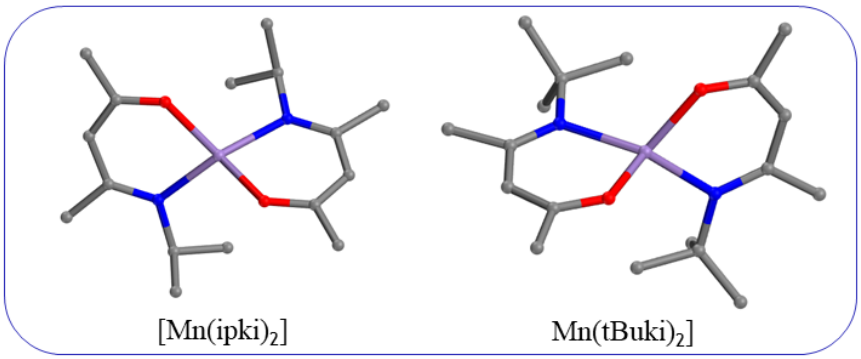


Figure 26 Optimised atomistic structures of namely $Mn(ipki)_2$ and $Mn(tBuki)_2$ in vacuum condition.

Table 18 Mn-N, Mn-O distances and N-Mn-O angles of $Mn(ipki)_2$ and $Mn(tBuki)_2$ precursors in vacuum conditions.

$Mn(ipki)_2$	**$Mn(tBuki)_2$**
Mn-N distances	
2.12 Å	2.16Å
2.12 Å	2.16 Å
Mn-O distances	
2.02 Å	2.02 Å
2.02 Å	2.02 Å
N-Mn-O bite angle	
91.28 °	93.00 °
91.30 °	92.99 °

Following a suggestion from our experimental colleagues, $Mn(tBu_2\text{-}famd)_2$ was used as model for chemical reaction simulation with oxygen. We have considered two different interaction sites of $Mn(tBu_2famd)_2$. In the first model the oxygen molecule was placed near the Mn-O bond of a non-bridging ligand while in the second model the oxygen molecule was placed near the Mn-O bond of a bridging ligand. **Fig. 27** shows the optimized structure of $Mn(tBu_2famd)_2$ precursors after the interaction with one oxygen molecule. From the first model, **Fig 27 (a)** we

see that oxygen inserts in the Mn-N bond to form a Mn-O-O-N bonds with 2.04 Å, 1.45 Å and 1.34 Å distances, respectively. However, the small calculated energy -0.02 eV shows that this reaction is not favourable. For the second model, **Fig 27 (b)** we see that the O-O bond breaks, one oxygen atom inserts in the O-N bond of the non-bridging ligand and forms new Mn-O-N bonds with distances 2.06 Å and 1.33 Å, respectively, and the second oxygen inserts in the N-C bond of the side chain of the bridging ligand and forms new N-O-C bonds with distances 1.41 Å and 1.43 Å. This reaction is favorable with a calculated energy of -1.44 eV. This finding proves the higher reactivity of bridging ligands as suggested from the calculated Mn-N distances.

We have also investigated the interactions between both ß-ketoimate precursors with oxygen, and both resulted in a positive energy (0.29 eV) indicating an unfavourable interaction. Therefore, we have considered water as an alternative. **Fig. 28** shows the optimised structures of $Mn(ipki)_2$ and $Mn(tBuki)_2$ after the interaction with one water molecule. For both precursors water binds to manganese with a Mn-O distance of 2.36 Å for $Mn(ipki)_2$ and 2.36 Å for $Mn(tBuki)_2$. Calculated interaction energies with water are -0.70 eV for $Mn(ipki)_2$ and -0.68 eV for $Mn(tBuki)_2$ and these show that in contrast to oxygen, water is a suitable coreactant for $Mn(ipki)_2$ and $Mn(tBuki)_2$.

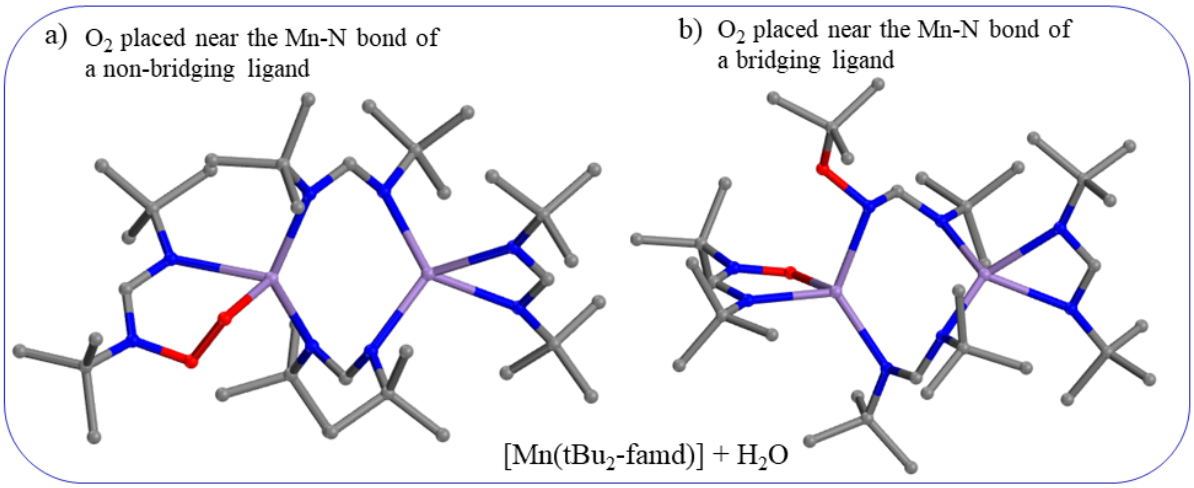


Figure 27 Optimised atomistic structures of $Mn(tBu_2\text{-famd})_2$ dimer after incorporating one oxygen molecule.

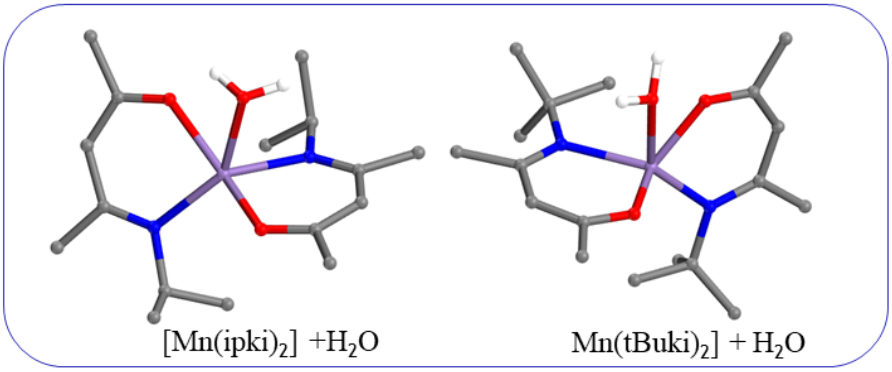
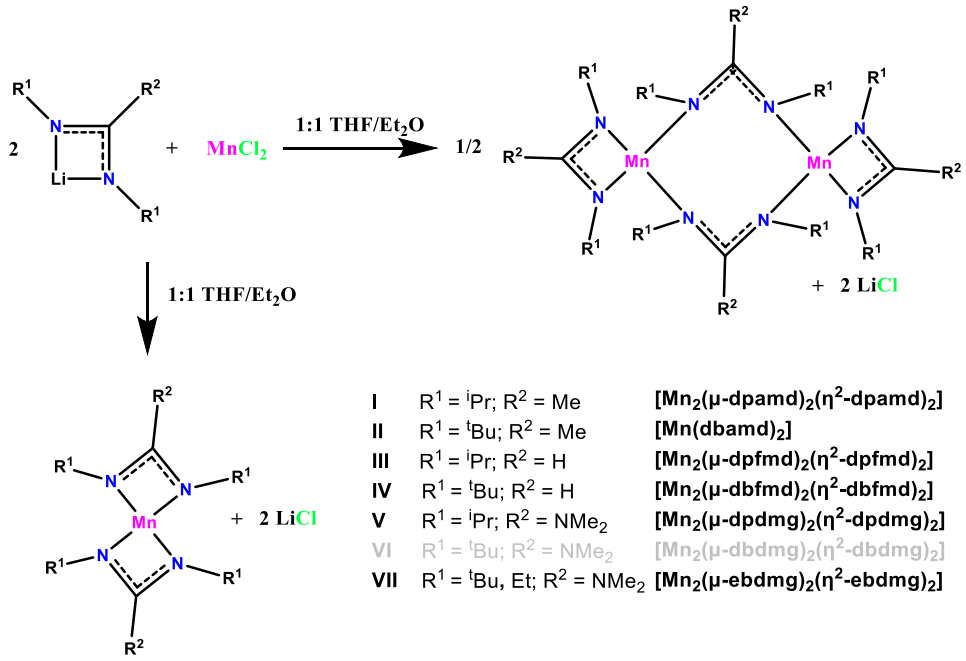


Figure 28 Optimised atomistic structures of $Mn(ipki)_2$ and $Mn(tBuki)_2$ after incorporating one water molecule.

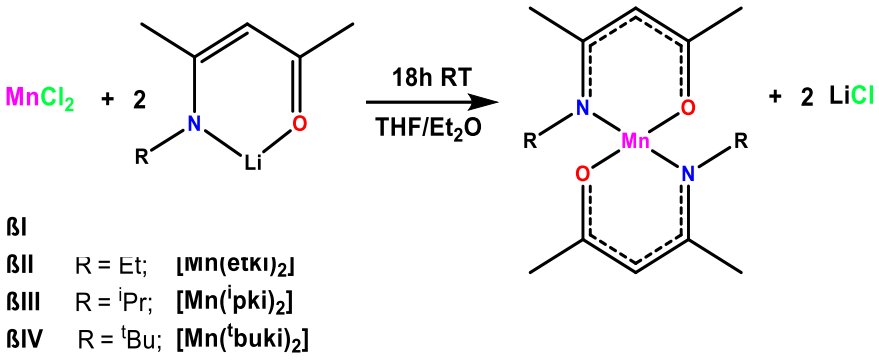
8.7.1.2 Selected experimental results (Ruhr University Bochum)

Precursor synthesis

The synthesis pathway for the targeted all nitrogen coordinated manganese precursors is presented in **Scheme 1** and for the O/N mixed coordinated manganese precursors in **Scheme 2**.



Scheme 5 Synthetic approaches for the formation of the target all nitrogen coordinated manganese precursors.



ßI
ßII R = Et; [Mn(etki)$_2$]
ßIII R = ^{i}Pr; [Mn(^{i}pki)$_2$]
ßIV R = ^{t}Bu; [Mn(^{t}buki)$_2$]

Scheme 6 Synthetic approaches for the formation of the target O/N mixed coordinated manganese precursors.

Nuclear magnetic resonance (NMR) characterisation

Evans method NMR was used to investigate the effective magnetic moment (μeff in Bohr magneton μB) which allows conclusions on the number of unpaired electrons. For all nitrogen coordinated precursors and O/N mixed coordinated precursors the investigated values range between 5.0 μ_B and 5.5 μ_B indicating 5 unpaired electrons.

Single crystal X-ray diffractometer (SC-XRD) characterisation

The solid-state crystalline structures of the precursors were recorded to gain a detailed understanding in their bonding situation. It was noticed that all nitrogen coordinated precursors crystallize in a dimeric structure while only Mn(tBu$_2$-amd)$_2$ crystallized in monomeric form, probably due to the steric bulk of the side chain and their repulsion towards the methyl group on the backbone which suppressed the ligand bridging required for dimerization. Contrary to the all nitrogen coordinated precursors, the ß-ketoiminates tend to form monomeric structures.

Electron-impact mass spectrometry (EI-MS) characterisation

To obtain insights in the fragmentation behaviour and the stability of the precursors in the gas phase after electron bombardment, EI-MS was performed. Contrary to the findings from the structure validation, for all precursors no m/z value above their respective monomeric M^+ peak was found in their respective EI-MS spectra. The found fragments with their respective intensities are tabulated in **Table 19**.

Table 19 Selected fragments for the all nitrogen coordinated manganese precursors obtained from EI-MS data.

Precursor	m/z (rel. Abund.)				
	$[M]_{mono}^{\bullet+}$	$[M\text{-}L]^{\bullet+}$	$[L]^{\bullet+}$	$[M\text{-}Me]^{\bullet+}$	$[sof]^{\bullet+}$
$Mn(iPr_2\text{-}famd)_2$	309 (12 %)	182 (24 %)	128 (19 %)	294 (26 %)	$[C_3H_5]^{\bullet+}$ 42 (100 %)
$Mn(tBu_2\text{-}famd)_2$	365 (18 %)	210 (19 %)	155 (7 %)	350 (100 %)	$[C_3H_5]^{\bullet+}$ 42 (20 %)
$Mn(iPr_2\text{-}amd)_2$	337 (31 %)	196 (54 %)	142 (3%)	322 (21 %)	$[C_3H_5]^{\bullet+}$ 42 (100 %)
$Mn(tBu_2\text{-}amd)_2$	393 (60 %)	224 (32 %)	168 (5 %)	378 (100 %)	$[C_3H_5]^{\bullet+}$ 42 (10 %)
$Mn(iPr_2\text{-}dmg)_2$	395 (5 %)	226 (16 %)	171 (4%)		$[^{i}Pr]^{\bullet+}$ 69 (100 %)
$Mn(tBu_2\text{-}dmg)_2$	395 (2 %)	226 (3 %)	171 (<1 %)		$[^{i}Pr]^{\bullet+}$ 69 (100 %)

ß-ketoiminates exhibit no significant higher m/z ratio than their respective monomeric molecular ion peak, which were over all evaluated with much higher intensities (86 %-100 %) as for the respective all nitrogen coordinated precursors in this work. **Table 20** shows selected interesting peaks with their respective intensities and suggested fragments.

Table 20 Selected fragments for the mixed O/N coordinated manganese ß-ketoiminate precursors obtained from EI-MS data.

precursors	m/z (rel. Abund.)			
	$[M]_{Mono}^{\bullet+}$	$[M\text{-}L]^{\bullet+}$	$[L]^{\bullet+}$	$[M\text{-}Me]^{\bullet+}$
(ßIII)	334 (100 %)	195 (77 %)	140 (39 %)	320 (6 %)
(ßIV)	363 (100 %)	209 (25 %)	155 (56 %)	349 (18 %)

8.8 Conclusion

This chapter presents the results of a series of six combined experimental and theoretical studies on different organometallic precursors. In each of the studies in this chapter, we used density functional theory (DFT) calculations to investigate the structure and reactivity of the new organometallic precursors using simple thermodynamics for precursor decomposition and energetics. We predict precursor stability based on the first ligand loss energies and their geometry. We also simulate the reactivity of precursors toward potential coreactants. Precursor that were found to have adequate volatility and thermal stability through thermal analysis and sufficient reactivity toward potential coreactants through our DFT calculations, were successfully employed for the deposition of the respective films through atomic layer deposition (ALD) and chemical vapour deposition (CVD). These precursors are also promising for molecular layer deposition (MLD) film growth (**Chapter 6**).

Carbene stabilized copper and silver precursors

A new carbene stabilized copper precursor, Cu(tBuNHC)(hmds) was developed as an excellent precursor for the APP-ALD of copper thin films. Bond dissociation energies calculated with DFT indicate the presence of stronger Cu–C/Cu–N interactions in Cu(tBuNHC)(hmds) compared to Ag-C/Ag-N interactions in Ag(tBuNHC)(hmds), suggesting a lower reactivity of Cu(tBuNHC)(hmds) compared to Ag(tBuNHC)(hmds). DFT also shows that while Ag(tBuNHC)(hmds) reacts favourably with hydrogen, Cu(tBuNHC)(hmds) does not, and this again confirms the higher reactivity of silver precursor compared to copper. The Cu(tBuNHC)(hmds) precursor was successfully employed for APP-ALD growth studies resulting in highly conductive and percolated (resistivity 2.9×10^{-5} Ω cm) copper thin films with a GPC of 0.23 Å/cycle and high purity with a serious potential for applications as electrodes.

Copper precursors

Four copper precursors, namely (tBuNHC)Cu(TBTMSA), (tBuNHC)Cu(SBTMSA), (iPrNHC)Cu(TBTMSA), (iPrNHC)Cu(SBTMSA), which differ from the ligand side chains were studies investigated with DFT. We found that SBTMAS precursors have shorter Cu-N bonds, higher bond dissociation energy and larger HOMO-LUMO energy gap compared to TBTMSA precursors. This indicates the higher stability of precursors with SBTMAS ligands.

DFT studies showed that hydrogen does not react with the copper precursors investigated in this study. In contrast to hydrogen, interaction energies and optimized structures showed that water reacts favorably with all precursors and this confirms that these precursors could be suitable for the deposition of thin films with water as a coreactant. To assess the potential to use (^{t}BuNHC)Cu(SBTMSA) with oxygen as a coreactant we investigated the reaction between this precursor with oxygen. The optimised structures and interaction energies showed that oxygen preferably inserts in the precursor molecule and the most sensitive bond toward oxygen is the Cu-C bond.

Cerium and ytterbium precursors

DFT study was used to analyse in detail the atomistic structure and the reactivity of $Ce(dpdmg)_3$, $Ce(dpamd)_3$, $Yb(dpdmg)_3$, and $Yb(dpamd)_3$ precursors in vacuum and in the presence of oxygen and water molecules. Interestingly, in the presence of a water molecule, the bond dissociation energy is lower for $Ce(dpdmg)_3$ and $Yb(dpdmg)_3$ than for $Ce(dpamd)_3$ and $Yb(dpamd)_3$, suggesting that guanidinate precursors exhibit a higher reactivity towards water, a well established ALD coreagent compared to the structurally related amidinates. The presence of oxygen molecules had almost no effect on ytterbium precursors, on the contrary $Ce(dpdmg)_3$ was found to have higher reactivity toward elemental oxygen than $Ce(dpamd)_3$ suggesting that it could also be used as a potential precursor for ALD with molecular oxygen. Based on the promising thermal properties in terms of volatility and thermal stability as well as data inferred from the reactivity of the molecules towards water from DFT studies, these precursors certainly bear the potential to serve as new ALD precursors.

Proof of principle studies for water-assisted ALD was performed with $Ce(dpdmg)_3$, yielding polycrystalline CeO_2 thin films on Si(100) substrates with a GPC 2.1 Å/cycle. The co-existence of Ce^{3+} and Ce^{4+} oxidation states in the films was evidenced from XPS analysis. UV/Vis analysis showed the direct allowed and indirect allowed bandgaps and hence these films could find scope for potential optical and catalytic applications.

Yttrium precursors

Four new homoleptic yttrium formamidinate precursors with different side chains, $Y(tBu_2\text{-famd})_3$, $Y(iPr_2\text{-famd})_3$, $Y(Et\text{-}tBu\text{-famd})_3$ and $Y(Cy\text{-famd})_3$ were investigated through DFT to predict how the different side chains effect their stability and reactivity towards water. It was found that all precursors tend to feature a comparable dissociation behavior, except $Y(Cy\text{-famd})_3$ which shows a slightly lower stability, and this is consistent with EI-MS findings. The

lower stability of $Y(Cy\text{-}famd)_3$ is most probably due to the steric effects of the bulky Cp ligands. While calculated interaction energies show that all precursors interact favourably with water, a more negative interaction energy was calculated for $Y(Cy\text{-}famd)_3$ which also reflects the higher reactivity of this precursor.

$Y(tBu_2\text{-}famd)_3$ was found to possess enhanced thermal stability and was selected for Y_2O_3 ALD process development where a broad ALD window ranging from 200-325°C was obtained, yielding high compositional quality films with a GPC of 0.67 Å/cycle.

Europium precursors

The reactivity of three new europium precursors, namely $Eu(dpfamd)_3$, $Eu(dpamd)_3$ and $Eu(dpdmg)_3$ towards S_2 and S_4 was assessed by DFT reaction analysis. We found that all three europium precursors react favourably with sulfur and this supports the presumption of reactive Eu-N-bonded precursors for vapor-phase deposition of EuS films. We found that all three europium precursors react favourably also with oxygen which indicates that these precursors are very promising for the deposition of Eu_2O_3 films too. In a direct comparison, the higher calculated precursor stability, expressed by the higher bond dissociation energy of precursors $Eu(dpfamd)_3$ and $Eu(dpdmg)_3$ compared to $Eu(dpamd)_3$, was in line with the findings from the reactivity studies, indicating a slightly enhanced reactivity of precursor $Eu(dpamd)_3$ toward sulfur species. This study also demonstrated for the first time the successful synthesis of high-quality, pure, and ferromagnetic EuS thin films via MOCVD.

Manganese precursors

DFT was used to examine the geometry and reactivity of six homoleptic all nitrogen coordinated manganese (II) precursors and two novel manganese ß-ketoiminates which are O/N mixed coordinated precursors. Bond dissociation energies indicate that that all nitrogen coordinated manganese precursors are more stable in the monomeric form then in the dimeric form. We have also calculated a higher stability of ß-ketoiminate precursors in comparison to nitrogen coordinated precursors. We show that $Mn(tBu_2\text{-}famd)_2$, which was selected as a representative precursor of all nitrogen coordinated precursors, reacts favourably with oxygen and promotes to breaking of the O-O bond. In contrast, ß-ketoiminates precursors showed unfavourable interaction with oxygen, most probably due to their high stability, while they reacted favourably with water. Therefore, we predict that oxygen can be used as a coreactant with nitrogen coordinated precursors and for ß-ketoiminates water is a more suitable coreactant.

8.9 References

1. N. Boysen, B. Misimi, A. Muriqi, J-L. Wree, T. Hasselmann, D. Rogalla, T. Haeger, D. Theirich, M. Nolan, Th. Riedl, Anjana Devi, *Chemical Communication*, **2020**, 56, 13752–13755.
2. J. P. Coyle, E. R. Sirianni, I. Korobkov, G. P. A. Yap, G. Dey, S. T. Barry, *Organometallics*, **2017**, 36, 2800–2810.
3. A. J. Arduengo, V. R. Dias, J. C. Calabrese, *Organometallics*, **1993**, 12, 3405–3409.
4. M. Rahm, R. Hoffmann, N. W. Ashcroft, *Chemistry—A European Journal*, **2016**, 22, 14625–14632.
5. J. Haber, T. Machej, L. Ungier, J. Ziółkowski, *Journal of Solid State Chemistry*, **1978**, 25, 207–218.
6. M. C. Biesinger, L. W. M. Lau, A. R. Gerson, R. S. C. Smart, *Applied Surface Science*, **2010**, 257, 887–898.
7. J. Chun, H. S. Lee, I. G. Jung, S. W. Lee, H. J. Kim, S. U. Son, *Organometallics*, **2010**, 29, 1518–1521.
8. P. Kaur, L. Mai, A. Muriqi, D. Zanders, R. Ghiyasi, M. Safdar, N. Boysen, M. Winter, M. Nolan, M. Karppinen A. Devi, *Chemistry-A European Journal*, **2021**, 27, 4913–4926.
9. A. P. Milanov, K. Xu, S. Cwik, H. Parala, T. Arcos, H. W. Becker, D. Rogalla, R. Cross, Sh. Pauld, A. Devi, *Dalton Transactions*, **2012**, 41, 13936–13947.
10. S. T. Barry, *Coordination Chemistry Reviews*, **2013**, 257, 3192–3201.
11. P. Lakshmanan, F. Averseng, N. Bion, L. Delannoy, J. M. Tatibouët, C. Louis, *Gold Bulletin*, **2013**, 46, 233–242.
12. Ch. Yang, X. Yu, S. Heissler, P. Weidler, A. Nefedov, Y. Wang, Ch. Wöll, Th. Kropp, J. Paier, Joachim Sauer, *Angewandte Chemie*, **2017**, 56, 16399–16404.
13. S. M. J. Beer, N. Boysen, A. Muriqi, D. Zanders, Th. Berning, D. Rogalla, C. Bock, M. Nolan, A. Devi, *Dalton Transactions*, **2021**, 50, 12944–12956.
14. Boysen, D. Zanders, Th. Berning, S. M. J. Beer, D. Rogalla, C. Bock, A. Devi, *RSC Advnces*, **2021**, 11, 2565–2574.
15. A. P. Milanov, R. A. Fischer, A. Devi, *Inorganic Chemistry*, **2008**, 47, 11405–11416.
16. R. G. Pearson, *Proceedings of the National Academy of Sciences of the United States of America*, **1986**, 83, 8440–8441.
17. S. D. Elliott, *Surface and Coatings Technology*, **2007**, 201, 9076–9081.
18. I. Kazadojev, D. J. Otway, S. D. Elliott, *Chemical Vapor Deposition*, **2013**, 19, 117–124.
19. C. Murray, S. D. Elliott, *ACS Applied Materials & Interfaces*, **2013**, 5, 3704–3715.
20. G. R. Clark, C. E. F. Rickard, P. W. J. Surman, and M. J. Taylor, *Journal of the Chemical Society, Faraday Transactions*, **1997**, 93, 2503–2507.
21. J. J. Dunsford, D. S. Tromp, K. J. Cavell, C. J. Elsevier, B. M. Kariuki, *Dalton Transactions*, **2013**, 42, 7318–7329.
22. S. M. J. Beer, A. Muriqi, P. Lindner, M. Winter, D. Rogalla, M. Nolan, A. Ney, J. Debus, A. Devi, *Chemistry of Materials*, **2022**, 34, 152–164.
23. P. Rouf, N. J. O'Brien, K. Rönnby, R. Samii, I. G. Ivanov, L. Ojamäe, H. Pedersen, *The Journal of Physical Chemistry C*, **2019**, 123, 25691–25700.

24. T. B. Thiede, M. Krasnopolski, A. P. Milanov, T. Arcos, A. Ney, H. W. Becker, D. Rogalla, J. Winter, A. Devi, R. A. Fischer, *Chemistry of Materials*, **2011,** 23, 1430–1440
25. S. L. Aeilts, M. P. Coles, D. C. Swenson, R. F. Jordan, V. G. Young, Ligands, **1998**, 7333, 3265–3270.
26. W. D. Horrocks, J. P. Sipe, *Science*, **1971**, 690, 6800–6804.
27. S. Cwik, S. M. J. Beer, M. Schmidt, N. C. Gerhardt, T. Arcos, D. Rogalla, J. Weßing, I. Giner, M. Hofmann, G. Grundmeier, A. D. Wieck, A. Devi, *Dalton Transactions*, **2019**, 48, 2926–2938.
28. M. Krasnopolski, C. G. Hrib, R. W. Seidel, M. Winter, H. W. Becker, D. Rogalla, R. A. Fischer, F. T. Edelmann, A. Devi, *Inoraganic Chemistry*, **2013**, 52, 286–296.

Chapter 9

Conclusion

9.1 Summary

In my thesis I have presented the results of first principles simulations to build up an atomistic level understanding of the chemistry of the deposition of hybrid inorganic-organic materials using molecular layer deposition (MLD). I employed density functional theory (DFT) calculations to investigate and predict the possible chemical reactions in hybrid film growth. We have collaborated also with experimental research groups on a certain number of studies as this is key to establish novel process schemes for hybrid films.

Chapter 4, presented the results of theoretical studies on aluminium based hybrid films known as "alucones". We investigated in detail the chemistry between predominant aluminium precursor for alucones, trimethylaluminium (TMA), and a wide range of organic molecules. We compared ethylene glycol (EG) and glycerol (GL) based alucones to support the experimental observations on hybrid films grown with EG and GL. We found that for both organic molecules it is most favorable to lie flat and create so-called double reactions through the two terminal hydroxyl groups. Double reactions for EG leave the surface with no hydroxyl groups available for TMA in the next cycle and the growth will be less favorable while for glycerol, the third hydroxyl group is available for continued growth. This investigation shows for the first time the origin of differences in hybrid films found for EG and GL and why GL performs better compared to EG. In addition, we investigate the chemistry between TMA and different homo- or hetero-bifunctional aromatic molecules with hydroxy and/or amino terminal groups. My findings show that aromatic molecules, in contrast to aliphatic molecules (EG and GL) preferentially assemble in an upright orientation and enable the ideal hybrid film growth. DFT also indicates that functionalisation of the aromatic rings can be done to target novel properties in the resulting hybrid film without negatively affecting the stability of the resulting film.

In **Chapter 5** we have explored the role that the substrate and the nature of titanium precursors play in promoting titanicone film growth. We have compared the reactivity of the titanium tetrachloride ($TiCl_4$) and tetrakis(dimethylamido)titanium ($Ti(DMA)_4$) precursors towards anatase TiO_2, rutile TiO_2 and Al_2O_3 surfaces and the reaction with the typical organic molecules

EG and GL. DFT shows that due to the presence of the weaker Ti-N bonds, $Ti(DMA)_4$ has a higher reactivity towards each surface and towards the organic molecules when compared to $TiCl_4$. Combined with the fact that a $Ti(DMA)_4$ based MLD process is associated with the release of noncorrosive byproducts (in contrast to $TiCl_4$) we suggest that $Ti(DMA)_4$ is more suitable for the deposition of titanicone films. Similar to alucone films, we found that organic molecules EG and GL prefer to lie flat and react with the surface with both terminal hydroxyl groups. However, with the right surface/inorganic precursor combination, the orientation of these molecules can be controlled to promote an upright binding mode of the organics. We show that with a rutile TiO_2-$TiCl_4$-EG/GL combination, the desired film growth, flexibility and stability can be achieved.

In **Chapter 6**, the results of combined experimental and DFT studies on novel magnesium, cerium and chitin based hybrid films were discussed. We explored the chemistry of these hybrid films and our findings were valuable in understanding the experimental observations. All developed processes led to hybrid films with useful properties: magnesium based films showed potential as reactive barrier layers, cerium based films showed potential for photo-emitting applications and chitin based films showed a very efficient antibacterial activity.

In **Chapter 7**, DFT results are combined with experiments at collaborators laboratories to analyse the infiltration of inorganic precursors into polymeric substrates with the vapour phase infiltration (VPI) technique. In the first study we investigated the interactions between RuO_4 with polystyrene (PS) and polymethyl methacrylate (PMMA). We found that while RuO_4 interacts favourably with PS, it does not interact with PMMA. Based on this we predicted that in a RuO_4/PS-b-PMMA VPI process the selective infiltration of the RuO_4 molecules only on PS would happen, which is important for the deposition of Ru nanostructures. This VPI process was developed experimentally and DFT data were backed from SE, XPS and FTIR characterisation techniques.

In the second study in this chapter we used DFT calculations to predict the possible reactions between the inorganic precursors trimethymindium (TMIn) and diethylzinc (DEZ) and the substrate parylene C for the deposition of indium oxide (In_2O_3) based hybrid films and zinc oxide (ZnO) based hybrid films, both with self-healing properties. Our DFT data were also supported from XPS and FTIR techniques.

In **Chapter 8**, we discuss the results of DFT studies and experimental results on new silver, copper, cerium, ytterbium, yttrium, europium and manganese precursors. Through the DFT

studies we provide atomistic level details regarding the chemistry of precursors and predict which precursors would be convenient for thin film deposition processes. Precursors suggested from DFT were employed for the deposition of metal oxides and hybrid materials.

Overall, the work in my thesis demonstrates the power and utility of atomistic level computational modelling and its importance in predicting and understanding atomic level details in precursor chemistry and thin film deposition processes and its potential to bridge theory and experiment.

9.2 Future work

In **Chapter 4** we predict the growth mechanism of alucone films based on aliphatic and aromatic organic molecules. We show that while aliphatic organics undergo the unwanted double reactions, aromatic molecules are self-assembled in an upright configuration. Based on this observation, we proposed that aromatic molecules are a more suitable candidate for MLD processes. However, in this study we do not consider the activation barriers. The kinetics of reactions of organic molecules with the surface nucleation sites can be important for the MLD growth, and are therefore important for any future work.

Temperature is a very important factor for the successful deposition of MLD films. It significantly affects the chemistry between the MLD precursors and especially the behaviour of the organic molecules in the hybrid films. Many studies have shown that the growth per cycle (GPC) of the MLD films decreases with increasing the temperature. [1-6] In **Chapter 5** we provide motivation to develop a rutile TiO_2-$TiCl_4$-EG/GL process for titanicone films, suggesting that the ideal layer-by-layer MLD film growth can be achieved. However, we have performed our DFT calculations in vacuum conditions, at 0 K. Therefore, a very interesting aspect to be considered in the future is the introduction of temperature in the TiO_2-$TiCl_4$-EG/GL process models and see if the configuration of organic molecules EG and GL changes from upright to lying flat.

Studies from experimental work show that the primary issue with most hybrid MLD films is their stability. They degrade so fast in contact with air that even the characterization of the films is often difficult. [7-10] Taking a wider perspective, the impact of ambient on stability is an interesting aspect for further study, which could be modelled using the interaction of water molecules with the hybrid material.

In my work I have used DFT to investigate the initial steps of MLD for different process. However, in reality the growth of MLD films is very complicated. Different reactions such as decomposition, desorption or condensation are believed to occur after multiple MLD cycles. [11-13] To investigate these reactions the description of more than one MLD cycle should be considered and this can be a possible next step.

A limitation of this work is that we considered the intrinsic interactions of precursors at the substrates and focused on single molecules. Future work in this area needs to consider coverage of precursors and its impact on the chemistry of hybrid material formation, which can be addressed by using larger supercells with different coverage of metal and organic precursors and even a mix of flat lying and upright precursors.

Despite this, the results of my thesis clarify many questions in the chemistry of MLD of hybrid materials and provide a strong foundation for future developments in MLD simulations.

9.3 References

1. N. M. Adamczyk, A. A. Dameron, S. M. George, *Chemistry of Materials*, **2008**, 20, 3315–3326.
2. B. Yoon, D. Seghete, A. S. Cavanagh, S. M. George, *Chemistry of Materials*, **2009**, 21, 5365–5374.
3. J. Kint, F. Mattelaer, S. S. T. Vandenbroucke, A. Muriqi, M. M. Minjauw, M. Nisula, Ph. M. Vereecken, M. Nolan, J. Dendooven, Ch. Detavernier, *Chemistry of Materials*, **2020**, 32, 4451–4466.
4. D. Choudhury, G. Rajaraman, S. K. Sarkar, *Journal of Vacuum Science and Technology*, **2018**, 108, 01A108.
5. K. Kerckhove, F. Mattelaer, J. Dendooven, Ch. Detavernier, *Dalton Transactions*, **2017**, 46, 4542–4553.
6. J. J. Brown, R. A. Hall, P. E. Kladitis, S. M. George, V. M. Bright, *ACS Nano*, **2013**, 7, 7812–7823.
7. B. Gong, G. N. Parsons, *ECS Journal of Solid State Science and Technology*, **2012**, 1, 210–215.
8. S. Lee, G. H. Baek, J. H. Lee, D. W. Choi, B. Shong, J. S. Park, *Applied Surface Science*, **2018**, 458, 864–871.
9. W. Zhou, J. Leem, I. Park, Y. Li, Z. Jin, Y. S. Min, *Journal of Materials Chemistry*, **2012**, 22, 23935–23943.
10. H. Jain, M. Creatore, P. Poodt, *Dalton Transactions*, **2022**, **51**, 7918-7927.
11. K. B. Klepper, O. Nilsen, P. A. Hansen, H. Fjellvåg, *Dalton Transactions*, **2011**, 40, 4636–4646.
12. B. H. Lee, V. R. Anderson, S. M. George, *Chemical Vapor Deposition*, **2013**, 19, 204–212.
13. K. Kerckhove, F. Mattelaer, D. Deduytsche, P. M. Vereecken, J. Dendooven, Ch. Detavernier, *Dalton Transactions*, **2016**, 45, 1176–1184.